Formation of Sub-Permafrost Methane Hydrate Reproduced by Numerical Modeling: Insights from LArge-scale Reservoir Simulator (LARS) to Mallik Site, Canadian Arctic

---

Kumulative Dissertation

zur Erlangung des akademischen Grades

doctor rerum naturalium (Dr. rer. nat.)

in der Wissenschaftsdisziplin Hydrogeologie

eingereicht an der

Mathematisch-Naturwissenschaftlichen Fakultät

der Universität Potsdam

Zhen Li

Disputation on

23 June 2023

Gutachter

Prof. Dr. Michael Kühn
Deutsches GeoForschungsZentrum GFZ
Department Geochemie
Sektion Fluidsystemmodellierung

und

Universität Potsdam
Mathematisch-Naturwissenschaftliche Fakultät
Institut für Geowissenschaften

apl. Prof. Dr. Judith Schicks
Deutsches GeoForschungsZentrum GFZ
Department Geochemie
Sektion Anorganische und Isotopengeochemie

und

Universität Potsdam
Mathematisch-Naturwissenschaftliche Fakultät
Institut für Chemie

Prof. Dr. Ann Cook
The Ohio State University
College of Arts and Sciences
School of Earth Sciences

Published online on the
Publication Server of the University of Potsdam:
https://doi.org/10.25932/publishup-60330
https://nbn-resolving.org/urn:nbn:de:kobv:517-opus4-603302

Abstract

Natural gas hydrates are ice-like crystalline compounds containing water cavities that trap natural gas molecules like CH_4, which is a potent greenhouse gas with high energy density. The Mallik site at the Mackenzie Delta in the Canadian Arctic contains a large volume of technically recoverable methane (CH_4) hydrate beneath the base of the permafrost. Understanding how the sub-permafrost hydrate is distributed can aid in searching for the ideal locations for deploying CH_4 production wells to develop the hydrate as a cleaner alternative to crude oil or coal. Globally, atmospheric warming driving permafrost thaw results in sub-permafrost hydrate dissociation, releasing CH_4 into the atmosphere to intensify global warming. It is therefore crucial to evaluate the potential risk of hydrate dissociation due to permafrost degradation.

To quantitatively predict hydrate distribution and volume in complex sub-permafrost environments, a numerical framework was developed to simulate sub-permafrost hydrate formation by coupling the equilibrium CH_4-hydrate formation approach with a fluid flow and transport simulator (TRANSPORTSE). In addition, integrating the equations of state describing ice melting and forming with TRANSPORTSE enabled this framework to simulate the permafrost evolution during the sub-permafrost hydrate formation. A modified sub-permafrost hydrate formation mechanism for the Mallik site is presented in this study. According to this mechanism, the CH_4-rich fluids have been vertically transported since the Late Pleistocene from deep overpressurized zones via geologic fault networks to form the observed hydrate deposits in the Kugmallit–Mackenzie Bay Sequences.

The established numerical framework was verified by a benchmark of hydrate formation via dissolved methane. Model calibration was performed based on laboratory data measured during a multi-stage hydrate formation experiment undertaken in the LArge scale Reservoir Simulator (LARS). As the temporal and spatial evolution of simulated and observed hydrate saturation matched well, the LARS model was therefore validated. This laboratory-scale model was then upscaled to a field-scale 2D model generated from a seismic transect across the Mallik site. The simulation confirmed the feasibility of the introduced sub-permafrost hydrate formation mechanism by demonstrating consistency with field observations. The 2D model was extended to the first 3D model of the Mallik site by using well-logs and seismic profiles, to investigate the geologic controls on the spatial hydrate distribution. An assessment of this simulation revealed the hydraulic contribution of each geological element, including relevant fault networks and sedimentary sequences. Based on the simulation results, the observed heterogeneous distribution of sub-permafrost hydrate resulted from the combined factors of the source-gas generation rate, subsurface temperature, and the permeability of geologic elements. Analysis of the results revealed that the Mallik permafrost was heated by 0.8–1.3 °C , induced by the global temperature increase of 0.44 °C and accelerated by Arctic amplification from the early 1970s to the mid-2000s.

This study presents a numerical framework that can be applied to study the formation of the permafrost-hydrate system from laboratory to field scales, across timescales ranging from hours to millions of years. Overall, these simulations deepen the knowledge about the dominant factors controlling the spatial hydrate distribution in sub-permafrost environments with heterogeneous geologic elements. The framework can support improving the design of hydrate formation experiments and provide valuable contributions to future industrial hydrate exploration and exploitation activities.

Kurzfassung

Gashydrate sind eisähnliche kristalline Verbindungen, die Moleküle wie Methan (CH_4) in Hohlräumen einschließen. Die Mallik-Lagerstätte im Mackenzie-Delta in der kanadischen Arktis enthält ein großes Volumen an technisch förderbarem CH_4-Hydrat unter dem Permafrostboden. Das Verständnis, wie die Hydrate verteilt sind, kann bei der Suche nach idealen Standorten für Förderbohrungen zu ihrer Erschließung als saubere Alternative zu Erdöl oder Kohle helfen. Weltweit führt die Erwärmung der Atmosphäre zum Auftauen des Permafrosts und zur Zersetzung der Hydrate, wodurch CH_4 in die Atmosphäre freigesetzt und die globale Erwärmung verstärkt wird. Es ist also entscheidend, das potenzielle Risiko der Hydratauflösung aufgrund der Permafrostdegradation zu bewerten.

Um die Verteilung und das Volumen von Hydraten in komplexen Sub-Permafrost Umgebungen quantitativ vorherzusagen, wurde ein numerischer Ansatz zur Simulation entwickelt. Hierzu wurde der Gleichgewichtsansatz für die CH_4-Hydratbildung mit einem Strömungs- und Transportsimulator (TRANSPORTSE) kombiniert. Die zusätzliche Integrierung der Zustandsgleichungen, die das Schmelzen und die Bildung von Eis beschreiben, ermöglichte die Simulation der Permafrostentwicklung während der Hydratbildung. Für den Standort Mallik wird ein modifizierter Bildungsmechanismus in dieser Studie beschrieben. Demzufolge wurden die CH_4-reichen Fluide seit dem späten Pleistozän aus tiefen Überdruckszonen vertikal über geologische Verwerfungssysteme transportiert, und haben die Hydratvorkommen gebildet.

Der numerische Ansatz wurde anhand eines Benchmarks zur Hydratbildung verifiziert. Messdaten eines mehrstufigen Hydratbildungsexperiments im LArge scale Reservoir Simulator (LARS) dienten zur Kalibrierung. Basierend auf der guten Übereinstimmung zwischen der simulierten und beobachteten Hydratsättigung, wurde das LARS-Modell validiert. Im Anschluss erfolgte die Übertragung auf ein 2D-Modell im Feldmaßstab, das mithilfe einer seismischen Transekte durch den Mallik-Standort erstellt wurde. Die Übereinstimmung mit den Feldbeobachtungen bestätigte den beschriebenen Mechanismus zur Hydratbildung unterhalb des Permafrosts. Das 2D-Modell wurde basierend auf Bohrlochprotokollen und seismischen Profilen zum ersten 3D-Modell des Mallik-Standorts erweitert, um die geologischen Einflüsse auf die Hydratverteilung zu untersuchen. Die Auswertung verdeutlichte den Beitrag jedes geologischen Elements zum hydraulischen System, einschließlich relevanter Verwerfungssysteme und sedimentärer Abfolgen. Die beobachtete heterogene räumliche Verteilung der Hydrate ist auf die Gasproduktionsrate der Quelle, die Untergrundtemperatur und die Durchlässigkeit der geologischen Einheiten zurückzuführen. Die Analyse der Ergebnisse ergab, dass der Mallik-Permafrost um 0,8–1,3 °C erwärmt wurde, was durch den globalen Temperaturanstieg von 0,44 °C verursacht und durch die sogenannte polare Verstärkung seit Anfang der 1970er bis Mitte der 2000er Jahre beschleunigt wurde.

Der in dieser Studie entwickelte numerische Ansatz zur Bildung von Permafrost-Hydrat-Systemen kann vom Labor- bis zum Feldmaßstab und über Zeitskalen von Stunden bis zu Millionen von Jahren angewendet werden. Mit den Simulationen konnten die dominierenden Faktoren identifiziert werden, welche die räumliche Hydratverteilung in Umgebungen mit heterogenen geologischen Strukturen steuern. Der Ansatz kann die Planung von Hydratbildungsexperimenten verbessern und einen wertvollen Beitrag für zukünftige industrielle Hydraterkundungen- und -erschließungen leisten.

Table of contents

List of figures

List of tables

List of acronyms and symbols

Abbreviations

1D	one-dimensional
2D	two-dimensional
3D	three-dimensional
AA	Arctic amplification
ANS	Alaska North Slope
BSR	bottom simulating reflector
CH_4	methane
DTS	distributed temperature sensing
EoS	equation of state
ERT	electrical resistivity tomography
GH	gas hydrate
GHPS	gas hydrate petroleum system
GHSZ	gas hydrate stability zone
GWP	global warming potential
HRS	HydrateResSim
IPCC	intergovernmental panel on climate change
ka	thousand years
kaBP	thousand years before present
LARS	LArge scale Reservoir Simulator
Ma	million years
MaBP	million years before present
MB	Mackenzie–Beaufort
mbgl	meters below ground level
mbsf	meters below seafloor
mbsl	meters below sea-level
MD	Mackenzie Delta
MHSZ	methane hydrate stability zone
mKB	depth in meters below rotary kelly-bushing
NGH	natural gas hydrate
NH	Northern Hemisphere
NMR	nuclear magnetic resonance
RCP	representative concentration pathway
RTD	resistance temperature detector
TFZ	Taglu fault zone
$T_{plus}H$	TRANSPORTSE+Hydrate
TRANSPORTSE	TRANSPORT Simulation Environment

Symbols

p	pressure	Pa
t	time	s
$\vec{v}$	Darcy velocity vector	$m \cdot s^{-1}$
W	fluid source or sink term	$kg \cdot m^{-3} \cdot s^{-1}$
k	effective permeability tensor	m^2
$\vec{g}$	gravitational acceleration vector	$m \cdot s^{-2}$
X	mass fraction	-
C	concentration matrix of mobile components	$kg \cdot m^{-3}$
D	hydrodynamic dispersion tensor	$m^2 \cdot s^{-1}$
Q	species source or sink term	$kg \cdot m^{-3} \cdot s^{-1}$
c_p	specific heat capacity	$J \cdot kg^{-1} \cdot K^{-1}$
T	temperature	°C
H	heat source or sink term	$W \cdot m^{-3}$
S	species saturation in the pore volume	-
x	molality	$mol \cdot kg^{-1}$
M	molecular weight	$kg \cdot mol^{-1}$
h	enthalpy	$J \cdot kg^{-1}$
α	matrix compressibility	Pa^{-1}
β	fluid compressibility	Pa^{-1}
κ	intrinsic permeability tensor	m^2
λ	thermal conductivity	$W \cdot m^{-1} \cdot K^{-1}$
μ	dynamic viscosity	Pa·s
ρ	density	$kg \cdot m^{-3}$
ϕ	effective porosity	-
φ	intrinsic porosity	-
χ	mole fraction	-

Indices

a	average value
eq	equilibrium
f	mobile components (pore fluid with dissolved components)
h	hydrate component
i	inhibitor component (NaCl)
m	methane component
r	immobile components (sand and hydrate)
s	quartz sand (matrix material)
w	water component
x	component in x-direction
y	component in y-direction
z	component in z-direction

Chapter 1

Introduction

1.1 Gas Hydrates in Arctic Sub-Permafrost Sediments

Methane (CH_4) is one of the most common greenhouse gases, whose global warming potential (GWP) is 27–30 times greater than carbon dioxide's GWP for a 100-year timescale (Myhre et al., 2013). CH_4 contributes significantly to the increasing atmospheric greenhouse gas concentration leading to present-day climate change (Hartmann et al., 2013; Saunois et al., 2016). A large amount of methane on the earth is naturally trapped in host sediments as gas hydrates (GHs), an ice-like crystalline inclusion compound composed of a hydrogen-bonded water network caging small guest gas molecules (Sloan and Koh, 2007). Although recent global estimates of methane hydrate inventories range over nearly two orders of magnitude (Boswell, 2009) from 500 to 55,800 Gt of methane carbon without clear convergence (Kretschmer et al., 2015), Pang et al. (2022) predict recoverable hydrate resources accounting for 20% of the total conventional oil and gas resources. While GHs have the potential to provide an immense fossil fuel resource to support the green energy transition to renewable energies, the challenges of quantifying their distribution in nature and realizing GHs extraction are substantial. Figure 1.1 shows that GHs are primarily localized in marine and sub-permafrost environments (Collett et al., 2009), but are also found under continental ice sheets, as illustrated in Figure 1.2.

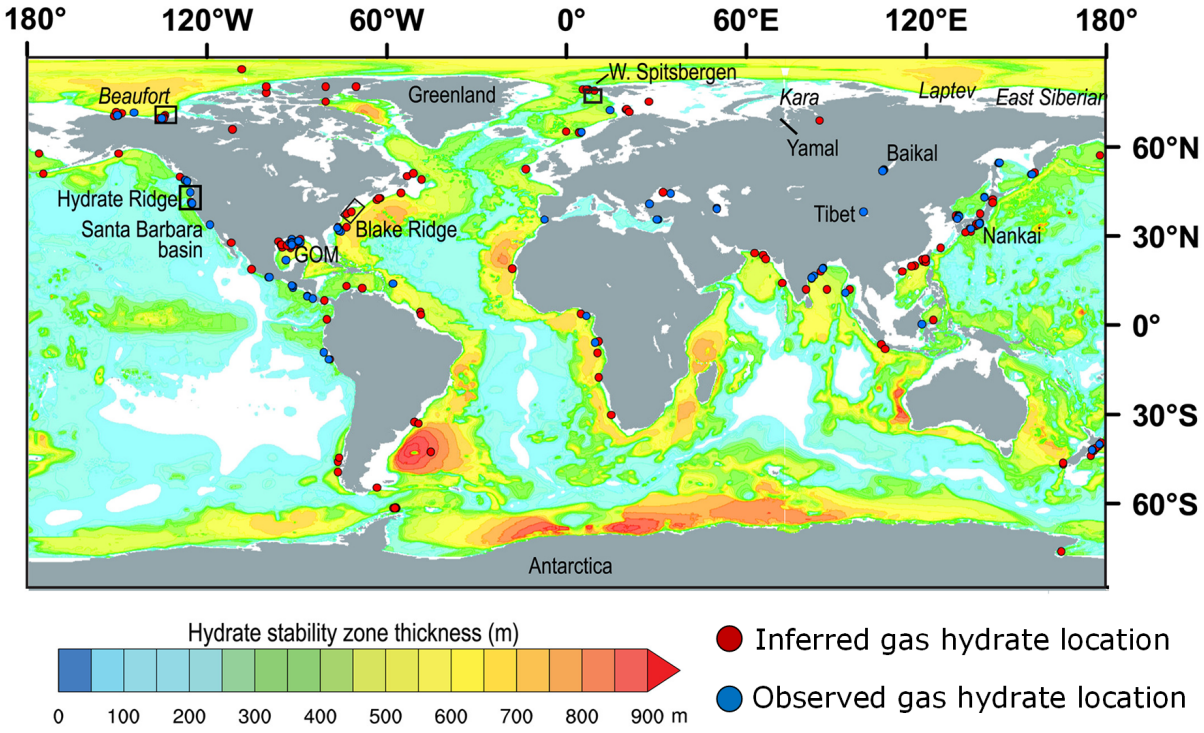

Figure 1.1: Global gas hydrate stability zone (GHSZ) thickness and locations map. Global GHSZ thickness under present-day climate conditions as the base map (Kretschmer et al., 2015), with superposed locations of observed and inferred gas hydrate (based on well logs or geophysical markers), reused from Ruppel and Kessler (2017) with copyright permission granted by John Wiley and Sons, Inc. (2023).

GHs are exclusively stable under appropriate conditions of high pressure (p) and/or low temperature (T), but they are extremely sensitive to slight variations in p-T conditions. When GHs are outside the gas hydrate stability zone (GHSZ), it will trigger GHs dissociation, which has implications for the global carbon and water cycles. GHs are a type of energy-dense, clean fossil fuel. According to Ruppel and Kessler (2017), dissociating 1 m^3 GHs from the solid phase releases a maximum of 180 m^3 of gaseous CH_4 under the standard temperature (0 °C) and pressure (1 atm). The exacerbated release of CH_4 from dissociating GHs in response to a warming event results in positive climate feedback (Berbesi et al., 2014; Kroeger and Funnell, 2012) between the geosphere and atmosphere systems.

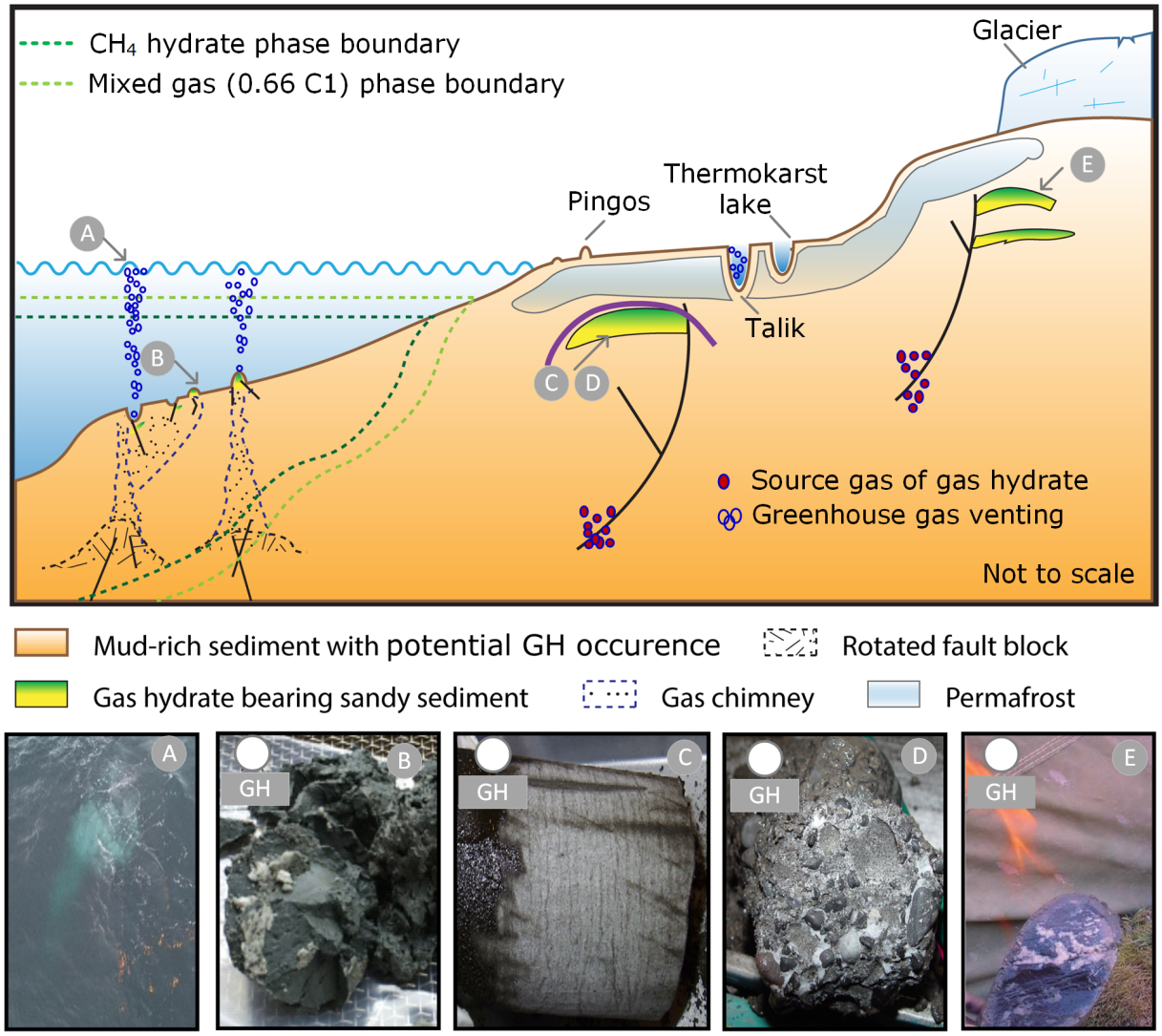

Figure 1.2: Schematic depiction of generalized gas hydrate-bearing sediments under various high-attitude and high-latitude environments. Typical gas emission and GH sample images courtesy of as follows (**A**) visual observation of bubbling CH_4 flux rising through water in the East Siberian Sea (Chuvilin et al., 2022); (**B**) GH mounds in the southwestern slope of the Chukchi Plateau, Arctic Ocean (Kim et al., 2020b); (**C**) pore-filling GH-bearing sandstone recovered from Mount Elbert (Winters et al., 2011); (**D**) GHs in the onshore arctic conglomerate, collected from Mallik, Canada (Dallimore et al., 2005a); (**E**) burning NGH sample cored from the Muli area of South Qilian Basin, China (Zhu et al., 2021). The general locations of the labeled samples by grey circles are shown, modified after Boswell et al. (2020).

Arctic GH deposits are estimated to hold 100–500 gigatons of carbon (Kretschmer et al., 2015; Marín-Moreno et al., 2016), representing more than 10% of the carbon stored in the global GH repository (Kretschmer et al., 2015). In addition, the Arctic region

is the most sensitive to climatic breakdown, warming two- to fourfold faster than the global average rate (Rantanen et al., 2022). Under the representative concentration pathway (RCP) of the 8.5 scenario (Stocker et al., 2013), the average Arctic subaerial temperature may rise by 10 – 12 K in the period from 2010 to 2100, according to the prediction by the Intergovernmental Panel on Climate Change (IPCC). Concerns about the impact of GH dissociation on the climate have prompted a series of studies aiming at unraveling the formation mechanism of sub-permafrost GH-bearing sediments and quantifying the CH_4 trapped in the Arctic GH deposits (Chuvilin et al., 2000; Safronov et al., 2010; Yakushev et al., 2018).

The Arctic Ocean hosts numerous pockmarks (Kristoffersen et al., 2022; Panieri et al., 2017) and pingo-like features (Gwiazda et al., 2018; Serov et al., 2015) associated with presently active CH_4 seeps (Figure 1.2A) and GH mounds (Figure 1.2B) that are widespread over the seafloor. These CH_4 seeps are often directly connected to dissociating GHs, with the released free gas and gas-charged fluid. For instance, recent marine surveys reveal large CH_4 seeps in the Laptev Sea, East Siberian (Shakhova et al., 2015), with the observation of bubbling CH_4 fluxes rising through an approximate 45 m thick water column and reaching the sea surface as shown in Figure 1.2A (Chuvilin et al., 2022).

In the circum-Beaufort coastal area, Mount Elbert (Figure 1.2C), Mallik (Figure 1.2D), and Taglu sub-permafrost GHs have nearly 99.4% (Lorenson et al., 2011), 99.5% (Lorenson et al., 2005; Lorenson et al., 1999), and 99% (Dallimore and Collett, 1995) of CH_4 in their gas compositions, respectively. At the listed circum-Beaufort sites, simplification of the gas composition to pure CH_4 is practicable, but it is not appropriate for the GHs with a large fraction of non-CH_4 gases. The sub-permafrost GH deposits beneath the Muli permafrost (see Figure 1.2E) in Qilian Mountain (Zhang et al., 2019) form by mixed hydrocarbon gases, such as ethane, propane, and butane, with CH_4 contents ranging from 54% to 76% (Wang et al., 2014). Figure 1.2 shows the thicknesses of GHSZ derived from mixed gas with 66% CH_4 can be more than 1.3 times thicker than the GHSZ of pure methane (Wang and Lau, 2020).

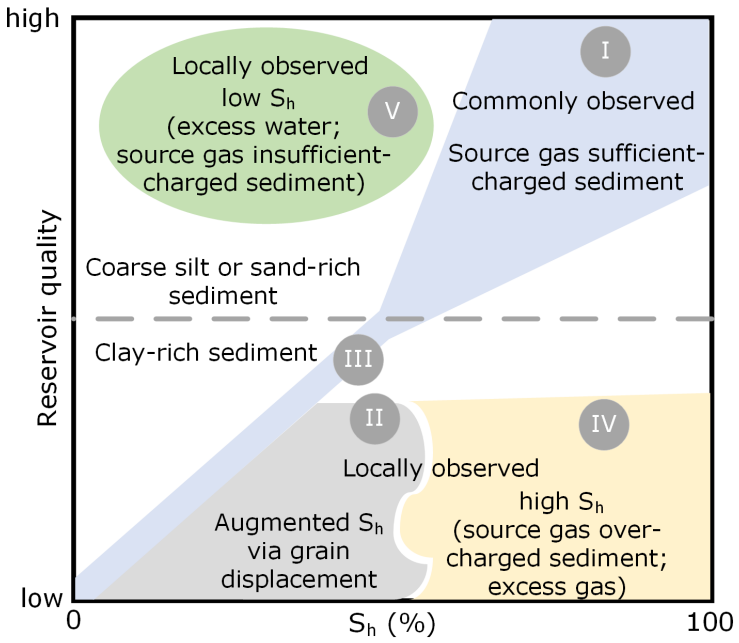

Figure 1.3: Association between gas hydrate saturation (S_h) and reservoir quality (i.e., intrinsic sediment permeability), after Boswell et al. (2020).

Permeable faults connecting source rock, mud volcano diapirism, gas chimneys, and seafloor craters are visible in the seismic data over the Beaufort fold belt (Helwig et al., 2011).

They act as vertical migrating pathways that connect deep thermogenic and shallow biogenic gases with the GHSZ, where GHs can form and accumulate. A study of subsurface temperature distributions in the Beaufort-Mackenzie Basin (Chen et al., 2008) supports the view of vertical transport for an active petroleum system from deep overpressurized zones. Highly permeable sand bodies composed of channel-shape sandstones provide lateral migrating pathways for the source gas migration, expanding the source gas-charged region and increasing GH distribution scales. Regions with a favorable coupling relationship between hydrocarbon migrating systems (e.g. faults, gas chimneys, craters) and tectonic structures (e.g. anticlines) are prospective targets for high S_h and enrichment (Wei et al., 2018). These regions are indicated in locations of C, D, and E in the upper panel of Figure 1.2.

Figure 1.3 depicts the observed GH morphologies as a function of reservoir quality versus S_h and shows five general categories of GH occurrences with varying CH_4 recoverability potentials (Boswell et al., 2020). The pore-filling (Waite et al., 2009) GH habit (categories I and III in Figure 1.3) assumes that GHs float and anchor in the middle of pore space, as consistent with the assumed GH habit in the LArge scale Reservoir Simulator (LARS). In addition, pore-scale observations (Lei et al., 2022b) also suggest GH particles in similar natural water-saturated samples also in pore-filling habit. Pore-filling GHs can occur across the entire range of reservoir quality. Whereas the observed S_h is relatively low in poor-quality fine-grained and clay-rich sediments (categories II to IV). In contrast, locally observed GHs with higher S_h (category II) are produced by grain displacement when the source gas charge is sufficient. Massive grain-displacing GHs, such as veins and nodules (category IV), can form when the source gas supply is abundant. GHs in good-quality sand- and silt-rich sediments with limited clay content (categories I and V) are commonly observed in the pore-filling habit. For example, the onshore arctic conglomerate GHs from the Mallik site (Figure 1.2D) fall under category I.

Since the discovery of GHs by Davy (1811) through a laboratory study, there has been significant progress in research on their microstructure and formation mechanisms. Modern analytical characterization instruments (Jain et al., 2019; Priegnitz et al., 2013; Priegnitz et al., 2015), such as electrical resistivity tomography (ERT) and nuclear magnetic resonance (NMR), have aided this research. Since the 1970s, the research focus has shifted toward GH deposits in natural environments (Makogon et al., 2007). The combination of experimental detection technologies and numerical simulations at both micro- and reservoir-scale has played a crucial role in supporting future GH research (Wu et al., 2018).

The LARS has been developed to reproduce the GH interval observed at the Mallik and to test new GH recovery techniques (Schicks et al., 2011). The Mallik site in the Canadian Mackenzie Delta (MD) is chosen as it holds one of the world's highest GH saturations (S_h) when Mallik wells were originally drilled and considered promising for extraction. In addition, the Mallik site has numerous similarities to marine GH deposits. Thus, the research conducted here could be applied to global GH deposits. The GH formation experiments conducted in LARS provide valuable observations to develop the numerical model in order to investigate the formation of sub-permafrost GH deposits at the Mallik site.

1.2 Needs of Developing a Permafrost-Hydrate Genesis Numerical Framework

The aims of this study are to reveal the formation mechanism of sub-permafrost GH-bearing sediments, predict GH deposit distributions, and evaluate the CH_4 trapped in

the Arctic GH deposits. The approach of this thesis is to create and verify the first numerical framework for modeling the sub-permafrost GHs formation process in laboratory-simulated and seismically inferred natural settings at the Mallik site. The purpose of developing a numerical framework (TRANSPORTSE+Hydrate, referred to as $T_{plus}H$) is to resolve the limitations found in HydrateResSim (HRS; Moridis et al. 2005). HRS is capable of describing the transport of multiple temperature-dependent components in multiple phases through a porous medium as well as GHs formation from various hydrate-forming gas in up to three spatial dimensions. However, numerous unfixed bugs (Gamwo and Liu, 2010) mean the HRS code cannot be applied to complete the work presented in this thesis. Therefore, $T_{plus}H$ was developed and verified by benchmarking it against the established HRS code to fulfill above mentioned tasks and aims of this study.

1.3 Thesis Objectives

Objectives 1–3 of this thesis focus on calibrating and validating the $T_{plus}H$-derived LARS model by using laboratory observation before applying $T_{plus}H$ to achieve the following objectives. The equilibrium GH formation approach was integrated with TRANSPORTSE to establish $T_{plus}H$, which enabled the investigation of a multi-stage GH formation experiment conducted by LARS in response to objectives 1–3. Then equations of state (EoS) for permafrost formation and degradation were developed to establish the first simulator to study the permafrost-hydrate system genesis. This innovation allowed for achieving objectives 4–8.

1. Confirm the feasibility of optional (kinetic or equilibrium) CH_4 hydrate reaction approaches for simulation that can accurately reproduce the experiment observations obtained from a multistage hydrate formation experiment conducted in LARS.
2. Verify the previously conducted ERT measurements in LARS and investigate the cause of the deviation between ERT-derived $S_{h,bulk}$ and $S_{h,bulk}$ determined by pore fluid sampling.
3. Investigate the accumulation pattern of GH crystals in the LARS specimen to confirm the optional assumptions of the GH crystals in-situ or off-site accumulation.
4. Investigate the feasibility of applying the GH formation approach employed in the laboratory-scale model to reproduce the evolution of field-scale Mallik GH deposits.
5. Examine the feasibility of the GH deposit formation mechanism proposed for Mallik site.
6. Examine the viability of the proposed timescale allowing for the formation of GH deposit.
7. Determine the influence of the geologic controls, such as geo-structural units, lithology variation, etc., on the observed spatial extent of GH deposits, and the hydrogeologic role that each fault may play during the accumulation of GH deposits.
8. Quantitative evaluation of the relationship between the near-surface temperature profiles in the MD and the permafrost warming due to modern climate changes.

1.4 Chapter Summary

The following section summarises the three published articles included in this cumulative doctoral thesis. These published articles are respectively presented in **Chapter 2**, **Chapter 3** and **Chapter 4**, and an extended discussion of the published chapters is comprehensively organized in **Chapter 5**. Conclusions with respect to the thesis objectives are given in **Chapter 6**.

The findings of this thesis consist of three main chapters. The first chapter focuses on the numerical study of the experiment conducted in LARS. The second chapter examines the

feasibility of the proposed sub-permafrost GHs genesis mechanism for the Mallik site through a 2D field-scale simulation study. The third chapter assesses the geological factors that control the distribution of GH deposits at the Mallik site through a 3D field-scale simulation study. Each chapter is briefly introduced below.

Chapter 2 presents the detailed code development of the EoS describing equilibrium GH formation, which is completed to integrate with a numerical flow and transport simulator (TRANSPORTSE) to establish $T_{plus}H$. This chapter fulfills objectives 1–3 by using the established simulator to reproduce a previously conducted multi-stage CH_4 hydrate formation experiment. The effectiveness and accuracy of the developed numerical framework were evaluated and verified by benchmarking. The LARS model was validated by the consistency between simulation results and experimental observations. The key parameters and an optimal combination of the initial and boundary conditions of the LARS experiment were determined via iterative history matching. This chapter is published as *"Numerical Simulation of Hydrate Formation in the LArge-scale Reservoir Simulator (LARS)"* in *Energies*, and cited as Li et al. (2022b) in the following.

Chapter 3 contains a sub-permafrost GH formation mechanism that CH_4-rich fluids are vertically transported from deep overpressurized zones via geologic fault networks since the Late Pleistocene and formed the present-day observed GH deposits in the shallower Kugmallit Sequence. The code of previously verified EoS has been further extended to be capable of quantifying the permafrost formation and thawing. Based on a 2D model generated from a seismic transect, this study simulated the evolution of the integrated permafrost-GH system at the Mallik site in order to quantify the thicknesses of permafrost and GH-bearing sediment, GH saturation, and ground temperature changes over geologic time. In this way, the aim of the study was to promote the understanding of the permafrost-GH system and the modern Arctic amplified permafrost warming and to confirm the introduced mechanism with the filed observations as constraints. This chapter fulfills objectives 4, 5, 6, and 8. The chapter is published as *"Numerical Simulation of Coastal Sub-Permafrost Gas Hydrate Formation in the Mackenzie Delta, Canadian Arctic"* in *Energies*, and in the following cited as Li et al. (2022a).

Chapter 4 is dedicated to fulfilling objectives 5–7 by assessing the hydrogeologic role of the regional fault networks in the CH_4-rich fluid migration and the spatial extent and S_h distribution of sub-permafrost GH deposits since the Late Pleistocene. The simulation was performed by employing $T_{plus}H$ in a 3D field-scale static model. The observations from well-logs and seismic profiles were employed to establish the first field-scale 3D model of the Mallik site, containing sedimentary sequences, anticlines, and fault networks. The simulation results were generally consistent with seismic observations and a variety of borehole evidence. Anticlines consisted of folds with reservoir-quality rocks in their core and impermeable seals in the outer layers of the fold. Due to the low permeable upward-doming zone of the anticline acting as a seal, a large amount of CH_4 was trapped and accumulated in the porous host sediment as hydrates. Away from the Mallik anticline, as observed in the weak seismic energy zones, more sediments were saturated with fluid rather than GH due to a lack of the impermeable seal in the outer layer. Without such structure, even if the *p-T* condition is suitable to form GHs, the CH_4-rich fluid that migrates along the faults may instead continue migrating upward through the permafrost strata, enter the thermokarst lake, and be released to the atmosphere rather than forming hydrates. The chapter is published as *"Geologic controls on the genesis of the Arctic permafrost and sub-permafrost methane hydrate-bearing system in the Beaufort–Mackenzie Delta"* in *Frontiers in Earth Science*.

Chapter 2

Numerical Simulation of Hydrate Formation in the LArge-scale Reservoir Simulator (LARS)

ABSTRACT

The large-scale reservoir simulator (LARS) has been previously developed to study hydrate dissociation in hydrate-bearing systems under in-situ conditions. In the present study, a numerical framework of equations of state describing hydrate formation at equilibrium conditions has been elaborated and integrated with a numerical flow and transport simulator to investigate a multi-stage hydrate formation experiment undertaken in LARS. A verification of the implemented modeling framework has been carried out by benchmarking it against another established numerical code. Three-dimensional (3D) model calibration has been performed based on laboratory data available from temperature sensors, fluid sampling, and electrical resistivity tomography. The simulation results demonstrate that temperature profiles, spatial hydrate distribution, and bulk hydrate saturation are consistent with the observations. Furthermore, our numerical framework can be applied to calibrate geophysical measurements, optimize post-processing workflows for monitoring data, improve the design of hydrate formation experiments, and investigate the temporal evolution of sub-permafrost methane hydrate reservoirs.

2.1 Introduction

Gas hydrates are ice-like crystalline compounds made of lattices of hydrogen-bond water molecules, in which hydrate-forming gas molecules are embedded (Kvenvolden et al., 1993; Sloan and Koh, 2007). Various hydrate-forming gases have been identified thus far, including some typical smaller hydrocarbons (e.g., CH_4, C_2H_6) and inorganic compounds (e.g., H_2S, CO_2), with methane (CH_4) being the most common one (Yin et al., 2018b). Naturally occurring gas hydrates are stable at elevated pressures and low temperatures, commonly present in marine environments and permafrost regions, where these conditions are fulfilled (Kvenvolden et al., 1993). Generally, approximately 97% of natural gas hydrates (NGH) are reported to be concentrated in marine environments, whereas the rest are accumulated below permanently frozen strata (Makogon, 2010), such as the Mallik NGH-bearing site in the Mackenzie Delta of Canada (Osadetz et al., 2005).

Gas hydrates are formed when gas and water molecules are in contact at high-pressure and low-temperature conditions (Koh et al., 2009). Due to the distinct cage-like hydrate structures, a high amount of gas can be embedded in the three-dimensional network of water cages. According to conservative predictions, the total amount of methane-carbon, ca. 500–2500 gigatons (Milkov, 2004), stored in worldwide NGH reservoirs is estimated to exceed the proven methane inventory of conventional gas reservoirs by about one order of magnitude (Wallmann and Schicks, 2018). Hence, NGH is considered an alternative fossil energy source and in-depth research is still required to study the NGH formation (Yin et al., 2018a) and dissociation kinetics (Yin et al., 2016) as well as their efficient utilization in sustainable

technologies (Hassanpouryouzband et al., 2020). Although methane extraction from NGH reservoirs has been investigated for almost four decades, it is still far from commercial production, and various knowledge gaps need to be addressed by scientific studies.

From micro- to macro-scale, various laboratory experimental devices (Broseta et al., 2017; Chandrasekharan Nair et al., 2018; Chong et al., 2016; Fitzgerald et al., 2012; Handa and Stupin, 1992; Heeschen et al., 2021; Li et al., 2017; Pan et al., 2020; Priest et al., 2009; Schicks et al., 2018; Schicks et al., 2020; Schicks et al., 2011; Thoutam et al., 2019; Winters et al., 2004; Yin et al., 2018b) combined with state-of-the-art monitoring equipment (Broseta et al., 2017; Heeschen et al., 2020; Pan and Schicks, 2021; Priegnitz et al., 2013; Priegnitz et al., 2015; Sa et al., 2016; Strauch et al., 2020; Zhang et al., 2017a), have been developed to investigate gas hydrate formation processes based on different hypotheses and to determine the optimum parameters for hydrate production. Evidently, it is impractical and challenging to extract intact and undisturbed NGH samples from hydrate-bearing layers. Therefore, the first objective in the laboratory study discussed here was the formation of hydrates in artificial sandy porous media, as shown in Table 2.1. Here, it has to be noted that the hydrate distribution types (hydrate habits) in the pore space have not yet been officially named or classified. As a consequence, there are many basically identical principles to categorize how gas hydrates may be embedded in a porous medium, i.e., grain coating (encrustation), cementing (cementation), load-bearing (matrix-supporting), and pore-filling hydrate habits, modified after Dai et al. (2004) by Sell et al. (2018) and Sell et al. (2016); pore-filling, load-bearing, and cementing hydrate habits by Yun et al. (2005) and Waite et al. (2009).

Table 2.1: Overview of laboratory-scale CH_4 hydrate formation tests conducted in laboratory reactors.

Experiment system	**Sample volume (L)**	**Sample material**	**NGH-bearing sediment type**
LSHV	70	quartz sand	gas-rich permafrost sediment
LARS	210	quartz sand	hydrate-rich permafrost sediment
GHASTLI	0.5	ottawa sand	gas-rich sediment
USGS-DOE	0.24	quartz sand	hydrate-rich marine sediment
NUS	0.98	silica sand	water-dominated sediment
	Hydrate formation methods	**Hydrate habits**	**Maximum $S_{h,bulk}$ (% of pore space)**
LSHV	"excess-gas"	load-bearing /cementing	~33
LARS	"dissolved-gas"	pore-filling	~90
GHASTLI	"excess-gas"	cementing	~70
USGS-DOE	"excess-gas" /"dissolved-gas"	cementing /pore-filling	-
NUS	"excess-water"	load-bearing	~40

LSHV: large-scale hydrate vessel (Fitzgerald et al., 2012; Tupsakhare et al., 2016);
LARS: LArge scale Reservoir Simulator (Heeschen et al., 2016; Priegnitz et al., 2013; Priegnitz et al., 2015; Schicks et al., 2013; Schicks et al., 2011; Spangenberg et al., 2014; Strauch et al., 2020);
GHASTLI: gas hydrate and sediment test laboratory instrument (Waite et al., 2004; Winters et al., 2004);
USGS-DOE: U.S. Geological Survey—U.S. Department of Energy (Choi et al., 2014; Waite et al., 2011);
NUS: National University of Singapore (Chong et al., 2016; Yin et al., 2019a; Yin et al., 2019b; Yin et al., 2018b).

Over the last few decades, four reliable operational procedures were developed for the synthetic formation of CH_4 hydrates in sample cells or cylindrical sample chambers for laboratory

studies. According to the theoretical basis of hydrate formation techniques reported in the literature indicated in Table 2.1, these are known as "excess-gas" (Fitzgerald et al., 2014; Fitzgerald et al., 2012; Gambelli et al., 2019; Handa and Stupin, 1992; Kono et al., 2002; Waite et al., 2004; Waite et al., 2011; Winters et al., 2004), "excess-water" (Chong et al., 2016; Cui et al., 2021; Feng et al., 2021; Priest et al., 2009; Yin et al., 2019a; Yin et al., 2019b; Yin et al., 2018b), and "dissolved-gas" methods (Choi et al., 2014; Heeschen et al., 2016; Priegnitz et al., 2015; Schicks et al., 2013; Schicks et al., 2011; Spangenberg et al., 2005; Strauch et al., 2020; Waite and Spangenberg, 2013; Waite et al., 2004).

The "excess-gas" method, also termed as "gas injection" by Fitzgerald et al. (2012) and originally presented by Handa and Stupin (1992), is the most widely used approach for hydrate formation in the laboratory. CH_4 hydrate forms in the space where injected water accumulations are trapped around grain contacts, exhibiting a cementation habit by employing the "excess-gas" method. Ordinarily, the hydrate growth rate in a gas-rich environment generated by the "excess-gas" method proves to be orders of magnitude higher than the "excess-water" method achieved in water-dominated systems. In comparison, Priest et al. (2009) reported that the outer layers of injected gaseous CH_4 bubbles are surrounded by synthetic CH_4 hydrate, showing a matrix-supporting habit by employing the "excess-water" method.

The "excess-gas" method, also termed as "gas injection" by Fitzgerald et al. (2012) and originally presented by Handa and Stupin (1992), is the most widely used approach for hydrate formation in the laboratory. CH_4 hydrate forms in the space where injected water accumulations are trapped around grain contacts, exhibiting a cementation habit by employing the "excess-gas" method. Ordinarily, the hydrate growth rate in a gas-rich environment generated by the "excess-gas" method proves to be orders of magnitude higher than the "excess-water" method achieved in water-dominated systems. In comparison, Priest et al. (2009) reported that the outer layers of injected gaseous CH_4 bubbles are surrounded by synthetic CH_4 hydrate, showing a matrix-supporting habit by employing the "excess-water" method.

CH_4 hydrate formation via the "excess-water" method requires a simpler laboratory setup and shorter experimental time periods in comparison to the "dissolved-gas" method. For mimicking the natural conditions present in hydrate-rich sediments, the "dissolved-gas" method was initially proposed by Spangenberg et al. (2005), using a sample cell filled with glass beads outfitted for a micro-scale experimental setup. Here, it was demonstrated that hydrate saturation reached approximately 95% until the termination of the experiment by the decrease in permeability. Although the occurrence of pore-filling hydrate habit was reported for the "dissolved-gas" method (Spangenberg et al., 2005; Waite and Spangenberg, 2013), pore-filling hydrate naturally turns into matrix-supporting hydrate when the local hydrate saturation reaches 25–40% (Berge et al., 1999; Yun et al., 2005). Moreover, Waite et al. (2004) and Choi et al. (2014) achieved a good balance between hydrate growth rate and high bulk hydrate saturation by using the "excess-gas" method to initiate hydrate nucleation before the continuity of hydrate growth by circulating dissolved CH_4-rich fluid.

In addition, Stern et al. (1996) suggested a special CH_4 hydrate formation technique called the "ice-seeding" method, which was originally designed to generate core-scale CH_4 hydrate samples from ice seed (pure H_2O), for further mechanical testing and the investigation of hydrate dissociation patterns. Although this method is rarely used to form CH_4 hydrates, Spangenberg et al. (2020) employed the "ice-seeding" method in combination with partial freezing to form CH_4 hydrates in sand samples.

According to our knowledge, most of these laboratory experiments involving CH_4 hydrate formation in synthetic sediments (Table 2.1) have not yet been reproduced by numerical

simulations, except for the work of Yin et al. (2019a), Yin et al. (2019b), and Yin et al. (2018b), who conducted several numerical investigations by means of the TOUGH + Hydrate simulator (Moridis, 2014). The authors aimed to explore different kinetic and equilibrium CH_4 hydrate formation models to improve the description of the "excess-water" method and establish a sensitivity analysis on the hydrate saturation distribution concerning different multi-stage cooling schemes within a core-scale cylindrical sample chamber (Chong et al., 2016; Yin et al., 2019a; Yin et al., 2019b; Yin et al., 2018b). Although many hydrochemical models and numerical codes have been developed and implemented to study CH_4 hydrate production as summarized by White et al. (2020), only a few of these are capable of reproducing hydrate formation by the "excess-gas" and "excess-water" methods. Among those numerical implementations, HRS (Gamwo and Liu, 2010; Moridis et al., 2005a) is the only available open-source and open-access code, describing both equilibrium and kinetic models of hydrate formation, and only a few studies (Wu and Hsieh, 2020; Zheng et al., 2018) have made use of it recently.

The large-scale reservoir simulator (LARS) has been established to study intermediate processes during hydrate formation via dissolved CH_4 at reservoir conditions and various hydrate dissociation strategies (Schicks et al., 2011). Laboratory tests previously undertaken in LARS offer data for calibrating numerical models to further improve process understanding as well as experimental strategies and workflows. To the author's knowledge, there is currently no numerical modeling study published that represents the observed hydrate formation or dissociation processes in LARS. Furthermore, CH_4 hydrate formation using the "dissolved-gas" method has not been simulated at core-sample scale. Consequently, the present study aims at developing a suitable numerical framework, verifying it against an established numerical simulator, and calibrating and validating it using a hydrate formation experiment undertaken in LARS.

For that purpose, a framework of equations of state (EoS) to simulate the physical properties of water with dissolved NaCl as well as CH_4 and equilibrium CH_4 hydrate formation has been developed, as demonstrated in Section 2.5.2. The EoS was then implemented and integrated with the TRANSPORT Simulation Environment (Kempka, 2020) to investigate time-dependent and spatial CH_4 hydrate formation in a porous medium at pressure and temperature (p-T) conditions representative for the Mallik site (Priegnitz et al., 2015; Uddin et al., 2014). The resulting simulation tool is referred to as $T_{plus}H$ in this study. Our simulation results demonstrate that the numerical model implementation is capable of reproducing the main processes of hydrate formation in LARS so that it can substantially support the further development of the experimental design and investigation of hydrate formation in water-dominated hydrate-rich sediments at the field scale.

2.2 Materials and Methods

2.2.1 Experimental Data from LARS

So far, eleven laboratory experiments have been successfully conducted in LARS, illustrated in Figure 2.1, including five different investigations into hydrate dissociation induced by thermal stimulation (Schicks et al., 2013; Schicks et al., 2011). Additionally, three other experiments focus on CH_4 hydrate formation along with dissociation triggered by depressurization (Heeschen et al., 2016; Priegnitz et al., 2013; Priegnitz et al., 2015;

Spangenberg et al., 2014), and the rest of the tests focused on CH_4–CO_2 or CH_4–CO_2–N_2 exchange processes (Heeschen et al., 2021; Schicks et al., 2018).

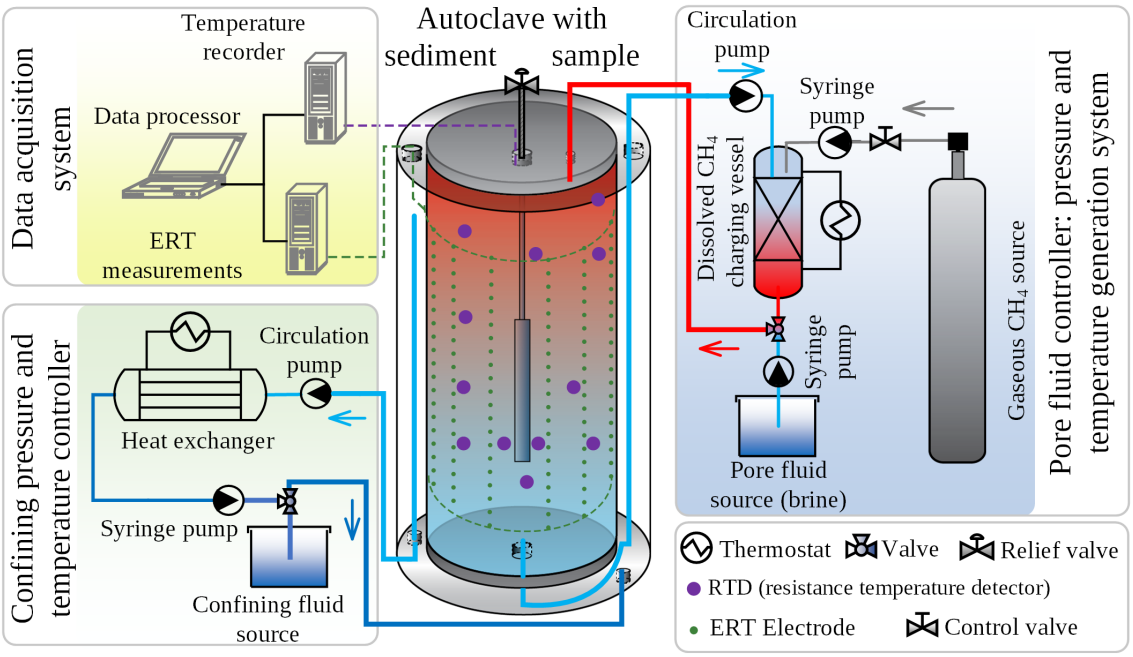

Figure 2.1: Schematic of LARS setup used in the CH_4 hydrate formation study (not to scale), modified from Spangenberg et al. (2014).

Those previously undertaken and well-analyzed laboratory tests provide numerous resources and supplement materials for the calibration and validation of numerical models. However, the major processes of those studies in LARS have neither been reproduced by numerical simulations nor addressed the fundamental hydro-chemical characteristics of the mechanisms of CH_4 hydrate formation from supersaturated dissolved CH_4 in saline fluids.

Priegnitz et al. (2015) performed two experiments to replicate the in-situ natural settings at the Mallik site (Uddin et al., 2014) and form hydrate using the "dissolved-gas" method, before the depressurization-induced CH_4 hydrate dissociation was studied in LARS (Heeschen et al., 2016; Priegnitz et al., 2015). In this course, key parameters such as the time-dependent spatial temperature distribution and bulk pressure within the sediment sample were continuously recorded based on an automatic protocol executed during the hydrate formation processes. Additionally, other crucial variables, for instance, bulk hydrate saturation ($S_{h,bulk}$) and fluid flow rate, were measured manually at regular intervals. Moreover, the workflow for quantification of the spatial hydrate saturation (S_h) distribution relied on achieving a thermal equilibrium before undertaking electrical resistivity tomography (ERT) measurements to map the spatial S_h distribution (Priegnitz et al., 2013; Priegnitz et al., 2015). Consequently, for the determination of S_h from ERT, the CH_4-loaded brine circulation was stopped to initiate temperature equilibration throughout the sandy sediment sample before performing the ERT measurement.

After a careful analysis of the experimental datasets, the early stages (ca. 15 days) of one experiment conducted by Priegnitz et al. (2015) have been selected to serve as the benchmark for model calibration and validation in the present study, as shown in Figure 2.2. Particularly, our research focuses on the conformance of simulated hydrate saturations with those derived from fluid sampling, temperature distribution, and ERT data collected during the hydrate formation experiment.

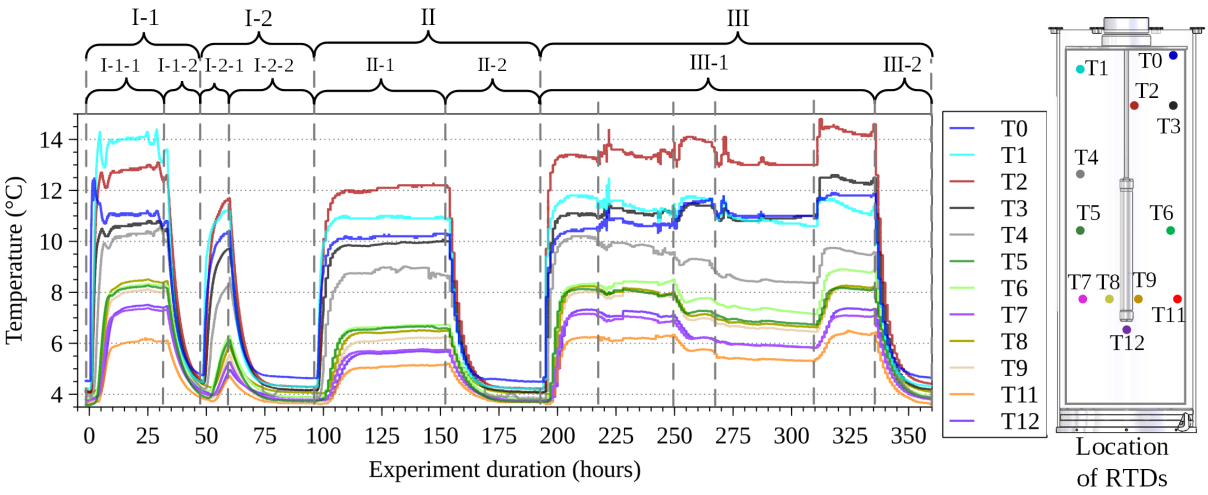

Figure 2.2: Temperatures observed at installed RTDs (cf. Table 2.2 for their coordinates) during the hydrate formation experiment in LARS (left) with their relative location (right, not to scale). Observations at T0–T12 are modified from a hydrate formation experiment conducted by Priegnitz et al. (2015)

Table 2.2: Spatial locations of RTDs employed in LARS with the temperature deviation considered for their calibration.

	T0	**T1**	**T2**	**T3**	**T4**	**T5**
Location (m) (radius, height)	(0.15, 1.28)	(0.15, 1.20)	(0.02, 1.05)	(0.16, 1.05)	(0.14, 0.85)	(0.15, 0.59)
Correction of measured T (°C)	3.2	3.0	3.0	3.1	3.2	3.3
	T6	**T7**	**T8**	**T9**	**T11**	**T12**
Location (m) (radius, height)	(0.14, 0.59)	(0.16, 0.44)	(0.06, 0.44)	(0.03, 0.44)	(0.22, 0.44)	(0.0, 0.35)
Correction of measured T (°C)	3.3	3.5	3.3	3.6	3.7	3.7

The accuracy class of RTD location is in a range from 0.01 to 0.05 m, and the measurement error of the applied Pt100 RTD is $\pm\,(0.3 + 0.005T)$ °C.

Hydrate Formation Experimental Schedule

At the onset of any hydrate formation experiments in LARS, a plastic mesh plate with fourteen mounted Pt100 temperature sensors (resistance temperature detector (RTD)) was first installed into the cylindrical sample chamber that was isolated by a neoprene rubber jacket. Subsequently, the sample chamber was filled with quartz sand and sealed by the lid of the pressure vessel from its top. Thereafter, the vessel lid combined with the sample chamber was inserted into a cylindrical autoclave, where the sample is separated from the cooling liquid, circulating in between the neoprene rubber jacket of the sample chamber and autoclave wall. Finally, the nuts and bolts of the autoclave were secured to complete the installation of the sample in LARS, and hydraulic integrity along with the availability of all types of sensors installed were verified before initiating the experiment.

Before the start of the experiment in LARS, a CH_4-free saline solution (3.68 g $NaCl{\cdot}L^{-1}$) sourced from the pore fluid container was circulated through a stainless porous filter plate from the bottom of the sample chamber to drive the air out (Priegnitz et al., 2015). After the saturation procedure, a confining pressure (ca. 14–15 MPa) was applied to the sandy specimen

by pressurizing the coolants circulating through the cooling chamber. The amount of water injected in the saturation procedure and expelled during the build-up of confining pressure was determined as a prerequisite for the estimation of the intrinsic porosity and $S_{h,bulk}$. In the next step, the brine was loaded with CH_4 and pressurized (ca. 11 MPa) in the dissolved gas charging vessel (Figure 2.1). It was then pumped into the sample chamber from the top through the hydrate-bearing sand at constant pressure and temperature. The prescribed temperature was slightly above the hydrate equilibrium temperature at the given pressure (ca. 13.6 °C at 11 MPa) to avoid the porous filter plate at the inlet from clogging by forming hydrates.

Inside the sample chamber, the temperature of the flowing pore fluid was reduced by the cooling circulation system to approximately 3.5 °C to achieve hydrate stability conditions. A considerable temperature drop of the inflowing warm CH_4-rich brine occurs close to the neoprene rubber jacket, and additional hydrate is thus formed when CH_4 solubility is decreased in the presence of hydrate nucleation (Waite and Spangenberg, 2013). Consequently, the CH_4-supersaturated pore fluid continuously releases CH_4 to form hydrate until the CH_4 concentration is reduced to maximum CH_4 solubility. The outflowing brine is then heated and reloaded with additional CH_4 in the gas charging vessel before re-entering the sample chamber for the next flow-through cycle.

Three major pore fluid circulation stages marked by Roman numbers (I to III) were considered in the numerical simulations, whereby Stage I has been divided into two Substages (I-1 and I-2) due to an unintentional interruption of the warm inflowing fluid flow for around 9 h, as indicated in Substage I-1-1 (Figure 2.2). Excluding this interruption, other intentional interruptions (Substages I-1-2, II-2, and III-2) of the inflow of warm CH_4-charged water resulted in a temperature "equilibration" of the sandy sediment sample close to the temperature of the circulating confining pressure fluid and a decline of CH_4 available for hydrate formation.

The ERT measurements taken at the end of Substages I-1-2, II-2, and III-2 (Figure 2.2) produced the most reliable resistivity distributions because the stationary conditions reduced the fluctuations in temperature and also improved the quality of the collected data. As CH_4 hydrate is an electrical insulator, ERT measurements allow for the determination of the spatial S_h distribution in the sample chamber (Priegnitz et al., 2015). Hereby, ions from the dissolved salt accumulate in the pore fluid, as only CH_4 and pure water are consumed during hydrate formation. As a result, the electrical conductivity of the pore fluid increases. Furthermore, the mass of accumulated CH_4 hydrate can be determined by using the S_h-dependent electrical conductivity approach presented by Waite et al. (2004) and Spangenberg et al. (2005). Based on that approach, the spatial S_h can be derived from spatial variation of the electrical conductivity in the hydrate-bearing sand.

According to Waite and Spangenberg (2013), the amount of CH_4 available for hydrate formation at about 5 °C amounts to approximately 42% of the initial CH_4 solubility in brine at 20 °C. By circulating the warmer CH_4-rich pore fluid through the sandy sediment sample, the accumulation rate of $S_{h,bulk}$ increases by 2 to 4.5% per day, filling almost 31% of the sample's pore space after Stage III.

Out of the fourteen installed RTDs, twelve operated and two malfunctioned (T10 and T13), with the latter excluded from previous (Priegnitz et al., 2015) to our current study. The calibration of RTDs was conducted before their installation inside LARS during the preparation of the first hydrate formation test in 2011. In addition, the original measurement deviations of the RTDs T4 and T8 were both 4.2 °C , falling out of the average measurement deviation of the other RTDs (3.3 °C). According to the correlation between the distance of these RTDs to the

fluid inlet and their temperature correction listed in Table 2.2, temperatures for RTDs T4 and T8 have been revised. Therefore, a re-correction was made in the present study using the proven temperatures of 3.2 °C and 3.3 °C for the originally calibrated temperatures for RTDs T4 and T8, respectively.

2.2.2 Mathematical Model

An equation of state (EoS) module for hydrate formation has been developed and coupled with a flow and transport simulator (Kempka, 2020) in the scope of the present study to investigate the coupled hydro-thermo-chemical processes in LARS as discussed in Section 2.2.1 (Priegnitz et al., 2013; Priegnitz et al., 2015). Kowalsky and Moridis (2007) demonstrated that an equilibrium reaction model is a feasible alternative to a kinetic approach for simulating gas hydrate behavior at the reservoir scale. However, temperature measurements in the LARS experiments were made every few seconds by the RTDs, and the sample volume of LARS is approximately 210 L. Therefore, we were not able to state until now that hydrate formation processes can be described by an equilibrium reaction approach given the aforementioned conditions. For the representation of short-term and core-scale (typically around 0.1 to 10 L) hydrate formation processes, the kinetic model is accurate and able to capture the transitional results of intermediate states (Gamwo and Liu, 2010; Kowalsky and Moridis, 2007), but its requirements in terms of computational power and numerical model convergence are substantially higher. Therefore, one objective of the present study was to investigate whether an equilibrium reaction approach is capable of representing hydrate formation via dissolved CH_4 in LARS using multi-stage cooling.

Modeling Assumptions

The developed equilibrium model utilizes the temperature and pressure-dependent relation proposed by Moridis (2003) at the hydrate-aqueous equilibrium. According to Kashchiev and Firoozabadi (2002), the aqueous solution has to be supersaturated with the hydrate-forming gas at the given pressure and temperature conditions; hydrate crystallization can then occur as the supersaturated gas is encased by the hydrate structure. Consequently, CH_4 hydrate formation or precipitation can be defined by the following reaction (Sloan and Koh, 2007):

$$CH_4 + nH_2O(\text{liquid}) \rightarrow CH_4 \cdot nH_2O(\text{solid}), \tag{2.1}$$

where the hydration number, n, commonly equals 5.9 in series of experimental studies undertaken in LARS (Priegnitz et al., 2015; Schicks et al., 2013; Spangenberg et al., 2014), with CH_4 hydrates of cubic structure I (Koh et al., 2009) being formed.

The applied numerical framework allows for conducting quantitative descriptions of the involved coupled thermal, hydraulic, and chemical processes in hydrate-bearing sand, which are presented in Section 2.5.1. Hereby, fluid migration is governed by density-driven flow in porous media (Darcy's Law), considering advective and diffusive transport of dissolved CH_4 and NaCl in the pore fluid. Moreover, heat transport and thermal energy exchange occur via conduction and convection (Kempka, 2020), complemented by the equilibrium-based CH_4 hydrate formation reaction.

In order to maintain the accuracy of the numerical solution of the non-linear system of partial differential equations, the underlying simplifications were considered to maintain computational efficiency and numerical convergence requirements:

1. The porous medium is completely filled by pore fluid and/or CH_4 hydrate, with single-phase flow considered in the entire modeling domain;
2. Deformation of the porous medium (hydrate-bearing sand) is assumed to be negligible due to the applied confining pressure of 14 to 15 MPa, with the porous medium matrix being evenly compacted and homogeneous;
3. Thermophysical properties of the aqueous solution do not consider the effects of the dissolved CH_4, as these are negligible for the present study. The dissolved inhibitor (NaCl) influences neither the molecular structure of the formed CH_4 hydrate nor the rate of hydrate formation, but fluid density, viscosity, heat conductivity and capacity as well as CH_4 solubility, only;
4. CH_4 from the supersaturated aqueous phase is directly consumed by equilibrium hydrate formation without any intermediate phase changes and side reactions;
5. Mobile components contain the aqueous phase with dissolved CH_4 and NaCl. All water-soluble species and liquids are non-volatile at the applied temperature range (0–25 °C) and pressure conditions (ca. 11 MPa).

The simplification of the inhibition effect of NaCl and other salts on hydrate formation is attributed to the fact that the salt ions bind water molecules, which are then no longer available for dissolving CH_4 molecules in the aqueous phase. Thus, the amount of CH_4 available for hydrate formation is reduced in saline aqueous solutions compared to deionized water, as presented by Malagar et al. (2019) and literature cited within it. In LARS, the saline fluid is almost fully saturated with CH_4 when it leaves the dissolved CH_4 charging vessel (Figure 2.1) and enters the sample chamber. Due to the continuous flow, CH_4 is continuously supplied as a hydrate former, so that the salting-out effect described above is reduced or even completely eliminated. Therefore, an instantaneous formation of CH_4 hydrate within LARS is observed when the salinity-corrected p-T condition is met under the equilibrium CH_4 hydrate formation approach.

Numerical Model Verification

The objective of the benchmark study discussed in the following was to verify the coupling between the CH_4 hydrate formation EOS implemented in the present study with the fluid flow and transport simulator presented by Kempka (2020). For that purpose, the well established numerical simulator HydrateResSim (Gamwo and Liu, 2010; Moridis et al., 2005a) has been used as a reference.

Figure 2.3a shows the 1D modeling domain, where the first left element acts as a cooling boundary at a constant temperature of 4 °C under the assumption of the presence of a negligible amount of hydrate nucleation. The pore space of all other elements is filled with CH_4-saturated water at an initial temperature of 16 °C. At the impermeable cooling boundary, heat exchange is allowed between it and its neighboring element. Figure 2.3b plots the T-dependent CH_4 solubility in water in the presence of hydrate (blue solid curve) derived from the equilibrium pressure and that at a constant pressure of 11 MPa without the presence of hydrate (dashed curve). With the reducing temperature of the inner modeling domain induced by the left cooling boundary, CH_4

solubility is decreased by up to approximately 52% of the initial CH_4 concentration in all other elements (Figure 2.3a), as indicated by the black arrow line in Figure 2.3b.

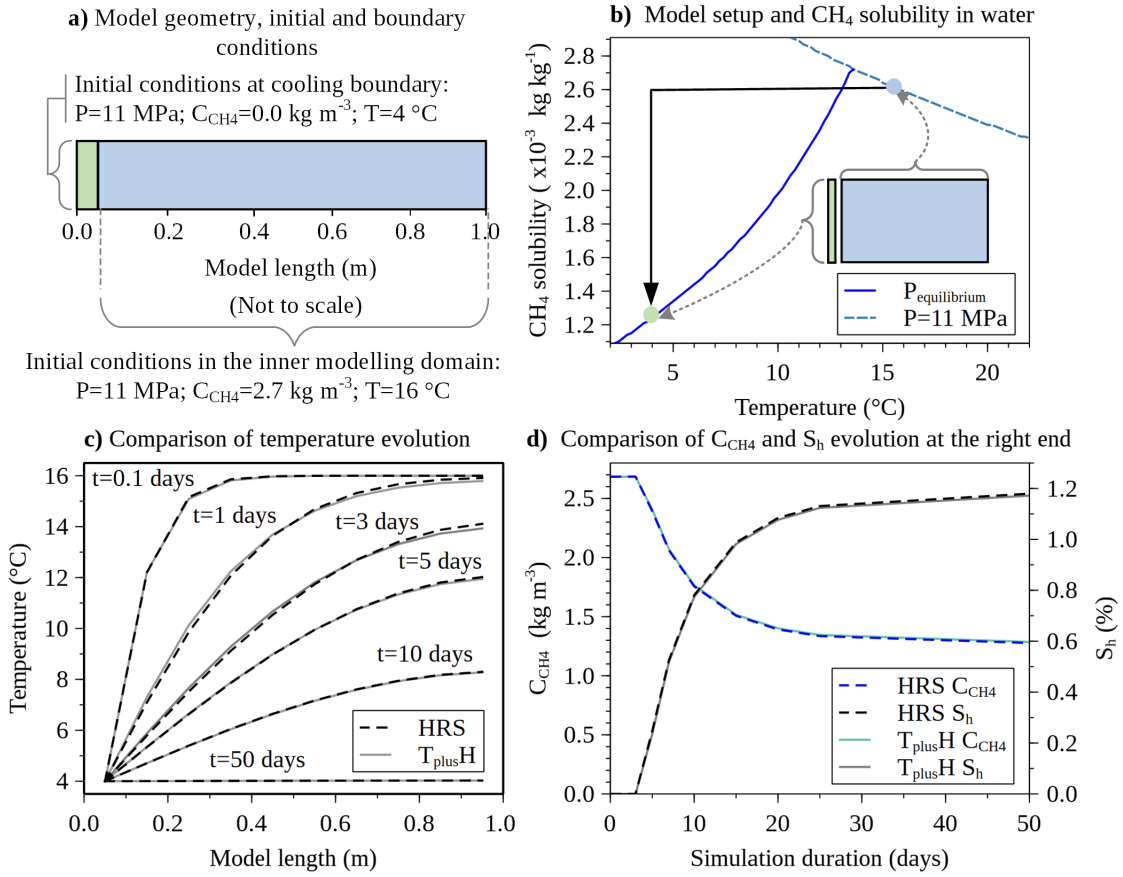

Figure 2.3: (**a**) The 1D benchmark used for verification of the implemented numerical modeling framework ($T_{plus}H$); (**b**) curves of CH_4 solubility in water in the presence of hydrate (solid curve, derived from the equilibrium pressure) and without the presence of hydrate (dashed curve, computed by the fixed pressure); (**c**) comparison of temperature distributions along the model length, computed by $T_{plus}H$ and compared against those produced by HydrateResSim (HRS); (**d**) comparison of hydrate saturation (S_h) and CH_4 concentration in fluid (C_{CH4}) at the right boundary, computed by $T_{plus}H$ against those produced by HRS.

The supersaturated dissolved CH_4 is instantly consumed by hydrate formation as the water temperature drops from 16 °C (blue dot) to 4 °C (green dot) during 50 days of simulation. Additionally, Figure 2.3c shows the temperature distribution in the model at simulation times of 0.1, 1, 3, 5, 10, and 50 days. Figure 2.3d presents the temporal evolution of the dissolved CH_4 concentration (C_{CH4}) and CH_4 hydrate saturation (S_h) at the right boundary for 50 days of simulation time as computed by $T_{plus}H$ and HRS.

Overall, the maximum relative deviation between the main simulation results, i.e., temperature, S_h and C_{CH4}, calculated by $T_{plus}H$ and HRS is < 0.5%. The main reasons for the deviations are attributed to the application of different equations of state, as well as the distinct realization for the same initial and boundary conditions in both simulators (i.e., the cooling boundary is implemented as an element with infinite volume in HRS, whereas it is a finite volume element in $T_{plus}H$). Further, additional error sources for these deviations may be attributed to the application of different temporal and spatial discretization schemes. Following the results of this benchmark, the $T_{plus}H$ simulation results show a similarly high accuracy, so we conclude that our code is capable of addressing the main objective of the study: the simulation of the hydrate formation experiment undertaken in LARS as discussed in the following section.

2.2.3 Model Implementation to Reproduce the LARS Experiments

Following the successful model verification, $T_{plus}H$ is calibrated using the experimental LARS data. For that purpose, temperature profiles determined by the installed RTDs and spatial hydrate saturations derived from geophysical monitoring as well as fluid sampling were reproduced numerically.

Model Geometry

Figure 2.4b shows the geometry and dimensions (1.3 m × 0.24 m × 0.24 m) of the implemented model, consisting of a cuboid containing a quarter of the LARS cylindrical sample chamber (height 1.28 m, radius 0.23 m) under the assumption of symmetry in both lateral directions. The top boundary represents the porous filter plate used to redistribute the inflowing fluid at the inlet into a surficial flux, with a source term marked by the red square in Figure 2.4a, derived from the assumption of partial clogging of the filter plate by hydrate and sand. The thicknesses of the inlet and outlet layers are both 0.01 m. In total, the entire 3D domain contains $24 \times 24 \times 130 = 74,880$ elements, whereby each cubic element has a volume of 1 cm^3.

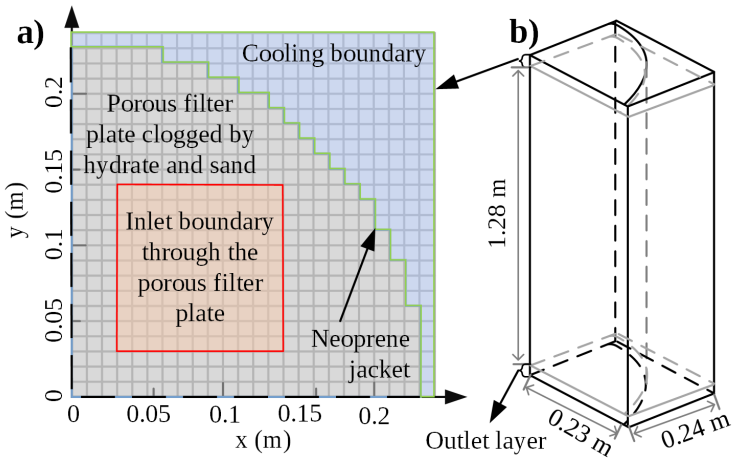

Figure 2.4: Simulation domain with numerical grid employed for the numerical simulations of the LARS experiment: (**a**) grid and inlet boundary geometry (porous filter plate at the top) with cooling boundary outside the neoprene jacket; (**b**) model geometry of the sample chamber and cooling boundary with the outlet layer at bottom (not to scale).

Initial and Boundary Conditions

The initially homogeneous thermophysical properties of the porous medium in LARS change with the increase in S_h, i.e., effective porosity and permeability as well as effective heat conductivity of the immobile components decrease. The sampled $S_{h,bulk}$ exceeded 89% and the local S_h observed by ERT reached ca. 94.2% at the end of the hydrate formation experiment, while the minimum local effective permeability calculated by the Carman–Kozeny relation (Equation 2.14) was 28.8 mDarcy (Priegnitz et al., 2015). In contrast to the ERT observations, the measured effective permeability was 2 mDarcy (Heeschen et al., 2020) at the final stage, maintained by a local S_h of 97.5% and residual pore fluid saturation of 2.5%. Applicable thermophysical properties for the porous medium in LARS were determined using an iterative matching approach and are summarized in Table 2.3.

Only limited information is provided in the description of the hydrate formation experiment in Priegnitz et al. (2015), comprising the estimated temperature ranges of the fluid at the inlet and the surrounding coolants as well as the average $S_{h,bulk}$ accumulation rates (ca.

Table 2.3: Thermophysical properties of the porous medium and related components in LARS.

Parameters	Value	Unit	Reference
Intrinsic permeability of porous medium	500	Darcy	Heeschen et al. (2016)
Intrinsic porosity of porous medium	0.35	-	Heeschen et al. (2016)
Salinity of pore fluid	5	kg m^{-3}	Heeschen et al. (2016)
Initial pore pressure	11	MPa	Priegnitz et al. (2015)
Density of quartz sand	2650	kg m^{-3}	Yin et al. (2018b)
Thermal conductivity of wet sand	2.36	W m^{-1} K^{-1}	Smits et al. (2010)
Thermal conductivity of CH_4 hydrate	0.68	W m^{-1} K^{-1}	Huang et al. (2005)
Specific heat of quartz sand	830	J kg^{-1} K^{-1}	Waite et al. (2009)
Specific heat of CH_4 hydrate	2100	J kg^{-1} K^{-1}	Waite et al. (2009)
Diffusion coefficient	1.3×10^{-9}	m^2 s^{-1}	Assumed
Density of inhibitor (NaCl)	2160	kg m^{-3}	Moridis et al. (2005a)
Compressibility of porous medium	1.0×10^{-10}	Pa^{-1}	Assumed

2% per day). Other data required for model parametrization, such as the average inlet fluid rate (ca. 80 L per day), were derived from experimental records of an identical experiment. As the actual fluid temperature after passing through the porous filter plate was not determined in the laboratory study, it was estimated from the provided temperature thresholds (13.6–16 °C). Hereby, the lower limit was chosen to ensure that the inflowing brine temperature remains above hydrate stability conditions (ca. 13.6 °C) at the given pressures. The evaluated upper temperature limit (ca. 16 °C) was determined based on a measurement in the dissolved CH_4 charging vessel undertaken at the start of the experiment.

Table 2.4: Main variables for determining thermo-physically reasonable initial and boundary conditions for model calibration.

Variable	Range	Precision	Unit
Fluid pressure	[11, 11.1]	±0.1	MPa
External coolant temperature	[3.5, 4.0]	±0.1	°C
Inflowing fluid temperature	[13.6, 16]	±1.5	°C
Dissolved CH_4 concentration	[60, 90]	±10	% of CH_4 solubility limit at given p-T conditions
Initial inflowing fluid rate	[50, 100]	±5	Liters per day

Moreover, the pore fluid control system (Figure 2.1) was implemented by means of a Neumann boundary condition in the numerical model (Figure 2.4a). The coolant circulation system and the confining chamber were introduced as Dirichlet boundary conditions with impermeable hydraulic properties, fixed pore pressure, and constant temperature gradient linearly increasing from the fluid inlet (ca. 3.5 °C) to the outlet (ca. 4.0 °C). The coolant temperature was measured once at the cooling chamber inlet, and then the coolant was assumed to be heated gradually by the thermal energy transmitted through the neoprene jacket from the sediment chamber. The temperature of the recycled coolant was determined once before entering the heat exchanger (Figure 2.1) at less than 4.0 °C. The main variables used to determine thermo-physically reasonable initial and boundary conditions, implemented for model calibration by means of an iterative history-matching procedure, are summarized in Table 2.4.

2.3 Results and Discussion

One multistage CH_4 hydrate formation experiment was chosen for the following model validation as indicated in Figure 2.2. This experiment is also referenced as "LARS RUN2" (Priegnitz et al., 2015) in the research on spatial S_h characterization by ERT as well as "experiment A" (Heeschen et al., 2016) in the investigation of gas production triggered by a multistage depressurization scheme. The temporal evolution of temperature profiles recorded at twelve RTDs is compared with the simulation results for model calibration. Hereby, the location of the temperature sensors was accordingly calibrated, and thus revised as discussed in Section 2.3.1. After calibration, the model was validated by comparison of the temporal and spatial evolution of the simulated and observed hydrate saturations presented in Section 2.3.3. An overview of the experimental temperature evolution and numerical predictions at an early period of the hydrate formation experiment is shown in Figure 2.5.

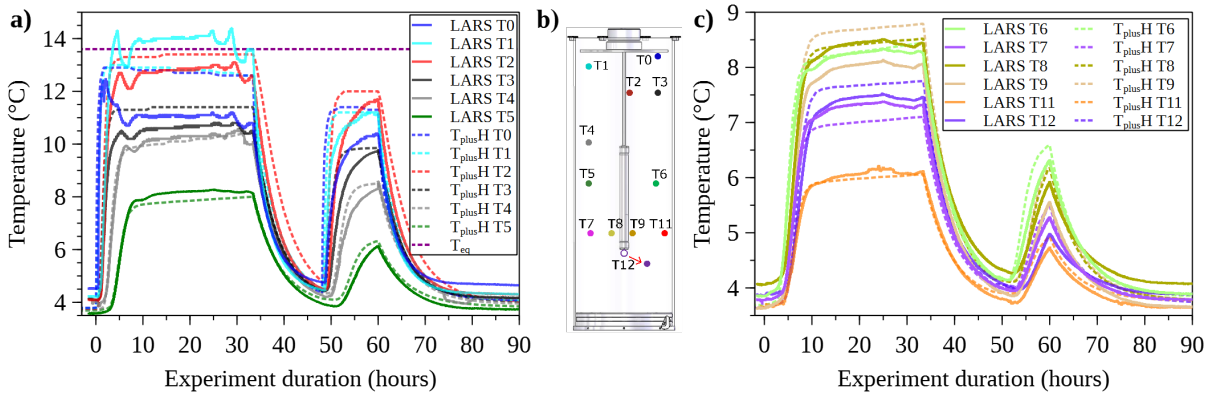

Figure 2.5: Overview of temperature evolution during 90 h of hydrate formation: comparison of observed temperatures at the RTDs T0–T5 (**a**) together with T6–T9, T11, and T12, (**c**) with the $T_{plus}H$ simulation results (dashed) obtained by revising the RTD locations in the numerical model; the equilibrium line T_{eq} identifies the CH_4 hydrate stability temperature of 13.6 °C at the given pressure and salinity; (**b**) schematic of the revised RTD locations within LARS (not to scale). LARS T0–T12 data were adapted from the CH_4 hydrate formation experiment conducted by Priegnitz et al. (2015).

2.3.1 Model Calibration

Model Calibration by Comparison of Simulated and Observed Temperature Evolution Profiles

The experiment and simulation started with the circulation of the CH_4-saturated brine sourced from the gas-charging vessel (Figure 2.1), defined as hour zero of the experimental time in Figure 2.5. Before hour zero, the hydrate-bearing sand is assumed to be filled with a negligible amount of hydrate crystals, and the porous filter plate is partially clogged by a mixture of hydrate and sand. Stage I is regarded as the most representative period of the hydrate formation experiment, considering that each period is influenced by different effects discussed in the following.

As outlined in Figure 2.2, Stage I has been divided into two Substages (I-1 and I-2) due to the occurrence of an unexpected discontinuity in the provision of the warm CH_4-rich fluid during the time period 33.4 to 47.5 h (Table 2.6). After the fluid flow interruption, the warm CH_4-rich fluid re-entered LARS from hour 47.5 on, until the pumping system was shut down 12.5 h later for ERT measurements to be taken at hour 90. Considering the uncertainties related to the manual temperature and rate control of the injected fluid, data in Figures 2.2 and 2.5

suggest that the inlet fluid parameters were occasionally not fully maintained according to the experimental plan.

The earliest rapid temperature increase was captured at RTD T0, with the shortest distance to the fluid inlet, and the peak temperature (slightly below 14.5 °C) was recorded by RTD T1 during Stage I-1 (Figure 2.5a). The simulated warm and CH_4-rich fluid reached T1, T2, and T3 at almost the same time, whereas the measured temperature front arrival delay between RTD T0 and T1 was about 2 h. In contrast to the respective experimental results, the numerically predicted arrival time of the elevated temperature front between T0 and T1 is over 0.8 h, and those between T1 and T2 as well as T3 are approximately 1.2 h, as the distances of T2 and T3 to the fluid inlet are identical.

RTD T0 was expected to record the highest temperatures during the entire experiment duration, because the inflowing warm fluid should reach RTD T0 first under the assumption of a homogeneous porous medium. However, the temperature curve at T0 barely reached 12.5 °C at the beginning, and then it gradually declined to about 10.8 °C after 4 h. The highest temperature reading at RTD T1 was more than 3 °C higher compared to the corresponding simulated one at T0 in Stage I-1. This anomalous behavior did not occur during the remaining experiment, where the numerical predictions at the T1 location were in line with the observed temperatures. Despite the possibility of instrumental failures and spatial displacement of RTDs during their installation, it is reasonable to assume that the region near RTD T0 had a higher CH_4 hydrate saturation than that obtained from the simulations. The region near RTD T1 was assumed to have a lower CH_4 hydrate saturation than the simulated one, and thus more inflowing warm water was redistributed from the area near sensor T0 to the location of T1. This may be explained by a considerable amount of hydrate being present at the top of the sample chamber before hour zero of the experiment, resulting in RTD T0 being coated or surrounded by hydrate much earlier than in our simulation.

The simulated temperatures obtained for the RTD positions T2–T6, T8, T11, and T12 match very well with their corresponding observations (Figure 2.5). Additionally, the general tendency of the simulated temperatures at RTDs T3, T7, and T9 is consistent with the observations, even though it shows maximum deviations of 8% during the time period of 10 to 33 h.

Calibration of RTD Locations

RTD locations in the model were adjusted to calibrate the simulated temperatures by the observed ones. For the simulation results presented in Figure 2.5, the obtained numerical predictions were not extracted from the exact coordinates plotted in Table 2.2, because (1) the RTDs' actual spatial detection range as well as pressure and flow rate sensitivity regarding its measurement accuracy are unknown; (2) it is very likely that unquantifiable deformation has been introduced during the installation of the sample chamber when it was hoisted for mounting into the pressure vessel; (3) further immeasurable deformation may occur during compaction of the sediment sample when the confining pressure is initially applied; (4) inevitable position deviation may emerge during the manual installation of the temperature sensors onto the reserved holes of the plastic frame.

To improve the match between the simulated and experimental data, the spatial RTD positions have been adopted within a range of 0.01 m (region close to sample chamber top) to 0.04 m (region close to sample chamber bottom), except for RTD T12 (Table 2.5). This noticeable deviation of the revised location of RTD T12 may be attributed to the heterogeneity introduced by local compactions of the hydrate-bearing sand during the installation of the counter-current

heat-exchange reactor (Schicks et al., 2013; Schicks et al., 2011) in the experimental setup (Figure 2.5b).

Table 2.5: Revised locations of the RTDs deployed in LARS.

	T0	**T1**	**T2**	**T3**	**T4**	**T5**
Revised location (m) (radius, height)	(0.18, 1.27)	(0.14, 1.2)	(0.02, 1.05)	(0.15, 1.07)	(0.13, 0.84)	(0.14, 0.6)
Displacement of relocation (m)	0.03	0.01	0.008	0.02	0.016	0.013
	T6	**T7**	**T8**	**T9**	**T11**	**T12**
Revised location (m) (radius, height)	(0.13, 0.6)	(0.14, 0.44)	(0.07, 0.43)	(0.03, 0.44)	(0.18, 0.43)	(0.08, 0.34)
Displacement of relocation (m)	0.028	0.018	0.028	0.036	0.032	0.085

In summary, data in Figure 2.5 show that the majority of the simulated temperatures are in very good agreement with the observed ones, excluding a few RTDs positioned close to the sample chamber boundaries. Consequently, the applied numerical model has been successfully calibrated using the temperatures recorded at the RTDs.

2.3.2 Model Calibration and Validation

By implementing the previously introduced initial and boundary conditions within the bandwidths listed in Table 2.4, the best-fit combinations with minimum deviation from the observations were obtained from the model calibration based on Stage I results in the previous section. Subsequently, further model calibration based on Stages II and III was achieved via an iterative history-matching procedure. As a result, the model parametrization was revised accordingly (Table 2.6). As shown in Figure 2.2 and Table 2.6, the CH_4-loaded brine inflow periods are represented by Substages I-1-1, I-2-1, II-1, and III-1, with the rest of the experimental duration determined by brine inflow suspension periods.

Table 2.6: Main parameters of the initial and boundary conditions employed in the simulation study on the CH_4 hydrate formation experiment performed in LARS (see Figure 2.2 for the division of Substages).

Substage	**Interval (hours)**	**Inflowing fluid temperature (°C)**	**Inflowing fluid rates (L/Day)**	**C_{CH4} (kg m^{-3})**
I-1-1	0–0.8–33.4	13.6	97.0	0–2.69
I-1-2	33.4–47.5	-	-	-
I-2-1	47.5–48.5–60	12.5	64.7	1.2–2.41
I-2-2	60–95.3	-	-	-
II-1	95.3–97–144.5–153.2	13.8	56.7–55.9–56.7	1.2–2.55–2.41
II-2	97–193.5	-	-	-
III-1	193.5–195–215–249 –265–282–310.5–314 –333.8–335	14.5–14.3–14.3–14.5 –14–14.5–16–15.5 –15.5	76.8–76.8–68.3–52.7 –49.8–46.1–58.5 –57.6–59.5	1.2–2.03–2.01–2.03 –2.01–1.96–1.89–1.93 –1.20
III-2	335–360	-	-	-

Model Calibration via Comparison of the Temporal Evolution of Simulated and Observed Temperature Profiles

During the LARS experiment and simulation, contribution to the temperature increment within the sample chamber is made by the combined effect of inflowing warmer CH_4-loaded fluid and the latent heat released from hydrate formation. Generally, the heat release of hydrate formation is ca. 54.4 kJ (mol CH_4)$^{-1}$, according to Gupta et al. (2008). As reported by Waite and Spangenberg (2013), given a small dissolved CH_4 consumption rate, the temperature increment is limited to < 0.5 °C even under the assumption that the components present in each element instantaneously absorb all released heat. However, the forming hydrate would gradually fill the available pore space in at least 200 h (Figure 2.7a,b), so that the contribution to temperature increment from the inflowing warmer CH_4-rich fluid is an order of magnitude higher than that from hydrate formation.

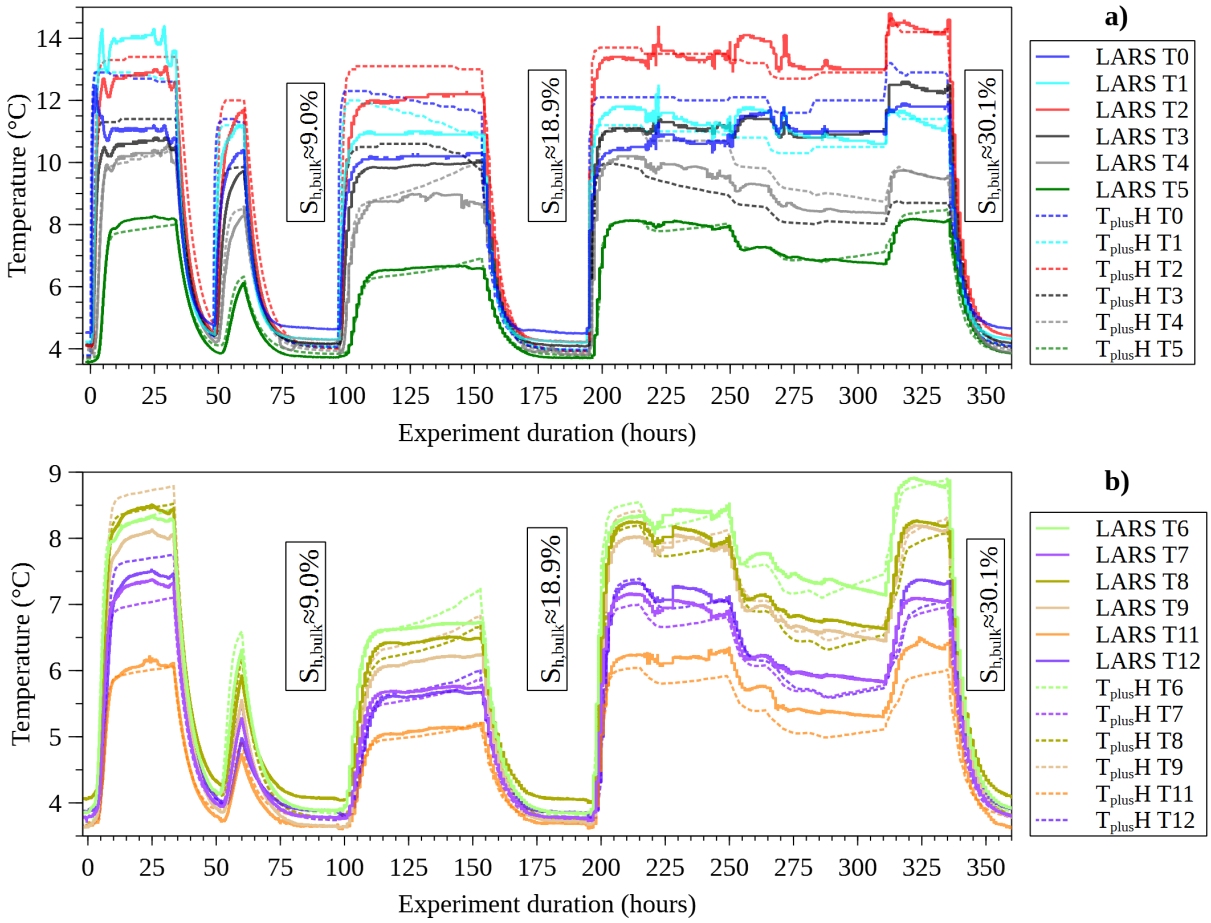

Figure 2.6: Observed and simulated temperature evolution during the 360-hour hydrate formation experiment at RTDs T0–T5 (**a**) together with T6–T9, T11, and T12; (**b**) based on the revised RTD locations (cf. Figure 2.5b and Table 2.5). LARS T0–T12 are modified from experimental data obtained by Priegnitz et al. (2015).

From 50 h on (Figure 2.6a), the measured and simulated peak temperatures are always observed at RTD T2. This shows that the temperature increment contributed by warm fluid in the vicinity of RTDs T0, T1, and T3 is less than that in Stage I-1 due to the local permeability decrease induced by hydrate accumulation. In contrast, warmer fluid flowed along T2 via the center of the sample, where permeability was much higher than at the nearby model boundary. This phenomenon indicates that a high permeable flow channel existed along the central axis of the model geometry near T2. Consequently, CH_4 hydrate is primarily formed at the model

boundary close to T0, T1, and T3, where the temperature is determined by external cooling in contrast to the conditions in the vicinity of T2.

Moreover, the vertical distance sequence of the RTDs in the upper sediment was T0 < T1 < T3 < T4 (sorted from top to bottom), whereas the observed temperature sequence was T1 > T0 > T3 > T4 (sorted from high to low temperatures) in Stages I-1, I-2, and II-1. The observed temperature sequence then changed to T1 > T3 > T0 > T4 at the early period of Stage III-1 and ended with T3 > T0 > T1 > T4 afterwards (Figure 2.6a). This phenomenon confirms the previous explanation that the warm inflowing fluid was redirected to RTD T1 at the start of the experiment due to pre-existing hydrate in the region of RTD T0. Moreover, hydrate was constantly amassed around RTD T1 until almost full hydrate saturation was achieved before Stage III. The redistributed warmer and CH_4-rich inflowing fluid then advanced to the region around RTD T3, and thus the observed temperature at RTD T1 became lower than that at RTD T0, due to its longer distance to the fluid inlet at the top.

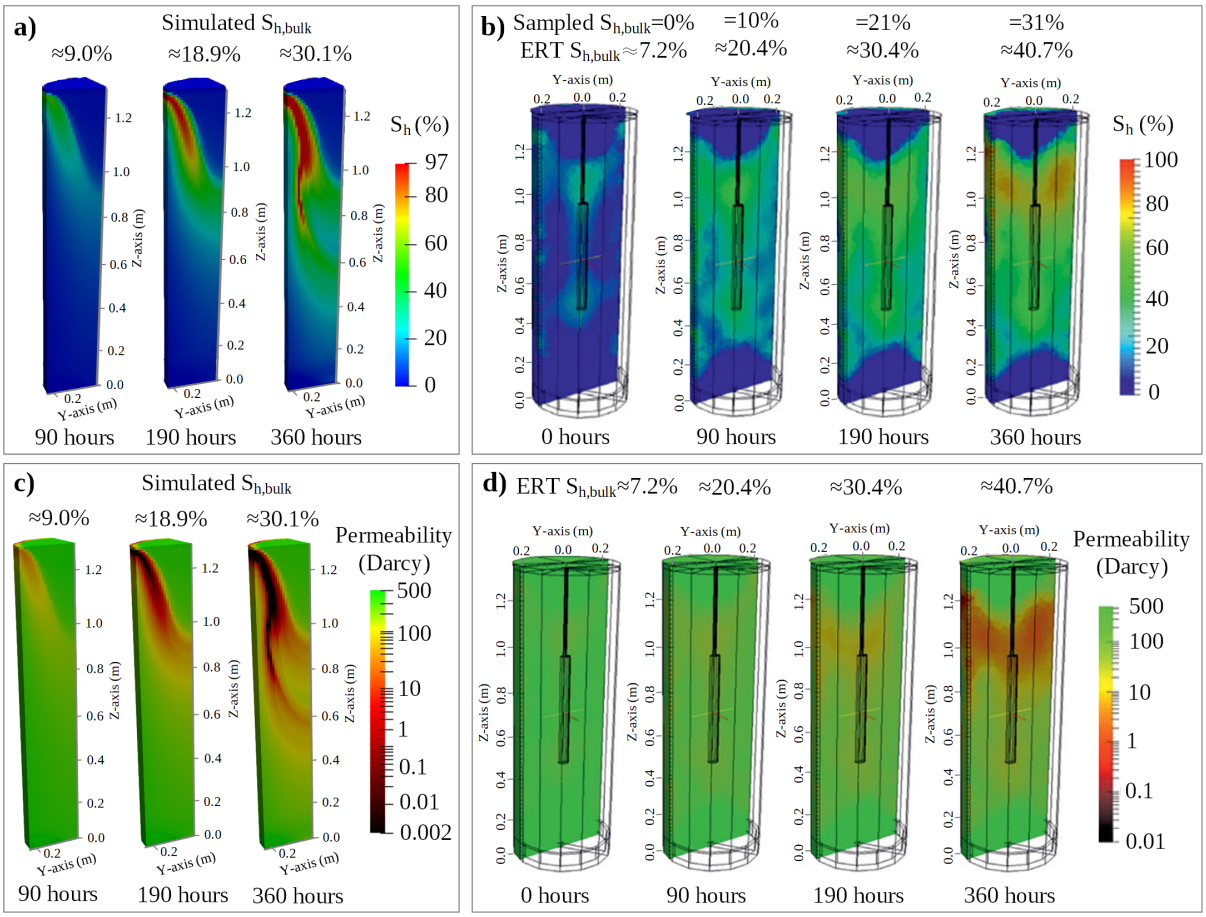

Figure 2.7: Model validation by: (1) comparison of the simulated hydrate saturation (S_h) distributions (**a**) against those measured by ERT (**b**) at experimental times of 0, 90, 190, and 360 h (Priegnitz et al., 2015); (2) comparison of the temporal evolution of simulated $S_{h,bulk}$ (**a**) against the ERT-measured and pore fluid sampled ones (Priegnitz et al., 2015) (**b**) over selected experimental and simulation times; (3) comparison of the simulated spatial hydraulic permeability distributions (**c**) against ERT measurements (**d**) over the selected experiment and simulation times, modified from Priegnitz et al. (2015).

However, the numerically predicted temperature sequence for the revised RTD positions maintains T0 > T1 > T3 > T4 (sorted from high to low temperatures) until the end of Stage II-1, complying with the aforementioned distance relation. In Stage III-1, the temperature sequence changes to T0 > T1 > T4 > T3, showing that the warmer inflowing fluid was redirected to T4 when the nearby region of T3 was occupied by hydrate. Hereby, the nearby regions of T0 and

T1 were not saturated with hydrate at the end of Stage III, as illustrated in Figure 2.7a. These findings further support the hypothesis that hydrate must have been present near RTDs T0 and T1 at the start of the experiment.

In Stage II-1, similar temperature changes are observed at T0, T1, and T3, whose simulated temperatures gradually drop by 0.6 to 1.0 °C. However, a reverse temperature change is observed during the same period at T4, whose simulated temperature steadily increases by approximately 1.1 °C (Figure 2.6a). This phenomenon indicates that the inflowing warm CH_4-loaded fluid was redirected from the nearby regions of lower permeability (T0, T1, and T3) to those around T4 with higher permeability. In addition, the simulated temperature development at T4 reflects that the hydrate formation process successively generated heat in the region around T4. This causes the simulated temperature at T4 to deviate from the corresponding observations by up to 13% during the experimental time period of 140 to 160 h.

During Stage III, the most noticeable difference between the simulated and observed temperatures is found at T3 with a maximum deviation of 40% during the time period from 220 to 310 h (Figure 2.6a). In this period, the region around T3 exhibits a decreasing permeability with the continuous accumulation of hydrate, as illustrated in Figure 2.7c,d. Considering these deviations at the RTD at the sample top near the neoprene jacket, the influence of a buffer layer (Dong et al., 2018; Hu et al., 2017; Sell et al., 2016; Wetzel et al., 2021) is expected. Although digital rock modeling (Hu et al., 2017) of the hydrate-bearing sample (Dong et al., 2018; Sell et al., 2016) is beyond the scope of the present study, the buffer layer of the unconsolidated sample built by gravity-driven sedimentation (Wetzel et al., 2021) is relevant to this study.

The latter indicates that the hydro-physical properties of the interface between the hydrate-bearing sand and the neoprene jacket as well as surrounding metal structures (the porous filter plates and the counter-current heat-exchange reactor) were probably influenced by the buffer layer. As a result, remarkably high porosities and one order of magnitude higher local permeabilities were observed at these locations (Wetzel et al., 2021). Consequently, a certain amount of warmer inflowing fluid migrated downwards along this high-permeable outer layer to reach RTD T3, supplying extra heat and increasing the observed temperatures at RTD T3 beyond the corresponding numerical predictions.

A substantial difference between the temperature evolution at the RTDs in the upper sample (T0–T4) and those in the lower one (T5–T9, T11, and T12) becomes obvious from Figure 2.6. The simulated and observed temperatures in the upper sample are higher than those in the lower one by more than 2 °C before Stage III. This shows that the temperature of the downward-flowing warm CH_4-loaded fluid is substantially reduced after passing RTDs T0–T4, whereby some amount of the initially dissolved CH_4 is consumed by hydrate formation, accompanied by the release of latent heat. Consequently, the highest hydrate accumulations occur in the upper sample according to the simulations and ERT measurements plotted in Figure 2.7a and b, respectively.

Although the distance from the fluid inlet to RTD T12 is farther than that to RTD T11, the lowest monitored and simulated temperatures are always observed at T11 rather than at T12. For the boundary region around T11, the heat transmitted from the inflowing fluid is superimposed by the external heat sink. In comparison, T12 is located in the aforementioned warm fluid flow channel, where the thermal conditions are contrary to those observed in the region near T11. Moreover, similar simulated and observed temperature change characteristics did not only exist at RTDs T8 and T9 within the warm fluid flow path, but also at RTDs T5 and T6 near the buffer layer. The same temperature change characteristics are also present for

the observed and simulated results at RTDs T7 and T12. Despite their maximum deviations extending to up to 9% for the time period of 140 to 160 h, simulated temperatures in the lower sample (T5–T9, T11, and T12) matched well with the corresponding observations after Stage I (cf. Figure 2.6).

Model Validation by Comparison of the Temporal and Spatial Evolution of Simulated and Observed Hydrate Saturation

The evolution of spatial hydrate saturation and hydraulic permeability distributions can be described by the numerical simulations and ERT observations, separately. At hour zero in Figures 2.7b and 2.8b, $S_{h,bulk} > 7.2\%$ was determined by ERT Priegnitz et al., 2015. At the end of Stage I (90 h), it is indicated by the simulation results that the majority of formed hydrate was accumulated under the bottom of the top porous filter plate and distributed along the warm-cool fluid interface present at 1.3–0.65 m of the specimen height. Moreover, the simulated $S_{h,bulk}$ reaches 9.0% (Figure 2.7a), showing good agreement with the pore fluid sampling data (10%), disregarding the deviation to $S_{h,bulk}$ of 20.4% determined from ERT measurements (90 h in Figure 2.7b).

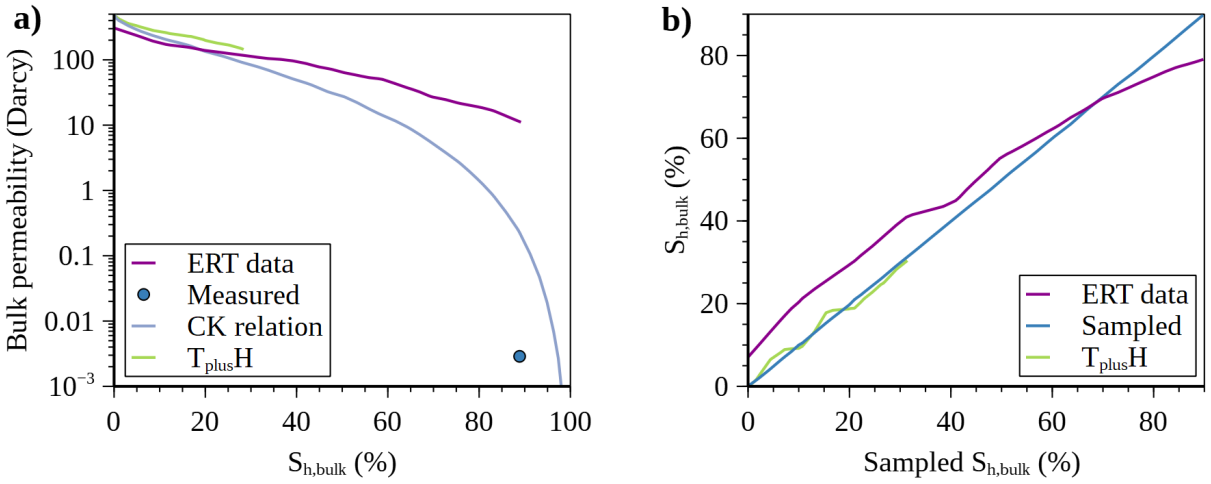

Figure 2.8: Observed and simulated bulk permeability alongside with the bulk hydrate saturation ($S_{h,bulk}$) evolution during the hydrate formation experiment: (**a**) comparison of the simulated volume-averaged permeability with the numerically inversed ERT results (Priegnitz et al., 2015), the Carman–Kozeny relation as a function of $S_{h,bulk}$, and the bulk permeability (blue dot) determined by hydraulic testing at the end of experiment (Priegnitz et al., 2015); (**b**) comparison of the simulated $S_{h,bulk}$ against the sampled and ERT-measured ones, modified from Priegnitz et al. (2015).

In Stage II, hydrate formation mainly occurred at 1.3–0.95 m of the specimen height, as shown for 190 h in Figure 2.7a,b. Furthermore, the maximum simulated S_h increased to 97% and the simulated $S_{h,bulk}$ to approximately 18.9% simultaneously, which closely matches with the fluid sampling result (21%) at 190 h. Subsequently, the front of accumulated hydrate advanced to 0.95–0.65 m of the specimen height, indicating a similar hydrate distribution pattern to the ERT-measured findings (cf. 360 h in Figure 2.7a,b). Finally, the simulated $S_{h,bulk}$ increased to about 30.1%, and is thus almost identical with the corresponding $S_{h,bulk}$ of 31% determined by fluid sampling at the end of Stage III. Despite the relative error of the ERT-measured $S_{h,bulk}$, it has been confirmed that hydrate initially formed at the top of the specimen, and then the front of hydrate formation advanced to the specimen center along the neoprene jacket.

In Figure 2.7a,b, the S_h observed by ERT and simulated are virtually zero at the bottom and top of LARS. At the top region near the inlet of LARS, the *p*-*T* conditions of the inflowing

CH_4-loaded fluid are outside of the CH_4 hydrate stability range. These conditions were chosen to avoid undesired blockages by intensive hydrate formation at the inlet. As the fluid flows through the sandy sample, it cools and eventually meets the CH_4 hydrate stability conditions, whereby the excess CH_4 is completely consumed. When the fluid flows to the bottom of the sandy sample, it is undersaturated with CH_4, so that CH_4 hydrate can no longer form despite matching the suitable *p-T* conditions.

The Carman–Kozeny Equation (2.14) shows that the bulk permeability is a function of $S_{h,bulk}$, as the predefined initial permeability is constant (Table 2.3). Accordingly, the change in local permeability reflects the variation of S_h. At hour zero of the experiment (Figure 2.7d), a slightly heterogeneously distributed permeability was observed in a range of 300 to 500 Darcy. Subsequently, accumulating hydrate reduced hydraulic permeability in the upper part of specimen. Some warmer CH_4-loaded brine advanced along the neoprene jacket, and a small amount migrated along the aforementioned buffer layer. Moreover, the electrical resistivity of the relevant region was appreciably increased (Spangenberg et al., 2014). On account of the constantly increasing hydrate accumulation, the permeability of the affected region was thus declining until 360 h. Finally, the minimum simulated local permeability is 2.1 mDarcy (Figure 2.7c) and identical to the hydraulic test results (2 mDarcy) represented by the blue dot in Figure 2.8a.

Overall, the simulation results confirm that ERT successfully monitored the spatial hydrate distribution within the specimen, and the volume-averaged $S_{h,bulk}$ was estimated at high precision by pore fluid sampling in previous laboratory studies (Priegnitz et al., 2015).

2.3.3 Uncertainties of Critical Parameters in the Experimental Study

Initially, several essential details were collected to determine practical ranges of input parameters (Table 2.4) and establish an equivalent geometrical model for calibration (Figure 2.4). The optimized input parameters were then determined by a history-matching procedure during model calibration, and the documented initial and boundary conditions were revised (Tables 2.5 and 2.6). Additionally, the exact locations of RTDs could not be derived by any measurement method once the sample chamber was filled with quartz sand. Thus, these had to be estimated iteratively in the present study (Table 2.5).

There are further uncertainties similar to those noted above. For instance, the initial intrinsic permeability of the specimen was too high and out of the measurement range of the experimental setup, thus it could exclusively be estimated empirically from porosity and grain size distribution. However, the final bulk permeability could be measured at the end of the hydrate formation experiment by a hydraulic test (Priegnitz et al., 2015), whose result is illustrated in Figure 2.8a. In addition to this, the boundary condition for the inflowing fluid became time-dependent, caused by the hydrate potentially forming inside the porous filter plate. Furthermore, some critical variables required for the presented simulation study were exclusively measured at the onset of the hydrate formation study, e.g., the external cooling and inflowing fluid temperatures as well as the dissolved CH_4 concentration in the inflowing fluid. Despite these uncertainties, most of them can be prevented or eliminated in future experimental designs by optimizing the execution of the experimental planning.

With regard to the uncertainties in the estimation of the initial permeability and $S_{h,bulk}$, the initial interpretation of Figure 2.8 was given in a previous study (Priegnitz et al., 2015). However, the remarkable differences between hydrate saturations derived from ERT measurements, pore fluid conductivity measurements, and simulation are still worth noting and require further

analysis. Figure 2.8b demonstrates that the simulation curve increases in the form of multiple steps, which is inconsistent with the simple linear growth pattern determined by pore fluid sampling and ERT measurements. It can be explained by the artificial acquisition intervals of experimental data being much larger than those in the numerical simulations. For example, the pore fluid sampling for pore fluid conductivity measurements was undertaken on a daily basis, whereas ERT measurements were only made at the end of each formation stage. Hence, these cannot characterize the detailed transition during hydrate accumulation.

Theoretically, the remarkable contrasts in electrical resistivities between the coexisting pore-filling components (pore fluid and hydrate) granted hydrate to be distinguished from the pore fluid and localized even at low S_h (Priegnitz et al., 2015), as hydrate is electrically non-conductive. However, it should be noted that the most significant deviation of the ERT-measured $S_{h,bulk}$ (ca. 7.2%) from the corresponding simulated and sampled $S_{h,bulk}$ (0%) was observed at the onset of the experiment (hour zero) in Figure 2.8b. This is attributed to the initial assumption and relevant post-processing routine for the conversion of electrical resistivity into S_h (Priegnitz et al., 2015). Hereafter, the difference in hydrate content from ERT and pore fluid electrical resistivity becomes less notable as the hydrate saturation increases, particularly at $S_{h,bulk} > 65\%$, when the sampled $S_{h,bulk}$ finally agrees with the ERT-observed one. Eventually, the ERT-observed $S_{h,bulk}$ resulted in a notable deviation of more than 10% from the corresponding sampled $S_{h,bulk}$ (ca. 89%) in Figure 2.8b.

The ERT measurements provided useful information regarding the location where hydrate started to form and how its distribution generally changed with time, which helped to adjust the way the experiment was conducted. However, the upper and lower 0.15 m of the sample chamber are not covered with electrodes, and the ERT is not able to capture effects close to the top and bottom steel closures with the fluid in- and outlets. In addition, the resolution of the ERT method is limited, and small-scale accumulations of hydrate with only little effect on electrical resistivity might not be recognized. Furthermore, the inversion process of converting the resistance measurements on the sample surface into a 3D electrical resistivity distribution is not unique (as for all potential methods). The transformation of electrical resistivity into S_h relies on an empirical rock-physical model, without any specific calibration for hydrates (Priegnitz et al., 2013; Priegnitz et al., 2015). This further explains the observed discrepancies in the numerical modeling.

2.4 Summary and Conclusions

The present study numerically reproduced a previously conducted multi-stage CH_4 hydrate formation experiment. The effectiveness and accuracy of the developed coupled numerical framework have been evaluated and demonstrated by a benchmark and comparisons to the experimental observations. Consequently, the key parameters and an optimum combination of initial and boundary conditions were determined. Our findings allow for the following conclusions:

1. The general consistency of the experimental observations with the simulation results proves that the employed equilibrium CH_4 hydrate formation model can represent the main processes of hydrate formation in LARS. The equilibrium reaction model is a practicable alternative to kinetic approaches at the macro-scale (vessel volume > 0.2 m^3) given the application of the "dissolved-gas" method. In contrast, kinetic reaction approaches tend to be irreplaceable for modeling hydrate formation by other methods,

because their CH_4 hydrate growth rates are orders of magnitude faster than that of the "dissolved-gas" method.

2. The deviations among the experimental observations (i.e., continuously recorded temperature profiles, periodically gathered $S_{h,bulk}$, and ERT-tomography derived spatial S_h distributions) and the corresponding numerical predictions were minimized through an iterative optimization procedure. It has been indicated that the combination of the thermal properties of inflowing CH_4-loaded fluid and the hydrate-bearing sand determine the spatial distribution of hydrate accumulations.
3. The presented spatial S_h distribution illustrates a heterogeneous accumulation within the hydrate-bearing sand at an early experimental period when $S_{h,bulk} < 30\%$, with the feature becoming less prominent until $S_{h,bulk} > 80\%$.
4. In the LARS hydrate formation experiment, a relatively large temperature gradient (ca. 10 °C/0.23 m) is generated between the inflow of warm brine and its surrounding coolants, leading to a heterogeneous hydrate distribution. In contrast, the sub-permafrost and sub-seafloor geothermal gradients in natural settings are substantially lower (3 °C/100 m) and steady for long time periods (Majorowicz et al., 1990), causing a lower and almost constant dissolved CH_4 concentration gradient in the saline fluid. Therefore, relatively uniformly distributed S_h were found within the NGH intervals with ignorable lateral variations at the Mallik site. These NGH accumulation intervals could be simplified as CH_4 hydrate layers formed via the continuous supply of dissolved CH_4, migrating through the up-dip natural faults in the Canadian Beaufort-Mackenzie Basin region.

The proposed numerical framework can be utilized to improve experimental designs and optimize post-processing workflows of monitoring data. Thereby it could contribute to calibrating the advanced geophysical identification techniques and investigate dynamic hydrate accumulation processes in water-dominated geological settings at the field scale.

2.5 Appendix

2.5.1 Governing Equations for Fluid Flow, Heat and Chemical Species Transport

The continuity equation for the mobile components in the fluid flow and transport simulator (Kempka, 2020) is represented by

$$\rho_f \left((1-\phi)\alpha + \phi\beta\right) \frac{\partial P}{\partial t} = -\rho_f \nabla \vec{v} + W. \tag{2.2}$$

In Equation 3.1, ϕ is the effective porosity of porous medium (hydrate-bearing sand); P stands for the pore fluid pressure; and α and β are the compressibilities of porous medium and fluid, respectively. Source/sink terms are represented by W.

The velocity of mobile components, $\vec{v}$, is defined to obey the single-phase Darcy's Law

$$\vec{v} = -\frac{k}{\mu_f}\left(\nabla P - \rho_f \vec{g}\right), \tag{2.3}$$

where the effective permeability of hydrate-bearing sand is described by k; μ_f is dynamic fluid viscosity and $\vec{g}$ is the gravity vector.

The density of the mobile components, ρ_f, is expressed as

$$\rho_f = X_w \rho_w + X_m \rho_m + X_i \rho_i, \tag{2.4}$$

where X_w, X_m, and X_i are the mass fractions of water, dissolved CH_4 and inhibitor (NaCl here), respectively. Accordingly, ρ_w, ρ_m, and ρ_i are the densities of water, dissolved CH_4 and inhibitor, respectively. In particular, the density of dissolved CH_4 can be ignored ($\rho_m = 0$).

The species transport by diffusion and advection is described by the mass balance equation (Kempka, 2020):

$$\phi \frac{\partial C}{\partial t} = \nabla\left(\phi D \nabla C - \vec{v} C\right) + Q. \tag{2.5}$$

In Equation 3.4, the concentration tensor of each mobile component is stored in the matrix of C; D represents the diffusion coefficient of mobile components (Fick's Law), and the source/sink term is given by Q.

The conductive and convective heat transport is taken into account by the energy balance equation (Kempka, 2020), written as

$$\left((1-\phi)\, c_{pr}\rho_r + \phi c_{pf}\rho_f\right) \frac{\partial T}{\partial t} = \nabla\left(\lambda_a \nabla T + \vec{v}\, c_{pf}\rho_f T\right) + H, \tag{2.6}$$

where c_{pf} is the specific heat capacity of mobile components, and H is the source/sink term.

The average thermal conductivity of immobile and mobile components, λ_a ($W{\cdot}m^{-1}{\cdot}K^{-1}$), is defined as

$$\lambda_a = (1-\phi)\,\lambda_r + \phi\lambda_f, \tag{2.7}$$

where λ_f is the thermal conductivity of the mobile components, and the thermal conductivity of the immobile components, λ_r, is expressed as

$$\lambda_r = \frac{(1-\varphi)\,\lambda_s + \varphi S_h \lambda_h}{1-\phi}. \tag{2.8}$$

In Equation 3.7, λ_s and λ_h are thermal conductivities of matrix of hydrate-bearing sand made of quartz sand and CH_4 hydrate, respectively; S_h is the CH_4 hydrate saturation of the pore space in the hydrate-bearing sand.

The specific heat capacity of the immobile components, c_{pr} ($J{\cdot}kg^{-1}{\cdot}K^{-1}$), is

$$c_{pr} = \frac{(1-\varphi)\,c_{ps} + \varphi S_h c_{ph}}{1-\phi}, \tag{2.9}$$

where c_{ps} and c_{ph} are specific heat capacities of quartz sand and CH_4 hydrate, respectively.

The density of the immobile components, ρ_r ($kg{\cdot}m^{-3}$), is

$$\rho_r = \frac{(1-\varphi)\,\rho_s + \varphi S_h \rho_h}{1-\phi}, \tag{2.10}$$

where ρ_s and ρ_h are densities of quartz sand and CH_4 hydrate, respectively.

To solve the aforementioned governing equations, additional equations restricting the behaviour of the related components are required. The conservation relation of mass fractions of each individual mobile component is

$$X_w + X_m + X_i = 1, \tag{2.11}$$

and the saturation summation of each component in the pore space is 1:

$$S_h + S_f = 1. \tag{2.12}$$

The effective porosity, ϕ, of the hydrate-bearing sand is proposed by Spangenberg (2001) as

$$\phi = S_f \varphi, \tag{2.13}$$

where φ is the intrinsic porosity of the hydrate-bearing sand.

Based on the assumption of pore filling hydrate formation mechanism (Spangenberg et al., 2014), the effective permeability, k (m^2), is assumed to obey the modified Carman–Kozeny relation (Kleinberg et al., 2003) and is defined as a function of hydrate saturation; that is

$$k = \kappa \frac{(1-S_h)^{n+2}}{\left(1+\sqrt{S_h}\right)^2}. \tag{2.14}$$

In Equation 2.14, κ is the intrinsic permeability of the hydrate-bearing sand; n is the linear relation with respect to the hydrate saturation by $n = 0.7S_h + 0.3$ (Delli and Grozic, 2013; Priegnitz et al., 2015; Spangenberg, 2001).

2.5.2 Equations of State for CH_4 Hydrate Equilibrium Formation

The dynamic viscosity of aqueous solutions, (Pa·s), is given by the equation for pure water (Nagashima, 1977) with the suitable modification (Phillips, 1981) by the correlation of the presence of NaCl as inhibitor:

$$\mu_f = A \exp\left(\frac{1 + B\,(T + 273.15)}{C\,(T + 273.15) + D\,(T + 273.15)^2}\right)\left(\sum_{j=0}^{3} a_j x_i + bT\,(1 - e^{cx_i})\right). \tag{2.15}$$

In Equation 2.15, $A = 1.2571873 \times 10^{-5}$, $B = -5.8064362 \times 10^{-3}$, $C = 1.1309108 \times 10^{-3}$, $D = -5.723952 \times 10^{-6}$, $a_0 = 1.0$, $a_1 = 0.0816$, $a_2 = 0.0122$, $a_3 = 0.000128$, $b = 0.000629$, $c = -0.7$, and x_i is the NaCl molality of solution.

The density of pure liquid water, ρ_w (kg·m^{-3}), as the function of temperature (Saul and Wagner, 1989; Wagner and Pruß, 2002) over range 0 to 25 °C in the experimental studies required pressure region (Table 2.4), is

$$\rho_w = \sum_{j=0}^{4} a_j T^{4-j}, \tag{2.16}$$

where $a_0 = -4.18113085 \times 10^{-6}$, $a_0 = -4.18113085 \times 10^{-6}$, $a_2 = -0.0126230251$, $a_3 = -0.0666415017$, and $a_4 = 1005.21463$.

The compressibility (Kell, 1975) of liquid water, β (Pa^{-1}), is represented by the temperature-dependent function:

$$\beta = \frac{a}{1 + bT} \sum_{j=0}^{5} c_j T^j. \tag{2.17}$$

In Equation 2.17, $a = 1.0 \times 10^{-11}$, $b = 1.967348 \times 10^{-2}$, $c_0 = 50.88496$, $c_1 = 0.6163813$, $c_2 = 1.459187 \times 10^{-3}$, $c_3 = 2.008438 \times 10^{-5}$, $c_4 = -5.847727 \times 10^{-8}$, and $c_5 = 4.10411 \times 10^{-10}$.

The thermal conductivity of fluid (O'Sullivan et al., 1985), λ_f (W·m^{-1}·K^{-1}), is

$$\lambda_f = \sum_{j=0}^{4} a_j T_j + P \sum_{j=0}^{3} b_j T_j + P^2 \sum_{j=0}^{3} c_j T_j, \tag{2.18}$$

where $a_0 = -0.92247$, $a_1 = 2.8395$, $a_2 = -1.8007$, $a_3 = 0.52577$, $a_4 = -0.07344$, $b_0 = -9.473 \times 10^{-9}$, $b_1 = 2.5186 \times 10^{-8}$, $b_2 = -2.0012 \times 10^{-8}$, $b_3 = 5.1536 \times 10^{-9}$, $c_0 = 1.6563 \times 10^{-16}$, $c_1 = -3.8929 \times 10^{-16}$, $c_2 = 2.9323 \times 10^{-16}$, $c_3 = -7.1693 \times 10^{-17}$, $T_0 = 1.0$, $T_1 = 1 + \frac{T}{273.15}$, $T_2 = T_1^2$, $T_3 = T_1^3$, and $T_4 = T_1^4$.

The specific heat capacity of NaCl solution, c_{pf} (J·kg^{-1}·K^{-1}), is calculated by the temperature-dependent function for the enthalpy of liquid water (Michaelides, 1981), h_w (J·kg^{-1}), with correlation for salt solution (Gudmundsson and Thráinsson, 1989) divided by T; that is

$$c_{pf} = \frac{\Delta h_w}{\Delta T}, \tag{2.19}$$

$$\text{where, } h_w = \frac{\sum_{j=0}^{3} A_j T^j}{1 + x_i M_{Nacl}} + \frac{B x_i \sum_{j=0}^{2} C_j T^{j+1}}{1 + x_i M_{Nacl}} + x_i \sum_{j=0}^{3} \sum_{k=0}^{2} a_{ij} T^j x_i^k. \tag{2.20}$$

In Equation 2.20, $A_0 = -29.578$, $A_1 = 4.81155$, $A_2 = -4.5137 \times 10^{-3}$, $A_3 = 1.2453 \times 10^{-5}$, $B = 0.004184$, $C_0 = -25.9293$, $C_1 = 50.88496$, $C_2 = -8.3624 \times 10^{-4}$, $a_{00} = -9633.6$, $a_{01} = -4080.0$, $a_{02} = 286.49$, $a_{10} = 166.58$, $a_{11} = 68.577$, $a_{12} = -4.6856$, $a_{20} = -0.90963$, $a_{21} = -0.36524$,

$a_{22} = 0.0249667$, $a_{30} = 0.0017965$, $a_{31} = 7.1924 \times 10^{-4}$, $a_{32} = -4.9 \times 10^{-5}$ and the molecular weight of NaCl, M_{Nacl}, is 58.448×10^{-3} kg·mol^{-1}.

The enthalpy of CH_4 hydrate formation reaction (Kamath, 1984; Moridis et al., 2005a), $h_{\Delta H}$ (J·kg^{-1}), is calculated by

$$h_{\Delta H} = a\left(b - 4.02\left(T + 273.15\right)\right), \tag{2.21}$$

where $a = 3.372995 \times 10^{-2}$, and $b = 1.3521 \times 10^{4}$.

For calculating the CH_4 solubility in brine, it is assumed that the amount of dissolved CH_4 concentration is so small that its dissolution in brine can be computed by the Henry's Law constant (Battistelli et al., 1997; Gamwo and Liu, 2010; Moridis et al., 2005a). By implementing polynomial regression fitting to the results in the table of the smoothed Henry's Law constant for CH_4 in water and brine provided by Cramer (1984), CH_4 Henry's Law constant with the correlation of the salting-out effect (Battistelli et al., 1997), H_m (MPa), is calculated as

$$H_m = 10^{\left(x_i \sum_{k=0}^{5} b_k T^k\right)} \sum_{j=0}^{9} a_j T^{(9-j)}, \tag{2.22}$$

where $a_0 = 3.77595983 \times 10^{-17}$, $a_1 = -5.55562536 \times 10^{-14}$, $a_2 = 3.39179531 \times 10^{-11}$, $a_3 = -1.08734945 \times 10^{-8}$, $a_4 = 1.85464755 \times 10^{-6}$, $a_5 = -1.32411649 \times 10^{-4}$, $a_6 = -2.57983366 \times 10^{-3}$, $a_7 = 0.264131301$, $a_8 = 71.0306921$, $a_9 = 2460.04129$, $b_0 = 0.164818$, $b_1 = -1.40166 \times 10^{-3}$, $b_2 = 1.3236 \times 10^{-5}$, $b_3 = -4.85733 \times 10^{-8}$, $b_4 = 7.87967 \times 10^{-11}$, and $b_5 = -5.52586 \times 10^{-14}$.

The CH_4 solubility in brine (Gamwo and Liu, 2010; Moridis et al., 2005a), χ_m (mol·mol^{-1}), is computed as

$$\chi_m = \begin{cases} \frac{P}{H_m} & \text{if } P_{eq} > P, \\ \frac{P_{eq}}{H_m} & \text{otherwise.} \end{cases} \tag{2.23}$$

P_{eq} (MPa) is the equilibrium pressure of CH_4 hydrate (Moridis, 2003) for $T > 273.2$ K, and can be expressed as follows:

$$P_{eq} = \exp\left(\sum_{j=0}^{5} a_j T_{shift}^{j}\right), \tag{2.24}$$

where, $a_0 = -194138.504464560$, $a_1 = 3310.18213397926$, $a_2 = -22.5540264493806$, $a_3 = 7.67559117787059 \times 10^{-2}$, $a_4 = -1.30465829788791 \times 10^{-4}$, $a_5 = 8.86065316687571 \times 10^{-8}$, and T_{shift} is the temperature of fluid shifted by inhibitors (Makogon, 1997), e.g., NaCl; that is

$$T_{shift} = \left(T + 273.15\right) + \Delta T_{shift}, \tag{2.25}$$

where the temperature depression, ΔT_{shift} (°C), induced by NaCl (Moridis, 2003) is

$$\Delta T_{shift} = \frac{2.0 \cdot \ln\left(1 - x_i\right)}{\ln\left(1 - 0.01335\right)}. \tag{2.26}$$

Chapter 3

Numerical Simulation of Coastal Sub-Permafrost Gas Hydrate Formation in the Mackenzie Delta, Canadian Arctic

ABSTRACT

The Mackenzie Delta (MD) is a permafrost-bearing region along the coasts of the Canadian Arctic which exhibits high sub-permafrost gas hydrate (GH) reserves. The GH occurring at the Mallik site in the MD is dominated by thermogenic methane (CH_4), which migrated from deep conventional hydrocarbon reservoirs, very likely through the present fault systems. Therefore, it is assumed that fluid flow transports dissolved CH_4 upward and out of the deeper overpressurized reservoirs via the existing polygonal fault system and then forms the GH accumulations in the Kugmallit–Mackenzie Bay Sequences. We investigate the feasibility of this mechanism with a thermo–hydraulic–chemical numerical model, representing a cross-section of the Mallik site. We present the first simulations that consider permafrost formation and thawing, as well as the formation of GH accumulations sourced from the upward migrating CH_4-rich formation fluid. The simulation results show that temperature distribution, as well as the thickness and base of the ice-bearing permafrost are consistent with corresponding field observations. The primary driver for GH distribution is the permeability of the host sediments. Thus, the hypothesis on GH formation by dissolved CH_4 originating from deeper geological reservoirs is successfully validated. Furthermore, our results demonstrate that the permafrost has been substantially heated by 0.8–1.3 °C , triggered by the global temperature increase of about 0.44 °C and further enhanced by the Arctic Amplification effect at the Mallik site from the early 1970s to the mid-2000s.

3.1 Introduction

3.1.1 Arctic Permafrost-Associated Gas Hydrates

Gas hydrates (GHs) are ice-like crystals storing enormous quantities of gas molecules such as methane (CH_4), and are possibly found in marine and permafrost-associated sediments, including gas-free and water-saturated Arctic sands (Boswell, 2009). GHs can form when favorable *p-T* conditions are met, and hydrate-forming gas is supplied either in free gas or supersaturated dissolved form. In Arctic permafrost-associated sediments, a series of continuously and uniformly distributed GH intervals of high CH_4 saturation were observed in core specimens sampled within the gas hydrate stability zone (GHSZ), as presented by Dallimore et al. (1999). The specifics of the hydrate-forming CH_4 supply (i.e., mass flow and physical state as well as other involved species) and their transport mechanisms (Wei et al., 2019) affect the heterogeneous characteristics of GH occurrences (i.e., their thickness and distribution in the deposit). However, the hydrodynamics of the subsurface system related to fluid flow and CH_4 transport, bridging the pool of deep hydrocarbon gases and shallower GH occurrences, cannot be intuitively identified (Waghorn et al., 2020; Wei et al., 2022). Therefore, numerical

simulation is an irreplaceable method to study the hydrodynamics of subsurface systems, especially for sub-permafrost-associated GH-bearing strata.

Permafrost, with near-surface temperatures below 0 °C for a minimum of two years (Woo, 2012), widely exists in the Canadian Arctic, and thus also in the Mackenzie Delta (MD) region. As illustrated by Figure 3.1, high-latitude terrestrial permafrost in general comprises a seasonally-thawed active layer underlain by perennially-frozen ground, often accompanied by thick thaw bulbs (taliks) overlain by thermokarst lakes (Frederick and Buffett, 2014; Ruppel and Kessler, 2017). Three factors mainly control the thermally equilibrated thickness of the permafrost and subsurface temperature gradient: (1) the mean annual temperature at the base of the active layer, (2) the thermal conductivity of sediments and (3) the basal heat flow (Dallimore et al., 2005a). During the recent glacial–interglacial history and regressive/transgressive marine cycles, permafrost forms or degrades, while the latent heat of the water–ice phase changes is consumed or released over considerable amounts of time (Matveeva et al., 2020; Mottaghy and Rath, 2006). In general, permafrost evolution is accompanied by the formation of permafrost-associated GHs, including the shallow pan-Arctic continental shelves and coastal plains (Overduin et al., 2019; Shakhova et al., 2010) and the Qinghai–Tibet Plateau (Zhu et al., 2021). Permafrost and permafrost-associated GHs in the MD may exist since about 1.0 MaBP. Moreover, the current subsea relict permafrost formed terrestrially during late Pleistocene low sea-level stands (Majorowicz et al., 2012a). Under contemporary global warming events, the relict permafrost degradation is continually promoted (Frederick and Buffett, 2014), whereby thick ice-bonded permafrost may prevent GHs from contributing greenhouse gases to the global carbon budget (Friedlingstein et al., 2022).

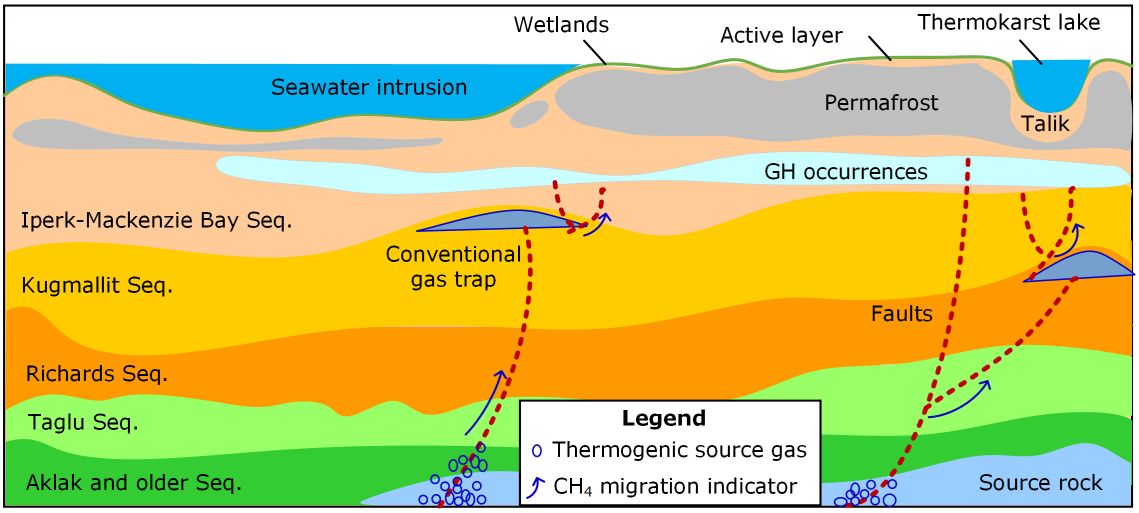

Figure 3.1: Illustration of the GH-associated permafrost lowlands along the Arctic coastal plain of the Beaufort Sea, according to Chen et al. (2021). A portion of the plain has been inundated by sea by thawing continental ice sheets at high northern latitudes. The thermogenic gaseous CH_4 migrates along the faults (red dashed lines) from deeper geological units (i.e., source rock) and accumulates in the upper sequences (e.g., Kugmallit–Richards Seq., Seq. = sequence, not to scale), which act as conventional gas reservoirs. Then, the accumulated CH_4 is transported upward into shallower sequences (e.g., Iperk–Mackenzie Bay Seq.), supporting the formation of GH occurrences.

After experiencing subaerial exposure during glacial episodes, permafrost-associated GHs (GRID-Arendal, 2020) occur within and below the permafrost and are thus defined as intra-permafrost and sub-permafrost GHs, respectively. Dallimore and Collett (1995) studied a sample containing intra-permafrost GHs recovered at a 336.4 m depth within the ice-bonded

permafrost near the Taglu gas accumulation in the MD, which proved intra-permafrost GH occurrence for the first time. Although the source gas composition of GH-bearing sediments varies, the CH_4 source of intra-permafrost GHs is likely derived from the degradation of in situ organic matter by microbial activity (methanogenesis) at low temperatures (Dallimore and Collett, 1995). Instead, the primary source of sub-permafrost GH accumulations is CH_4 migrating from deep conventional hydrocarbon deposits through specific tectonic features (i.e., faults) (Waghorn et al., 2020) acting as fluid flow pathways. This hydrate-forming source gas originates from the deeper sedimentary sequences (source rocks of feed gas) and has been formed by thermogenic activities (Lorenson et al., 2005; Lorenson et al., 1999), such as thermal cracking (Taladay et al., 2017). Thermogenic CH_4 has not only been found within Arctic circumpolar GH accumulations in the Beaufort Sea and Russia (Ruppel and Kessler, 2017), but also at the thermogenic basins lying between upper continental slopes and deep water sags, such as the Gulf of Mexico (Johnson et al., 2022) and the South China Sea (Qin et al., 2020; Ye et al., 2020).

3.1.2 Review of Numerical Studies on the Spatial-Temporal Evolution of Permafrost and Permafrost-Associated GHs in the Mackenzie-Beaufort Region

Present knowledge on the paleo-evolution of permafrost is mostly based on numerical experiments with the implementation of simple 1D and 2D geothermal models (Majorowicz et al., 2012a; Majorowicz et al., 2012b; Majorowicz et al., 2015; Overduin et al., 2019; Taylor et al., 2013; Taylor et al., 2008), considering thermal effects to describe the ice–water phase transition (i.e., latent heat). Recently, Frederick and Buffett (2014) established a more sophisticated multiphase fluid flow model to investigate the role of taliks as a potential pathway for gaseous CH_4 venting and predicted the degradation of Arctic permafrost-associated GH reservoirs in terms of their contribution to the global CH_4 budget (Frederick and Buffett, 2014). Additionally, they employed their models to verify if submarine groundwater discharge laterally transports dissolved CH_4 to the Mackenzie–Beaufort (MB) shelf to form GHs (Frederick and Buffett, 2015; Frederick and Buffett, 2016).

Using the numerical simulator TEMP/W (GEO-SLOPE International Ltd., 2014), Taylor et al. (2008) established several 1D geothermal models to compare the sensitivity of relict permafrost and subsea GHs to climate change. Taylor et al. (2013) further employed a 2D geothermal model to study the permafrost history under the inferred paleo-environment of the MB shelf and slope. In 2012, Majorowicz et al. (2012b) developed a series of 1D geothermal models to simulate profiles of permafrost and GHSZ bases, and validated these models by matching numerical results to field data. In addition, they studied GH and permafrost stability histories in the context of climate change (Majorowicz et al., 2012a) in the MB area. Moreover, Majorowicz et al. (2015) utilized 1D and 2D geothermal models to predict the talik, permafrost and permafrost-associated GH histories in the MB region and concluded that the primary control in talik formation is lithology.

3.1.3 Comparison of Numerical Validations of Source Gas Migration Mechanisms during GH Formation and Accumulation

From the previous quantitative studies reviewed by You et al. (2019), CH_4 hydrate formation models are categorized into six classifications by their respective gas migration

mechanisms: M1—local biogenesis with/without diffusion; M2—local diffusion of dissolved gas; M3—advection with upward fluid flow and/or diffusion; M4—CH_4 recycling; M5—buoyancy-driven CH_4 gas flow; M6—in situ conversion of gaseous CH_4 accumulations into GH deposits as the GHSZ base shifts downward below the top of the gaseous CH_4 accumulations. Moreover, this classification should be extended by including the mechanism of GH formation via CH_4 transported in the dissolved state (M7), as suggested by Frederick and Buffett (2015) and Frederick and Buffett (2016) and by Egeberg and Dickens (1999).

According to the migration distance of the source gas (Wei et al., 2019; Wei et al., 2022), these mechanisms can be further classified into (1) short-range (M1, M2, M3 and M6); (2) medium-range (M4); and (3) long-range migration mechanisms, including M5, (Wei et al., 2022; You et al., 2019; You and Flemings, 2018) and M7 (Frederick and Buffett, 2016). The major type of source gas origin used in the abovementioned CH_4 hydrate formation and accumulation models can be mainly either thermogenic (M4, M5 and M7), mixed (M6) or biogenic (M1, M2, M3, M4 and M5).

Table 3.1: Summary of numerical models used to investigate GH accumulation mechanisms and comparisons of deposit features characterizing the evolution pattern of GH occurrences

Drilling site	**Location**	**Source gas state**	**GH layer conditions**	**S_h distribution along GH intervals**
GMGS1-SH2	Shenhu area, slope of South China Sea	Dissolved CH_4	Marine GH	0–25% (60–250 mbsf), peak at 48% (210–220 mbsf)
GMGS3-W19	Shenhu area, slope of South China Sea	Gaseous CH_4	Marine GH	0–45% (130–160 mbsf)
Beaufort Shelf	Canadian Beaufort Shelf	Dissolved CH_4	Permafrost-associated GH	~ 3%
GC 955	Green Canyon, Gulf of Mexico	Gaseous CH_4	Marine GH underlain by gaseous CH_4	79–93% (413–442 mbsf)
Mount Elbert-01	Alaskan North Slope	Gaseous CH_4	Sub-permafrost GH	50% in average with peak at 75% (615–628 and 650–662 mbgl)
	Simulation timescale	**Model dimension**	**GH accumulating mechanism**	**Reference**
GMGS1-SH2	1.5 Ma	1D	GH sedimentation and formation (M3)	Su et al. (2012)
GMGS3-W19	30 ka	1D	M5	Fang et al. (2019)
Beaufort Shelf	100 ka	1D/2D	M7	Frederick and Buffett (2015;2016)
GC 955	5.6 ka	1D/2D	M5	Wei et al. (2022)
Mount Elbert-01	Not applied	1D	M6	Behseresht and Bryant (2012)

Almost all explored marine CH_4 hydrate-bearing sediments can be described by the first five abovementioned mechanisms. M6 was defined to interpret the observed CH_4 hydrate distributions acquired from the sub-permafrost sediments at the Mount Elbert prospect (Behseresht and Bryant, 2012; Hunter et al., 2011), as listed in Table 3.1. In addition, M1 can be applied to describe the intra-permafrost hydrate occurrences discussed in Dallimore and Collett (1995). Through comparisons of the GH accumulation time period and

its hydrate saturation (S_h) distribution (Table 3.1), the formation rate of high-saturation GHs at the GMGS3-W19 site (Fang et al., 2019) is presumed to be about 2–3 orders of magnitude higher than of those at the GMGS1-SH2 and GC 955 sites (Su et al., 2012). This difference in GH formation rates implies that the GH-forming gas at the GMGS3-W19 and GMGS1-SH2 sites is transported in the free-gas (M5) and dissolved (M7) states, respectively. Furthermore, it demonstrates that the notable complexity of GH-bearing environments and the diversity of GH formation mechanisms exist even in adjacent regions in approximately 14 km distance (Sun et al., 2021) in the Pearl River Mouth Basin, South China Sea. In comparison, the coastal sub-permafrost GH fields of the Alaskan (e.g., Mount Elbert) and Canadian (e.g., Mallik) Beaufort Sea (Behseresht and Bryant, 2012; Boswell et al., 2011; Dallimore et al., 2005b) likely experienced similar heterogeneous distributions of different GH formation mechanisms.

To date, most well-studied sub-permafrost GH accumulations are located along the Arctic shoreline and contain high CH_4 hydrate saturations in the pore space of the respective sediments (e.g., Mallik (Dallimore et al., 2005b) and Mount Elbert (Behseresht and Bryant, 2012; Boswell et al., 2011)). Although M4 (Nole et al., 2018) and M5 (You and Flemings, 2018) can explain and predict the formation of CH_4 hydrate deposits with thick, high-saturation GH intervals in marine environments, they do not apply to concentrated terrestrial sub-permafrost GH accumulations. Boswell et al. (2011) compared the GH occurrence zone characteristics of the Mallik and Mount Elbert sites and confirmed that the interpretation of M6 does not apply to the Mallik site, whose intermediate and bottom GH intervals result from the lack of gaseous CH_4 supply. Instead, Frederick and Buffett (2015) and Frederick and Buffett (2016) proposed a new hypothesis considering fluid circulation below the permafrost transporting dissolved CH_4 into the GHSZ (referred to as M7 in this study) and promoting the formation of an 800 m-thick permafrost-associated CH_4 hydrate occurrence with GH saturations of about 3%. Their results reasonably explain the existence of intra-permafrost GH around the Taglu gas field as observed by Dallimore and Collett (1995). However, they do not achieve an agreement with the field data of the sub-permafrost GH intervals observed at the Mallik scientific drilling sites (Dallimore et al., 2005a; Dallimore et al., 1999), as listed in Table 3.7. Consequently, the spatio-temporal evolution of the permafrost and permafrost-associated CH_4 hydrate systems does not match the field observations without assuming that the dissolved CH_4-rich fluid flows through the underlain fault systems into the targeted GHSZ of the Mallik site.

3.1.4 Hypothesis and Main Objectives of the Present Study

Conclusively, the mechanism controlling the formation of sub-permafrost CH_4 hydrate-bearing accumulations has not yet been sufficiently well understood. Thus, knowledge gaps still exist in terms of the interactions and interrelationships between the tectonic settings, as well as permafrost and permafrost-associated GH systems. The present study investigates the hypothesis that fluid flow transports dissolved CH_4 upward and out of the overpressurized zones via pre-existing polygonal fault systems, which serve as feed gas migration pathways. Then, the dissolved CH_4 forms GH accumulations in the upper sequences, where the combination of large anticline systems, fault throws, and sandy sediments act as hydrocarbon traps (Figure 3.1). To our knowledge, a conceptual model has not yet been developed or quantitatively investigated based on the proposed formation mechanism of a sub-permafrost GH accumulation. Thus, the primary objective of this study is to validate the proposed mechanism by comparing the simulated spatio-temporal profiles of permafrost and permafrost-associated GH systems against temperature profiles and GH distributions observed at the Mallik site.

3.2 Materials and Methods

3.2.1 Geological Settings at the Mallik Site

GH Research and Industry Exploration Wells

Initially, the sub-permafrost GH occurrences in the MB area were inferred from seismic data obtained from conventional hydrocarbon exploration in the mid-1980s. Subsequently, the GH accumulations at the Mallik site have been subject to a series of international scientific joint investigations over the last decades. Up to now, four GH research (Mallik 2L-38, 3L-38, 4L-38, and 5L-38) and four industry exploration wells (Mallik P-59, L-38, J-37, and A-06) at the Mallik site have encountered the underlain sub-permafrost GH sediments (Collett, 1999; Osadetz et al., 2005). Overall, two production research (Mallik 2L/5L-38) and two monitoring or water-reinjection wells (Mallik 3L/4L-38) have been drilled throughout the permafrost and its underlain GH intervals in the course of the numerous scientific Mallik field programs, as shown in Table 3.7.

According to previous studies (Mestdagh et al., 2017; Ruppel and Kessler, 2017), pan-Arctic permafrost-associated GHs are not as climate-vulnerable as the shallow marine GHs on the upper continental slopes, the subglacial GHs and the terrestrial plateau permafrost-associated GHs (Zhu et al., 2021). Although the relict permafrost degradation in the MD area has been continuously promoted by the contemporary climate change, leading to an increased probability of further GH destabilization, no significant amount of free gas has been monitored directly below the GHSZ base at the Mallik site (Bellefleur et al., 2007; Collett, 1999). Consequently, the decomposition of sub-permafrost GHs at the Mallik site has not yet been observed, as the GHSZ bottom is the region most sensitive to temperature changes induced by climate warming, as reported by Mestdagh et al. (2017) and Tréhu et al. (2006).

Available Seismic Data

Reflection seismic imaging is a feasible geophysical exploration technique for identifying GH deposits. High-saturation GH deposits usually correlate with observable, reverse-polarity bottom simulating reflectors (BSRs), high resistivity and low acoustic travel-time differences (Mestdagh et al., 2017). The appearance of BSRs indicates the high impedance contrast between the GH-bearing sediments with high seismic velocity and the underlying free or dissolved gas-charged sediments with low seismic velocity (MacKay et al., 1994). As a result, the BSR is regularly associated with the base of the GHSZ, and the higher the GH saturation (S_h), the more pronounced any BSR anomalies are (Zhang et al., 2017b).

In Figure 3.2, the seismic profile 85987 (Collett, 1999) crosses the Mallik anticline and runs to the north. Numerous normal faults penetrate the crest of this anticline with high dipping angles. Beneath and along the crest of the Mallik anticline, the seismic transect A-A' shows a number of high-amplitude reflectors indicated by the orange shading in Figure 3.2b, implying the sub-permafrost GH sediments. In addition, the phase boundary (p-T) marks the GHSZ base on the northern flank of the Mallik anticline. As plotted in Figure 3.2b, the Mallik anticline is bounded to the southwest trend by a large high dipping angle normal fault, which extends down into deeper stratigraphic sequences.

Uncertainties and Limitations of Seismic Reflection Measurements

The field parameters of seismic imaging were not optimal for evaluating shallow GH-related features since these campaigns aimed at exploring deep conventional oil and

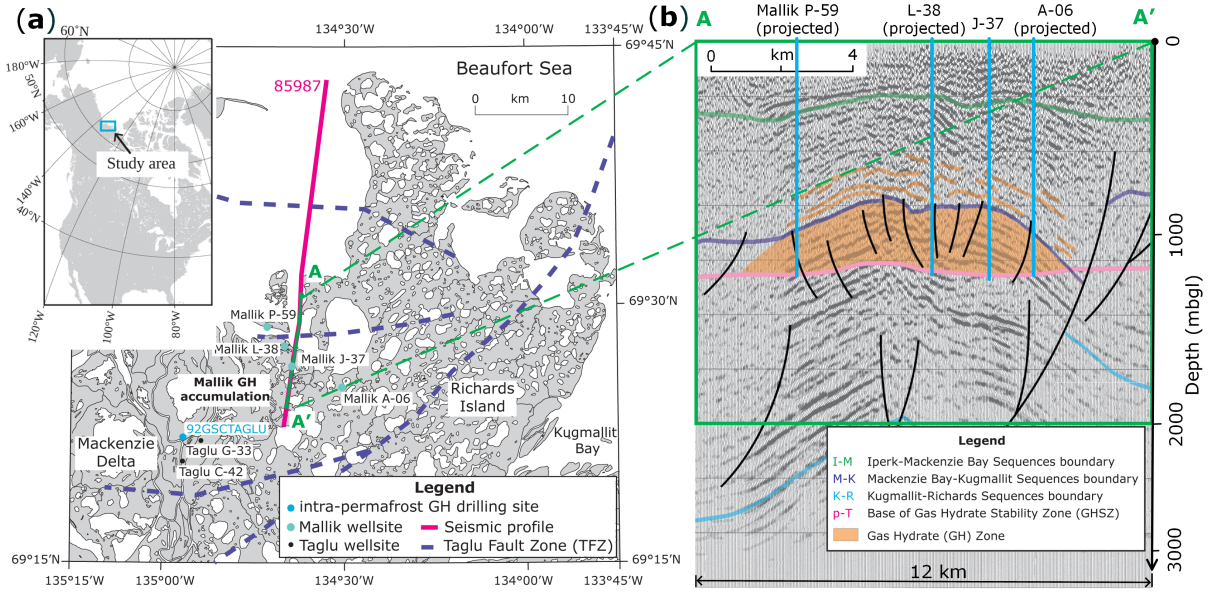

Figure 3.2: (**a**) Map of permafrost terrain in the Mackenzie Delta showing the seismic profile 85987, the location of the transect A-A' and the Mallik and Taglu sites, modified from Collett (1999); (**b**) inset of Mallik anticline and well locations obtained from the seismic profile, modified after Collett (1999). The 2D seismic transect A-A', modified on the basis of the seismic profile 85987, crossing the Mallik J-37 well location, with the industrial exploration wells Mallik P-59, J-37 and A-06 projected onto the transect. Figures presented with permission from Natural Resources Canada under the Open Government License—Canada version 2.0.

gas deposits (Collett, 1999). Additionally, ice-bearing permafrost and GH occurrences have similar seismic and electrical properties (Frederick and Buffett, 2016). Therefore, BSRs cannot be expected within the ice-bearing permafrost (Ruppel, 2015), and it is nearly impossible to determine intra-permafrost GH by any standard surface-based geophysical observation technique. Despite these limitations, the reprocessing of industry seismic data (Bellefleur et al., 2009) provides valuable insights into the dominating sedimentological and structural features on the distribution of inferred sub-permafrost GH accumulations.

In terms of the seismic characteristics of the Mallik site, the previously qualitative mapping of GH reservoirs, as well as the coarse resolution of the GH reservoir boundaries and thicknesses could not meet industrial production needs. In this context, Bellefleur et al. (2009) addressed the lateral and depth-dependent geologic variations and lateral extent of the GH occurrences at further distances to the wells. In addition, Huang et al. (2009) demonstrate that attenuation of seismic energy may be primarily attributed to scattering from small-scale heterogeneities and highly attenuate leaky mode propagation of seismic waves through larger-scale heterogeneities in sediments rather than the intrinsic attenuation of GH-bearing sediments.

Characteristics of the Phase Boundary at the Hydrocarbon Trap Bottom

The upper Cretaceous–Tertiary basin-fill and pre-Cenomanian rifted strata contain significant fossil fuel resources in the MD area. The combinations of large anticlines, fault-related structures and porous sandy sediments produce efficient hydrocarbon traps. The anticlines are large-amplitude structures with up to 3 km of relief and generally have rounded hinges (Dixon et al., 2019), as shown in Figure 3.2b. They are thus commonly inferred to be structural traps containing the bulk of potential hydrocarbons. Most anticlines are asymmetric, with the steep branches usually facing basinwards, and many are cored with north- or northeast-verging thrust faults (Dallimore et al., 2005a).

At the Mallik site, the observed high-saturation GH intervals occupy > 80% of the pore space of the unconsolidated clastic sediments, located at depths of 900–1100 mbgl and localized at the crest of the Mallik anticline (Dallimore et al., 2005a). Moreover, the seismic characteristics of the top, middle and bottom GH zones, identified by the A, B and C zones, respectively, were examined to assess the localized geologic influence on the GH distribution. The phase boundary at the bottom of zone C coincides with the GHSZ base with no free gas below, further indicating a lack of gaseous CH_4 supply (Dallimore et al., 2005b) at the Mallik site, which suggests that the formation mechanism M7 is valid here instead of M6 (gaseous CH_4 accumulations in situ conversion into GH deposits). As a comparison, Behseresht and Bryant (2012) attributed a different S_h distribution but a similar vertical variation of the S_h profile observed at the Alaskan Milne Point area to the discontinuous supply of gaseous CH_4 during the formation of two GH intervals via M6 instead of M7. The fact in support of this conclusion is that the mean value of S_h significantly declined from ca. 60% to 15% at the bottom of the lower GH interval, which agrees with the GH distribution pattern generated by M6.

However, three well-log inferred GH zones (Collett, 1999) were confirmed by on-line mud-gas monitoring (Wiersberg et al., 2005), but the previous interpretation of the BSR as a free-gas zone below 1112 mbgl (the assumed GHSZ base shown in Figure 3.2b) was not identified in the mud-gas analysis of the Mallik 5L-38 well. This observation is consistent with the seismic measurements (Miller et al., 2005), as well as the velocity and attenuation tomograms of the Mallik 5L-38 well (Bauer et al., 2005a), showing no clear indication of a free gas phase below the GH zone C. Moreover, Bellefleur et al. (2007) improved the resolution of the surface 3D seismic data by compensation for attenuation effects of permafrost and GH-bearing sediments. They demonstrated the occurrence of a 5 m-thick free-gas interval located at ca. 75 m below the GHSZ base of the Mallik L-38 well and reported the absence of free gas within any GH intervals and directly underneath the *p-T* boundary at the Mallik site. According to MacKay et al. (1994), super-saturated dissolved gas in the pore fluid may also produce a similar BSR event as the presence of a free-gas phase, which may explain the above mentioned BSR near the *p-T* boundary at the Mallik site. As a result, these findings support our assumption of CH_4 in dissolved form as the feed gas to form hydrate at the crest of the Mallik Anticline.

3.2.2 Model for Validating the Formation Mechanism of Sub-Permafrost GH Deposits

Faults as Feed Gas Migration Pathways

Faults are internally complex volumetric zones, playing a critical role as primary conduits for the convection of fluids beneath the permafrost, facilitating GH formation, gas migration and tectonics (Hillman et al., 2020). For example, many substantial dipping angle faults occur in the major Taglu Fault Zone (TFZ) adopted from Chen et al. (2021) and Chen et al. (2008), as presented in Figure 3.2a, representing barriers to lateral fluid flow across the fault plane. However, fault damage zones may serve as preferential flow paths for the vertical migration of CH_4-rich fluids originating at depth, causing temperature anomalies (Chen et al., 2008).

Some large high-dipping angle faults are depicted at the bottom of Figure 3.2b, with main GH accumulations above these faults, indicating that some faults are efficient pathways for CH_4-bearing formation fluids. However, it is not yet fully understood to what extent these faults control the subsurface geothermal distribution and CH_4-rich fluid migration near the TFZ and how they impact the heterogeneity of GH accumulations at the Mallik site. Using the

fault geometries (Figure 3.3) derived from Figure 3.2b, the role of normal faults contributing to the formation of highly-saturated GH accumulations is investigated in the present study. Furthermore, we determine whether these faults are hydraulically conductive to fluid flow by altering their hydraulic properties (i.e., porosity and permeability) employed in the numerical model.

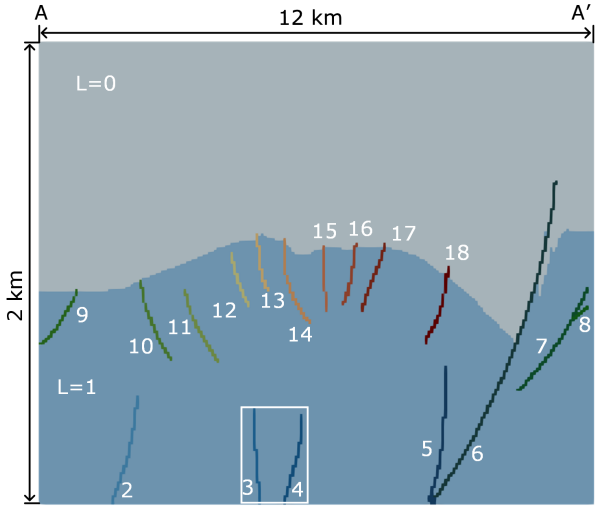

Figure 3.3: Model domain and geometry of the interpreted seismic transect A-A' modified after Collett (1999). The lithology markers (L) represent the sediments of the Iperk–Mackenzie Bay (0) and Kugmallit–Richards Sequences (1). The 17 faults considered in the model are identified by the lithology markers 2 to 18. Faults 3 and 4 (located within the white rectangle) are the sources for the dissolved CH_4-rich fluid flowing into the modeling domain (cf. Figure 3.2a,b).

Origin of GH Feed Gases as well as Characteristics of the GHs and their Host Sediments

Characterization of the GH research wells in the MD via geochemical analyses, such as the Mallik 5L-38 well, shows that gases from sequences shallower than 500 mbgl are considered biogenic (Waseda and Uchida, 2005). At depths of 550–850 mbgl, gases are mixtures of biogenic and thermogenic origin, while gases from more than an 890 mbgl depth, including the GH interval at depths of 890–1108 mbgl, are thermogenic. Generally, organic- and gas-geochemical analyses show that thermogenic gases probably migrated from thermally-matured sediments below 5000 mbgl, whereas low-maturity gases were generated from in situ organic matter, particularly the lignite layers of the Kugmallit Sequence (Zhu et al., 2005). Geochemical studies suggest that thermogenic gases have migrated up-dip along faults and stratigraphic boundaries, were adsorbed by lignite-rich strata and then intermixed with local microbial gases. In addition, the archaeal DNA and microbial analyses suggest exceedingly low methanogenic archaeal populations and activities in deep sediments (Colwell et al., 2005), supporting our simplification of the feed gas as thermogenic gas (CH_4) in the numerical simulations.

Based on core samples from the Mallik 2L/5L-38 wells, petrophysical analyses indicate GH accumulations of varying saturations in sand-rich sediments overlain by moderate to good seals (Moridis et al., 2005b). As a result, the assumption of impermeable boundaries for caprocks is reasonable, given the relatively higher intrinsic permeability of the GH-bearing sediments (Uddin et al., 2012). This also suggests that GHs occurred as a pore-filling type within a frame-supported pore-structure texture (Katsube et al., 2005). The Mallik GH deposits are controlled by the lithology of their host sediments, separated by fine-grained, silty facies and clay. Within the cored intervals located at depths from 890 to 1108 mbgl, coarse-grained

sandstone sediments contain abundant GHs, whereas fine-grained sediments, i.e., the siltstone and mudstone, act as no-flow barriers, showing minor to absent GH saturations.

The GH feed gas may have migrated into the GHSZ in numerous ways (Collett et al., 2009). As a result, the migration of gas dissolved in formation fluids is required to form high-saturation GHs (Zhang et al., 2017b). However, there is no valid evidence for the presence of a free gas phase within the GH zone (also referenced as the mixing layer) or directly below the GHSZ base, as discussed in Section 3.2.1. Therefore, our hypothesis on dissolved CH_4-rich fluid migrating out of the overpressurized zone along preferential faults (Chupeng et al., 2020; Gongzheng, 2020; Osadetz and Chen, 2010) to the host sediments within the GHSZ is further supported, given the sediment below zone C shows a lack of free gas presence at the Mallik site.

3.2.3 Numerical Model Implementation

Mathematical Model and Modeling Assumptions

A framework of equations of state (EoS) for equilibrium CH_4 hydrate formation has been integrated with the flow and transport simulator TRANSE (Kempka, 2020), referred to as $T_{plus}H$ (TRANSE + Hydrate) in a previous study (Li et al., 2022b). In the current study, an EoS module describing the reversible processes of water-freezing and ice-thawing (Mottaghy and Rath, 2006) has been implemented and integrated with $T_{plus}H$ to investigate the interactive processes of permafrost formation and degradation, as well as sub-permafrost GH formation.

To preserve the solution accuracy of the non-linear system of partial differential equations, we assume the following simplifications to maintain computational efficiency and numerical convergence requirements:

1. The assumptions proposed by Li et al. (2022b) are considered, while temperature (−20–45 °C) and pressure ranges (0–20 MPa) were extended in the updated EoS. Volume changes during ice–fluid and vice versa phase transitions are neglected;
2. GH accumulations were categorized into various classes in previous simulation studies, depending upon varying boundary conditions. According to Moridis and Collett (2004), Class-II deposits are defined as GH sediments overlain by impermeable rocks and underlain by gas-free aquifers. In the numerical history matching for a six-day depressurization test, Uddin et al. (2012) and Uddin et al. (2014) defined the three GH zones at the Mallik 2L-38 well as Class-II deposits. Moreover, data from specimen analysis suggests that processes of solute migration and GH formation at the Mallik site occurred in a semi-closed hydrodynamic system (Wright et al., 2005). Therefore, this study will employ the assumption of the presence of semi-closed Class-II GH sediments to investigate the formation of the sub-permafrost GH deposits overlain by impermeable upper sediments comprising permafrost and structural traps;
3. Beneath the GH sequences at the Mallik site, fluid migration pathways are represented by faults of which the widths are unknown but assumed to be 60 m. The dissolved CH_4-rich fluid flows into the modeling domain via two high dipping-angle Faults 3 and 4, shown at the bottom of Figure 3.3;
4. The depositional processes of the stratigraphic sequences and coastal erosion in the MD region, changes in sea level and tectonic subsidence or uplift since the late Pleistocene showed negligible influences on the evolution of sub-permafrost GH accumulations. Thus, these are not considered in the present modeling work.

Model Geometry

Figure 3.3 shows the lithology of the considered seismic cross section at the Mallik site as implemented into the numerical model, as well as its geometry and dimensions (12,000 m in horizontal and 2000 m in the vertical direction). It comprises two sequences with the respective lithology markers L = 0 and L = 1, and 17 faults (L = 2–18). The lateral model boundaries are represented by Dirichlet boundary conditions in terms of transported species concentrations and *p*-*T* terms to mimic an infinite aquifer. Moreover, the upper model boundary is represented by a Dirichlet boundary with fixed *p*-*T* conditions, overlying those aforementioned impermeable sediments. Finally, constant pressure and basal heat flow are applied at the model bottom, excluding the grid elements representing Faults 3 and 4. The latter represents source elements for the inflowing CH_4-rich formation fluid, with constant temperature conditions and a pre-determined fluid flow rate. The grid element thicknesses along the lateral and vertical directions equal 60 m and 10 m, respectively. In total, the 2D modeling domain consists of $200 \times 200 = 40,000$ elements.

Model Parametrization

The hydrothermal properties of the sediments at the Mallik site were determined using an iterative history-matching procedure resulting in the parameters summarized in Table 3.2. The initially uniformly distributed hydrothermal properties of the permafrost and GH-bearing sediments change with the local increase in S_h and ice saturation (S_{ice}), i.e., effective porosities and permeabilities will decrease in turn, as explained in Section 3.6.2.

Table 3.2: Hydrothermal properties of the permafrost and GH-bearing sediments as well as other parameters used in the present study.

Parameter	Value	Unit	Reference
Effective permeability of I-M sequence	$\kappa_x = 10^{-5}$, $\kappa_y = 10^{-7}$	Darcy	Assumed
Intrinsic permeability of K-R sequence	$\kappa_x = 5$, $\kappa_y = 1$	Darcy	Assumed
Intrinsic permeability of Faults 2–18	$\kappa_x = 50$, $\kappa_y = 10$	Darcy	Assumed
Intrinsic porosity of sediment matrix	0.3	-	Collett (1999)
Salinity of pore fluid	10	kg m^{-3}	Collett (1999)
Initial pore pressure gradient	1.012×10^4	Pa m^{-1}	Henninges (2005)
Density of sediment grain	2650	kg m^{-3}	Collett (1999)
Hydration number	6.1	-	Ripmeester et al. (2005)
Thermal conductivity of wet sediment	2.45	W m^{-1} K^{-1}	Henninges (2005)
Thermal conductivity of CH_4 hydrate	0.68	W m^{-1} K^{-1}	Waite et al. (2009)
Specific heat of sediment matrix	830	J kg^{-1} K^{-1}	Waite et al. (2009)
Specific heat of CH_4 hydrate	2100	J kg^{-1} K^{-1}	Waite et al. (2009)
Diffusion coefficient	1.0×10^{-10}	m^2 s^{-1}	Li et al. (2022b)
Density of inhibitor (NaCl)	2160	kg m^{-3}	Moridis et al. (2005a)
Compressibility of porous medium	1.0×10^{-10}	Pa^{-1}	Li et al. (2022b)

According to the log interpretation and results from core analyses undertaken at the Mallik 2L- and 5L-38 wells, the GH-bearing sediment is mainly composed of sand interbedded by shale, whereas the average effective porosity is between 0.24–0.4 and mean permeability about 2.9 mDarcy. Moreover, the highly saline residual pore fluid sampled at the GH intervals

implies that fluid migration in the GH-bearing sediments at the Mallik site is slow due to the permeability reduction by GH accumulation and the in situ hydraulic properties (i.e., presence of interbedding shales).

In Table 3.3, the subaerial surface temperature is implemented at the top model boundary based on the arithmetic mean of the paleo-climate evolution derived from Taylor et al. (2013) and Majorowicz et al. (2012a). The listed initial fluid flow rate is the optimal input parameter derived from validating the respective simulated subsurface temperature distributions against the reported temperature profiles and anomalies in the MD region in Chen et al. (2008) via an iterative modeling workflow. In addition, the thick permafrost and GH sequences may have persisted for about 1.0 Ma (Majorowicz et al., 2012a), but offshore permafrost formed during the Wisconsinan glacial period (Dallimore et al., 2005a), when the Beaufort Shelf was exposed by seaward regression. However, the influence of sea-level changes is negligible in view of the deep buried onshore GH deposits residing under the thick permafrost at the Mallik site, and thus sea-level changes are not considered in the present study. Instead, a change in subaerial surface temperature from −16 °C to −8.3 °C is considered after the first stage at a simulation time of 997 ka to take into account the paleoclimate evolution. For that purpose, parameters reflecting average values reported in the literature are employed for model parametrization, as listed in Tables 3.2 and 3.3. Unless otherwise stated, the employed parameters are not changed after the implementation of the transitional boundary conditions.

Table 3.3: List of applied initial and boundary conditions in the simulation.

Parameter	Value	Unit	Reference
Simulation time of the first stage	997	ka	Modified after Majorowicz et al. (2012a)
Inflowing fluid rate	6.0×10^{-10}	kg m^{-3} s^{-1}	Assumed
Dissolved CH_4 concentration	2.1	kg m^{-3}	Assumed
Subaerial surface temperature since 1 MaBP	−16	°C	Modified after Taylor et al. (2013)
Basal heat flow	57	mW m^{-2}	Taylor et al. (2013)
Freezing point of pore fluid	−1.5	°C	Taylor et al. (2013)
Frozen point of pore fluid	−2.5	°C	Taylor et al. (2013)
Specific latent heat of water-ice phase change	333.6	kJ kg^{-1}	Waite et al. (2009)
Transitional boundary condition used since 3 kaBP			
Simulation time of the second stage	3	ka	Modified after Majorowicz et al. (2012a)
Current subaerial surface temperature	−8.3	°C	Modified after Taylor et al. (2013)

3.3 Simulation Results

3.3.1 Regional Distribution of Permafrost and Sub-Permafrost GH Accumulations

Figure 3.4a shows the assessed boundaries of the seismically-inferred distribution of the two significant GH accumulations at the Taglu and Mallik sites on Richards Island, based on the seismic data reprocessed by Collett (1999) and initially acquired by the oil and gas industry in the

mid-1980s. As depicted in Figures 3.2b and 2.4b, sub-permafrost GH deposits were seismically inferred and numerically confirmed at the crest of the Mallik anticline with a connection to the deeply buried hydrocarbon GH feed gas via Faults 2–7 illustrated in Figure 3.3. Figure 3.4a shows that the GH deposit at the Mallik site is laterally continuously distributed and covers an area (green shaded) of ca. 51 km^2 (Collett, 1999). The portion of the delineated GH deposit with the dark green shading denotes an area of higher GH saturations. Figure 3.4b suggests that GHs mainly accumulate in the upper host sediments of the Mallik anticline crest.

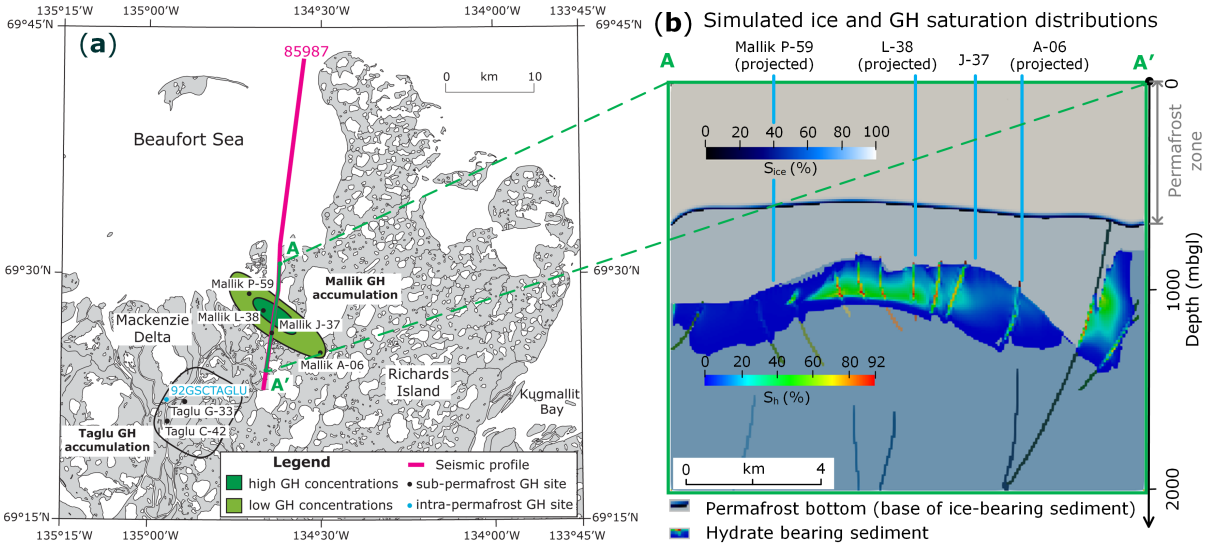

Figure 3.4: (**a**) Map illustrating the saturation distribution of seismic- and well-log-inferred Mallik GH accumulations in the outer Mackenzie Delta, modified after Collett (1999); (**b**) simulated regional permafrost and sub-permafrost GH accumulation distributions after a simulation time of 1 Ma (cf. Figure 3.3 for modeling dimensions). (**a**) presented with permission from Natural Resources Canada under the Open Government License—Canada version 2.0.

As interpreted from Figure 3.5b, the simulation results (cf. Figure 3.5 and Table 3.4) are acquired from the Mallik J-37 well and projected locations of the industrial exploration wells (Mallik P-59, L-38, and A-06) onto the 2D seismic transect A-A' to allow for model validation. Our simulation results reach a very good agreement with the well-logged and seismic observations (Collett, 1999) from the Mallik wells P-59, L-38, J-37 and A-06, which reveal highly variable S_h of the Mallik GH deposit throughout the horizontal profiles shown in Figure 3.4a. The simulated S_h profile presented in Figure 3.5b also confirms that the Mallik GH occurrences are highly concentrated around the location of the Mallik L-38 well, illustrated by the dark green shading in Figure 3.4a. Moreover, the simulated S_h profiles (cf. Figure 3.5a,c,d) are consistent with the respective seismic-inferred GH concentrations from the Mallik P-59, J-37 and A-06 wells, located within the light green shaded delineation in Figure 3.4a.

Figure 3.5e demonstrates that the S_h profile of the GH interval is highly heterogeneous in line with the lithology along the borehole profile. It also indicates that coarse-grained sediments consisting of sand and pebbles contain abundant GH, whereas fine-grained sediments made of shale and silt host little to no GHs. This supports the conclusion that the S_h distribution is lithologically controlled, as previously stated by Matsumoto et al. (2005). According to Katsube et al. (2005), analysis of the petrophysical data (i.e., porosity, permeability and pore-size distribution) of the core samples acquired at the Mallik 5L-38 well support that relationship between S_h and the lithological properties. It is known that silty and clayey sediments with relatively low porosities (0.25–0.3) have medium to very low permeabilities (generally 0.1–10 mDarcy). Overall, sediments of poor reservoir quality (i.e., low porosity and permeability)

show a significantly lower potential to host GHs compared to those of good reservoir quality (i.e., high porosity and permeability) in the MD region.

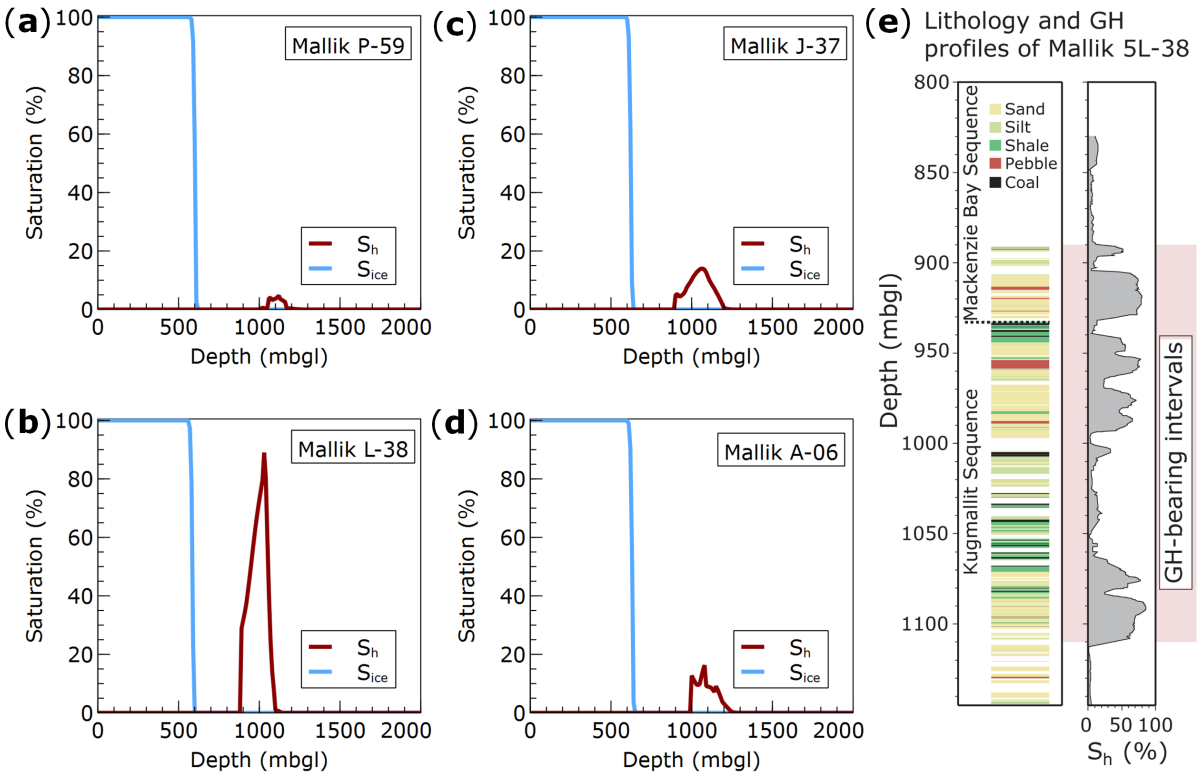

Figure 3.5: Simulated ice-bearing permafrost saturation (S_{ice}) and sub-permafrost gas hydrate saturation (S_h) profiles obtained for the respective locations of the Mallik P-59 (**a**); L-38 (**b**); J-37 (**c**); and A-06 (**d**) wells after a simulation time of 1 Ma; (**e**) lithology and S_h profiles recorded at the Mallik 5L-38 well, modified after Bauer et al. (2005b). (**e**) presented with permission from Natural Resources Canada under the Open Government License—Canada version 2.0.

According to Boswell et al. (2011), the intervals with high GH saturations ($S_h > 50\%$) exhibit high intrinsic permeabilities (often 1–5 Darcy), which are only known for sand-type and pebble-type sediments of high porosity (0.3–0.4). Consequently, a uniform porosity is employed in the simulations with varying permeabilities, rendering permeability the dominant factor of the lithology variations undertaken in the present study.

In Figure 3.5e, the relation between sediment characteristics and S_h indicates that varying permeabilities in our simulations are the principal local constraint on pore occupancy within the GH columns. This also implies that the three GH zones occurring within the sand-dominated intervals at depths of ca. 905–930 mbgl, 940–995 mbgl and 1065–1112 mbgl are preserved under the caprocks composed of shale and silt, interbedded with coal at depths of about 895–905 mbgl, 930–940 mbgl and 995–1070 mbgl, respectively. The presumption that fractures within the caprock connect those adjacent sand-rich sediments and supply dissolved CH_4-rich fluid to facilitate GH formation until these clog the fractures is also supported by the previous findings. In contrast, the simulated S_h profile at the Mallik L-38 well near the Mallik 5L-38 observation well demonstrates a relatively uniform GH distribution within the assumed homogeneous sandy host sediment, as shown in Figure 3.5b.

Throughout Table 3.4, the comparison of simulated and observed data implies that most of the numerically determined parameters, including the bases of the ice-bearing permafrost and peak GH saturations, match very well with the field observations with negligible deviations

of up to 2.3%. In addition, all the simulated GHSZ bases are within the uncertainty range of the corresponding observations, which amounts to about 9%. Although most of the simulated total GH interval thicknesses are consistent with the observed data with minor deviations of up to 8.5%, a relatively high deviation of ca. 26% is outlined between the observed and simulated results at the location of the Mallik A-06 well, which was projected on the respective cross section. This deviation may be directly related to the fact that the Mallik A-06 well exhibits the greatest distance to that cross section, as presented in Table 3.7. Furthermore, it should be noted that the actual projection of the Mallik A-06 well is located outside of the green shaded area with a distance of about 500 m, as shown in Figure 3.4a.

Table 3.4: Comparison of the well-log-inferred data with the simulated key parameters of the GHSZ and permafrost distributions as well as GH saturation profiles.

Parameter/Well	P-59		L-38	
	Observed	**Modeled**	**Observed**	**Modeled**
Depth of ice-bearing permafrost base (mbgl)	638	630	605	600
Depth of GHSZ base (mbgl)	1200 ± 100	1240	1100 ± 100	1130
Total thickness of sub-permafrost GH intervals (m)	156.8	150	213.1	230
Peak S_h within GH intervals (%)	-	5	90	91
Parameter/Well	**J-37**		**A-06**	
	Observed	**Modeled**	**Observed**	**Modeled**
Depth of ice-bearing permafrost base (mbgl)	615	620	632	630
Depth of GHSZ base (mbgl)	1300 ± 100	1220	1300 ± 100	1280
Total thickness of sub-permafrost GH intervals (m)	292.2	300	182.8	230
Peak S_h within GH intervals (%)	-	15	-	18

Note: The well-log-inferred data are adopted from Collett (1999) and Dallimore et al. (2005a). Well-log-inferred results that could not be derived from field reports (Collett, 1999; Dallimore et al., 2005a) are represented by dashes.

In the MD, exhaustive studies have not yet been completed to survey the distribution of permafrost-associated GH. So far, the GH distribution observed by geophysical methods may be attributable to the fact that these measurements are easier to employ to explore large-scale and highly saturated GH deposits in the vicinity of hydrocarbon deposits, as noted by Frederick and Buffett (2016). As a result, it may be assumed that small-scale and less saturated GH deposits exist outside the green shaded areas in Figure 3.4a. Moreover, given the lack of extensive field observations on S_h for each GH interval at the Mallik P-59, J-37 and A-06 wells, it is not feasible to conduct a quantitative analysis, but only qualitative comparisons of the peak saturations based on the limited available information.

3.3.2 Observed and Simulated Temperatures in the Vicinity of the Mallik L-38 Well

Subsurface *p-T* conditions control the stability of permafrost and sub-permafrost GH accumulations, while permafrost stability is much less susceptible to pressure perturbations (e.g., caused by regressive/transgressive marine cycles) but is more sensitive to temperature changes. Generally, a change in temperature at the ground surface will disrupt the subsurface temperature profile, which is originally in thermal equilibrium with the corresponding basal heat flow below the permafrost and the GH-bearing sandy columns. The transition of the

temperature profile to a new thermal equilibrium condition is shown in Figure 3.6a, as the result of implementing transitional boundary conditions at a simulation time of 3 kaBP to mimic the paleo-climate evolution from the Late Holocene Epoch on (cf. Table 3.3), according to Majorowicz et al. (2012a) and Taylor et al. (2013). As the arithmetic mean of subaerial surface temperature shifts from −16 °C to −8.3 °C, the simulation continues for a subsequent period of 3 ka until the final simulation time of 1 Ma is reached.

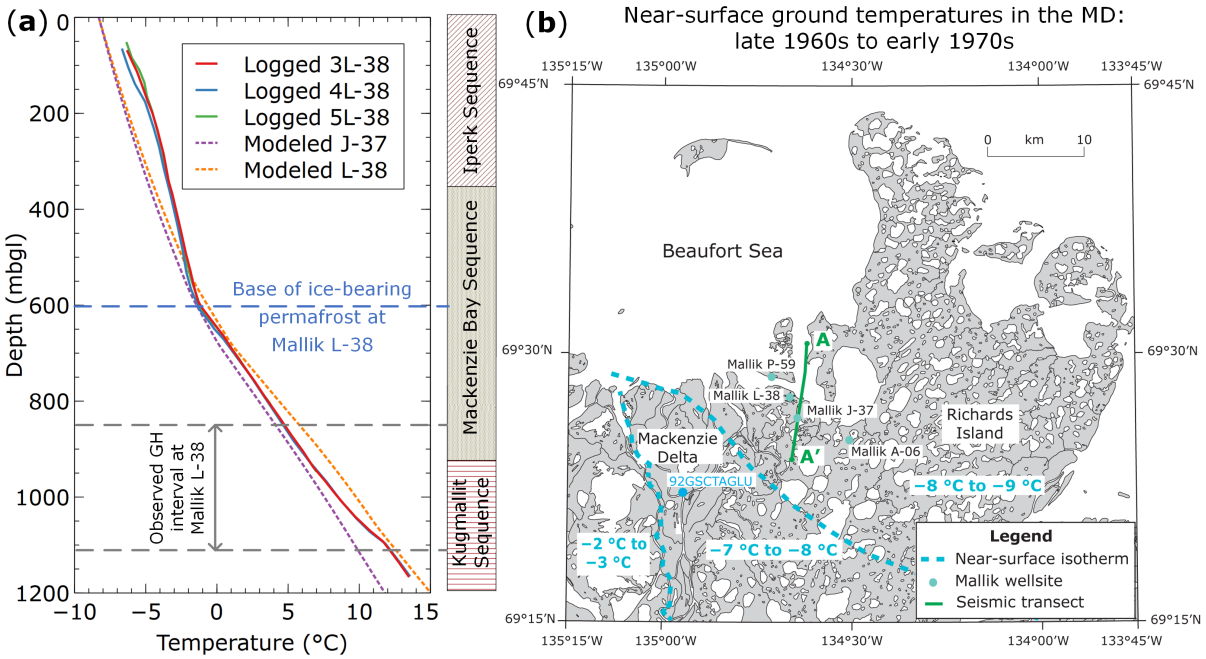

Figure 3.6: (**a**) Comparison between Distributed Temperature Sensing (DTS)-logged and simulated temperature profiles. The DTS temperature profiles acquired at the Mallik 3L/4L/5L-38 wells were obtained after 622, 605 and 575 days of their completions (Henninges et al., 2005), respectively. Sequence boundaries are modified after Dallimore et al. (1999); (**b**) map of the near-surface ground temperature distribution in the Mackenzie Delta, in which the representative ground temperature data was collected from hydrocarbon exploration wells developed in the late 1960s and early 1970s, modified after Dallimore et al. (2005a). Figures presented with permission from Natural Resources Canada under the Open Government License—Canada version 2.0.

With some modifications based on the map presented by Dallimore et al. (2005a), Figure 3.6b shows the representative near-surface temperatures acquired at several hydrocarbon exploration wells. As indicated in Figure 3.6b, the current near-surface ground temperature ranges from −8 °C to −9 °C at the Mallik site, which matches the arithmetic mean of the subaerial surface temperatures of −8.3 °C listed in Table 3.3. However, the sub-permafrost parts (depth > 600 mbgl) of the simulated and observed temperature profiles demonstrate that the GH intervals (depth > 900 mbgl and < 1100 mbgl) are still located above the GHSZ base. This supports the conclusion that even though submergence of the shelf and coastal retreat occurred with rising sea levels since the Holocene, there has not been enough time to trigger significant permafrost degradation (Dallimore et al., 2005a) and GH dissociation by the increase in temperature. Based on the observations and simulation results, Table 3.5 lists the depths of the GHSZ and ice-bearing permafrost bases.

When comparing the profiles in Figure 3.6a, the simulated sub-permafrost temperature profile of the Mallik L-38 well is consistent with the DTS-logged observations, while the simulated temperature at the Mallik J-37 well deviates from the observations of the Mallik

3L/4L/5L-38 wells by almost 2.0 K at the GHSZ base. This suggests an almost 100 m-deeper simulated base of the GHSZ at the Mallik J-37 well compared to the logged GHSZ bases at the Mallik 3L/4L/5L-38 wells and the simulated GHSZ base at the Mallik L-38 well, as indicated in Table 3.4. Furthermore, the relatively large variation between the location of the Mallik J-37 to L-38 wells matches the prediction of the subsurface temperature field presented by Chen et al. (2008). It has been demonstrated that subsurface temperature variation could reach about 5.0 K/km along the lateral direction at the given depth of 1100 mbsl. As addressed in Section 3.2.1, Mallik J-37 was a legacy well from previous industrial drilling activities, probably conducted in the 1970s. Unfortunately, temperature data for the Mallik J-37 well are not available in any existing open-access datasets and publications. Therefore, the simulation results are compared to the adjacent DTS-logged observations of the scientific research wells Mallik 3L-38, 4L-38 and 5L-38 in Figure 3.6a.

Table 3.5: Comparison of DTS-logged data with the simulated key parameters of the permafrost and GHSZ.

Parameter (mbgl)/Well	Observed			Simulated	
	3L-38	**4L-38**	**5L-38**	**J-37**	**L-38**
Depth of ice-bearing permafrost base	599.4 ± 3.5	604.4 ± 3.5	600.4 ± 3.5	620	600
Depth of GHSZ base	1104 ± 3.5	1105 ± 3.5	-	1210	1130

Note: Observations of Mallik 3L/4L/5L-38 wells are originally obtained from Henninges et al. (2005) with the units of 'mKB', which were converted into 'mbgl' by compensating the relative depth to rotary kelly-bushing which is ca. 4.6 m above the ground level. The dash represents field observation data that could not be derived from Henninges et al. (2005).

However, the intra-permafrost intervals of the simulated and observed temperature profiles demonstrate that the observed near-surface temperatures (depth < 50 mbgl) are higher than in the numerical predictions by up to 0.8 to 1.3 K. This can be accounted as the combined consequence of the global warming above the pre-industrial levels before 2004 (Hoegh-Guldberg et al., 2019) and an overestimation of the ice content within the pore space in the permafrost intervals (Nitzbon et al., 2020) as discussed in the following section.

3.4 Discussion

As addressed in Section 3.1.3, notable variations in GH formation mechanisms have been identified in the vicinity of the same GH-bearing basins, even though their host sediments have similar lithologic properties. Likewise, although the sediment properties of the Mallik and Mount Elbert sites are identical, the formation mechanisms of their sub-permafrost GH accumulations are entirely different. Therefore, the present study focused on the numerical validation of the proposed formation mechanism of GH accumulations at the Mallik site to test further hypotheses on GH formation and investigate the impact of climate change on the stability history of sub-permafrost GH deposits.

3.4.1 Factors Impacting the GH Saturation Distribution

Figure 3.2b shows that some potential GH-bearing intervals, inferred from the 2D seismic response and depicted in orange shading, accumulate along the Kugmallit–Mackenzie Bay Sequences boundary (KMB), and appear as several scattered belts above the KMB. However,

since the scattered belt-like GH intervals above 890 mbgl (Figure 3.2b) were not confirmed by well logging obtained at the Mallik site, the corresponding sediments are parametrized to be impermeable caprocks as listed in Table 3.3. Likewise, Figure 3.4b indicates that one simulated GH accumulation is distributed along Fault 6 and above Faults 7 and 8 with a thickness up to ca. 300 m. However, it is not found in the seismic interpretation shown in Figure 3.2b. This inconsistency suggests either a likely undiscovered GH accumulation located ca. 2 km south from the Mallik J-37 well near the Taglu GH accumulation or that Fault 7 was not hydraulically active since the Late Pleistocene. However, it is not possible to form any definite conclusions without additional field observations from the boreholes that penetrate the potential GH-bearing sediments in this area due to the fact that this region has not been the target of previous hydrocarbon exploration and scientific investigation activities. Therefore, it merits further attention to promote the mapping precision of GH resources, as additional field data become available.

As discussed in Section 3.3.2, lithology and fault architecture control the spatial evolution of the S_h profiles within the simulated and observed GH intervals. In addition, their common local constraint on pore occupancy (i.e., maximum S_h) within the GH columns is the sediment permeability. Although Figure 3.5e reflects the lithological heterogeneity along the GH-bearing column at the location near the Mallik L-38 well, it is not feasible to integrate this lithologic variation into the model geometry in the form of permeability variations due to the lack of field data covering the area presented in Figure 3.2a.

The variations in the sequence boundary depths between the projected locations of the Mallik L-38 and Mallik 2L/5L-38 wells are not negligible. As shown in Figures 3.5e and 3.6a, the KMB of the Mallik 5L-38 well is at a depth of ca. 930 mbgl, while the KMB at the projected location of the Mallik L-38 well is at ca. 900 mbgl, as plotted in Figures 3.2b and 3.3. This limitation is expected to be overcome by implementing a 3D regional model geometry for subsequent simulation studies based on the available 2D seismic profiles, interpreted cross sections and well data.

In addition, Figure 3.4a also illustrates that some faults (Faults 12–17), located directly beneath the caprock and above Faults 3 and 4 contain the highest $S_h \approx 92\%$ of the whole Mallik GH deposit. For comparison, the nearby region of Faults 12–17 contains $S_h < 70\%$. This regional S_h variation strongly correlates with the intrinsic permeability difference between the faults and sediments (Table 3.2). Therefore, this clearly shows that the simulated and observed heterogeneities of S_h distribution at the Mallik site are mainly dominated by structural geology and lithology.

3.4.2 Impact of Climate Change on Permafrost Heating

Permafrost heating mainly refers to the temperature increment of the ice-bearing sediment addressed in the present study. Permafrost has been significantly heated during the past 3–4 decades (Blunden and Arndt, 2017). Smith et al. (2022) conclude that heating rates are generally below 0.3 K per decade in sub-Arctic regions for warmer discontinuous permafrost with near-surface ground temperatures close to 0 °C. However, for cooler continuous permafrost with near-surface ground temperatures below −2 °C, heating rates could be up to ca. 1 K per decade in the high-latitude Arctic areas. The Arctic Amplification (AA) phenomenon (Biskaborn et al., 2019; Fang et al., 2022) well documents that the Arctic is warming at a twofold to a threefold rate of the global average, with some typical AA heating gradient trends discussed by Biskaborn et al. (2019). Their study demonstrates that the annual amplitude

temperature of permafrost near the ground surface increased globally by 0.29 ± 0.12 K during 2007–2016, whereas an increase by 0.39 ± 0.15 K has been observed for the continuous permafrost such as the Mallik and Mount Elbert sites as listed in Table 3.6.

Table 3.6: Comparison of permafrost heating and its projection on the increased near-surface annual amplitude temperature of permafrost at the Mallik site from 1969 to 2004.

Mode	Permafrost heating rate (K/decade)	Permafrost type	Projected temperature increment (K)	Reference
Biskaborn	0.39 ± 0.15	Continuous	1.365 ± 0.525	Biskaborn et al. (2019)
Smith	0.3	Discontinuous	1.05	Smith et al. (2022)
AA	Two to threefold rate of the global temperature increment average	Discontinuous/ continuous	0.88–1.32	Biskaborn et al. (2019) and Fang et al. (2022)

Note: The average global temperature increment is obtained from the observation shown in Figure 3.7a, which is ca. 0.44 K from 1969 to 2004.

Figure 3.6a shows that near-surface ground temperatures deviate from 0.8–1.3 K between the simulated and observed temperature profiles at depths < 50 mbgl. As interpreted in Section 3.3.2, this deviation could be caused by overestimating the ice content within the permafrost because the pore volume of the ice-bonded permafrost is not often fully saturated with ice (Brown et al., 2002) but contains large amounts of organic matter and minerals instead. Hence, these materials will not experience the consumption of latent heat in the process of permafrost heating. This may cause the observed climate change-driven permafrost degradation to be substantially faster than in previous predictions (Irrgang et al., 2022), even without taking thermokarst-inducing processes (Nitzbon et al., 2020) and AA effects (Biskaborn et al., 2019; Cohen et al., 2018) into account.

The projections of the current ground surface temperatures vary from ca. −7.0 °C (Mallik 3L/5L-38 wells) to ca. −7.5 °C (Mallik 4L-38 well), derived from the extrapolation of the DTS-logged temperature profiles, shown in Figure 3.6a. This inferred ground temperature range also approximately matches the DTS-measured near-surface temperature of −7.8 °C at the Alaskan Ignik Sikumi field in 2009, which was recovered from drilling-induced temperature disturbance and cementing effects after 128 days of well completion (Boswell et al., 2017). Furthermore, the near-surface ground temperature distribution (Figure 3.6b) is inferred from the dataset of hydrocarbon exploration wells drilled between the late 1960s and early 1970s (Burn and Kokelj, 2009; Dallimore et al., 2005a), while the DTS-logged temperature profiles were recorded in September 2003 (Figure 3.6a). The above DTS-logged ground temperature range of −7.0 to −7.5 °C (2003) is consistent with the near-surface ground temperatures recorded from 2004 to 2007 at the Mallik site (Figure 3.7b), considering a non-negligible AA-enhanced temperature increment of ca. 0.2 to 0.3 K within these three years.

According to Burn and Kokelj (2009), the near-surface ground temperatures were generally increased by 2.0 K from the initial estimate of −8 to −9 °C (Figure 3.6b) in the early 1970s to the observed −6 to −7 °C (Figure 3.7b) at the Mallik site in the mid-2000s. As shown in Figure 3.7a, during the same period, global warming triggered a temperature increase by 0.55 K from ca. 0.29 °C in 1968 to ca. 0.84 °C in 2007 (Hoegh-Guldberg et al., 2019), indicating that the estimated permafrost heating intensity of the Mallik site is over three times higher than the global warming average, confirming the AA effect.

As shown in Table 3.6, the impact of global warming on the near-surface ground temperature of the continuous permafrost at the Mallik site is estimated to be in the range of 0.88–1.32 K from the late 1960s through the mid-2000s, considering the above mentioned AA trend. This forecasted temperature increment is in perfect agreement with the above mentioned deviation of 0.8 to 1.3 K between the observations and simulations, as shown in Figure 3.6a. This suggests that the temperature increase caused by climate change is the main reason for the deviations between the simulated and observed near-surface temperatures at the Mallik site. Moreover, it also implies that the bias sources are broader than the impact of climate change, owing to interactions between soil erosion, wildfire (Nitze et al., 2018), vegetation and ground ice content (Smith et al., 2022).

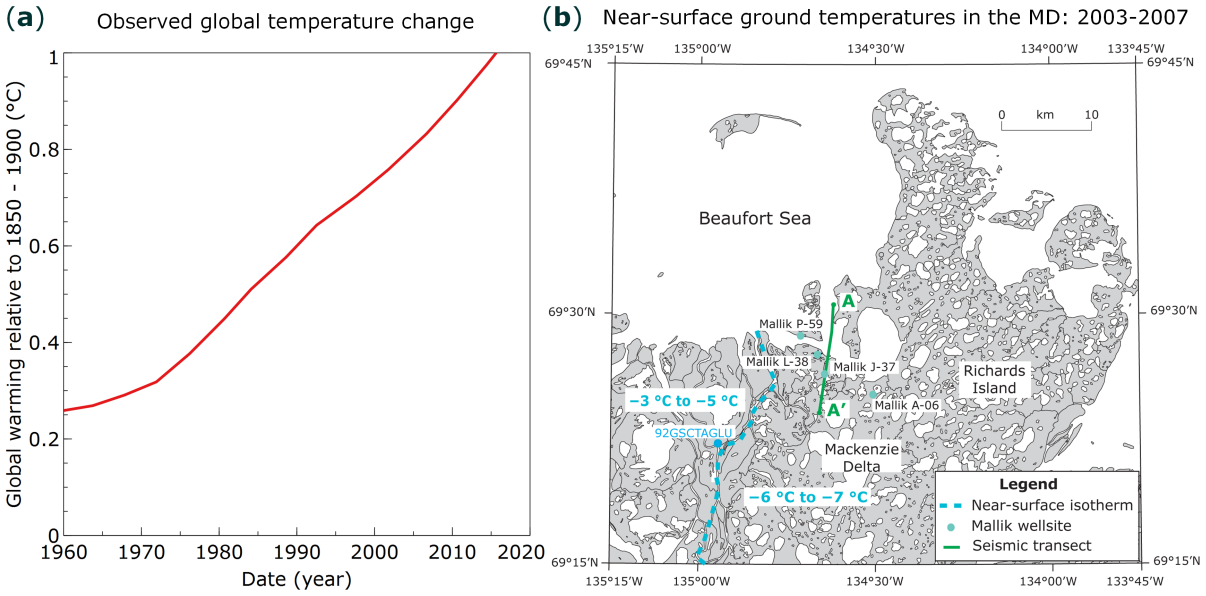

Figure 3.7: (**a**) Observed monthly global mean surface temperature change and estimated temperature increase due to global warming from 1960 to 2017, adopted from Hoegh-Guldberg et al. (2019); (**b**) map of the near-surface ground temperature distribution, measured between 2003 and 2007 in the Mackenzie Delta with temperatures adopted from Burn and Kokelj (2009). (**b**) presented with permission from Natural Resources Canada under the Open Government License—Canada version 2.0.

According to Min et al. (2008), the anthropogenic influence on the Arctic Sea ice became detectable already in the early 1990s. Thus, it can be deduced that global warming has significantly driven permafrost heating since the early 1970s at the Mallik site. Unfortunately, unlike glaciers and snow covers, the lack of data on the evolution of permafrost in temporal and spatial terms cannot yet be effectively compensated by remote sensing (IPCC, 2022). Consequently, our inference on the permafrost heating time period requires validation by additional field observations.

3.5 Conclusions

In this study, we have developed and applied a thermo–hydro–chemical model to study the spatio-temporal evolution of permafrost and the formation of sub-permafrost GH accumulations, facilitated by the upward migration of dissolved CH_4-rich fluids flowing out of an overpressurized zone along the fault systems at the Mallik site. The simulated temperature profiles, the base of the ice-bearing permafrost, the thickness of the hydrate intervals and the peak S_h are in very good agreement with corresponding field observations. Consequently, the above presented simulation results support us to make the following conclusions:

1. The feed gas (thermogenic CH_4) transport mechanism proposed in this study has been validated with regard to its dissolved migration state and highly dipping faults as migration pathways. Simultaneously, our simulations prove the general feasibility of the previously addressed laboratory-scale CH_4 hydrate formation method (Li et al., 2022b) at field scale for the sub-permafrost GH accumulations at the Mallik site.
2. GH-rich accumulations are generally formed in favorable geothermal environments, preserving thick GHSZ and occurring in areas with moderate tectonic deformation intensity. Hence, the varying GH saturations observed along the well intervals can be attributed to the variability of the physical properties of the host sediments and lithology at the Mallik site.
3. Our simulation results exhibit an undiscovered GH accumulation located ca. 2 km south of the Mallik J-37 well along the transect A-A', given that Fault 6 (Figure 3.3) has been hydraulically active since the Mid-Pleistocene. Moreover, Faults 3 and 4 (Figure 3.3) may still be hydraulically active in the present day, and thus deserve further attention and investigation in view of their role in the stability of the GH accumulations.
4. At the Mallik site, the sub-permafrost GH accumulations did not release significant CH_4 in view of the global carbon budget under the contemporary global warming events (Ruppel and Kessler, 2017) until the mid-2000s, because they are well preserved below the thick ice-bounded permafrost within the undisturbed GHSZ. Our numerical simulations evidently support field observations on permafrost heating at the Mallik site, induced by the AA-enhanced pan-Arctic climate warming, which has been observed since the early 1970s.

The presented numerical modeling framework can be applied for the calibration of geophysical measurements and the validation of the interpretation of BSRs derived from seismic reflection profiles at the reservoir scale. This framework is capable of investigating and projecting the potential gas hydrate enrichment and resource density within the target Arctic sandy sediments. Moreover, it supports improving the understanding of sub-permafrost groundwater migration and the evolution of hydraulic conductivity of geologic fault systems. In addition, the model can be used to quantify the AA phenomenon on the evolution of the mean annual near-surface temperature distribution in pan-Arctic permafrost regions. The 2D model used in this study will be extended to a 3D model in the near future, using available 2D seismic cross-sections and well data to further quantitatively investigate the role of the detected geologic faults in the formation of the GH deposit at the Mallik site.

3.6 Appendix

3.6.1 Scientific and Industry Exploration Wells at the Mallik Site

Table 3.7: Coordinates of the Mallik wells and their distances to the Mallik J-37 well serving as the projection origin.

Wellsite	Coordinates (latitude, longitude)	Distance	Reference
Mallik J-37	69°26′38″ N, 134°38′23″ W	-	Osadetz et al. (2005)
Mallik 2L-38	69°27′40.7″ N, 134°39′30.4″ W	2034 m	
Mallik 3L-38	69°27′38.3″ N, 134°39′41.6″ W	2047 m	
Mallik 5L-38	69°27′39.5″ N, 134°39′38.3″ W	2066 m	
Mallik A-06	69°25′01″ N, 134°30′16″ W	6071 m	
Mallik P-59	69°28′49″ N, 134°42′45″ W	4940 m	

Note: Mallik J-37 well directly crosses the transect A-A′ of the 2D seismic profile 85987 adapted from Collett (1999), whereas all other wells are projected onto the transect A-A′.

3.6.2 Governing Equations Describing Water-Ice Thermal State Transitions

The mass balance, energy balance and continuity equations employed in the scope of the present numerical simulation are presented by Li et al. (2022b) and Kempka (2020). By introducing the frozen state of pore fluid (i.e., ice) as an additional component, the following EoS were integrated into TRANSE. The volume fraction relation of interstitial pore components are defined as:

$$\phi_h = S_h \varphi, \tag{3.1}$$

$$\phi_f = \Theta \left(1 - S_h\right) \varphi, \tag{3.2}$$

$$\phi_{ice} = \left(1 - \Theta\right) \left(1 - S_h\right) \varphi, \tag{3.3}$$

where φ is intrinsic porosity, S_h stands for the CH_4 hydrate saturation.

The terms of ϕ_f, ϕ_h and ϕ_{ice} refer to the effective porosity available for the flow of the mobile component (i.e., fluid), as well as the pore volume fraction occupied by hydrate and ice, respectively. The constraint $\phi_h + \phi_f + \phi_{ice} = 1$ implies that pore space is fully saturated. Additionally, Θ denotes the unfrozen fraction of fluid within the pore space and is generally assumed to be a temperature-dependent piece-wise function in the interval of phase transition (Lunardini, 1988), such as

$$\Theta = \begin{cases} exp\left[-\left(\frac{T-T_L}{\omega}\right)^2\right] & \text{if } T \leq T_L, \\ 1 & \text{if } T > T_L. \end{cases} \tag{3.4}$$

In Equation (3.4), T describes the mixture temperature in the pore space; T_L is the temperature of the thawing/freezing point (liquidus, usually −1.5 °C in the MB region (Taylor et al., 2013)); and w denotes the phase transition interval, i.e., $w = T_L - T_S$ (usually $w = 1$ °C in the MB region (Taylor et al., 2013)), where T_S is the temperature of the frozen point (solidus).

The derivative of the above partition function Θ is integrated into the EOS to improve the convergence of the numerical solution; that is

$$\frac{d\Theta}{dT} = \begin{cases} -\frac{2(T-T_L)}{w^2} exp\left[\left(-\frac{T-T_L}{\omega}\right)^2\right] & \text{if } T \leq T_L, \\ 0 & \text{if } T > T_L. \end{cases} \tag{3.5}$$

For fluid-saturated, frozen and CH_4 hydrate-bearing sediments, the energy balance equation is updated by replacing the term of effective porosity ϕ with ϕ_h, then re-written as

$$\left(\left(1-\phi_f\right) c_{pr}\rho_r + \phi_f c_{pf}\rho_f\right) \frac{\partial T}{\partial t} = \nabla\left(\lambda_a \nabla T + \vec{v} c_{pf}\rho_f T\right) + H. \tag{3.6}$$

In Equation (3.6), c_{pr} is the specific heat capacity of the immobile components, including the sediment matrix, ice and hydrate, which is modified by introducing the ice component to the formula and taking the latent heat of ice formation, L (Matveeva et al., 2020), into account:

$$c_{pr} = \frac{(1-\varphi)\, c_s + \phi_{ice} c_{ice} + \phi_h c_h + L\varphi\,(1-S_h)\,\frac{d\Theta}{dT}}{1-\phi_f}. \tag{3.7}$$

In Equation (3.7), c_s, c_{ice} and c_h are the heat capacities of the sediment matrix, ice and CH_4 hydrate, respectively, while L is the specific latent heat of ice formation (cf. Table 3.3). The following terms are updated by adding the ice component to each formula.

The average thermal conductivity of the immobile and mobile components, λ_a, is expressed as

$$\lambda_a = \left(1-\phi_f\right)\lambda_r + \phi_f \lambda_f, \tag{3.8}$$

where λ_f is the heat conductivity of the pore fluid (mobile components), while the heat conductivity of the immobile components, λ_r, is described by

$$\lambda_r = \frac{(1-\varphi)\,\lambda_s + \phi_{ice}\lambda_{ice} + \phi_h \lambda_h}{1-\phi_f}, \tag{3.9}$$

where λ_s, λ_{ice} and λ_h are heat conductivities of the sediment matrix, ice and CH_4 hydrate, respectively. The density of the immobile components, ρ_r, is

$$\rho_r = \frac{(1-\varphi)\,\rho_s + \phi_{ice}\rho_{ice} + \phi_h \rho_h}{1-\phi_f}, \tag{3.10}$$

where ρ_s, ρ_{ice} and ρ_h are the densities of the sediment matrix, ice and CH_4 hydrate, respectively.

Chapter 4

Geologic Controls on the Genesis of the Arctic Permafrost and Sub-Permafrost Methane Hydrate-bearing System in the Beaufort–Mackenzie Delta

ABSTRACT

The Canadian Mackenzie Delta (MD) exhibits high resources of prospected sub-permafrost gas hydrates (GHs) mainly consisting of thermogenic methane (CH_4) at the Mallik site, which migrated from deep conventional hydrocarbon source rocks. The objective of the present study is to confirm the proposed sub-permafrost GHs formation mechanism, implying that CH_4-rich fluids were vertically transported from deep overpressurized zones via geologic fault systems and formed the present-day GH deposit in the shallower Kugmallit Sequence since the Late Pleistocene. Given this hypothesis, the coastal permafrost began to form since the early Pleistocene sea-level retreat, steadily increasing in thickness until 1 Ma ago. Data from well logs and 2D seismic profiles were digitized to establish the first field-scale static geologic 3D model of the Mallik site, and to comprehensively study the genesis of the regional permafrost and the associated GH system. Numerical simulations using a proven thermo-hydro-chemical simulation framework were employed to provide insights into the hydrogeologic role of the regional fault systems in view of the CH_4-rich fluid migration and the geologic controls on the spatial extent of the sub-permafrost GH accumulations during the past 1 Ma. For > 87% of the Mallik well sections, the predicted permafrost thickness deviates from the observations by less than 0.8%, which validates the general model implementation. The simulated ice-bearing permafrost and GH interval thicknesses as well as sub-permafrost temperature profiles are consistent with the respective field observations, confirming our previously introduced hypothesis on the Arctic sub-permafrost GH formation mechanism in the Canadian MD. Spatial GH distribution constraints are determined by, among other factors, the source-gas generation rate, temperature regime in the sub-permafrost sediments, and permeability of the GH-bearing sandy sediments in interplay with the geologic fault system. Overall, the good agreement between simulations and observations demonstrates that the present modeling study provides a valid representation of the geologic controls driving the complex permafrost-GH deposit system. The model's applicability for the prediction of GH deposits in permafrost settings in terms of their thicknesses and saturations can provide relevant contributions to future GH exploration and exploitation activities.

4.1 Introduction

The Mackenzie Delta (MD) is a river-mouth depocentre, the second largest Arctic delta (Forbes et al., 2022). It is the most economically accessible area along the Arctic coast of the Beaufort-Mackenzie Delta Basin (Dixon et al., 2019). The basin is an essential component of the Canning-Mackenzie deformed assessment unit (Houseknecht et al., 2020), also recognized as the Beaufort-Mackenzie tectono-sedimentary element (Chen et al., 2021). A high amount of methane stored as the sub-permafrost gas hydrate (GH) resource has been deterministically appraised in MD (Osadetz and Chen, 2010). GHs are ice-like crystalline solids consisting of hydrate-forming gases, such as methane (CH_4), trapped within the water molecules forming

cage-shaped structures (Sloan and Koh, 2007). Permafrost refers to subsurface sediments exhibiting temperatures below 0 °Cfor at least two consecutive years, regardless of the sediment composition (Woo, 2012).

Decades of industrial exploration (Judge et al., 1981; Taylor and Judge, 1976) and scientific research (Dallimore et al., 2005a; Dallimore et al., 1999; Dallimore et al., 2012) in this petroliferous region have produced a broad spectrum of geoscientific data and knowledge on the basin. The GH composition found at the Mallik sites, including the Mallik P-59, L-38, 2L-38, 3L-38, 4L-38, 5L-38, J-37, and A-06 wells (see Figure 4.1), is dominated by thermogenic CH_4, which migrated from deep conventional hydrocarbon deposits located in the Taglu and Richards Sequences illustrated in Figure 4.2 (Lorenson et al., 2005; Lorenson et al., 1999). According to the hypothesis addressed by Chen et al. (2008), the CH_4-rich fluid is migrating upward out of the deeper hydraulic overpressure zone (Hu et al., 2018) through gas-source faults to form CH_4 hydrates in the shallower Kugmallit Sequence Figure 4.1 over geological times. When the CH_4-rich fluid enters the Methane Hydrate Stability Zone (MHSZ), the dissolved CH_4 is converted from the supersaturated solution into the hydrate phase (Kashchiev and Firoozabadi, 2002). This hypothesis on the sub-permafrost GH formation mechanism is to be validated by the 3D numerical model developed in the scope of the present study.

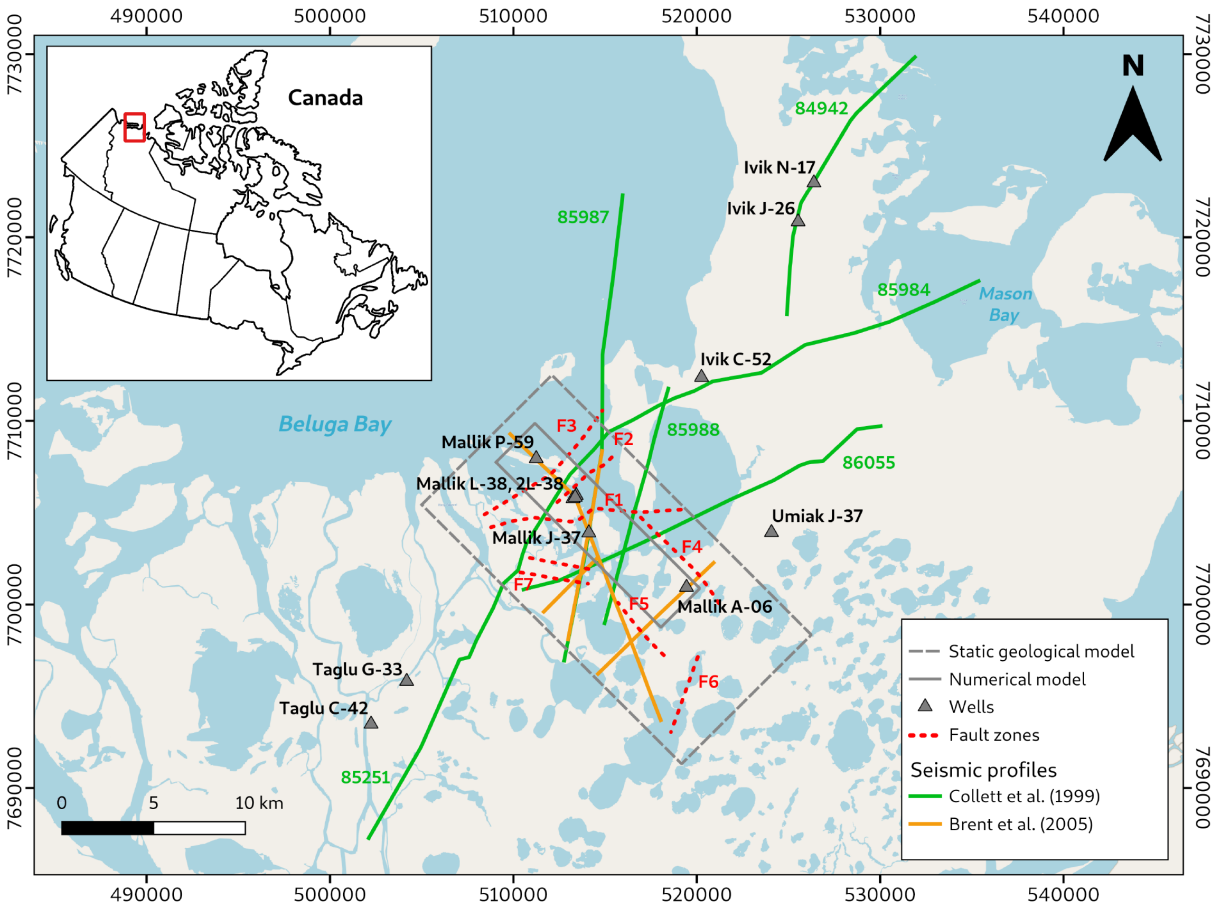

Figure 4.1: Overview map of the study area with the trend of employed seismic profiles, wells, and regional fault zones in the Ivik–Mallik–Taglu region. Map created using the free and open source software QGIS with a base map from OpenStreetMap; Spatial reference: WGS 84 / UTM zone 8N, modified after Chabab and Kempka (2023).

A significant amount of GH was formed and preserved in the Kugmallit Sequence, mainly consisting of sandstones Figure 4.2A due to the presence of the Mallik anticline which is sealed by the Mackenzie Bay Sequence with a lithology mainly composed of shale (Huang, 2009).

The GH presence was observed in seismic responses and well logs which are summarized in Table 4.1. In the far-field of the anticline, the pore space within the sandy sediment is occupied by CH_4-loaded fluids rather than highly-saturated with GHs due to the lack of a geologic trap and the absence of CH_4 super-saturated formation fluids (Huang, 2009).

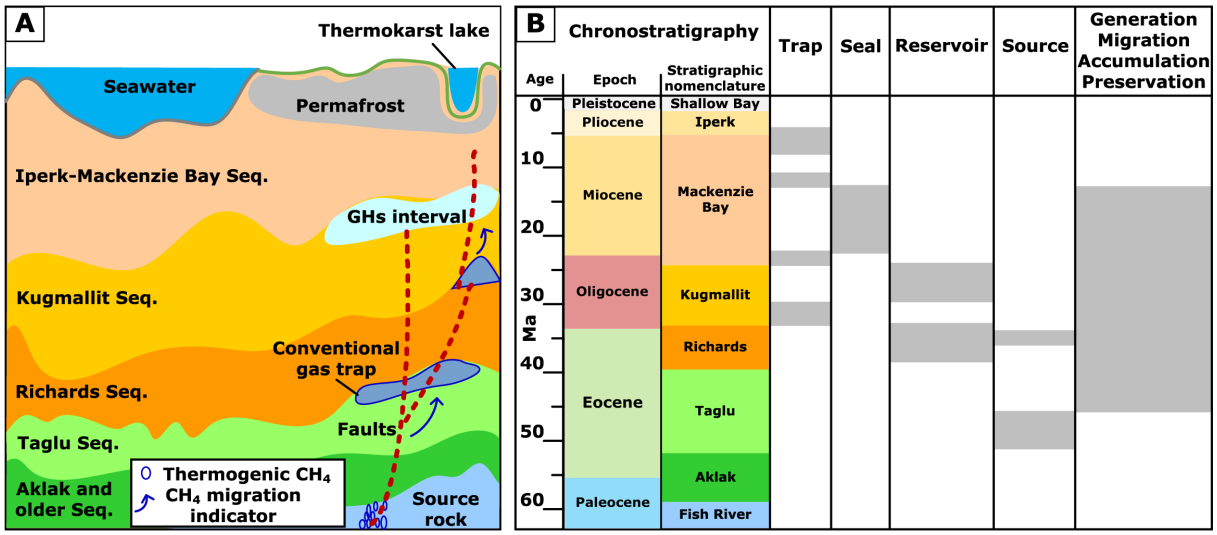

Figure 4.2: (**A**) Schematic and (**B**) chronology of the sub-permafrost GH-bearing system at the Mallik site with an active source rock generating thermogenic CH_4, its geological elements (trap, seal, reservoir, and source intervals), and processes (migration, accumulation, and preservation), modified after Li et al. (2022a), according to Chen et al. (2008) and Kroeger et al. (2008). (Seq. = sequence, not to scale)

In view of previously undertaken modeling activities, earlier basin-wide 3D geothermal hydrocarbon flow models (Kroeger et al., 2008; Kroeger et al., 2009) to identify the origin of the hydrocarbon province and recent lithosphere-scale 3D structural models (Sippel et al., 2015; Sippel et al., 2013) on the temperature and maturity history did not investigate the genesis of GHs. Nevertheless, these models were an important basis for the present study, aiming to quantitatively assess the spatial distribution of GH occurrences in relation to the potential CH_4 migration pathways. Furthermore, available geothermal models focusing on permafrost evolution (Majorowicz et al., 2012a; Majorowicz et al., 2012b; Majorowicz et al., 2015; Overduin et al., 2019; Taylor et al., 2013) were exclusively realized in one and two dimensions and validated by only a limited number of bottom-hole temperature data acquired from the basin, neglecting the presence of sub-permafrost GHs. To date, Frederick and Buffett (2014), Frederick and Buffett (2015), and Frederick and Buffett (2016) have presented a more sophisticated multiphase fluid flow simulator to account for permafrost-associated GH formation via dissolved CH_4. In addition to GH formation, their simulator was also applied to investigate GH dissociation under present and future global warming events (Frederick and Buffett, 2014). Although their 2D simulation approaches could predict the intra-permafrost GH formation with GH saturation (S_h) less than 3.5%, they did not simulate the formation of highly saturated sub-permafrost GH intervals. Besides, their approach is not capable of quantifying the influence of structural geological heterogeneity (i.e., anticlines, faults) on GH distribution.

As mentioned above, the integrated permafrost and sub-permafrost GH reservoir system has not yet been sufficiently investigated. To promote the understanding of this complex system, we previously employed a 2D hydrogeological model (Li et al., 2022a) to study the spatial-temporal patterns of permafrost and the genesis of sub-permafrost GH accumulations

facilitated by upward-migration of CH_4-rich formation fluid. The proposed mechanism for the formation of highly saturated sub-permafrost GH via dissolved CH_4-rich fluid has been quantitatively validated by comparison to observed temperature profiles and seismic-inferred GH distributions.

Although the previous 2D model (Li et al., 2022a) used basic structural geology data, a more detailed mapping of the model geometry and comprehensive spatial structural analyses are required to refine the regional model. For instance, it has already been suggested before that many adjacent structures are known, but they have not yet been adequately investigated for their GH migration and trapping potentials (Lane, 2002). In addition, 3D geological models are significantly more potent for developing and visualizing geological knowledge than 2D cross-sections under heterogeneous subsurface environments (Thornton et al., 2018). By applying various methods to reprocess the 3D seismic-reflection data acquired from the Mallik 5L-38 site in 2002 (Brent et al., 2005), the complexity of the sub-permafrost GH-bearing sediment has been visualized and demonstrated in a series of studies conducted by Bellefleur et al. (2007), Bellefleur et al. (2012), Bellefleur et al. (2006), and Riedel et al. (2009). These studies report that local heterogeneity within sedimentary rocks significantly influences the GH distribution at the Mallik site. Therefore, the need for implementing a 3D simulation based on a 3D static model for quantifying the geologic controls on GH distribution is substantial. For instance, it is not feasible to parameterize specific faults near the model boundary as hydraulically impermeable in a 2D simulation, because this would turn a semi-closed model into a closed system, while a 3D model can easily overcome this obstacle by extending the simulation domain accordingly. Additionally, the projection of the Mallik wells onto a 2D transect does not necessarily represent the in-situ geothermal conditions and structural geology at the well locations, leading to less reliable simulation results. For a 3D model, the additional dimension allows a full spatial representation of the hydraulic dynamics and role of geologic faults in terms of the upward-migrating CH_4-rich fluid, and thus a qualitative and quantitative assessment of the geologic controls on the spatial extent of heterogeneous sub-permafrost GH accumulations.

Conclusively, the previous 2D model does not suffice to comprehensively evaluate the permafrost and GH-bearing system, but rather provides qualitative information on the general validity of the previously introduced hypothesis. Therefore, we present a 3D structural model covering approximately 38 onshore-km^2 of the MD in the present study. In addition to well logs (Table 4.1), published seismic interpretations (Dallimore et al., 2005a; Dallimore et al., 1999) were employed to construct a full-scale 3D model of the Mallik anticline GH trap. Our model is used to quantitatively assess the structural geologic controls provided by the hydraulically conductive fault and anticline systems as well as hydrocarbon traps on the temporal and spatial development of the sub-permafrost GH occurrences since the Late Pleistocene.

4.2 Methods and Input Data

4.2.1 Geological Setting And 3D Structural Geological Model

The Beaufort MD Basin is an important petroleum province due to its abundant petroleum resources. The Taglu gas field discovery in 1971 led to exploratory efforts primarily focusing on oil during the 1970s to the mid-1980s (Dallimore et al., 1999). For example, the Mallik L-38 well was drilled into a fault-bounded anticline. Initially, GH deposits were considered a drilling hazard in the exploration of deeper petroleum prospects. Once assumed to be rare, GHs are

now expected to occur globally in vast volumes. Recent research activities have been aimed at advancing the potential for cost-effective usage of GH deposits as a reliable alternative energy resource and bridging technology during the energy transition from fossil fuels to renewables. In the MD, the first GH sample was cored from the permafrost at the Taglu field (Dallimore and Collett, 1995), and deliberate GH studies were inaugurated in 1998 by drilling the Mallik 2L-38 well (Dallimore et al., 1999), followed by the development of the Mallik 3L-38, 4L-38, and 5L-38 wells in 2002, as listed in Table 4.1.

Table 4.1: Overview of scientific and industrial exploration wells at the Mallik site.

Well	Latitude (N), Longitude (W)	Heat flux (mWm^{-2})	Drilling period	Well type
J-37	69°26′38″, 134°38′23″	49 ± 7	1970s	Industrial petroleum exploration
A-06	69°25′01″, 134°30′16″	55 ± 8	1975	
P-59	69°28′49″, 134°42′45″	43 ± 6	1970s	
L-38	69°27′44″, 134°39′25″	55 ± 8	1971	
2L-38	69°27′40.7″, 134°39′30.4″	-	1998	Scientific GHs exploration and production
3L-38	69°27′38.3″, 134°39′41.6″	-	2002	
4L-38	69°27′40.8″, 134°39′34.9″	-	2002	
5L-38	69°27′39.5″, 134°39′38.3″	-	2002	

Note: The distance between Mallik 2L-38, 3L-38, 4L-38, 5L-38 to L-38 are respective 117 m, 252 m, 146 m, and 200 m, as illustrated by Ashford et al. (2012). The details of Mallik J-37, A-06, P-59 and L-38 are adopted from field reports, such as coordinates (Osadetz et al., 2005), drilling period (Judge et al., 1981; Taylor and Judge, 1976), and heat flux (Majorowicz and Smith, 1999). The information of Mallik 2L-38, 3L-38, 4L-38 and 5L-38 are adopted from field reports, such as coordinates (Ashford et al., 2012) and drilling period (Dallimore et al., 2005a).

Geology of the Beaufort Sea and Mackenzie Delta Region

The MD is part of a rifted continental margin basin in the Canadian Arctic that was formed during the Early Cretaceous. Deposits in the delta and Beaufort Sea continental shelf cover the geological period from the Paleozoic to the Holocene. Westward-thickening Paleozoic rocks, intersected by numerous faults, are overlain by the main post-rift basin-fill, a thick sedimentary succession formed by deltaic processes that marks a regional unconformity at the boundary between Upper Cretaceous and pre-Cretaceous rocks (Collett, 1999; Dixon and McNeil, 1992; Dixon and Dietrich, 1988). Marine organic-rich muds deposited during the Upper Cretaceous transition into younger Cenozoic deltaic sandstones and shales result from a series of sedimentation cycles of the progressing Laramide orogeny southwest of the present coastline (Dixon and McNeil, 1992; Dixon and Dietrich, 1988; Miller et al., 2005). Modern deltaic sediments and older fluvial and glacial deposits cover the Mesozoic and Cenozoic strata, whose thickness tends to increase northwards towards the coast to 12 – 16 km below sea level (Collett, 1999). Major unconformities terminate each transgressive-regressive sequence within the Cenozoic strata (Chen et al., 2021; Collett, 1999; Dixon and McNeil, 1992; Dixon and Dietrich, 1988; Miller et al., 2005). The GH-containing Cenozoic sequence within the MD in the Ivik–Mallik–Taglu area encompasses four distinct lithostratigraphic units.

The Eocene Richards Sequence consists of fine-grained distal pro-delta and delta-slope deposits that comprise mostly mudstones and siltstones. These are unconformably overlain by coarser delta-front and delta-plain deposits from the Oligocene Kugmallit Sequence, which exhibits the thickest sediment deposition among the present lithostratigraphic units (Dixon and

McNeil, 1992; Dixon and Dietrich, 1988). Predominantly outer shelf and deep-water deposits comprising mudstones and siltstones define the Late Oligocene to Middle Miocene Mackenzie Bay Sequence, which lies unconformably above the Kugmallit Sequence and older strata. Near-shore sand and gravel facies transitioning to mud and silt deposits on the continental slope are characteristic of the thick and comparatively less deformed deposits of the Pliocene to Pleistocene Iperk Sequence, which unconformably covers underlying sequences and truncates most of the early to mid-Cenozoic structural features at its base (Dixon and McNeil, 1992; Dixon and Dietrich, 1988; Osadetz et al., 2005). Cenozoic tectonics with extensional deformation phases, following the Mesozoic rifting due to the opening of the Canada Basin and compressional deformation during the Early Eocene to Late Miocene have overprinted the basin-fill in the MD. Normal, thrust and strike-slip faulting of the underlying strata together with a predominantly north-west trending folding resulted in several large-amplitude anticlinal systems, such as the Mallik anticline, which serve as efficient structural traps for the accumulation of GHs. The required methane most likely migrated upward from deep conventional hydrocarbon reservoirs through the existing fault systems (Brent et al., 2005; Dixon and McNeil, 1992). According to the sediment thicknesses, the bulk of reserves rests under the Beaufort Sea and about one-third are located onshore (Dallimore and Collett, 1999; Osadetz et al., 2005).

3D Structural Geological Model Implementation

The structural geological 3D static model covers an area of 10 km × 20 km. With an areal size of 12.7 km × 3 km, the numerical model encompasses the central geological model area, including the Mallik anticline, major F1 Fault, and Mallik wells (Figure 4.1). The surfaces of the Iperk/Mackenzie Bay, Mackenzie Bay/Kugmallit, and Kugmallit/Richards Sequence boundaries were generated using six 2D high-resolution seismic reflection profiles (84942, 85251, 85984, 85987, 85988, and 86055), which have been commissioned by Imperial Oil Ltd. in 1984 as part of the seismic survey across the Ivik–Mallik–Taglu area and reprocessed by Collett (1999). Further, three 2D seismic reflection profiles from Brent et al. (2005) were used to identify lithological contacts and fault zones. In the first instance, the reflection profiles were georeferenced to the UTM grid system (Spatial reference: EPSG Projection 32608 - WGS 84 / UTM zone 8N). Two-way traveltimes of the sequence boundaries were digitized from the 2D seismic reflection profiles using the Petrel^{TM} software package (Schlumberger, 2012) and converted to elevation depth based on average checkshot- and VSP-derived velocities in the Mallik area between 2.25 km/s and 3.0 km/s (Brent et al., 2005). Vertical fault lines of six major regional fault zones were derived from the seismic profiles. Fault strikes were adopted from the two-way traveltime structure map from Brent et al. (2005) for Faults F1-F6. Two additional fault zones at the top of the Mallik anticline structure were interpreted from the 2D seismic profiles in Collett (1999) for Fault F7. The derived set of polylines was then used to calculate the elevation depth of the surfaces and to generate the fault zones using the convergent interpolation algorithm (Schlumberger, 2012).

Available log data from Collett (1999) on the depth of the relevant sequence boundaries from eleven wells in the Ivik–Mallik–Taglu area, all drilled by Imperial Oil Ltd. in the early 1970s, were used for depth adjustment of the processed surfaces (Figure 4.3). In addition, reflection profiles and wells outside the study area were taken into account to implement stratification inclination trends correctly. For a more detailed description of the model implementation, the reader is kindly referred to Chabab and Kempka (2023).

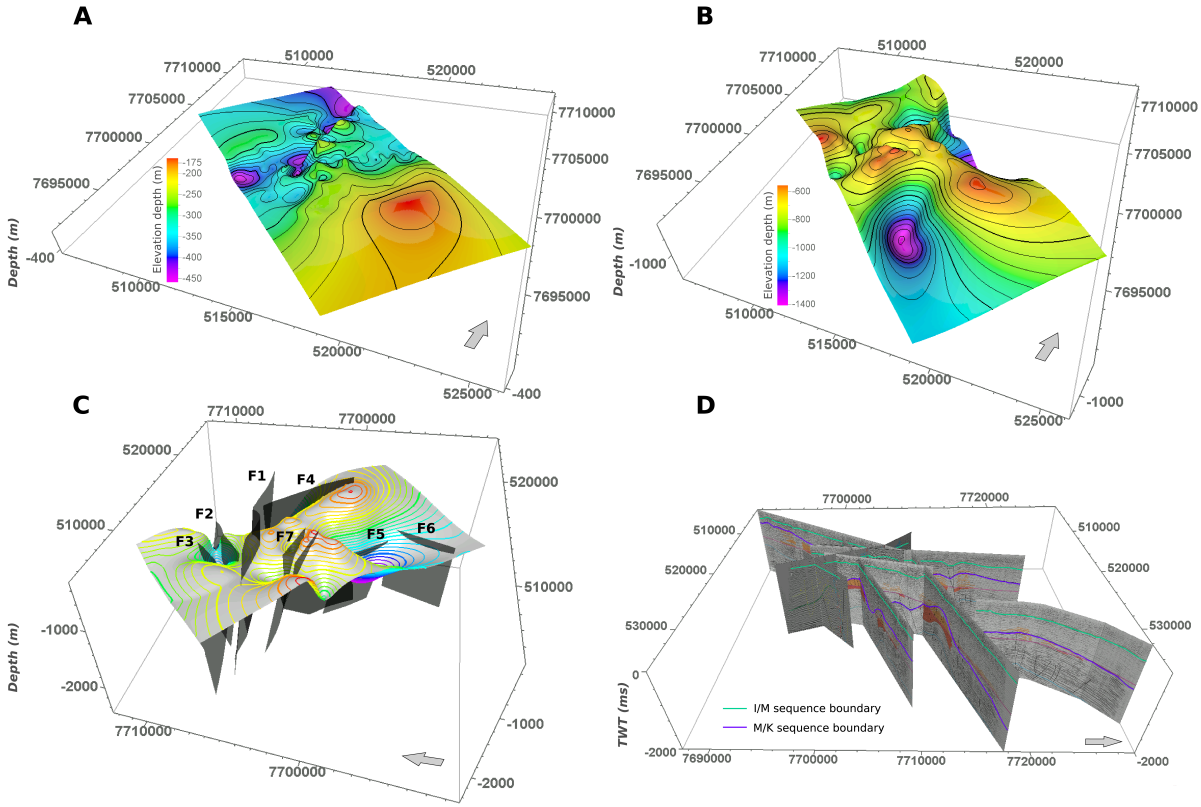

Figure 4.3: Domain and geometry of the implemented 3D Mallik static geological model with major sequence boundaries. (**A**) Elevation depth of Iperk/Mackenzie Bay and (**B**) Mackenzie Bay/Kugmallit sequence boundaries, (**C**) implemented regional faults zones of the Ivik–Mallik–Taglu area, and (**D**) sequence boundaries digitized from two-way traveltime of employed seismic profiles. Vertical exaggeration by 5 times, spatial reference: WGS 84 / UTM zone 8N, modified after Chabab and Kempka (2023). For a more detailed view of the employed 2D seismic profiles, the reader is kindly referred to Brent et al. (2005) and Collett (1999).

4.2.2 Numerical Model Implementation

Numerical Modeling Assumptions

A framework of equations of state for equilibrium CH_4 hydrate formation and the reversible processes describing permafrost aggrading/degrading (i.e., water-freezing and ice-melting (Mottaghy and Rath, 2006)) has been coupled with the open-source flow and transport simulator (TRANSPORTSE) developed by Kempka (2020) and verified for complex reactive transport problems (Kempka et al., 2022; Kempka, 2020). This coupling was referred to as $T_{plus}H$ (TRANSPORTSE + Hydrate) in our previous studies (Li et al., 2022a; Li et al., 2022b).

Specimen analyses (Wright et al., 2005) suggest that migration of dissolved CH_4 and GH formation occurred in a semiclosed hydrodynamic system in the vicinity of the Mallik 5L-38 well. The GH intervals at the Mallik 2L-38 were defined as Class-II GH deposits (Uddin et al., 2012; Uddin et al., 2014). According to Moridis and Reagan (2011), Class-II GH deposits are GH intervals capped by impermeable rocks and underlain by aquifers without the presence of a free gas phase. Here, the implementation of impermeable permafrost and caprock sequences located above the GH-bearing sediments introduces a Class-II GH deposit system in the present simulation.

Hydrocarbon fluids from the deeper sequences are likely to migrate upward through present fault systems (Xia et al., 2022), gas chimneys (McNeil et al., 2011), mud diapirs, mud volcanoes (Zhang et al., 2021), and unconformities (Levell et al., 2010). However, gas chimneys

and unconformities, mud diapirs, and mud volcanoes have not yet been reported near the onshore sub-permafrost GH reservoirs in the MD. Therefore, the fault systems detected by seismic surveys are regarded as primary conduits for the circulation of fluids beneath the permafrost, facilitating the migration of CH_4 dissolved in these fluids and the formation of GH accumulations (Hillman et al., 2020).

According to the analysis of core samples from the GH-bearing intervals undertaken by Lorenson et al. (2005) and Lorenson et al. (1999), the feed gas composition of the GH derived from the methane-to-hydrocarbon molecular gas ratios is composed of approximately >99.5% thermogenic CH_4. This supports the model implementation based on the GH-forming gas being solely composed of CH_4. In addition, the vitrinite reflectance of the GH-bearing sediments found in the Mallik 2L-38 well is relatively low with <0.28% (Snowdon, 1999). This indicates that the maturity of the organic matter within the sediment is too low to result in methanogenic activities. Therefore, the feed gas trapped in the GH intervals must have been generated from deeper, thermally matured sequences, probably at depths above >5000 mbgl (Lorenson et al., 2005; Lorenson et al., 1999). This gas migrated upward into the overlying sequences including the Taglu and Richards Sequences, and was then trapped within conventional natural gas reservoirs until its secondary migration via geologic faults supplied the feed gas to shallower geologic units such as the Kugmallit Sequence (Figure 4.2).

As demonstrated in our previous study (Li et al., 2022a), thick hydrate-bearing sediment intervals with high S_h are commonly associated with deeper conventional petroleum reservoirs connected to extensional faults. They are closely correlated to the high spatial density of the number of structural elements (i.e., faults and anticlines). Hence, many high-angle dipping faults (F1, F2, F3, and F7, see Figure 4.4) occurring in the Taglu fault zone (Dixon et al., 2019) have the potential to be preferential pathways for the vertical migration of CH_4-rich fluids (Chen et al., 2008). However, a quantification of the extent to which these faults control the subsurface temperature regime and CH_4-rich fluid migration, and the heterogeneous distribution of GH accumulations with high S_h has not yet been undertaken. Furthermore, altering the permeabilities of the faults in the numerical model allows for the identification of hydraulically active and closed faults, acting as fluid flow paths or barriers.

Numerical Model Geometry and Parametrization

The input dataset derived from the 3D static geological model covers a volume of 20 km × 10 km × 2 km, and considers seven faults (F1 to F7) and two sedimentary sequence boundaries, including the Iperk-Mackenzie Bay (I-M) and Mackenzie Bay-Kugmallit (M-K) ones. Based on these pre-processed data, a 3D numerical model geometry (Figure 4.4) of the Mallik site was elaborated for the first time. Subsequently, that model was further applied in the numerical investigation on the geologic controls determining the temporal and spatial formation of sub-permafrost GH accumulations.

Figure 4.4 shows the spatial extent of the employed numerical 3D model for the present simulation study, consisting of three Sequences (Iperk, Mackenzie Bay, and Kugmallit Sequences) and four geologic fault zones (F1, F2, F3, and F7). The grid elements located at the P3-P5 and P2-P8 planes represent open flow boundaries, implemented by constant chemical species concentrations and p-T conditions (Dirichlet boundary conditions, Figure 4.4B). Moreover, the grid elements located at the P1-P3 plane represent the ground surface and are applied as the impermeable boundary with constant p-T conditions (Neumann no-flow boundary condition). Figure 4.4C shows the grid elements of the I-M Sequences, representing the above-mentioned

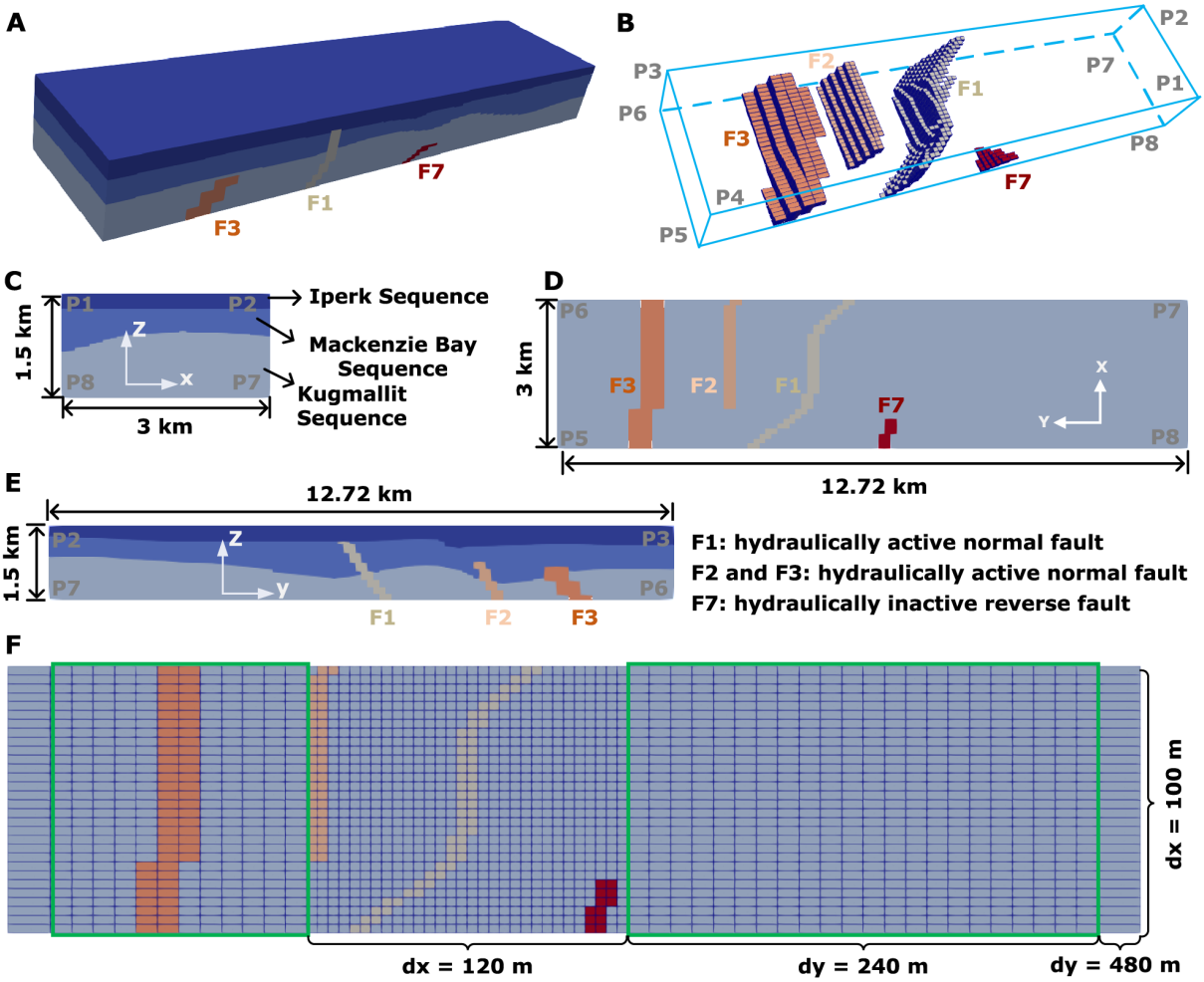

Figure 4.4: (**A**, **B**) Overview of the model geometry, including the fault systems (F1, F2, F3, and F7) as well as Iperk, Mackenzie Bay, and Kugmallit Sequences. (**C**,**D**,**E**) Model geometry dimensions along the z-x, z-y, and x-y planes, respectively. (**F**) Grid discretization employed in the present simulations.

impermeable boundary, acting as impermeable anticline sediment that overlies the GH trapping layer. In addition, constant pressure and regionally-dependent heat flux (Table 4.2) conditions apply for the grid elements on the P5-P7 plane (Figure 4.4D,F), except for the grid elements belonging to F1. The grid elements at the bottom of F1 (Figure 4.4F) serve as an inlet for the CH_4-rich fluid, which flows into the model domain at a constant rate and is parametrized with constant temperature conditions, as listed in Table 4.2. The applied initial temperature of the constant temperature condition is determined from the permafrost formation simulation study, which lasts about 0.6 Ma prior to the subsequent simulation on sub-permafrost GH formation for 1.0 Ma.

As depicted in Figure 4.4, the study domain with a spatial extent of 12,720 m × 3000 m × 1500 m, is discretized by 148,500 (66 × 30 × 75) grid elements. For optimum computational efficiency, grid elements along the y-direction are discretized by variable sizes of 480 m, 240 m, and 120 m (Figure 4.4F), while a constant discretization of 100 m and 20 m along the x- and z-directions is applied, respectively.

The subsurface temperature regime in the MD has been affected by low subaerial temperatures since the Middle Pliocene (ca. 3 MaBP). Meanwhile, thin permafrost might progressively form as the Arctic subaerial temperature decreased below the freezing point and heat flux dropped back to the regional mean value of 55 mW m^{-2} from its peak of 80 mW m^{-2}

Table 4.2: Initial and boundary conditions applied in the present simulations.

Parameter	Value	Unit	Reference
Inflowing CH_4-rich fluid rate	3.3×10^{-10}	kg m^{-3} s^{-1}	Iteratively determined
Initial temperature of inflowing CH_4-rich fluid	21.5	kg m^{-3} s^{-1}	Permafrost formation modeling determined
Dissolved CH_4 concentration	2.1	kg m^{-3}	Li et al. (2022a)
Subaerial temperature since 1 MaBP	−15	°C	Kroeger et al. (2008)
Basal heat flow	[42,52]	mW m^{-2}	Taylor et al. (2013)
Simulation duration	10^6	year	Li et al. (2022a)

triggered by the Late Miocene uplift event (Kroeger et al., 2008). As a result, the permafrost bottom accelerated to deepen and eventually pushed the freezing point isotherm downward to the base of the Iperk Sequence since the early Pleistocene sea-level retreat (Figure 4.5A), whereby the permafrost thickness kept growing until 1 Ma ago. Under the impermeable section provided by the thick permafrost (Chuvilin et al., 2022), super-saturated dissolved CH_4 could be stored in the form of GHs and prevented from escaping through upper sequences into the atmosphere. Overall, Figure 4.5 implies that there may be a time window allowing for the formation of thick permafrost during the past 1.6 Ma to 1.0 Ma, and the subsequent genesis of sub-permafrost GH occurrences since 1 MaBP. The time window derived from recent studies (Dallimore et al., 1999; Hansen et al., 2013) is consistent with the GH formation timing (Collett, 1993), assuming that GH occurrences found on the Alaska coastal plain of the circum-Beaufort Sea are likely younger than 1.65 Ma.

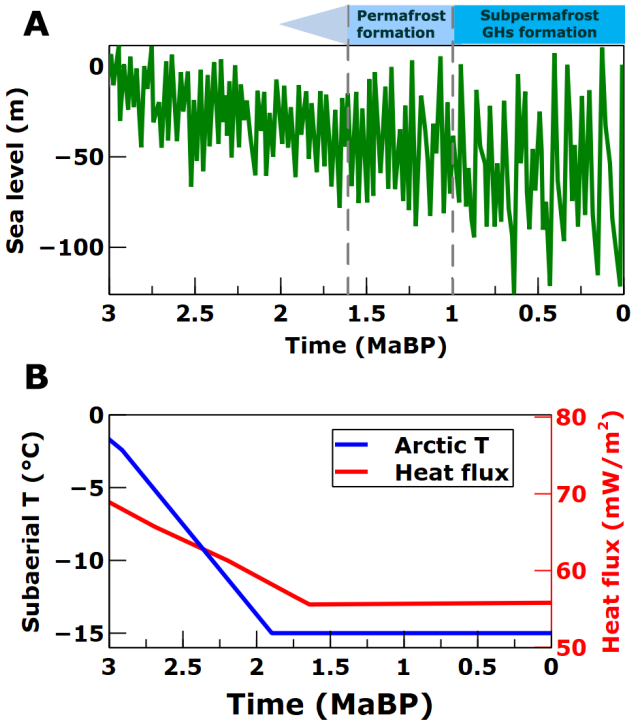

Figure 4.5: (**A**) Global mean sea-level estimations relative to the Late Holocene sea-level since 3 MaBP (Hansen et al., 2013). (**B**) Time series of Arctic subaerial temperature (Arctic *T*) and basal heat flow in the past 3 Ma, adopted from Kroeger et al. (2008).

According to the active source rock depth limit (Pang et al., 2020), the basin's heat flow generally controls the maximum burial depth for source rocks to generate and expel hydrocarbons produced by the thermal cracking of kerogen (Behar et al., 1997). Since 1.6 MaBP, the Beaufort MD Basin exhibits an approximate heat flow of 55 mW m^{-2} (Figure 4.5B) in agreement with the moderate-heat-flow (40-60 mW m^{-2}) basin suggested by Pang et al. (2020). It implies that the upper limit of hydrocarbon generation, migration and accumulation is below 2500 mbgl, conforming to the assumption (Dallimore et al., 1999) that the GHs-forming thermogenic gases originated from the Taglu Sequence (Figure 4.2B). Above 2500 mbgl, the accumulated hydrocarbons initially migrated from the underlying source rocks, coinciding with our previously validated GH formation mechanism (Li et al., 2022a).

The boundary conditions and hydrothermal properties of the sediments representing the Mallik site were determined by applying an iterative history matching procedure and are summarized in Tables 4.2 and 4.3. The model employs the parameters reflecting a general average of values reported in the literature. According to well log interpretations and core analyses of the Mallik 2L-38 and 5L-38 wells, the effective porosity is 0.24–0.4 with a mean permeability of 2.9 mD. Fluid pressure is hydrostatic, and the water table is assumed to coincide with the ground surface. The initially relatively homogeneous geophysical property distribution within the GH-bearing sediments is altered significantly, as effective composite porosities and permeabilities decreased with the increment in S_h.

4.3 Results and Discussion

Our simulation results confirm that CH_4 originating from the deep conventional hydrocarbon reservoirs started to flow into the target sandy sediments via Fault F1 in the dissolved state since 1 MaBP. As a hydraulically active preferential pathway, Fault F1 allows the upward migration of CH_4 into the MHSZ located within the Kugmallit Sequence below the Mallik anticline crest. Concurrently, Fault F2 acts as an active hydrological conduit for lateral CH_4-rich fluid flow, while Fault F3 is as permeable as the sandy sediments of the Kugmallit Sequence. In contrast, the normal (F7) and reverse faults (F4 and F6 in Figure 4.1) are impermeable hydrological barriers. During the past 1 Ma, the super-saturated amount of dissolved CH_4 was instantly consumed by GH formation, triggered by the decrement in CH_4 solubility as fluid migrated to shallower depths, where p and T decreased. As shown in Figure 4.4A,C, the Iperk Sequence is penetrated by the top of Fault F1, which supplies super-saturated dissolved-CH_4 formation fluids that facilitate the formation of intra-permafrost GHs (Dallimore and Collett, 1995) until Fault F1 is clogged by the local decrease in porosity. However, the genesis of intra-permafrost GH is beyond the focus of the present study. Consequently, the upper part of Fault F1 intersecting with the Mackenzie Bay Sequence was parametrized as impermeable.

4.3.1 Simulated Permafrost, Sub-Permafrost GH Interval, and Subsurface Temperature Distributions

Figure 4.6A shows the simulated sub-permafrost S_h distribution after a simulation time of 1 Ma, implying that the spatial density of the number of structural elements positively correlates with the heterogeneous spatial distribution of sub-permafrost GH accumulations. The densest GH enrichment surrounds Fault F1 below the anticline crest and extends coastward, where subsurface flow discharges into the sea. Further, Figure 4.6A indicates the locations of the

Table 4.3: List of hydrothermal properties of the permafrost and GH-bearing sediments, and other parameters used in the presented simulations.

Parameter	Value	Unit	Reference
Effective permeability of I-M Sequence	$\kappa_x = \kappa_y = \kappa_z = 1.0 \times 10^{-25}$	m^2	Assumed
Intrinsic permeability of Kugmallit Sequence	$\kappa_x = \kappa_y = 5.0 \times 10^{-15}$, $\kappa_z = 1.0 \times 10^{-15}$	m^2	Assumed
Intrinsic permeability of F1 and F2	$\kappa_x = \kappa_y = \kappa_z = 5.0 \times 10^{-14}$	m^2	Assumed
Intrinsic permeability of F3	$\kappa_x = \kappa_y = 5.0 \times 10^{-15}$, $\kappa_z = 1.0 \times 10^{-15}$	m^2	Assumed
Intrinsic permeability of F7	$\kappa_x = \kappa_y = \kappa_z = 1.0 \times 10^{-20}$	m^2	Assumed
Salinity of pore fluid	10	kg m^{-3}	Collett (1999)
Hydration number	6.1	-	Ripmeester et al. (2005)
Intrinsic porosity of sediment matrix	0.3	-	Collett (1999)
Density of sediment grain	2650	kg m^{-3}	Collett (1999)
Thermal conductivity of wet sediments	2.45	W m^{-1} K^{-1}	Henninges et al. (2005)
Compressibility of porous sediments	1.0×10^{-10}	Pa^{-1}	Li et al. (2022b)
Density of salt (NaCl)	2160	kg m^{-3}	Moridis et al. (2005a)
Diffusion coefficient	1.0×10^{-10}	m^2 s^{-1}	Li et al. (2022b)
Specific heat of sediment matrix	830	J kg^{-1} K^{-1}	Waite et al. (2009)
Specific heat of CH_4 hydrate	2100	J kg^{-1} K^{-1}	Waite et al. (2009)
Thermal conductivity of CH_4 hydrate	0.68	W m^{-1} K^{-1}	Waite et al. (2009)
Specific latent heat of water-ice phase transition	333.6	kJ kg^{-1}	Waite et al. (2009)
Freezing point of pore fluid	−1.5	°C	Taylor et al. (2013)
Frozen point of pore fluid	−2.5	°C	Taylor et al. (2013)

Mallik well, for which the present 3D simulation results are compared against our previous 2D numerical simulation results, as illustrated in Figure 4.6B,C,D,E. According to the sedimentologic analysis conducted by Medioli et al., 2005 for Mallik 5L-38, GH occurs mostly in pore spaces within the thick sand packages from 886 to 1108 m (Figure 4.6F). It indicates the thickness of the GH interval at Mallik 5L-38 is 222 m, which deviates from the GH interval thickness of Mallik L-38 by approximately 3% (Table 4.4). Therefore, the short distances (ca. 117 – 252 m) between the industrial well Mallik L-38 and scientific wells Mallik 2L-38, 3L-38, 4L-38, and 5L-38 (Table 4.1) are negligible. Consequently, the simulation results acquired from the Mallik L-38 well equivalently represent its four neighboring wells, since their close proximity is represented by one grid element in the numerical model.

For >87% of the Mallik wells summarized in Table 4.1, the permafrost thickness predicted by the 3D model agrees with the well logs and seismic observations by >99.2% (8 m) in Table 4.4, which validates the overall permafrost evolution model implementation. Around the Mallik anticline, the ice-bearing permafrost and GH interval thicknesses as well as sub-permafrost

temperature profiles simulated by the 3D model are consistent with their respective field observations at the Mallik P-59, L-38, 2L-38, 3L-38, 4L-38, 5L-38, and J-37 wells. This confirms our hypothesis on the Canadian Arctic sub-permafrost GH formation mechanism and the validity of the input parameters listed in Tables 4.2 and 4.3. As plotted in Figure 4.6C,D, the S_{ice} and S_h profiles simulated by means of the present 3D model are in excellent agreement with our previously presented 2D simulation results for the Mallik wells L-38 and J-37. Deviations between the 2D and 3D simulation results regarding the S_h increase with the projection distances from the Mallik P-59 and A-06 wells to the Mallik J-37 well, as indicated in Figure 4.6B,E.

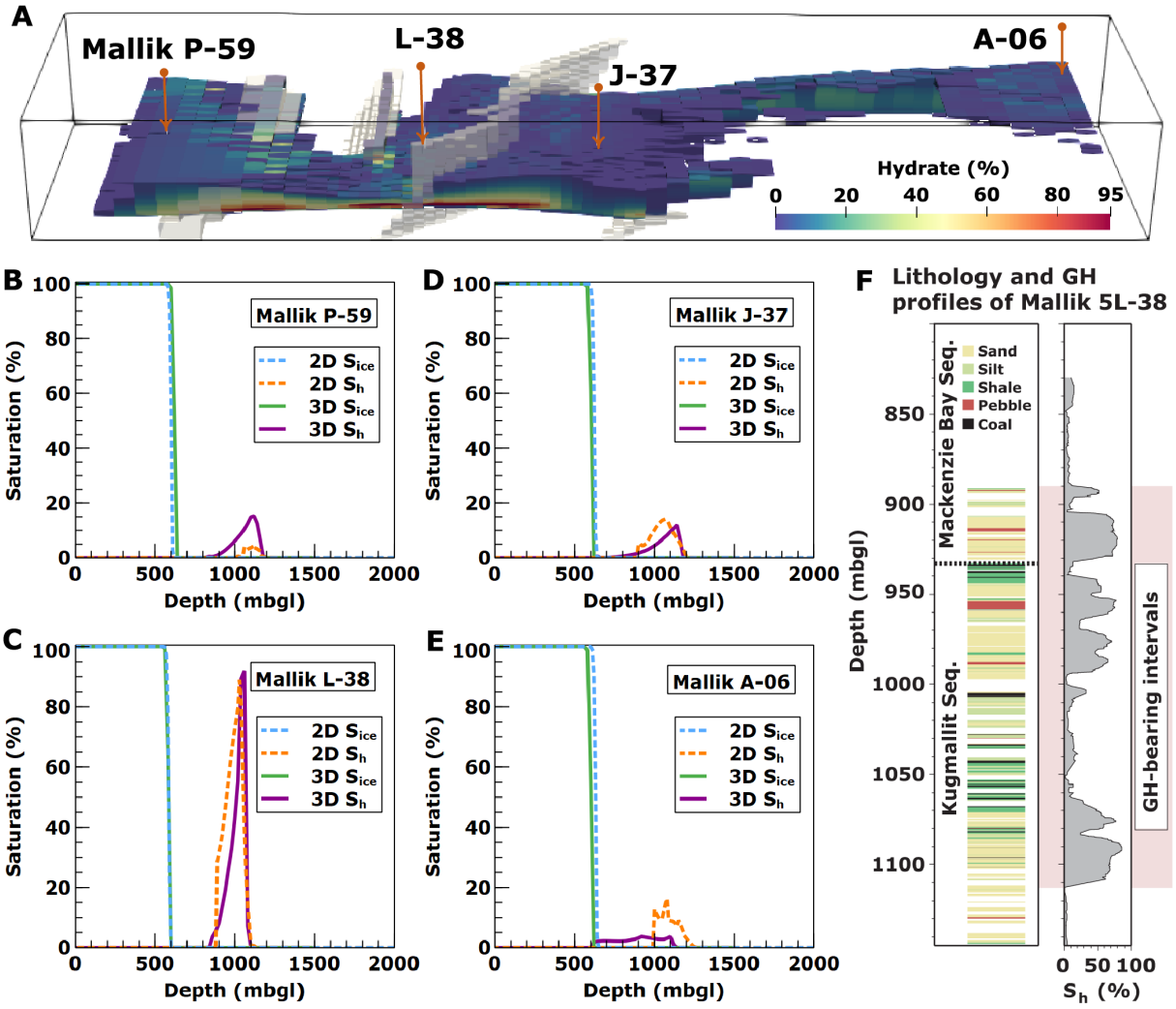

Figure 4.6: (**A**) Simulated field-scale sub-permafrost GH accumulation distribution at a simulation time of 1 Ma (see Figure 4.4 for model geometry). Simulated ice-bearing permafrost saturation (S_{ice}) and sub-permafrost gas hydrate saturation (S_h) profiles obtained for the respective locations of the (**B**) Mallik P-59, (**C**) L-38, (**D**) J-37, and (**E**) A-06 wells. (**F**) Lithology and S_h logs from the Mallik 5L-38 well after Bauer et al. (2005b), presented with permission from Natural Resources Canada under the Open Government License—Canada version 2.0.

The 2D simulation results on the Mallik P-59 and A-06 wells were acquired from the projected well locations onto the transect of the seismic profile 85987 (Li et al., 2022a), which intersects the Mallik J-37 well. It should be noted that the 2D projected location of the Mallik A-06 well is not located in the seismic and well-logging domains (Collett, 1999) but at a distance of ca. 500 m (Li et al., 2022a). To date, the published lithology, S_h, and subsurface temperature data observed at the Mallik P-59, L-38, J-37, and A-06 wells are limited due to the resolution of the industrial exploration that was targeted at the deep oil reservoirs in the 1970s (Taylor and

Judge, 1976). For this reason, the lack of observed peak S_h is insufficient to validate the simulated data listed in Table 4.4. Thus, it merits further efforts to improve the mapping resolution of the geophysically interpreted GH resources as new field data become available, as advocated by Bellefleur et al. (2012).

Figure 4.6F shows that there is an evident correlation between the well-logged highly heterogeneous S_h with regard to lithology along the borehole profile of the Mallik 5L-38 well (Table 4.1). This indicates that coarse-grained layers consisting of permeable sands and pebbles host abundant GHs, whereas fine-grained sediments with nearly no permeability (Katsube et al., 2005), including shales and silts, contain significantly fewer GHs (Medioli et al., 2005). This relationship implies the conclusion that the S_h distribution is lithologically controlled (i.e., by porosity and permeability) according to Jenner et al. (1999) and Matsumoto et al. (2005). In contrast to Figure 4.6E, the simulated 2D and 3D S_h intervals at the Mallik L-38 well demonstrate a relatively uniform S_h distribution within the Kugmallit Sequence, which is parameterized with homogeneous permeability (Figure 4.6C). Since homogeneous porosities and pore-size distributions were employed in all simulations, it is suggested that permeability is the local constraint on the pore occupancy limit by GH. However, exhaustive surveys on the distribution of sub-permafrost GH resources have not yet been undertaken at the Mallik site. Furthermore, our simulations are subject to the poorly investigated petrophysical properties regarding the spatial permeability distribution in the reservoir. Reliable data supporting the parameterization of a heterogeneous permeability distribution in the reservoir sequences of interest cannot be derived from these.

Table 4.4 shows that the ice-bearing permafrost thicknesses and peak S_h match the field observations with negligible deviations ranging from −1.9% to 0.8%, and 2.2%, respectively. All simulated depths of the MHSZ base are within the tolerance range of the corresponding observations. In addition, the simulated total thicknesses of the GH intervals near the Mallik anticline match their respective observations with minor deviations of only 2.6 – 4.7%, which is close to the employed simulation resolution of 1.3% along the vertical direction. However, our model overestimates the thicknesses of the sub-permafrost hydrate-bearing sediment layer at the Mallik A-06 and P-59 wells. This probably indicates that the reservoir quality as determined by porosity, shale-to-sandstone ratio, and intrinsic permeability (Boswell et al., 2020; Boswell et al., 2011) in the far-field of the Mallik anticline, is much poorer than the available near-field data suggests.

Another aspect noted by Frederick and Buffett (2016) is that the thick GH intervals with high S_h are easier to delineate, whereas GH intervals with low S_h are not likely to be detected by geophysical measurements. For example, GHs have been documented where no Bottom Simulating Reflector (BSR) was observed (Paull et al., 1996). Consequently, a BSR is a strong indicator for the presence of at least low-S_h GHs, but the lack of a BSR does not necessarily imply the absence of GHs, as stated by Tréhu et al. (2006). Thus, it is very likely that the industrial exploration of hydrocarbon resources may have underestimated the far-field thicknesses of the identified GH intervals.

The 3D simulation results reveal the highly variable S_h of the Mallik GH deposit throughout its vertical and horizontal directions. The largest economically developable GH occurrences are concentrated under the northern flank of the Mallik anticline along Fault F1, as illustrated in Figure 4.6A. In contrast to the scientific wells, such as Mallik 5L-38, it is not feasible to conduct quantitative analyses but qualitative comparisons of the peak S_h at the Mallik A-06, J-37, and P-59 wells, given the limited observations on S_h derived from the boreholes. Despite

Table 4.4: Comparison of Mallik well logs with simulated permafrost and intervals of GH-bearing sediment.

Parameter/Well	P-59		L-38	
	Observed	**Modeled**	**Observed**	**Modeled**
Depth of ice-bearing permafrost base (mbgl)	638	640	605	600
Depth of GHSZ base (mbgl)	1200 ± 100	1200	1100 ± 100	1100
Total thickness of sub-permafrost GH intervals (m)	156.8	260	229.2	240
Peak S_h within GH intervals (%)	-	~16	~90	~92
Parameter/Well	**J-37**		**A-06**	
	Observed	**Modeled**	**Observed**	**Modeled**
Depth of ice-bearing permafrost base (mbgl)	615	620	632	630
Depth of GHSZ base (mbgl)	1300 ± 100	1200	1150 ± 50	1140
Total thickness of sub-permafrost GH intervals (m)	292.2	300	182.8	480
Peak S_h within GH intervals (%)	-	~12	-	~4

Note: The well-log-inferred data are adopted from Majorowicz and Smith (1999), Collett (1999), and Dallimore et al. (2005a). The dashes represent field observation data that could not be derived from field reports (Collett, 1999; Dallimore et al., 2005a; Majorowicz and Smith, 1999).

the much less concentrated S_h of < 5% predicted by the numerical simulations at the Mallik A-06 well, the far-field remains worthwhile for further investigation in the scope of new drilling campaigns.

The subsurface *p-T* conditions dominate the stability of the permafrost and the sub-permafrost GH occurrences, while permafrost stability is much more susceptible to global warming than pressure perturbations caused by sea-level fluctuations. Generally, a change in temperature at the ground surface will disrupt subsurface temperature regimes originally equilibrated with the basal heat flux below the permafrost and the GH-bearing sandy sediment. For permafrost at depths of <600 mbgl, the temperature profiles simulated by the 2D model and those logged by DTS demonstrate that the present-day permafrost is warmer by 0.8 to 1.3 K compared to the 2D numerical predictions, as analyzed and discussed in our previous work (Li et al., 2022a). According to representative near-surface temperatures collected from the exploration wells, the present-day near-surface ground temperature ranges from −8 °C to −9 °C at the Mallik wells (Burn and Kokelj, 2009). Without implementing the previously proposed transitional boundary condition to mimic the climate changes since the Late Holocene (Li et al., 2022a), the present 3D model reproduces the paleo-geothermal conditions of the Arctic permafrost very well.

As shown in Figure 4.7, the sub-permafrost temperature profiles (depth >600 mbgl) at the Mallik L-38 and J-37 wells simulated by the 3D model are consistent with the DTS observations adopted from the Mallik 3L-38, 4L-38 and 5L-38 wells. In contrast, the temperature at the Mallik J-37 well simulated by the 2D model deviates from the DTS observations by almost 2 K. Although this relative variation may fit the 2D prediction of the regional temperature constraint by Chen et al. (2008), the authors suggested that subsurface temperature variations could reach about 5 K/km along the lateral direction at a depth of 1100 mbgl. This may be attributed to the uncertainty arising from plotting well data linked to line charts on the temperature cross sections (Chen et al., 2008) or changes in the sub-permafrost geothermal

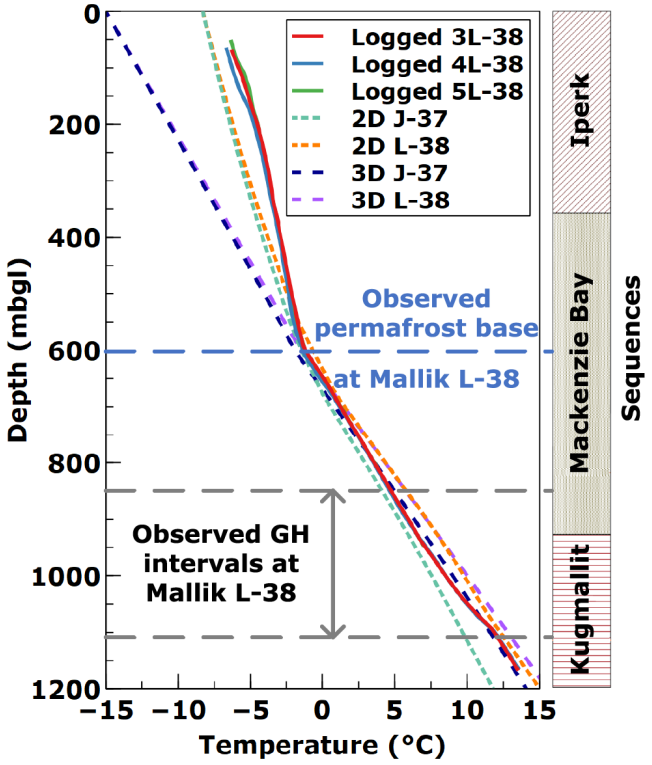

Figure 4.7: Distributed Temperature Sensing (DTS)-logged and simulated temperature profiles. DTS-observations at the Mallik 3L-38, 4L-38, and 5L-38 wells were obtained after 622, 605, and 575 days of their final cementation during the second post-field DTS survey (2003/09/19–21), after Henninges et al. (2005). 2D simulation results were adopted from our previous model (Li et al., 2022a), and the 3D temperature profiles extracted from the present simulations after the sub-permafrost GH formation of 1 Ma. Sequence boundaries are modified after Dallimore et al. (1999).

environment under contemporary climate settings and fault activities induced by historical seismicity (Hyndman et al., 2005). On the other hand, the consistency between the 3D-simulated and DTS-logged temperature profiles within the sub-permafrost GH intervals (860 mbgl < depth < 1100 mbgl) suggests that the Late Holocene climate warming has not yet significantly altered the thermal GH interval environment.

4.3.2 Geologic Controls on the Subsurface Temperature, Permafrost, and GH Interval Distribution

The spatial and temporal evolution of the vertically averaged S_h and cumulative GH thicknesses are presented in Figure 4.8. At first, the upward migrating CH_4-rich fluid flows into the sandy Kugmallit Sequence within the MHSZ via the preferential pathway Fault F1, which is overlain by the Mallik anticline crest. After a simulation time of 0.1 Ma (Figure 4.8A), the average S_h of the accumulated GHs reaches ca. 21% at the upper part of Fault F1. As GHs continue to form up to a simulation time of 1 Ma, more GHs accumulate along Faults F2 and F3 towards the coast in the MD. This observation implies that the simulated CH_4-rich fluid flows towards the coast, joining the groundwater discharge to the sea, which contradicts the 2D model results indicating that the CH_4-rich fluid migrates inland. This also emphasizes the influence of lithological controls on the GH distribution and S_h enrichment. As mentioned earlier, the simulation results reach a very good agreement with the well logs and seismic interpretations (Collett, 1999) from the Mallik P-59, L-38, J-37, and A-06 wells (Table 4.4), which exhibit substantially variable S_h distributions along both lateral and vertical directions.

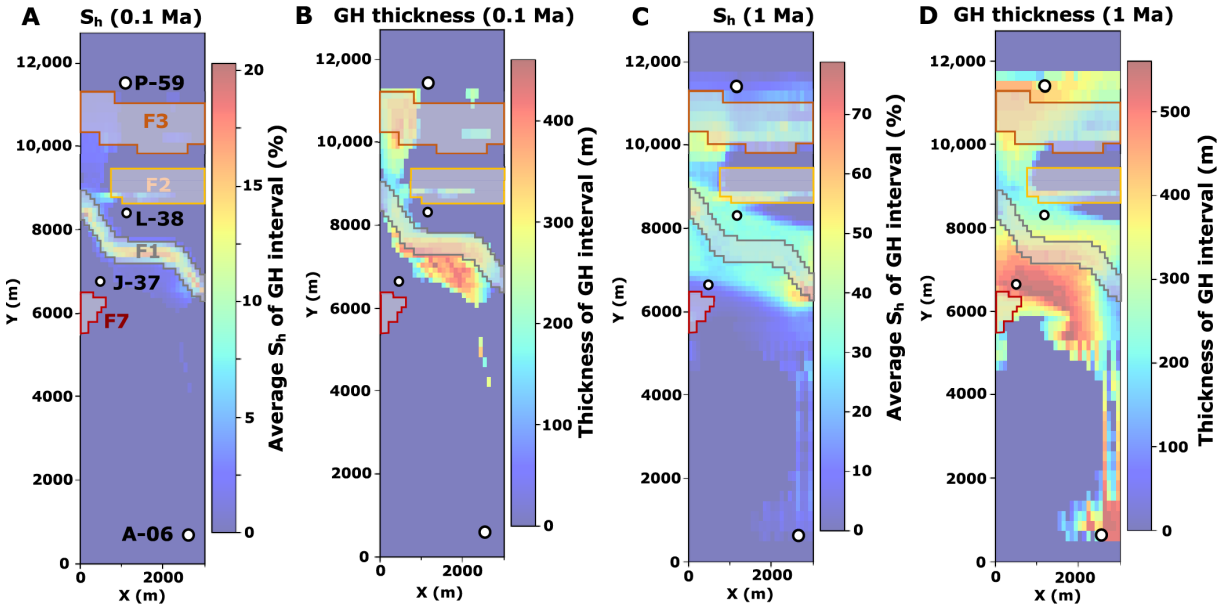

Figure 4.8: Plan view of temporal series of (**A**,**C**) average GH saturations (S_h), and (**B**,**D**) total GH thicknesses within the GH-bearing intervals following the sub-permafrost GH formation after (**A**,**B**) 0.1 Ma, and (**C**,**D**) 1 Ma.

Figure 4.8C shows that the GH deposit at the Mallik site is laterally heterogeneously distributed and covers an area of ca. 9 km^2, where an average vertical S_h above 30% persists after a simulation time of 1 Ma. Moreover, Figure 4.8D indicates that the GH deposit encompasses an area of thick GH-bearing sediments (thickness >250 m). Red shading outlines the reservoir with the thickest GH-bearing sediments (thickness >500 m) located below the Mallik anticline, which are penetrated by the Mallik J-37 well. However, the majority of the GH-bearing intervals only contains negligible S_h < 1% along the Mallik J-37 well (Figure 4.6D), as shown in Figure 4.8C.

One important trend reproduced by the 3D model is that GHs mainly accumulate below the crest of the anticline trap bounded by the Faults F1 and F3 (Figure 4.8C,D). The reason for this distribution pattern lies in variations in the lithology and geothermal environment, indicating differences in sediment permeability as well as specific heat conductivity and capacity, mainly controlled by the shale and sand contents of the respective sedimentary units. Besides, the GH occurrences with the highest concentrations cover a region of ca. 3 km^2 along the northern flank of the Mallik anticline and east of the connection line between the J-37 to L-38 wells, conditioned by the overlain I-M Sequences which act as hydraulic barriers. Since neither seismic nor borehole data are available to confirm the presence or absence of these highly concentrated GH accumulations along the anticline flank bounded by Fault F1, it highlights the feasibility of the employed 3D model to predict yet undiscovered GH resources.

4.4 Conclusions

In the course of the present study, we developed a field-scale static structural geological model of the Mallik anticline based on available well and seismic data. In addition, we employed a thermo-hydro-chemical simulator, previously validated against Mallik field data, to study the geologic controls on the genesis of permafrost and sub-permafrost GH accumulations. The simulation results show that the calculated sub-permafrost temperature profiles, thicknesses of permafrost and hydrate intervals, as well as peak S_h are consistent with field observations. Simultaneously, the locally predicted GH distributions match the observed GH occurrences. Therefore, the proposed feed gas (thermogenic CH_4) migration and sub-permafrost GH

accumulation mechanisms have been validated by the present study, with the following conclusions reached:

1. The complex stratigraphic and structural controls on the heterogeneity of the GH distribution at reservoir scale have been quantitatively confirmed by iterative history matching of the permeability of the underlying faults and lithological units in the Mallik anticline. Since the Late Pleistocene, the major normal fault F1, serving as an active hydraulic conduit, permits the upward migration of hydrate-forming gas in the dissolved state into the MHSZ within the reservoir sequences below the Mallik anticline crest. Furthermore, the normal fault F2 acts as a hydrological conduit for lateral CH_4-rich fluid flow, while the normal fault F3 is as permeable as the sandy GH-bearing sediments. The normal (F7) and reverse faults (F4, F6) are most likely hydrological barriers.

2. At the Mallik site, the GH occurrences mainly develop in the sandy sediments within the Kugmallit Sequence, whereas the Iperk and Mackenzie Bay Sequences act as seals (barriers for CH_4 transport). The stability of sub-permafrost GHs is mainly determined by the present geothermal regime and hydrodynamic conditions. Concentrated GH accumulations under the Mallik anticline crest are preserved by the favorable thermal conditions around Faults F1, F2, and F3, accompanied by a high spatial density of structural elements.

3. By comparing the simulated results against corresponding well-log data, the presented numerical framework confirms the solid quality of the established static geological model elaborated on the basis of published interpretations of the seismic reflection profiles. The introduced simulation framework can be applied to support the interpretation of such geophysical measurements.

The presented results allow for the assessment and projection of potential GH enrichments at the Mallik site and provide a new perspective on present Arctic sub-permafrost hydrocarbon systems. Moreover, they contribute to the understanding of sub-permafrost groundwater flow, demonstrating that the CH_4-rich fluid prefers to flow coastward to join the groundwater discharge in the Canadian MD. Our model also shows excellent potential for investigating the genesis of similar integrated natural systems and the evolution of permafrost under various climatological events in the North American coastal region of the Beaufort Sea. The validated simulation framework can be applied to other world-wide GH deposits to contribute to the assessment of global GH resources.

Chapter 5

Discussion

To numerically reproduce the permafrost-GH system dynamics from laboratory to field scales for the first time, a modeling framework ($T_{plus}H$) was established and verified in the present study. The key parameters for characterizing GH deposits are the hydrate spatial extent, S_h distribution, and GH abundance. Non-intrusive geophysical measurements are widely employed with the utilization of first principles-based models to determine S_h. However, these predictions deviate from reality (i.e., sampling results) under certain circumstances, such as low S_h-saturated sediments and intra-permafrost conditions. Since ice and hydrate have similar physical properties, detecting intra-permafrost GHs using standard geophysical measurements is nearly impossible. In Section 5.1, a comparative evaluation of challenges is presented based on the ERT-observations adopted from LARS experiments (Chapter 2), by quantifying the deviation patterns of these observations from non-intrusive geophysical S_h measurements to sampled results. Each elemental volume of employed models generally needs to be increased during the upscaling from the laboratory (Chapter 2) to the field scale (Chapter 3). This may result in an uncertainty of upscaled permeability, which can lead to a significant difference in permeability under the same S_h, as presented in Section 5.2.

Due to the high spatial heterogeneity of geophysical properties, the employed 2D geologic model, generated from a seismic transect of the Mallik site in Chapter 3, can not accurately quantify the spatial geologic controls on GH volume and distribution. Thus, the first field-scale static 3D Mallik geologic model has been established using well-logs and seismic profiles. By comparing their differences, the significance and necessity of extending model dimensions are given in Section 5.3. Chapters 3 and 4 of this study have validated the feasibility of my proposed sub-permafrost GHs formation mechanism using 2D and 3D simulation studies. These studies showed that CH_4-rich fluids were vertically transported from deep overpressurized zones through geologic fault systems since the Late Pleistocene, ultimately resulting in the observed GH deposits in the Kugmallit Sequence. Moreover, Chapters 3 and 4 also validated the timing of permafrost-GH genesis that coastal permafrost started to form since the early Pleistocene sea-level retreat (ca. 1.6 MaBP) and steadily increased in thickness for 0.6 Ma prior to sub-permafrost GH formation. Consequently, the findings in Chapters 3 and 4 give support to improving the understanding of the Arctic GH petroleum system and conducting a comparative study on the spatiotemporal factors of permafrost-GH system genesis, as respectively presented in Sections 5.4 and 5.5.

Below the base of the permafrost, the DTS-logged subsurface ground temperature profiles provided valuable constrained conditions for model calibration in 2D and 3D field-scale simulations at the Mallik site. However, unlike the sub-permafrost temperature distributions, the near-surface temperatures in the circum-Beaufort region were sustainably increased, as evidenced by the DTS logs obtained from the Mallik, Taglu, and Ignik Sikumi sites. As presented in Section 5.6, the impact of climate warming in the circum-Beaufort permafrost region is evident, and this warming trend has been significantly accelerated by Arctic amplification over the last few decades.

In this study, the discussion of the main findings is focused on six points:

- Challenge in predicting S_h through geophysical methods (Section 5.1).
- Uncertainty of upscaling the numerical model from laboratory to field scale (Section 5.2).
- Significance and necessity of extending the field-scale model dimensions from 2D to 3D for the numerical study at the Mallik site (Section 5.3).
- Generalization of an improved GH petroleum system resulting from the summary of the comprehensive spatiotemporal prerequisite of the generation, migration, accumulation, and preservation factors controlling Arctic sub-permafrost S_h distribution (Section 5.4).
- Timescale and mechanism of the permafrost-GH system genesis in the circum-Beaufort coastal region (Section 5.5).
- Impact of climate change on Arctic near-surface ground temperatures and permafrost warming (Section 5.6).

5.1 Challenge in Predicting Hydrate Saturation Through Geophysical Methods

The most challenging reservoir properties to be accurately determined for GH deposits to enable the economic evaluation of their technically recoverable potentials are porosity and S_h. In such systems, directly-measured features (well logs) commonly serve as a primary source of porosity-determining data. As suggested by Chong et al. (2022), the downhole porosity-logging can better represent S_h than the first principles-based models (e.g., the NMR- and ERT-derived S_h models). Notwithstanding, well logs in GH- or ice-bearing layers are generally subject to error. According to Matsumoto et al. (2005), the NMR-porosity logs estimated S_h match the geochemically determined S_h. However, Jain et al. (2019) reported that using the constant longitudinal to transverse relaxation time ratio (T1/T2) causes the conventional NMR-based porosity of GH-bearing intervals to be underestimated by ca. 36 porosity units, leading to the systematical overestimation of NMR-derived S_h by ~8–10%. Therefore, using the first principles-based porosity-determining data to calculate S_h still needs to be improved.

In Figure 5.1, the most significant deviation between the ERT-measured and pore fluid sampled $S_{h,bulk}$ emerges at the low and high limits of pore fluid sampled $S_{h,bulk}$ range in LARS, and it converges to almost 0% when $S_{h,bulk}$ is narrowed down to a range of ~50–70%. This phenomenon is similar to the observed critical S_h of ~50–60%, which highly distinguishes GH distribution behavior in GH formation experiments (Gil et al., 2019). Figure 5.1b shows that the ERT measurements applied in LARS generally overestimate S_h by up to ~8–11% when the benchmark S_h<45% but constantly underestimates S_h by up to 11% when the benchmark S_h>45%. As evident by the deviation analysis of NMR-derived and ERT-based S_h, the ERT-predicted S_h is slightly more precise than the NMR method. In general, when the actual S_h is low, both ERT and NMR-based measurements tend to overestimate S_h, suggesting that the physical properties of GH-bearing sediment are substantially altered by even a small amount of GHs.

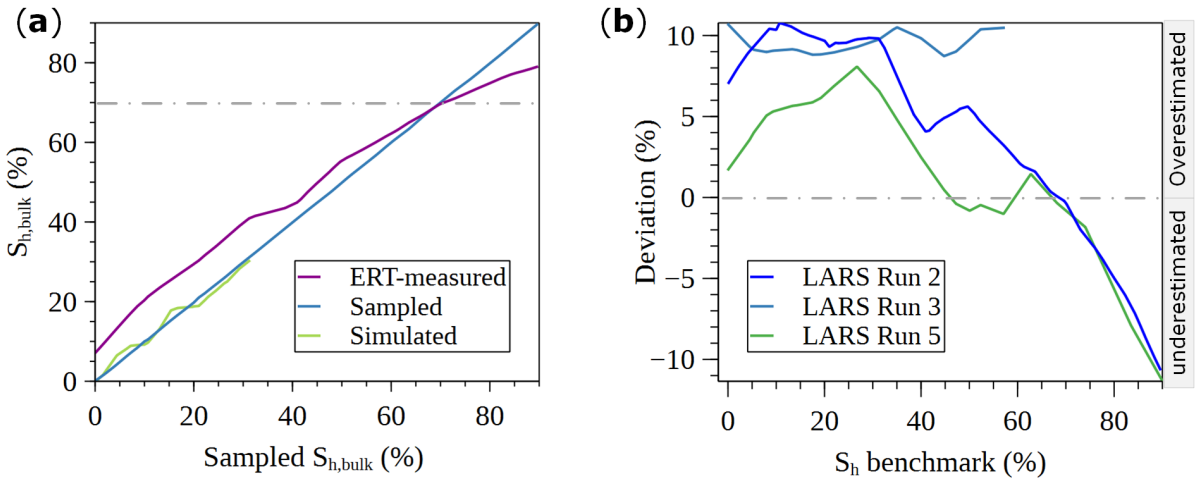

Figure 5.1: (**a**) ERT-measured (LARS Run 2), pore fluid sampled, and simulated bulk hydrate saturation ($S_{h,bulk}$) evolution during the hydrate formation experiment, obtained from Li et al. (2022b) and Priegnitz et al. (2015). (**b**) Deviations between ERT-measured $S_{h,bulk}$ and sampled ones, modified after Priegnitz et al. (2015).

5.2 Uncertainty in Model Upscaling from Laboratory- to Field-scale

The GHs, formed by using the "dissolved-gas" method (Priegnitz et al., 2015), initially present in inter-pore as the pore-filling habit (Figure 5.2a). The pore-filling assumption (Waite et al., 2009) suggests that GH particles float and anchor in the center of inter-pore space. In fact, GH can hardly remain in the pore center due to the impact of buoyancy due to the density difference between pore fluid and GH. Therefore, GHs are supposed to stay in physical contact with sediment particles to counteract the buoyancy (Lei et al., 2022b). Subsequently, pore-filling GH may turn into load bearing as the local S_h reaches 25–40% (Waite et al., 2009). For instance, the machine learning-driven three-phase saturation (GH, water, free-gas) identification leads to the critical S_h of ~50% Kim et al. (2020a). Moreover, Pan et al. (2021) reported that flow path clogging starts at S_h > ~68%, which may indicate the alteration of GH habits. Coincidently, the deviation between the ERT-measured $S_{h,bulk}$, and pore fluid sampled ones converges to 0% when $S_{h,bulk}$ reaches approximately 68%, as shown in Figure 5.1b.

In the present study, the applied model has been developed based on the assumption of homogeneous S_h distribution in an isotropic sample. With this assumption, it is straightforward to assume the pore-filling GH to be ideally distributed in the pore when upscaling, as shown in Figure 5.2a. However, it is rare to see such uniform distribution in large-scale laboratory-formed GH-bearing specimens, including LARS, because GHs preferentially accumulate at cold boundaries (Lei et al., 2019a). Therefore, GH distribution in the specimen reflects the geometry of the thermal boundary within the sample chamber, as shown in Figure 5.2b,c. If the high-S_h zone is impermeable, the GH distribution in Figure 5.2c will result in a clogged specimen along the vertical direction compared to the other case, despite the three cases having the same $S_{h,bulk}$.

Figure 5.2 indicates that inter-pore GH distribution has a much greater influence on sediment permeability, and uneven GH distribution can result in drastic permeability anisotropy. Overall, the connectivity of the unfilled pores, rather than GH habits within the pore, is a more determining factor in fluid permeability. Moreover, it should be expected that neither the GH host sediment nor the S_h distribution in natural GH deposits is isotropic or homogeneous.

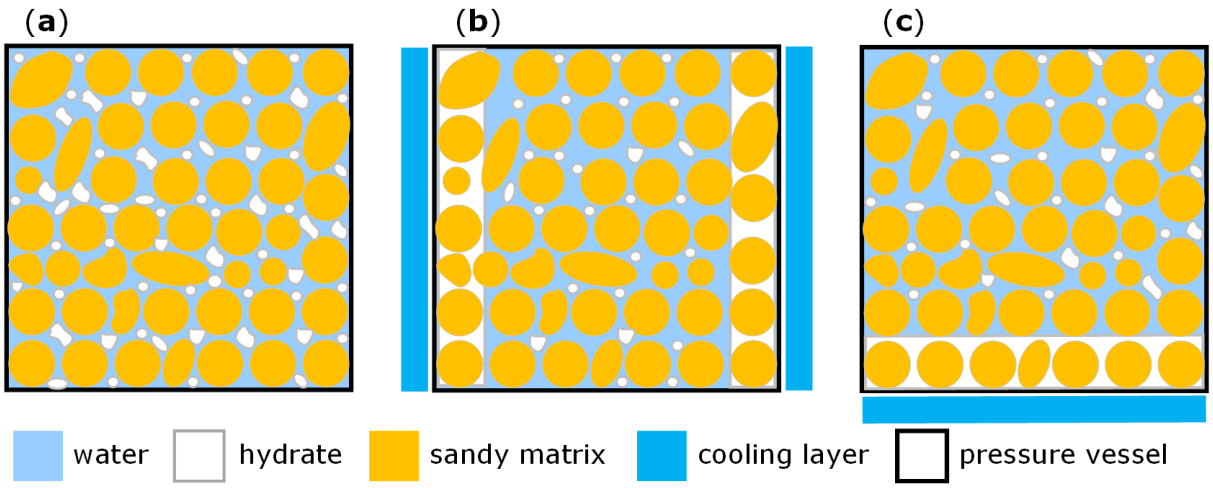

Figure 5.2: Potential cases during upscaling under the same $S_{h,bulk}$. (**a**) Ideal uniform GH distribution in an overall homogeneous sediment sample. (**b**) and (**c**) heterogeneous GH distribution where GHs concentrated along the cooling boundary, after Pan et al. (2021).

Therefore, the synthetic sample of LARS developed based on the homogeneous assumption certainly can not reflect the reality of GH host sediments, but can instead represent a fraction of the interval of GH-bearing sediment with highly concentrated hydrate, as observed at the Mallik site. Hence, heterogeneity in the geophysical and lithologic properties of hosting sediments should be considered when dealing with GH-bearing deposits in natural conditions in the future.

5.3 Significance of Extending the Model Dimensions from 2D to 3D in the Field-scale Studies

Using seismic data acquired in 1985 (Collett, 1999), the 2D and 3D static geological models are employed to reconstruct the sedimentary successions and the structures of the underlying faults and anticlines at the Mallik site. In Chapters 3 and 4, the simulation results from the Mallik P-59, L-38, and J-37 wells showed an excellent match between the 2D and 3D models, proving the accuracy of the employed modeling approach and geometry implementation in the near-field of the Mallik anticline. However, the static geological models can still be improved, as indicated by the deviations between the simulated and logged GH-bearing layer thicknesses (Table 4.4) in the far-field region near the Mallik A-06 well. The degree of accuracy in static models and subsequent simulations is typically associated with the level of enrichment and quality of the input data sets. Overall, previous studies presented in Chapters 3 and 4 demonstrate the feasibility of using seismic-derived data and well-logs for investigating the permafrost-GH system in a remote and mainly inaccessible area. These old industrial data still hold unexploited potential in reservoir-scale modeling research.

Figure 5.3a shows an extended model geometry of the previously applied 3D static model covering an area of approximately 70 km^2, containing the surrounding faults around the Mallik anticline. In Chapter 4, the marginalized Faults F4 and F6 are interpreted and parametrized as impermeable faults to minimize the difference between simulated and observed subsurface temperature distributions via iterative history matching. The green box in Figure 5.3a highlights the spatial location of the seismic transect shown in Figure 5.3b. By comparing the 2D and 3D fault interpretations, some of the differences presented in Figure 5.3 are recognized. For instance, the disconnected Faults L4 and L15 are likely reinterpreted from the 2D model as a connected Fault F1, further intruding into the bottom of the Iperk Sequence in the 3D model. The 2D inlet

of CH_4-rich fluid is composed of the bottom of L3 and L4, while the bottom of F1 acts as the 3D inlet. The separated, permeable faults L6 and L7 from the 2D model are reinterpreted as a 3D-connected impermeable fault (F7) in the 3D model.

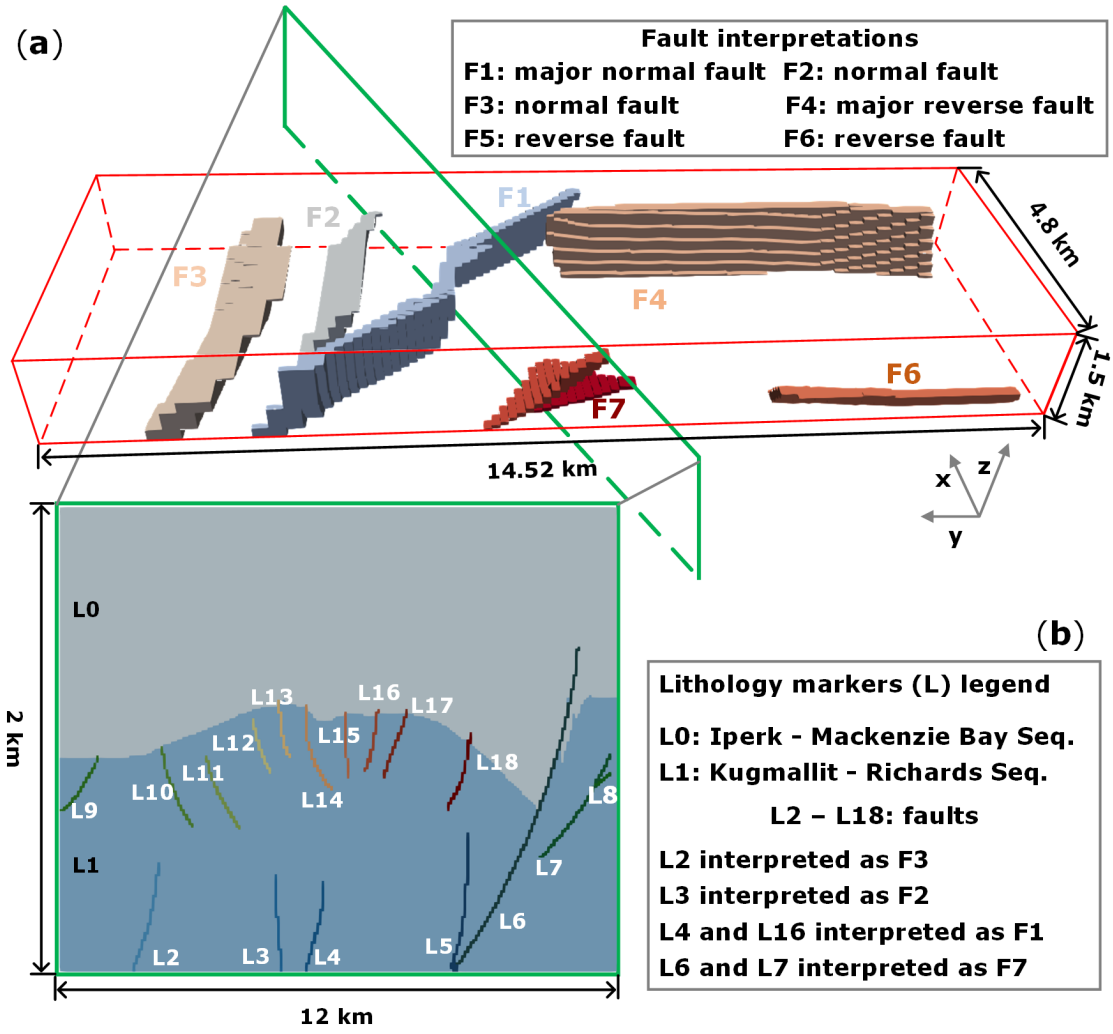

Figure 5.3: Comparison of applied 2D and 3D model geometry at the Mallik site. (**a**) 3D model geometry generated from the interpreted geological units from seismic profiles (see Figure 5.6b for the location of AA') shows the surrounding faults of the Mallik anticline, based on Collett (1999), as well as Dallimore et al. (2005b). (**b**) 2D model geometry of the interpreted transect of seismic profile 85987 after Collett (1999), adopted from the previous study (Li et al., 2022a).

3D geological models are significantly more potent in terms of developing and visualizing geological knowledge than 2D cross-sections in heterogeneous natural environments (Thornton et al., 2018). Therefore, certain studies, such as understanding the geologic control of structural elements to sub-permafrost GH distribution in Chapter 4, demand 3D geological models that are detailed, accurate, and spatially extensive. For instance, the Mallik anticline is located in a fault-developed zone, where the Mackenzie–Kugamllit Sequences have been faulted into complex geometrical arrangements by tectonic forces. As assumed in Table 4.3, the sandy Kugamllit Sequence as hydrate-bearing sediment is several orders of magnitude more permeable than the nearly impermeable permafrost (Chuvilin et al., 2022) within the overlying Iperk Sequence and fault F7, but it is an order of magnitude less permeable than faults F1 and F2 serving as the conduit of feed gas. This assumed reservoir permeability is based on the interpretations from the well logs and core analyses of the Mallik 2L-38 and 5L-38 wells

(Dallimore et al., 2005b). The assumed permeabilities of faults are determined via iterative history matching. The significant contrasts in the hydraulic conductivity with these stratigraphic geometry elements (sequences and faults) exert a profound influence on the groundwater flow pattern, which alters the geothermal distribution and determines GH deposit distribution, as demonstrated by the 3D numerical flow modeling in Chapter 4. Besides, employing L6 as an impermeable fault in the 2D simulation is unfeasible because this turns the semi-closed system with the closed top and bottom boundaries into a one-end open system. This change raises the likelihood of numerical oscillation for inflowing CH_4-rich fluid. Compared to the 2D model, the 3D model does not show this obstacle because the impermeable fault F7 does not block the fluid outflowing pathway. Using the 3D model has proven its advantages in quantifying the hydraulic contribution of subsurface geological units at the reservoir and million-year scales.

The quality of the 3D static model depends on the density of geological surveys and the spacing of applied 2D cross-sections (Lin et al., 2017). In further studies, more precise 3D geological models with the application of spatially heterogeneous reservoir properties are desirable to reproduce the variation of S_h distribution in centimeter scale within the GH-bearing sediments. Applying such heterogeneous fine-grid models require more accurate high-resolution downhole measurements of regional lithological characteristics, as presented by Lei et al. (2022a). Moreover, the subsequent 3D simulation study also demands an efficient automatized workflow to integrate these anisotropic variables as the initial and boundary conditions for modeling.

5.4 Gas Hydrate Petroleum System Analysis

Classical petroleum system analysis (Jang et al., 2020; Max and Johnson, 2014) incorporates various geological information to assist in hydrocarbon exploration to identify and evaluate their commercial exploitation potential. The aim of GH petroleum system (GHPS) analysis is to advance the understanding of several fundamental issues, including the origin, migration, and accumulation of the source gas composing the GH deposit. In general, the generation, migration, accumulation, and preservation processes determines the distribution of GH reservoirs and the viability of their economic recovery.

Oil and natural gas deposits that form in the basin may have diverse generation histories, stratigraphic and structural settings, and they may have persisted for a wide range of geological ages and depths once they were trapped. Compared to most conventional hydrocarbon resources, the formation of GH has been more firmly restricted by timing and pressure (i.e., sedimentary burying depth) conditions. Particularly, GHs are confined to the GHSZ, whereas conventional natural gas deposits can be discovered over a significantly greater vertical distance in hydrocarbon and petroleum provinces.

Max and Johnson (2014) considered the GHPS to be composed of three major components: (1) the CH_4 source; (2) the CH_4 migration pathway; and (3) the reservoir self-trap unit. As GHs crystallize in sandy sediment within the GHSZ, the porous GH-bearing sediment itself comprises both the reservoir and the trap. Thus, GH formation is a process of thermodynamic trapping hydrate-forming gas to a solid phase. To facilitate the assessment of GH reservoir potential, Jang et al. (2020) further define the reservoir self-trap unit as a coarse-grain composed permeable host sediment and a separate overlying fine-grain composed low-permeability seal. The overlying seal can restrict feed gas (CH_4) migration out of the coarse-grained reservoir over time and elevate the CH_4 concentration of pore water to excess the CH_4 solubility limit to initially form GH in the coarse sediment. Therefore, the fine-grained sediment, retaining

the feed gas within its underlying GH reservoir, merits consideration as a distinct seal in the improved GHPS. In contrast to traditional seals, the seal of GHPS does not have to last a long time or maintain high pressures because the accumulating GH will aid in the seal.

Due to the restriction by the *p-T* limits of GHSZ, GHs are geologically recent deposits and are quite responsive to environmental (*p-T*) changes. Table 5.1 shows the essential prerequisite factors of improved GHPS. Many factors have close paragenesis relations during GH deposit formation. For instance, GHs only exist in a dynamic equilibrium within the GHSZ under certain *p-T* conditions. Further, the GH formation via the listed cases requires a sufficient groundwater supply and a low-permeable geological seal overlying the correspondence GH reservoir. In case I, natural gas accumulated in shallow hydrocarbon traps is initially outside the GHSZ but moves into the GHSZ due to the paleo-climate cooling, thus causing the formation of intra- and sub-permafrost GHs by in-situ conversion of the gas deposit into a GH deposit. In case II, the expelled gaseous and/or dissolved gas fluxes from their sources ascendingly migrate along permeable conduits (e.g. permeable layers, faults, or a combination of these) towards the suitable host sediments within the GHSZ, where GHs may occur. The migration pathways are required to stay active during the accumulation of GHs. However, they are not required to be present in the currently observed state before the GH deposit formation or persist after the GH deposit formation. Overall, all of these tick-marked factors in Table 5.1 have to stay active during the critical duration for the growth of GH deposits over a relatively wide geological timespan, ranging from tens of thousands of years to over a million years.

Table 5.1: Spatiotemporal prerequisite factors of the improved GH petroleum system under two GHs formation cases in the Arctic.

GH petroleum system factor	Case I: GHs in-situ converted from gas deposit	Case II: GHs formation facilitated by gas flux
Reservoir	✓	✓
Seal	✓	✓
GHSZ	✓	✓
Groundwater supply	✓	✓
Feed gas flux		✓
Trapped feed gas	✓	
Feed gas pathway		✓

5.5 Permafrost-GH System Genesis in the Circum-Beaufort Coastal Region

The assessment of global paleo environmental change associated with the modern industrial age remains a critical objective in GH research. The objective of this comparison study is to develop a generalized concept model that explains the history of GH formation in the circum-Beaufort coastal plains and deltas.

Thermal conditions conducive to the permafrost and GH formation may have persisted in Northern Alaska since the past ca. 1.65 Ma (Collett, 1999), which is consistent with the adopted timescale of 1.6 Ma (Figure 5.4a) for the genesis of the Mallik permafrost-hydrate system in Chapters 3 and 4. In Figure 5.4b, Dai et al. (2011) combined various information sources to reconstruct the evolution of the stratigraphy, ground surface, permafrost base, and potential

GH stability zone at the Mount Elbert region on the Alaska North Slope (ANS). Under the assumption of 1D spatial-temporal evolution history for GH and permafrost in Figure 5.4b, the GHs could form in host sediments almost a million years before the onset of permafrost formation at the Mount Elbert site (Dai et al., 2011). The thickness of the GH stability zone (GHSZ) enlarges as the base of the permafrost deepens. With the base of permafrost propagating to the pre-existing GH-bearing sediment (Figure 5.4b), the presence of ice and GH may be superposed at the same depth as the ground surface cooled in the Pleistocene epoch.

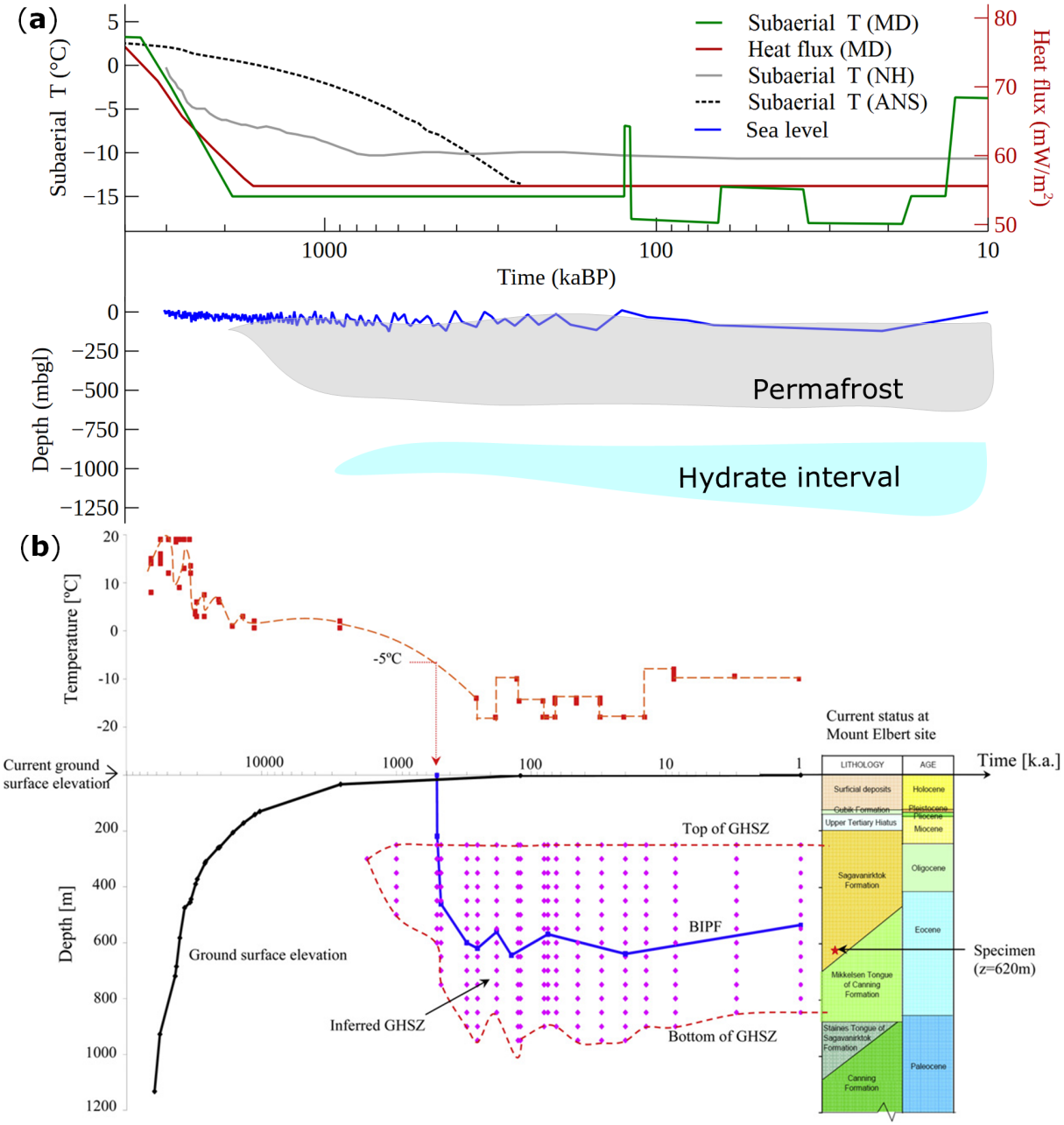

Figure 5.4: (**a**) Geological history at the Mallik site in the Mackenzie Delta (MD). Time series compiled from the literature include: sub-Arctic Northern Hemisphere (NH) and Arctic (MD) subaerial temperatures (Bintanja and Wal, 2008; Kroeger et al., 2008; Taylor et al., 2013), basal heat flow in the MD (Kroeger et al., 2008), and global mean sea-level estimations (Hansen et al., 2013). (**b**) Geological history at the Mount Elbert site on the Alaska North Slope (ANS), reprinted from Dai et al. (2011) with copyright permission from Elsevier (2023). Time axes are shown in logarithmic scale.

Since 2 MaBP, the change in ground surface elevation was limited to less than 20 m and changes in global sea level led the circum-Beaufort coast plain to submerge for a negligible

period (Dai et al., 2011) in Figure 5.4b. Therefore, their finding supports the previously adopted assumption in Chapters 3 and 4 that the variations in sea level, depositional processes of the stratigraphic sequences and tectonic activities had minimal effects on the evolution of sub-permafrost GH accumulations since the Late Pleistocene. In Figure 5.4b, the dotted line adopted from the temperature history (Dai et al., 2011) on the Alaska North Slope (Figure 5.4b) shows a significant difference from the applied subaerial temperature estimates for the Mackenzie Delta (Kroeger et al., 2008; Majorowicz et al., 2012a) and the sub-Arctic Northern Hemisphere subaerial temperature projections (Bintanja and Wal, 2008) in Chapters 3 and 4. From 2 MaBP to 0.15 MaBP (Figure 5.4a), the applied subaerial temperature for the Mackenzie Delta is lower than the sub-Arctic temperatures of the Northern Hemisphere by a range of 7 K to 5 K. Conversely, the arctic subaerial temperature on the Alaska North Slope (Dai et al., 2011) is even consistently higher than the Northern Hemisphere temperature (Bintanja and Wal, 2008) by up to 8 K from the past 3 Ma to 0.4 Ma, as indicated by the dot line in Figure 5.4a. The arctic subaerial temperature adopted by Dai et al. (2011) certainly cannot stand as a true reflection of the paleoclimatic conditions, even when considering the relatively high uncertainty of the limited numbers of proxy data-based Arctic subaerial temperatures relative to the well-established subarctic Northern Hemisphere surface air temperatures (Bintanja and Wal, 2008).

On the Alaska North Slope, the formation of GH with high S_h in the coarse-grained sediments was due to either the transportation of dissolved CH_4 in water through high-conductivity faults, or gaseous CH_4 invasion due to the low capillary entry pressures (Collett, 1993; Dai et al., 2011). GH formation was sustained by the upwards migration of deep thermogenic gases, which became trapped together with shallower biogenic gases within the current GHSZ and converted into GHs (Boswell et al., 2011; Dai et al., 2011). To describe the history of GH formation, four possible scenarios for the GH origin mechanisms in the circum-Beaufort coastal plains and deltas (e.g., Alaska Prudhoe Bay and Canadian Mackenzie Delta in Figure 5.5a) are proposed and listed in Table 5.2.

Table 5.2: Assumptions on the origin of circum-Beaufort sub-permafrost GH accumulations.

Scenario	Migration pathway	Source gas	Permafrost-GH genesis timing	Reference
I	Fault	Thermogenic dissolved gas	Since 1.6 MaBP, permafrost base keeps deepening for 0.6 Ma, then GHs form for 1 Ma	Li et al. (2022a)
II	Fault	Thermogenic free gas	Permafrost formation since Pleistocene, sub-permafrost GHs formation during Wisconsinan Glaciation (~75–11 kaBP)	Collett (1993)
III	Fault	Thermogenic and microbial free gas	In-situ conversion of the natural gas reservoir into GH reservoir induced by climate cooling over the last 1.7 Ma	Collett (1993) Boswell et al. (2011) Dai et al. (2011)
IV	Fault or permeable layer	Thermogenic and microbial dissolved gas	In-situ diffusion of microbial gas and short- or long-range advective migration of thermogenic gas since the Pleistocene	Collett (1993)

The near-surface part (10 mbgl < depth < 100 mbgl) of the temperature profile recently measured at the Ignik Sikumi #1 in the Prudhoe Bay was lower than these recent corresponding observations at the Mallik site by a threshold of 0.8 to 1.8 K, as shown in Figure 5.5b,c. This temperature difference indicates that the paleo subaerial temperature (ANS) was likely lower

than the one (MD) by almost 2 K since the Late Pleistocene. Therefore, the adopted temperature in Figure 5.4b is likely to be overestimated by a range of 15 K to 5 K, from 2 MaBP to 0.4 MaBP. Consequently, the depth of permafrost base in Figure 5.4b is over-predicted by ca. 140 m compared to the simulated depth of permafrost base in Majorowicz et al. (2012a), as the temperature has reached −10 °C since 8 kaBP (Figure 5.4b).

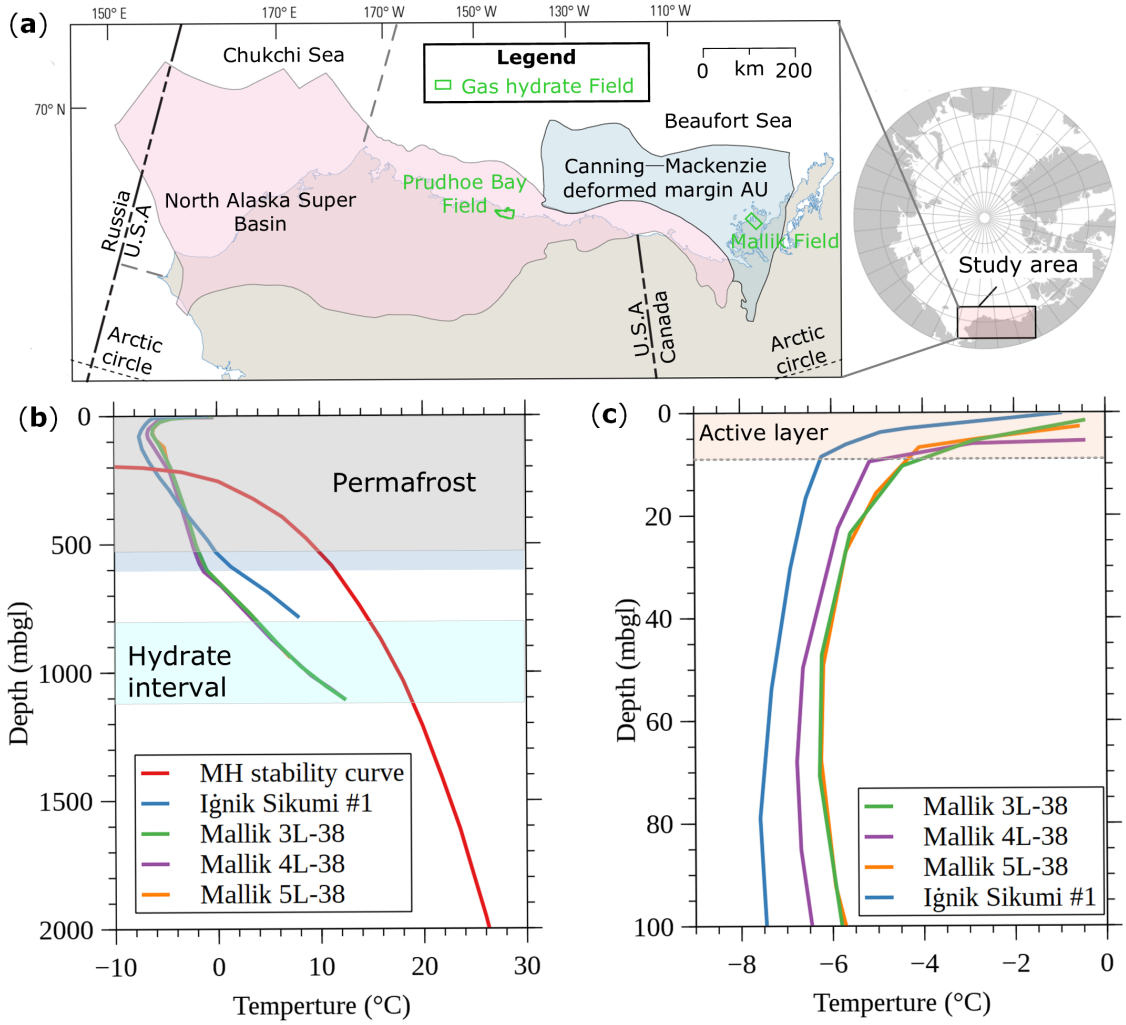

Figure 5.5: (**a**) Location map for North Alaska Super Basin and Canning–Mackenzie deformed assessment unit (AU) within the Arctic petroleum province defined by Houseknecht and Bird (2011), Houseknecht et al. (2020), and Masterson and Holba (2021), adopted from Houseknecht and Bird (2011). (**b**) MH phase stability curve shows the depth and temperature conditions suitable for the GH formation, adopted from Moridis et al. (2011). (**b**,**c**) Temperature profiles measured by fiber optic Distributed Temperature Sensor (DTS) cable embedded within cement between the well casing and sediment. The DTS observations at the Mallik 3L-38, 4L-38, 5L-38, and Ignik Sikumi #1 wells are adopted from Henninges et al. (2005) and Boswell et al. (2017).

Overall, the history of Arctic subaerial temperatures and the presence of gas traps in the circum-Beaufort coastal region is still poorly understood, thus multiple scenarios are plausible, as stated by Collett (1993) and Dai et al. (2011). Furthermore, the age of circum-Beaufort sub-permafrost GHs is likely no older than Pleistocene (approximately 1.65 MaBP) but can be as young as Wisconsin Glacial Episode (approximately 70 to 10 kaBP). However, according to a more recent study by Lei et al. (2019b), GHs formed from free gas (Scenarios II and III in Table 5.2) at significant depth could host residual free gas for millions of years. For example, as no groundwater percolation occurs through the assumed 1-meter-thick gas-saturated sediment, it

requires ten million years to transfer all the trapped gaseous CH_4 into GH in the coarse-grained sediment (Lei et al., 2019b). Given such a lengthy geologic process, the gaseous methane trapped inside hydrate film should be found commonly. Thus, the gaseous CH_4, GH, and water within the GHSZ should ubiquitously coexist under Scenarios II and III. As summarized in Section 3.2.1, free gas was not observed within or at the bottom of the GHSZ at the Mallik site, which considerably raises the credibility of Scenario I in contrast to others, as presented in Chapters 3 and 4.

5.6 Near-surface Ground Temperature Change and Permafrost Warming

Terrestrial sub-permafrost GH deposits are relatively unstable compared to deep oceanic ones because the water temperature in the deep oceanic environment only has minimal variations compared to the onshore subaerial temperature. Based on the observation of natural consolidation subsidence in 2010, scenarios for future relative sea-level and inundation hazards in the outer Mackenzie Delta (MD) are evaluated until 2100 (Forbes et al., 2022). Under the 95th percentile projection of RCP8.5, 85% of the outer MD will be underwater by about 1.2 m due to the future sea level rising, including the Taglu and Mallik sites. Hence greater knowledge and insights into permafrost degradation (Mestdagh et al., 2017), sub-permafrost CH_4 seepage (Hodson et al., 2020), and permafrost ecosystem responses to seawater inundation (Schuur et al., 2022) are needed. The evolution of the talik and thermokarst lakes (Ruppel and Kessler, 2017) under various future global warming scenarios also deserves to be investigated. The state of permafrost is highly dynamic and requires constant follow-up surveys.

The change of near-surface ground temperature directly reflects the evolution of the permafrost thermal state, as shown in Figure 5.6b,d. In Figure 5.6a, the extension lines of Mallik near-surface temperature logs, adopted in 2003, fall into the threshold of −6 °C to −7 °C, which is consistent with the near-surface temperatures as depicted in Figure 5.6d. The bottom part of Mallik's simulated near-surface temperature profile agrees with the observation at the Ignik Sikumi #1 measured during the summer-autumn of 2011 (Figure 5.6a) in Prudhoe Bay (Boswell et al., 2017). This agreement indicates that the arithmetic means of near-surface ground temperature at Prudhoe Bay was likely within the range of −9 °C to −10 °C since the Holocene, which is presumed to be slightly lower than the observed temperatures at the Mallik site in the early 1970s (Figure 5.6b). Figure 5.6a shows the depths of inflection points of logged temperature profiles from Mallik and Ignik Sikumi are 70 m and 80 m, respectively. The inflection point represents the propagation front of permafrost heating induced by contemporary climate warming. The deeper depths of the inflection points may be attributed to the field DTS survey being conducted at the Ignik Sikumi site almost eight years later than that performed at the Malik site.

The 10-meter deeper inflection point (Figure 5.6a) may indicate that the permafrost at Ignik Sikumi was heating faster than the Mallik permafrost, as a result of a stronger Arctic Amplification (AA) effect at the Ignik Sikumi site (Hunter et al., 2011) with 45' higher latitude than the Mallik site. From 1970 to 2006, the Arctic temperature anomaly increment was approximately 1.5 K (red dashed line, Figure 5.6c), while the observed regional ground temperature increment is 2 K in the MD, according to Burn and Kokelj (2009). This temperature increment difference is a consequence of the Arctic amplified warming (Chylek et al., 2022;

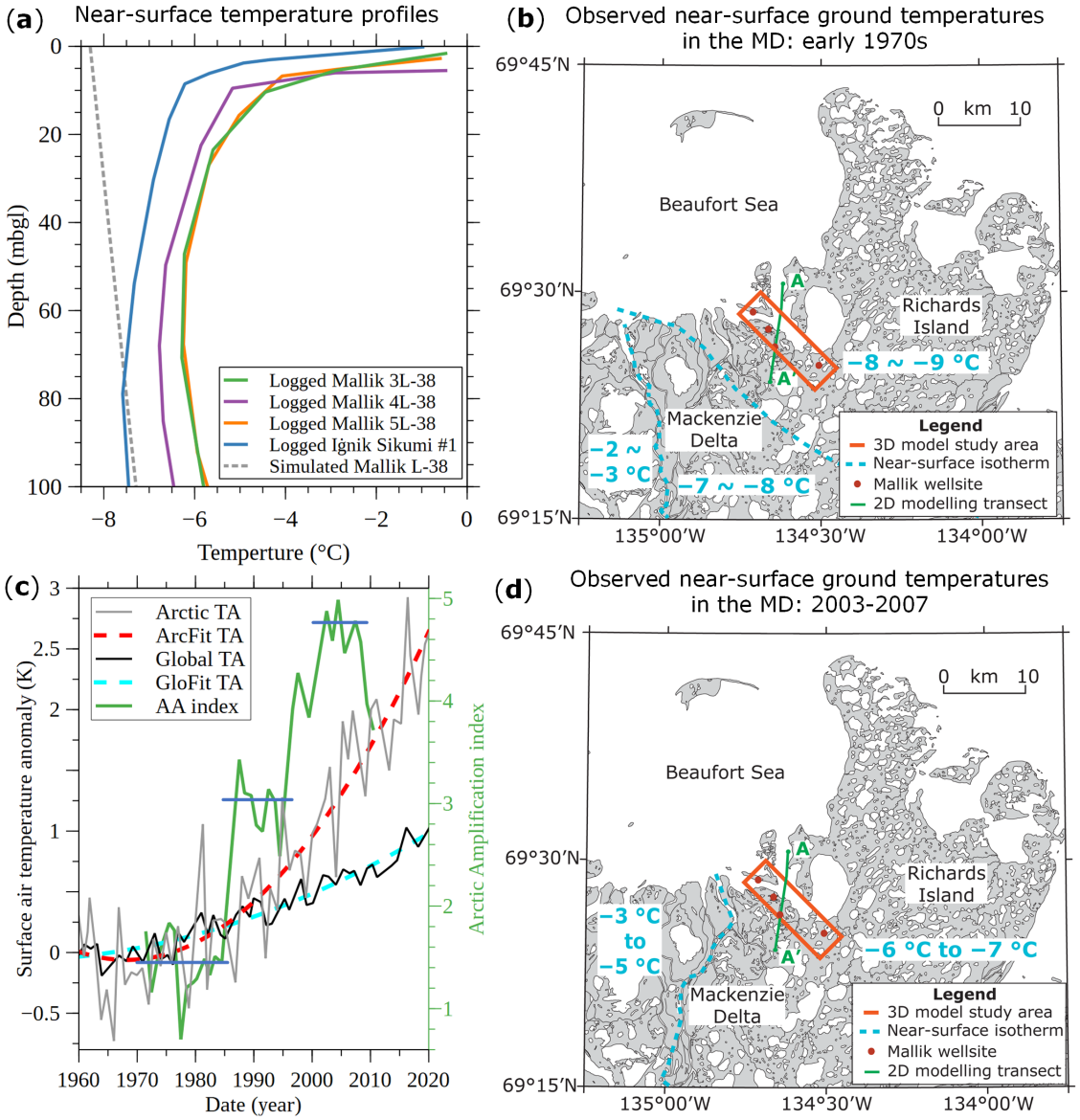

Figure 5.6: (**a**) Comparison between DTS-logged and simulated temperature profiles. The DTS-observation at the Mallik 3L-38, 4L-38, 5L-38, and Ignik Sikumi #1 wells are adopted from Henninges et al. (2005) and Boswell et al. (2017), respectively. The simulated near-surface temperature profile at the Mallik L-38 well is adopted from Li et al. (2022a). (**b**) Map of the near-surface ground temperatures in the MD, in which the representative ground temperature data was collected from hydrocarbon exploration wells developed in the early 1970s, modified after Dallimore et al. (2005b). (**c**) Temporal series of Arctic (grey) and global annual-mean subaerial temperature anomalies (black) relative to 1951–1980 mean (England et al., 2021) and their high-order approximations (dashed lines), and Arctic amplification (AA) index as well as its step-like approximants (blue horizontal lines) (Chylek et al., 2022). (**d**) Map of the near-surface ground temperatures measured between 2003 and 2007 in the MD, showing the locations of seismic reflection profiles as well as the Mallik 3D seismic survey (blue outline), used in the present study, adopted from Burn and Kokelj (2009). (**b**,**d**) The projections of previously numerically studied 2D transect (Li et al., 2022a) and 3D model domain outlined on the map, figures presented with permission from Natural Resources Canada under the Open Government License—Canada version 2.0.

England et al., 2021; Fang et al., 2022; Rantanen et al., 2022). It confirms that the area with higher latitudes suffers a more significant AA effect.

Arctic warming is inherently much more intensive than the global rate, as shown in Figure 5.6c. The amplified Arctic warming is very likely to be a consistent feature of climate change over a temporal range of millennium (Fang et al., 2022). The first

step-like approximant of the annual-mean AA index (green line) is approximately 1.5 during 1970–1985 (Chylek et al., 2022). The AA indices change in two sudden step-like increments, whose values exceed three and four during 1986–1999 and 2000–2010, respectively. Although the AA index increased significantly during 1970–2012, the ongoing and future AA index are likely to converge to the reconstructed millennial baseline (Fang et al., 2022). AA becomes weakened with decreasing temperature gradients between the subarctic and Arctic regions (Liang et al., 2022). From 2007 to 2020 (Figure 5.6c), the high-order approximations of Arctic annual-mean subaerial temperature anomaly increment was approximately 1.3 K. Therefore, the ground temperature at the Mallik site is likely to rise by approximately 2 K, reaching a range of −4 °C to −5 °C by 2021.

In addition, highly dynamic fluvial processes characterise deltas, and the changing climate will cause considerable evolution of the riverine environment. As reported by Vesakoski et al. (2017), MD experienced constant channel planform evolution at a highly varying rate from 1983 to 2013. Overall, permafrost in Arctic deltas is expected to experience major alterations due to climate change and increased human influence in the near future.

5.7 Prospect of Future Code Development and Studies

Numerical Investigation of the Genesis of Permafrost-GH System on the Alaska North Slope in Circum-Beaufort Region

Table 5.2 lists possible scenarios for the GH genesis in the circum-Beaufort coastal region (cf. Figure 5.5a). On the Alaska North Slope, GHs occur below the Eocene unconformity in the Prudhoe Bay and Kuparuk River areas, containing a mixture of deep-source thermogenic and shallow microbial gases (Collett, 1993). The thermogenic gas is probably composed of free gas and oil-associated dissolved gas that migrated along faults within the Eileen fault zone from deeper reservoirs into the shallow host sediments. After entering the host sediments, the supersaturated source gas may be directly converted to GH (Scenarios II and IV in Table 5.2) or concentrated in pre-existing structural/stratigraphic traps as gas deposits outside the GHSZ before being converted to GH deposits due to entering the GHSZ after permafrost thickness increasing (Scenario III). Dai et al. (2011) consider that the genesis of the GH deposit at Mount Elbert is due to either Scenario II or Scenario IV. According to the modified GHPS in Section 5.4, Scenario III requires a series of spatiotemporal prerequisite factors shown by Case I in Table 5.1. Behseresht and Bryant (2012) provided the first explanatory mode to predict S_h distribution under Scenario III, but it was only applied to explain the logging profiles from Mount Elbert GH stratigraphic test well. The model has not yet been validated by a field-scale simulation of the Mount Elbert site, unlike the validation of Scenario I in Chapter 3 and Chapter 4. Although the interpretation of geophysical observations presented in most recent studies (Behseresht and Bryant, 2012; Boswell et al., 2011; Winters et al., 2011) strengthens the possibility of Scenario III, the likelihood of Scenarios II and IV has not yet been excluded by any numerical investigations.

Current $T_{plus}H$ is capable of simulating Scenario IV when an interpreted geophysical observation-derived field-scale model is available. Scenarios II and IV can be studied by $T_{plus}H$-derived models in the future as $T_{plus}H$ has the potential to be extended to a multiphase flow simulator. To establish field-scale 3D static models of the ANS hydrate site for simulation studies, open-access geophysical data, such as the interpreted seismic data of the Mallik site, is required. The need for detailed data to improve the simulated result resolution of heterogeneous S_h distribution and GH thickness variation calls for further 3D seismic campaigns to be deployed

and exploration wells to be drilled for high-resolution downhole measurements. Generally, more detailed data acquisition can lead to the establishment of static models with finer resolution.

Numerical Simulation of Sub-Permafrost GHs Formation via Mixed Gases

At the well-studied circum-Beaufort GH sites, Mount Elbert, Mallik, and Taglu sub-permafrost GHs contain nearly 99.4% (Lorenson et al., 2011), 99.5% (Lorenson et al., 2005; Lorenson et al., 1999), and 99% (Dallimore and Collett, 1995) of CH_4 in their gas compositions, respectively. Simplification of the gas composition to pure CH_4 is practicable for these sites, but it is not appropriate for the sub-permafrost GHs in China due to the high fraction of non-CH_4 gases. In the northwest high-altitude region of China, the sub-permafrost GH deposits, such as the Juhugeng orefield in the Qilian Mountain, contain CH_4 contents ranging from 54% to 76% (Wang et al., 2014).

The current reservoir simulation codes, such as HydrateResSim (Moridis et al., 2005a) and SUGAR Toolbox (Kossel et al., 2013), are developed only for modeling hydrate formation via a single-component gas. They cannot simulate the formation of GHs via mixed hydrocarbon gases (Wang and Lau, 2020). Therefore, it is essential to improve the capability of the developed numerical framework ($T_{plus}H$) to forecast the formation of GHs beneath the Muli permafrost in Qilian Mountain (Zhang et al., 2019) from mixed hydrocarbon gases, such as ethane, propane, and butane. According to Zhang et al. (2019), the genesis mechanism of the sub-permafrost GH deposits in the Qilian Mountains is entirely distinct from the circum-Beaufort GH deposits. The Muli model deserves to be compared with the formation model of Siberian pan-Arctic GH deposits in future studies.

Chapter 6

Conclusions

Based on the verified modeling framework ($T_{plus}H$), the numerical models investigating the genesis of permafrost-GH system from laboratory to field scales were established and validated for the first time in this study. In Chapter 2, $T_{plus}H$ was verified by benchmarking its simulation results against the HRS modeled ones prior to calibrating the $T_{plus}H$-derived LARS model under the constraint condition of ERT-measured S_h distribution and temperature observations. The model was then validated due to the substantial agreement between the simulated and sampled $S_{h,bulk}$. Subsequently, a laboratory scale model was upscaled to a field-scale 2D model to validate the proposed permafrost-GH system genesis mechanism and timescale, as presented in Chapter 3. Finally, the field-scale 2D model of the Mallik site was extended to a 3D model in Chapter 4 to examine the impact of geologic controls on the spatial GH distribution. Overall, the findings of this work allow for the fulfillment of the above objectives in Section 1.2 and result in the following conclusions:

1. The equilibrium formation model for CH_4 hydrates used by $T_{plus}H$ is a practical alternative to kinetic approaches. The employed model can reasonably represent the multi-stage GH formation experiment in LARS, where the "dissolved-gas" method is employed.
2. An iterative optimization procedure minimized deviations between the simulation results and the observed temperature profiles as well as the ERT-derived $S_{h,bulk}$. After model calibration, the simulated $S_{h,bulk}$ matched the periodically sampled $S_{h,bulk}$ verifying ERT-measured spatial S_h distribution in LARS.
3. As supported by the consistency of simulated and sampled $S_{h,bulk}$, the validation of the $T_{plus}H$-derived LARS model confirmed the observation that no GH particles were transported out of the specimen by the out-flowing fluid in LARS. Additionally, the good agreement between the simulated and ERT-measured spatial S_h distribution could be explained by the assumption that GH particles were anchored in the pore space between sediment grains (in-situ accumulation) rather than flowing with fluid (off-site accumulation).
4. The laboratory-scale GH formation modeling approach applied for LARS can be upscaled to investigate the field-scale sub-permafrost hydrate formation and accumulation processes in water-dominated geological environments, such as the Mallik site.
5. Employing the upward migrating thermogenic CH_4 in a dissolved state as feed gas and the highly dipping faults as migration pathways resulted in a model consistent with field observations. Therefore, it proved the feasibility of the proposed sub-permafrost hydrate formation mechanism for the Mallik site.
6. The proposed timescale of 1.6 Ma (Collett, 1999) to allow for the permafrost-GH deposit genesis is viable. Furthermore, due to the diversity of sub-permafrost GH formation mechanisms, there is still a theoretical possibility for the generation of GH deposits via gaseous CH_4 in the relatively short geologic time within the duration of the Wisconsinan Glaciation (~75–11 kaBP). However, the present-day seismic observation and borehole evidence have not provided any solid support for this assumption because of the absence

of gaseous CH_4 within and directly below the GH-bearing sediment. Consequently, observations at the Mallik site are not consistent with the coexistence of gaseous CH_4, GH, and water within the GHSZ under Scenarios II and III, as discussed in Section 5.5. Thus indicating that Scenario I is the most credible assumption to date, as presented in Chapters 3 and 4.

7. The complex stratigraphic and structural controls on the heterogeneity of the GH distribution at the Mallik site have been quantitatively accessed. Since the Late Pleistocene, the major normal fault F1, serving as an active hydraulic conduit, permitted the upward migration of hydrate-forming gas in the dissolved state into the GHSZ within the reservoir sequences below the Mallik anticline crest. Meanwhile, the normal fault F2 acted as a hydrological conduit for lateral CH_4-rich fluid flow, but the normal fault F3 was as permeable as the sandy GH-bearing sediments. The normal (F7) and reverse faults (F4, F6) were most likely hydrological barriers.
8. The permafrost has been substantially heated by 0.8–1.3 °C, triggered by the global temperature increase of approximately 0.44 °C and further enhanced by the Arctic amplification effect at the Mallik site from the early 1970s to the mid-2000s.

In conclusion, the equilibrium GH formation approach utilized in this study is capable of characterizing the GH accumulation process across laboratory and field scales, as well as across timescales ranging from hours to millions of years. The heterogeneity of physical properties in subsurface geological elements, such as significant contrasts in hydraulic conductivity, makes 3D modeling essential for capturing the formation dynamics of GH deposits at the field scale. Furthermore, the spatial distribution of GHs in LARS was mainly influenced by its thermal boundary geometry within the sample chamber when $S_{h,bulk}$ was below 40%. To reproduce GH deposits observed in natural conditions, laboratory studies require a large-volume reactor to avoid boundary interference. In contrast to controlled laboratory environments, the spatial distribution of GHs in natural environments such as the Mallik site was influenced by multiple factors, including source-gas generation rate, subsurface temperature, permeability of GH host sediment, and hydraulic capability of geologic faults.

References

ASHFORD D., NUMASAWA M, MARTIN C., YAMAMOTO K., DALLIMORE S., WRIGHT J., NIXON F., APPLEJOHN A. and TAYLOR A. (2012): Overview of engineering and operations activities conducted as part of the JOGMEC/ NRCan/Aurora Mallik 2007–2008 Gas Hydrate Production Research Well Program, Part B: 2008 field program. *Scientific results from the JOGMEC/NRCan/Aurora Mallik 2007-2008 gas hydrate production research well program, Mackenzie Delta, Northwest Territories, Canada*. Geological Survey of Canada, Bulletin 601, 53–65. DOI: 10.4095/292082

BATTISTELLI A., CALORE C. and PRUESS K. (1997): The simulator TOUGH2/EWASG for modelling geothermal reservoirs with brines and non-condensible gas. *Geothermics* 26 (4), 437–464. DOI: 10.1016/S0375-6505(97)00007-2

BAUER K., HABERLAND C, PRATT R. G., HOU F, MEDIOLI B, E and WEBER M. H. (2005a): Ray-based cross-well tomography for P-wave velocity, anisotropy, and attenuation structure around the JAPEX/JNOC/GSC et al. Mallik 5L-38 gas hydrate production research well. *Scientific Results from the Mallik 2002 Gas Hydrate Production Research Well Program, Mackenzie Delta, Northwest Territories, Canada*. Vol. 585. Geological Survey of Canada, Bulletin 585, 21. DOI: 10.4095/220883

BAUER K., PRATT R. G., WEBER M. H., RYBERG T, HABERLAND C. and SHIMIZU S (2005b): Mallik 2002 cross-well seismic experiment: project design, data acquisition, and modelling studies. *Scientific Results from the Mallik 2002 Gas Hydrate Production Research Well Program, Mackenzie Delta, Northwest Territories, Canada*. Geological Survey of Canada, Bulletin 585, 14. DOI: 10.4095/220866

BEHAR F., VANDENBROUCKE M., TANG Y., MARQUIS F. and ESPITALIE J. (1997): Thermal cracking of kerogen in open and closed systems: determination of kinetic parameters and stoichiometric coefficients for oil and gas generation. *Org. Geochem.* 26 (5), 321–339. DOI: 10.1016/S0146-6380(97)00014-4

BEHSERESHT J. and BRYANT S. L. (2012): Sedimentological control on saturation distribution in Arctic gas-hydrate-bearing sands. *Earth Planet. Sci. Lett.* 341-344, 114–127. DOI: 10.1016/j.epsl.2012.06.019

BELLEFLEUR G, RIEDEL M, BRENT T, WRIGHT F and DALLIMORE S. R. (2007): Implication of seismic attenuation for gas hydrate resource characterization, Mallik, Mackenzie Delta, Canada. *J. Geophys. Res.* 112 (B10), B10311. DOI: 10.1029/2007JB004976

BELLEFLEUR G., RIEDEL M., HUANG J., SAEKI T.and Milkereit B., RAMACHANDRAN K. and BRENT T. (2012): Scientific results from the JOGMEC/NRCan/Aurora Mallik 2007–2008 gas hydrate production research well program, Mackenzie Delta, Northwest Territories, Canada. Vol. 601. Geological Survey of Canada, Bulletin 601, p. 107–123. DOI: 10.4095/292086

BELLEFLEUR G, RIEDEL M. and BRENT T (2006): Seismic characterization and continuity analysis of gas-hydrate horizons near Mallik research wells, Mackenzie Delta, Canada. *Lead. Edge* 25 (5). 599–604. DOI: 10.1190/1.2202663

BELLEFLEUR G., RIEDEL M., RAMACHANDRAN K., BRENT T. and DALLIMORE S. (2009): Recent advances in mapping deep permafrost and gas hydrate occurrences using industry seismic data, Richards Island area, Northwest Territories, Canada. *Proceedings of the Frontiers+ Innovation—2009 CSPG CSEG CWLS Convention, Calgary, AB, Canada*, Citeseer, 4–8.

BERBESI L., DI PRIMIO R., ANKA Z., HORSFIELD B. and WILKES H. (2014): Methane leakage from evolving petroleum systems: Masses, rates and inferences for climate feedback. *Earth Planet. Sci. Lett.* 387, 219–228. DOI: 10.1016/j.epsl.2013.11.014

BERGE L. I., JACOBSEN K. A. and SOLSTAD A. (1999): Measured acoustic wave velocities of R11 (CCl3F) hydrate samples with and without sand as a function of hydrate concentration. *J. Geophys. Res. solid earth* 104 (B7), 15415–15424. DOI: 10.1029/1999JB900098

BINTANJA R and WAL R. S. W. van de (2008): North American ice-sheet dynamics and the onset of 100,000-year glacial cycles. *Nature* 454 (7206), 869–872. DOI: 10.1038/nature07158

BISKABORN B. K., SMITH S. L., NOETZLI J., MATTHES H., VIEIRA G., STRELETSKIY D. A., SCHOENEICH P., ROMANOVSKY V. E., LEWKOWICZ A. G., ABRAMOV A., ALLARD M., BOIKE J., CABLE W. L., CHRISTIANSEN H. H., DELALOYE R., DIEKMANN B., DROZDOV D., ETZELMÜLLER B., GROSSE G., GUGLIELMIN M., INGEMAN-NIELSEN T., ISAKSEN K., ISHIKAWA M., JOHANSSON M., JOHANNSSON H., JOO A., KAVERIN D., KHOLODOV A., KONSTANTINOV P., KRÖGER T., LAMBIEL C., LANCKMAN J.-P., LUO D., MALKOVA G., MEIKLEJOHN I., MOSKALENKO N., OLIVA M., PHILLIPS M., RAMOS M., SANNEL A. B. K., SERGEEV D., SEYBOLD C., SKRYABIN P., VASILIEV A.,

WU Q., YOSHIKAWA K., ZHELEZNYAK M. and LANTUIT H. (2019): Permafrost is warming at a global scale. *Nat. Commun.* 10 (1), 264. DOI: 10.1038/s41467-018-08240-4

BLUNDEN J. and ARNDT D. S. (2017): State of the Climate in 2016. *Bull. Am. Meteorol. Soc.* 98 (8), Si–S280. DOI: 10.1175/2017BAMSStateoftheClimate.1

BOSWELL R. (2009): Is Gas Hydrate Energy Within Reach? *Science* 325 (5943), 957–958. DOI: 10.1126/science.1175074

BOSWELL R., HANCOCK S., YAMAMOTO K., COLLETT T., PRATAP M. and LEE S.-R. (2020): 6 - Natural Gas Hydrates: Status of Potential as an Energy Resource. *Future Energy*. Ed. by T. M. LETCHER. 3rd Ed. Elsevier, 111–131. DOI: 10.1016/B978-0-08-102886-5.00006-2

BOSWELL R., ROSE K., COLLETT T. S., LEE M., WINTERS W., LEWIS K. A. and AGENA W. (2011): Geologic controls on gas hydrate occurrence in the Mount Elbert prospect, Alaska North Slope. *Mar. Pet. Geol.* 28 (2), 589–607. DOI: 10.1016/j.marpetgeo.2009.12.004

BOSWELL R., SCHODERBEK D., COLLETT T. S., OHTSUKI S., WHITE M. and ANDERSON B. J. (2017): The Iġnik Sikumi Field Experiment, Alaska North Slope: Design, Operations, and Implications for CO2–CH4 Exchange in Gas Hydrate Reservoirs. *Energy Fuels* 31 (1), 140–153. DOI: 10.1021/acs.energyfuels.6b01909

BRENT T. A., RIEDEL M., CADDEL M., CLEMENT M., COLLETT T. S. and DALLIMORE S. R. (2005): Initial geophysical and geological assessment of an industry 3D seismic survey covering the JAPEX/JNOC/GSC Mallik 5L-38 gas hydrate research well. *Scientific Results from JAPEX/JNOC/GSC Mallik 5L-38 Gas Hydrate Research Well, Mackenzie Delta, Northwest Territories, Canada*. Ed. by S. R. DALLIMORE and T. S. COLLETT. Geological Survey of Canada, Bulletin 585. Ottawa: ARRAY(0x55aa16400708), 14.

BROSETA D., RUFFINE L. and DESMEDT A. (2017): *Gas Hydrates 1: Fundamentals, Characterization and Modeling*. Hoboken, NJ, USA: John Wiley & Sons.

BROWN J., FERRIANS JR. O., HEGINBOTTOM J. and MELNIKOV E. (2002): *Circum-Arctic map of permafrost and ground-ice conditions, Version 2*. ENGLISH. Tech. rep. Boulder, Colorado USA: NSIDC: National Snow and Ice Data Center. DOI: 10.7265/skbg-kf16

BURN C. R. and KOKELJ S. V. (2009): The environment and permafrost of the Mackenzie Delta area. *Permafr. Periglac. Process.* 20 (2), 83–105. DOI: 10.1002/ppp.655

CHABAB E. and KEMPKA T. (2023): 3D structural geological model of the Mallik Anticline, Canadian Arctic. DOI: 10.5880/GFZ.3.4.2023.001

CHANDRASEKHARAN NAIR V., MECH D., GUPTA P. and SANGWAI J. S. (2018): Polymer flooding in artificial hydrate bearing sediments for methane gas recovery. *Energy Fuels* 32 (6), 6657–6668. DOI: 10.1021/acs.energyfuels.8b00874

CHEN Z., DIETRICH J., LANE L. S., LI M. and DIXON J. (2021): Beaufort–Mackenzie Tectono-Sedimentary Element. *Geol. Soc. Lond. Mem.* 57. DOI: 10.1144/M57-2016-3

CHEN Z., OSADETZ K. G., ISSLER D. R. and GRASBY S. E. (2008): Hydrocarbon migration detected by regional temperature field variations, Beaufort-Mackenzie Basin, Canada. *AAPG Bull.* 92 (12), 1639–1653. DOI: 10.1306/07300808011

CHOI J.-H., DAI S., CHA J.-H. and SEOL Y. (2014): Laboratory formation of noncementing hydrates in sandy sediments. *Geochem. Geophys. Geosystems* 15 (4), 1648–1656. DOI: 10.1002/2014GC005287

CHONG L., SINGH H., CREASON C. G., SEOL Y. and MYSHAKIN E. M. (2022): Application of machine learning to characterize gas hydrate reservoirs in Mackenzie Delta (Canada) and on the Alaska north slope (USA). *Comput. Geosci.* 26 (5), 1151–1165. DOI: 10.1007/s10596-022-10151-9

CHONG Z. R., PUJAR G. A., YANG M. and LINGA P. (2016): Methane hydrate formation in excess water simulating marine locations and the impact of thermal stimulation on energy recovery. *Appl. Energy* 177, 409–421. DOI: 10.1016/j.apenergy.2016.05.077

CHUPENG Y., JIE L., RUI Y., YONGJIAN Y., XUEJIE L. and MING S. (2020): Accumulation model of natural gas hydrate in the Beaufort-Mackenzie Delta Basin, the Arctic. *Mar. Geol. Quat. Geol.* 40 (6), 146–158. DOI: 10.16562/j.cnki.0256-1492.2020052602

CHUVILIN E., BUKHANOV B., YURCHENKO A., DAVLETSHINA D., SHAKHOVA N., SPIVAK E., RUSAKOV V., DUDAREV O., KHAUSTOVA N., TIKHONOVA A., GUSTAFSSON O., TESI T., MARTENS J., JAKOBSSON M., SPASENNYKH M. and SEMILETOV I. (2022): In-situ temperatures and thermal properties of the East Siberian Arctic shelf sediments: Key input for understanding the dynamics of subsea permafrost. *Mar. Pet. Geol.* 138, 105550. DOI: 10.1016/j.marpetgeo.2022.105550

CHUVILIN E. M., YAKUSHEV V. S. and PERLOVA E. V. (2000): Gas and Possible Gas Hydrates in the Permafrost of Bovanenkovo Gas Field, Yamal Peninsula, West Siberia. *Polarforschung* 68, 215–219. DOI: 10013/epic.29809

CHYLEK P., FOLLAND C., KLETT J. D., WANG M., HENGARTNER N., LESINS G. and DUBEY M. K. (2022): Annual Mean Arctic Amplification 1970–2020: Observed and Simulated by CMIP6 Climate Models. *Geophys. Res. Lett.* 49 (13). e2022GL099371. DOI: 10.1029/2022GL099371

COHEN J., PFEIFFER K. and FRANCIS J. A. (2018): Warm Arctic episodes linked with increased frequency of extreme winter weather in the United States. *Nat. Commun.* 9 (1), 869. DOI: 10.1038/s41467-018-02992-9

COLLETT T. S. (1999): Seismic- and well-log-inferred gas hydrate accumulations on Richards Island. *Scientific results from JAPEX/JNOC/GSC Mallik 2L-38 gas hydrate research well, Mackenzie Delta, Northwest Territories, Canada*. Vol. 544. Geological Survey of Canada, Bulletin 544, 357–376.

COLLETT T. S. (May 1993): Natural Gas Hydrates of the Prudhoe Bay and Kuparuk River Area, North Slope, Alaska1. *AAPG Bull.* 77 (5), 793–812. DOI: 10.1306/BDFF8D62-1718-11D7-8645000102C1865D

COLLETT T. S., JOHNSON A. H., KNAPP C. C. and BOSWELL R. (2009): Natural Gas Hydrates: A Review. *Natural Gas Hydrates—Energy Resource Potential and Associated Geologic Hazards*. American Association of Petroleum Geologists. DOI: 10.1306/13201142M891602

COLWELL F. S., NUNOURA T, DELWICHE M. E., BOYD S, BOLTON R, REED D. W., TAKAI K, LEHMAN R. M., HORIKOSHI K, ELIAS D. A., PHELPS T and J (2005): Evidence of minimal methanogenic numbers and activity in sediments collected from the JAPEX/JNOC/GSC et al. Mallik 5L-38 gas hydrate research well. *Scientific Results from the Mallik 2002 Gas Hydrate Production Research Well Program, Mackenzie Delta, Northwest Territories, Canada*. Vol. 585. Geological Survey of Canada, Bulletin 585, 11. DOI: 10.4095/220787

CRAMER S. D. (1984): Solubility of methane in brines from 0 to 300.degree.C. *Ind. Eng. Chem. Process Des. Dev.* 23 (3), 533–538. DOI: 10.1021/i200026a021

CUI J., LI K., CHENG L., LI Q., SUN Z., XIAO P., LI X., CHEN G. and SUN C. (2021): Experimental investigation on the spatial differences of hydrate dissociation by depressurization in water-saturated methane hydrate reservoirs. *Fuel* 292, 120277. DOI: 10.1016/j.fuel.2021.120277

DAI J., XU H., SNYDER F. and DUTTA N. (2004): Detection and estimation of gas hydrates using rock physics and seismic inversion: Examples from the northern deepwater Gulf of Mexico. *Lead. Edge* 23 (1), 60–66. DOI: 10.1190/1.1645456

DAI S., LEE C. and CARLOS SANTAMARINA J. (2011): Formation history and physical properties of sediments from the Mount Elbert Gas Hydrate Stratigraphic Test Well, Alaska North Slope. *Mar. Pet. Geol.* 28 (2). 427–438. DOI: 10.1016/j.marpetgeo.2010.03.005

DALLIMORE S. R., COLLETT T and S (2005a): Scientific Results from the Mallik 2002 Gas Hydrate Production Research Well Program, Mackenzie Delta, Northwest Territories, Canada. *Scientific results from JAPEX/JNOC/GSC Mallik 2L-38 gas hydrate research well, Mackenzie Delta, Northwest Territories, Canada*. Canada: Geological Survey of Canada, Bulletin 585, 140. DOI: 10.4095/220702

DALLIMORE S. R. and COLLETT T. S. (1995): Intrapermafrost gas hydrates from a deep core hole in the Mackenzie Delta, Northwest Territories, Canada. *Geology* 23 (6), 527. DOI: 10.1130/0091-7613(1995)023<0527:IGHFAD>2.3.CO;2

DALLIMORE S. R. and COLLETT T. S. (1999): Regional gas hydrate occurrences, permafrost conditions, and Cenozoic geology, Mackenzie Delta area. *Scientific results from JAPEX/JNOC/GSC Mallik 2L-38 gas hydrate research well, Mackenzie Delta, Northwest Territories, Canada*. Vol. 544. Geological Survey of Canada, Bulletin 544, 357–376.

DALLIMORE S. R., UCHIDA T and COLLETT T. S. (1999): Scientific results from JAPEX/JNOC/GSC Mallik 2L-38 gas hydrate research well, Mackenzie Delta, Northwest Territories, Canada. English. Canada: Geological Survey of Canada, Bulletin 544, 403. DOI: 10.4095/210723

DALLIMORE S. R., COLLETT T and S (2005b): Summary and implications of the Mallik 2002 Gas Hydrate Production Research Well Program. *Scientific Results from the Mallik 2002 Gas Hydrate Production Research Well Program, Mackenzie Delta, Northwest Territories, Canada*. Vol. 585. Geological Survey of Canada, Bulletin 585, 36. DOI: 10.4095/220714

DALLIMORE S. R., YAMAMOTO K., WRIGHT J. F. and BELLEFLEUR G. (2012): Scientific results from the JOGMEC/NRCan/Aurora Mallik 2007–2008 gas hydrate production research well program, Mackenzie Delta, Northwest Territories, Canada. Vol. 601. Geological Survey of Canada, Bulletin 601, 291. DOI: 10.4095/291751

DAVY H. (1811): VIII. On a combination of oxymuriatic gas and oxygene gas. *Philos. Trans. Royal Soc.* 101, 155–162. DOI: 10.1098/rstl.1811.0008

DELLI M. L. and GROZIC J. L. (2013): Prediction Performance of Permeability Models in Gas-Hydrate-Bearing Sands. *SPE J.* 18 (02), 274–284. DOI: 10.2118/149508-PA

DIXON J D. J. R. and MCNEIL D. H. (1992): *Upper Cretaceous to Pleistocene sequence stratigraphy of the Beaufort-Mackenzie and Banks Island areas, Northwest Canada*. Tech. rep. Canada, 90. DOI: 10.4095/133237

DIXON J and DIETRICH J. R. (1988): The Nature of Depositional and Seismic Sequence Boundaries in Cretaceous-Tertiary Strata of the Beaufort-Mackenzie Basin. *Sequences, Stratigraphy, Sedimentology: Surface and Subsurface; Proceedings Of A Canadian Society Of Petroleum Geologists Technical Meeting*. Canadian Society of Petroleum Geologists, Memoir no. 15, p. 63–72.

DIXON J., LANE L., DIETRICH J., MCNEIL D. and CHEN Z. (2019): Chapter 17 – Geological History of the Late Cretaceous to Cenozoic Beaufort-Mackenzie Basin, Arctic Canada. *The Sedimentary Basins of the United States and Canada*. Ed. by A. D. MIALL. 2nd. Elsevier, 695–717. DOI: 10.1016/B978-0-444-63895-3.00017-6

DONG H., SUN J., LIN Z., FANG H., LI Y., CUI L. and YAN W. (2018): 3D pore-type digital rock modeling of natural gas hydrate for permafrost and numerical simulation of electrical properties. *J. Geophys. Eng.* 15 (1), 275–285. DOI: 10.1088/1742-2140/aa8a8e

EGEBERG P. K. and DICKENS G. R. (1999): Thermodynamic and pore water halogen constraints on gas hydrate distribution at ODP Site 997 (Blake Ridge). *Chem. Geol.* 153 (1-4), 53–79. DOI: 10.1016/S0009-2541(98)00152-1

ENGLAND M. R., EISENMAN I., LUTSKO N. J. and WAGNER T. J. W. (2021): The Recent Emergence of Arctic Amplification. *Geophys. Res. Lett.* 48 (15). e2021GL094086. DOI: 10.1029/2021GL094086

FANG M., LI X., CHEN H. W. and CHEN D. (2022): Arctic amplification modulated by Atlantic Multidecadal Oscillation and greenhouse forcing on multidecadal to century scales. *Nat. Commun.* 13 (1), 1865. DOI: 10.1038/s41467-022-29523-x

FANG Y., LU J., LIANG J., KUANG Z., CAO Y. and CHEN D. (2019): Numerical studies of gas hydrate evolution time in Shenhu area in the northern South China Sea. *China Geol.* 2 (1), 49–55. DOI: 10.31035/cg2018054

FENG J.-C., LI B., LI X.-S. and WANG Y. (2021): Effects of depressurizing rate on methane hydrate dissociation within large-scale experimental simulator. *Appl. Energy* 304, 117750. DOI: 10.1016/j.apenergy.2021.117750

FITZGERALD G. C., CASTALDI M. J. and SCHICKS J. M. (2014): Methane Hydrate Formation and Thermal Based Dissociation Behavior in Silica Glass Bead Porous Media. *Ind. amp; Eng. Chem. Res.* 53 (16), 6840–6854. DOI: 10.1021/ie4036737

FITZGERALD G. C., CASTALDI M. J. and ZHOU Y. (2012): Large scale reactor details and results for the formation and decomposition of methane hydrates via thermal stimulation dissociation. *J. Pet. Sci.* 94-95, 19–27. DOI: 10.1016/j.petrol.2012.06.018

FORBES D., CRAYMER M., JAMES T. and WHALEN D. (2022): Subsidence drives habitat loss in a large permafrost delta, Mackenzie River outlet to the Beaufort Sea, western Arctic Canada. *Can. J. Earth Sci.* 59 (11), 914–934. DOI: 10.1139/cjes-2021-0127

FREDERICK J. M. and BUFFETT B. A. (2014): Taliks in relict submarine permafrost and methane hydrate deposits: Pathways for gas escape under present and future conditions. *J. Geophys. Res. Earth Surf.* 119 (2), 106–122. DOI: 10.1002/2013JF002987

FREDERICK J. M. and BUFFETT B. A. (2015): Effects of submarine groundwater discharge on the present-day extent of relict submarine permafrost and gas hydrate stability on the Beaufort Sea continental shelf. *J. Geophys. Res. Earth Surf.* 120 (3), 417–432. DOI: 10.1002/2014JF003349

FREDERICK J. M. and BUFFETT B. A. (2016): Submarine groundwater discharge as a possible formation mechanism for permafrost-associated gas hydrate on the circum-Arctic continental shelf. *J. Geophys. Res. Solid Earth* 121 (3), 1383–1404. DOI: 10.1002/2015JB012627

FRIEDLINGSTEIN P., JONES M. W., O'SULLIVAN M., ANDREW R. M., BAKKER D. C. E., HAUCK J., LE QUÉRÉ C., PETERS G. P., PETERS W., PONGRATZ J., SITCH S., CANADELL J. G., CIAIS P., JACKSON R. B., ALIN S. R., ANTHONI P., BATES N. R., BECKER M., BELLOUIN N., BOPP L., CHAU T. T. T., CHEVALLIER F., CHINI L. P., CRONIN M., CURRIE K. I., DECHARME B., DJEUTCHOUANG L. M., DOU X., EVANS W., FEELY R. A., FENG L., GASSER T., GILFILLAN D., GKRITZALIS T., GRASSI G., GREGOR L., GRUBER N., GÜRSES O., HARRIS I., HOUGHTON R. A.,

Hurtt G. C., Iida Y., Ilyina T., Luijkx I. T., Jain A., Jones S. D., Kato E., Kennedy D., Klein Goldewijk K., Knauer J., Korsbakken J. I., Körtzinger A., Landschützer P., Lauvset S. K., Lefèvre N., Lienert S., Liu J., Marland G., McGuire P. C., Melton J. R., Munro D. R., Nabel J. E. M. S., Nakaoka S.-I., Niwa Y., Ono T., Pierrot D., Poulter B., Rehder G., Resplandy L., Robertson E., Rödenbeck C., Rosan T. M., Schwinger J., Schwingshackl C., Séférian R., Sutton A. J., Sweeney C., Tanhua T., Tans P. P., Tian H., Tilbrook B., Tubiello F., Werf G. R. van der, Vuichard N., Wada C., Wanninkhof R., Watson A. J., Willis D., Wiltshire A. J., Yuan W., Yue C., Yue X., Zaehle S. and Zeng J. (2022): Global Carbon Budget 2021. *Earth Syst. Sci. Data* 14 (4), 1917–2005. DOI: 10.5194/essd-14-1917-2022

Gambelli A. M., Castellani B., Nicolini A. and Rossi F. (2019): Experimental study on natural gas hydrate exploitation: Optimization of methane recovery, carbon dioxide storage and deposit structure preservation. *J. Pet. Sci. Eng.* 177, 594–601. DOI: 10.1016/j.petrol.2019.02.088

Gamwo I. K. and Liu Y. (2010): Mathematical Modeling and Numerical Simulation of Methane Production in a Hydrate Reservoir. *Ind. Eng. Chem. Res.* 49 (11), 5231–5245. DOI: 10.1021/ie901452v

GEO-SLOPE International Ltd. (2014): *Thermal modeling with TEMP/W*. Tech. rep.

Gil S.-M., Shin H.-J., Lim J.-S. and Lee J. (2019): Numerical Analysis of Dissociation Behavior at Critical Gas Hydrate Saturation Using Depressurization Method. *J. Geophys. Res. Earth Surf.* 124 (2), 1222–1235. DOI: 10.1029/2018JB015847

Gongzheng Ma; Hailong L. J. L. G. H. Y. G. (2020): Polygonal fault in marine sediments and its impact on gas hydrate occurrence. *Geol. China* 47 (1), 1–13. DOI: 10.12029/gc20200101

GRID-Arendal (2020): Coastal and Offshore Permafrost in a Changing Arctic. In: Rapid Response Assessment of Coastal and Offshore Permafrost, Story Map. Accessed: 2023-02-17. URL: https://storymaps.arcgis.com/stories/c163de04de7849cdb917fee88015dd73.

Gudmundsson J.-S. and Thráinsson H. (1989): Power potential of two-phase geothermal wells. *Geothermics* 18 (3), 357–366. DOI: 10.1016/0375-6505(89)90062-X

Gupta A., Lachance J., Sloan Jr E. and Koh C. A. (2008): Measurements of methane hydrate heat of dissociation using high pressure differential scanning calorimetry. *Chem. Eng. Sci.* 63 (24), 5848–5853. DOI: 10.1016/j.ces.2008.09.002

Gwiazda R., Paull C. K., Dallimore S. R., Melling H., Jin Y. K., Hong J. K., Riedel M., Lundsten E., Anderson K. and Conway K. (2018): Freshwater Seepage Into Sediments of the Shelf, Shelf Edge, and Continental Slope of the Canadian Beaufort Sea. *Geochem. Geophys. Geosystems* 19 (9), 3039–3055. DOI: 10.1029/2018GC007623

Handa Y. P. and Stupin D. Y. (1992): Thermodynamic properties and dissociation characteristics of methane and propane hydrates in 70-.ANG.-radius silica gel pores. *J. Phys. Chem.* 96 (21), 8599–8603. DOI: 10.1021/j100200a071

Hansen J., Sato M., Russell G. and Kharecha P. (2013): Climate sensitivity, sea level and atmospheric carbon dioxide. *Philos. Trans. R. Soc. A* 371 (2001), 20120294. DOI: 10.1098/rsta.2012.0294

Hartmann J., West A. J., Renforth P., Köhler P., De La Rocha C. L., Wolf-Gladrow D. A., Dürr H. H. and Scheffran J. (2013): Enhanced chemical weathering as a geoengineering strategy to reduce atmospheric carbon dioxide, supply nutrients, and mitigate ocean acidification. *Rev. Geophys.* 51 (2), 113–149. DOI: 10.1002/rog.20004

Hassanpouryouzband A., Joonaki E., Vasheghani Farahani M., Takeya S., Ruppel C., Yang J., English N. J., Schicks J. M., Edlmann K., Mehrabian H., Aman Z. M. and Tohidi B. (2020): Gas hydrates in sustainable chemistry. *Chem. Soc. Rev.* 49 (15) (15), 5225–5309. DOI: 10.1039/C8CS00989A

Heeschen K. U., Abendroth S., Priegnitz M., Spangenberg E., Thaler J. and Schicks J. M. (2016): Gas Production from Methane Hydrate: A Laboratory Simulation of the Multistage Depressurization Test in Mallik, Northwest Territories, Canada. *Energy Fuels* 30 (8), 6210–6219. DOI: 10.1021/acs.energyfuels.6b00297

Heeschen K. U., Deusner C., Spangenberg E., Priegnitz M., Kossel E., Strauch B., Bigalke N., Luzi-Helbing M., Haeckel M. and Schicks J. M. (2021): Production Method under Surveillance: Laboratory Pilot-Scale Simulation of CH4–CO2 Exchange in a Natural Gas Hydrate Reservoir. *Energy Fuels* 35 (13), 10641–10658. DOI: 10.1021/acs.energyfuels.0c03353

Heeschen K. U., Janocha J., Spangenberg E., Schicks J. M. and Giese R. (2020): The impact of ice on the tensile strength of unconsolidated sand - A model for gas hydrate-bearing sands? *Mar. Pet. Geol.* 122, 104607. DOI: 10.1016/j.marpetgeo.2020.104607

HELWIG J., KUMAR N., EMMET P. and DINKELMAN M. G. (2011): Chapter 35 Regional seismic interpretation of crustal framework, Canadian Arctic passive margin, Beaufort Sea, with comments on petroleum potential. *Geol. Soc. Lond. Mem.* 35 (1), 527–543. DOI: 10.1144/M35.35

HENNINGES J. (2005): Thermal Properties of Gas-Hydrate-Bearing Sediments and Effects of Phase Transitions on the Transport of Heat Deduced from Temperature Logging at Mallik, NWT, Canada. Doctoral Thesis. Berlin: Technische Universität Berlin, ehemalige Fakultät VI - Bauingenieurwesen und Angewandte Geowissenschaften. DOI: 10.14279/depositonce-1204

HENNINGES J., SCHRÖTTER J., ERBAS K. and HUENGES E. (2005): Temperature field of the Mallik gas hydrate occurrence – implications on phase changes and thermal properties. *Scientific Results from the Mallik 2002 Gas Hydrate Production Research Well Program, Mackenzie Delta, Northwest Territories, Canada*. Geological Survey of Canada, Bulletin 585, 14. DOI: 10.4095/220890

HILLMAN J. I. T., CRUTCHLEY G. J. and KROEGER K. F. (2020): Investigating the role of faults in fluid migration and gas hydrate formation along the southern Hikurangi Margin, New Zealand. *Mar. Geophys. Res.* 41 (1), 8. DOI: 10.1007/s11001-020-09400-2

HODSON A. J., NOWAK A., HORNUM M. T., SENGER K., REDEKER K., CHRISTIANSEN H. H., JESSEN S., BETLEM P., THORNTON S. F., TURCHYN A. V., OLAUSSEN S. and MARCA A. (2020): Sub-permafrost methane seepage from open-system pingos in Svalbard. *Cryosphere* 14 (11), 3829–3842. DOI: 10.5194/tc-14-3829-2020

HOEGH-GULDBERG O., JACOB D., TAYLOR M., BOLAÑOS T. G., BINDI M., BROWN S., CAMILLONI I. A., DIEDHIOU A., DJALANTE R., EBI K., ENGELBRECHT F., GUIOT J., HIJIOKA Y., MEHROTRA S., HOPE C. W., PAYNE A. J., PÖRTNER H.-O., SENEVIRATNE S. I., THOMAS A., WARREN R. and ZHOU G. (2019): The human imperative of stabilizing global climate change at 1.5 °C. *Science* 365 (6459), eaaw6974. DOI: 10.1126/science.aaw6974

HOUSEKNECHT D. W. and BIRD K. J. (2011): Geology and petroleum potential of the rifted margins of the Canada Basin. *Geol. Soc. Mem.* (35), 509–526. DOI: 10.1144/M35.34

HOUSEKNECHT D. W., BIRD K. J., GARRITY C. P. and SURVEY U. S. G. (2020): Geology and assessment of undiscovered oil and gas resources of the Amerasia Basin Province, 2008. *The 2008 Circum-Arctic Resource Appraisal*. Ed. by T. E. MOORE and D. L. GAUTIER. U.S. Geological Survey Professional Paper 1824, 33p. DOI: 10.3133/pp1824BB

HU K., DIETRICH J., CHEN Z. and HANNIGAN P. (2018): *Petrophysical analyses of hydrocarbon reservoirs and overpressure zones in Tertiary deep-marine strata in the northern Beaufort-Mackenzie Basin, Arctic Canada*. Tech. rep. DOI: 10.4095/306960

HU X., GUAN J., WANG Y., KEATING A. and YANG S. (2017): Comparison of boundary and size effect models based on new developments. *Eng. Fract. Mech.* 175, 146–167. DOI: 10.1016/j.engfracmech.2017.02.005

HUANG D., FAN S., LIANG D. and FENG Z. (2005): Gas Hydrate Formation and Its Thermal Conductivity Measurement. *Chin. J. Geophys.* 48 (5), 1201–1207. DOI: 10.1002/cjg2.765

HUANG J.-W. (January 2009): Seismic imaging of gas hydrate reservoir heterogeneities. Ph.D. thesis, University of Toronto, Canada.

HUANG J.-W., BELLEFLEUR G. and MILKEREIT B. (2009): Seismic modeling of multidimensional heterogeneity scales of Mallik gas hydrate reservoirs, Northwest Territories of Canada. *J. Geophys. Res.* 114 (B7), B07306. DOI: 10.1029/2008JB006172

HUNTER R. B., COLLETT T. S., BOSWELL R., ANDERSON B. J., DIGERT S. A., POSPISIL G., BAKER R. and WEEKS M. (2011): Mount Elbert Gas Hydrate Stratigraphic Test Well, Alaska North Slope: Overview of scientific and technical program. *Mar. Pet. Geol.* 28 (2), 295–310. DOI: 10.1016/j.marpetgeo.2010.02.015

HYNDMAN R., CASSIDY J., ADAMS J, ROGERS G. and MAZZOTTI S (2005): Earthquakes and seismic hazard in the Yukon-Beaufort-Mackenzie. *CSEG Recorder* 5, 32–66.

IPCC (2022): *Climate Change 2022: Impacts, Adaptation and Vulnerability*. Summary for Policymakers. Cambridge, UK and New York, USA: Cambridge University Press, 3–33. DOI: 10.1017/9781009325844.001

IRRGANG A. M., BENDIXEN M., FARQUHARSON L. M., BARANSKAYA A. V., ERIKSON L. H., GIBBS A. E., OGORODOV S. A., OVERDUIN P. P., LANTUIT H., GRIGORIEV M. N. and JONES B. M. (2022): Drivers, dynamics and impacts of changing Arctic coasts. *Nat. Rev. Earth Environ.* 3 (1), 39–54. DOI: 10.1038/s43017-021-00232-1

JAIN V., SAUMYA S., VIJ J., SINGH J., SINGH B., PATTNAIK S., OLI A., KUMAR P. and COLLETT T. S. (2019): New technique for accurate porosity estimation from logging-while-drilling nuclear magnetic resonance data, NGHP-02 expedition, offshore, India. *Mar. Pet. Geol.* 108. 570–580. DOI: 10.1016/j.marpetgeo.2018.11.001

JANG J., WAITE W. F. and STERN L. A. (2020): Gas hydrate petroleum systems: What constitutes the "seal"? *Interpretation* 8 (2), T231–T248. DOI: 10.1190/INT-2019-0026.1

JENNER K., DALLIMORE S., CLARK I., PARÉ D. and MEDIOLI B. (1999): Sedimentology of gas hydrate host strata from the JAPEX/JNOC/GSC Mallik 2L-38 gas hydrate research well. *Scientific results from JAPEX/JNOC/GSC Mallik 2L-38 gas hydrate research well, Mackenzie Delta, Northwest Territories, Canada*. Vol. 544. Geological Survey of Canada, Bulletin 544, p. 57–68. DOI: 10.4095/210748

JOHNSON J. E., MACLEOD D. R., PHILLIPS S. C., PHILLIPS M. P. and DIVINS D. L. (2022): Primary deposition and early diagenetic effects on the high saturation accumulation of gas hydrate in a silt dominated reservoir in the Gulf of Mexico. *Mar. Geol.* 444, 106718. DOI: 10.1016/j.margeo.2021.106718

JUDGE A. S., TAYLOR A. E., BURGESS M and ALLEN V. S. (1981): *Canadian geothermal data collection: northern wells, 1978-80*. Tech. rep., 190. DOI: 10.4095/8275

KAMATH V. A. (1984): Study of heat transfer characteristics during dissociation of gas hydrates in porous media. Doctoral Thesis. PA (USA): University of Pittsburgh.

KASHCHIEV D. and FIROOZABADI A. (2002): Driving force for crystallization of gas hydrates. *J. Cryst. Growth* 241 (1-2), 220–230. DOI: 10.1016/S0022-0248(02)01134-X

KATSUBE T. J., DALLIMORE S. R., JONASSON I. R., CONNELL-MADORE S, MEDIOLI B. E., UCHIDA T, WRIGHT J. F. and SCROMEDA N (2005): Petrophysical characteristics of gas-hydrate-bearing and gas-hydrate-free formations in the JAPEX/JNOC/GSC et al. Mallik 5L-38 gas hydrate production research well. *Scientific Results from the Mallik 2002 Gas Hydrate Production Research Well Program, Mackenzie Delta, Northwest Territories, Canada*. Vol. 585. Geological Survey of Canada, Bulletin 585, 14. DOI: 10.4095/220729

KELL G. S. (1975): Density, thermal expansivity, and compressibility of liquid water from 0.deg. to 150.deg.. Correlations and tables for atmospheric pressure and saturation reviewed and expressed on 1968 temperature scale. *J. Phys. Chem. Ref. Data* 20 (1), 97–105. DOI: 10.1021/je60064a005

KEMPKA T., STEDING S. and KÜHN M. (2022): Verification of TRANSPORT Simulation Environment coupling with PHREEQC for reactive transport modelling. *Adv. Geosci.* 58, 19–29. DOI: 10.5194/adgeo-58-19-2022

KEMPKA T. (2020): Verification of a Python-based TRANsport Simulation Environment for density-driven fluid flow and coupled transport of heat and chemical species. *Adv. Geosci.* 54, 67–77. DOI: 10.5194/adgeo-54-67-2020

KIM S., LEE K., LEE M. and AHN T. (2020a): Data-Driven Three-Phase Saturation Identification from X-ray CT Images with Critical Gas Hydrate Saturation. *Energies* 13 (21). DOI: 10.3390/en13215844

KIM Y.-G., KIM S., LEE D.-H., LEE Y. M., KIM H. J., KANG S.-G. and JIN Y. K. (2020b): Occurrence of active gas hydrate mounds in the southwestern slope of the Chukchi Plateau, Arctic Ocean. eng. *Episodes* 43 (2), 811–823. DOI: 10.18814/epiiugs/2020/020053

KLEINBERG R. L., FLAUM C, GRIFFIN D. D., BREWER P. G., MALBY G. E., PELTZER E. T. and YESINOWSKI J. P. (2003): Deep sea NMR: Methane hydrate growth habit in porous media and its relationship to hydraulic permeability, deposit accumulation, and submarine slope stability. *J. Geophys. Res. Solid Earth* 108 (B10). DOI: 10.1029/2003JB002389

KOH C. A., SUM A. K. and SLOAN E. D. (2009): Gas hydrates: Unlocking the energy from icy cages. *J. Appl. Phys.* 106 (6), 061101. DOI: 10.1063/1.3216463

KONO H. O., NARASIMHAN S., SONG F. and SMITH D. H. (2002): Synthesis of methane gas hydrate in porous sediments and its dissociation by depressurizing. *Powder Technol.* 122 (2-3), 239–246. DOI: 10.1016/S0032-5910(01)00420-X

KOSSEL E., BIGALKE N., PIÑERO E. and HAECKEL M. (2013): The SUGAR Toolbox - A library of numerical algorithms and data for modelling of gas hydrate systems and marine environments. Bremerhaven. DOI: 10013/epic.41749.d002

KOWALSKY M. B. and MORIDIS G. J. (2007): Comparison of kinetic and equilibrium reaction models in simulating gas hydrate behavior in porous media. *Energy Convers. Manag.* 48 (6), 1850–1863. DOI: 10.1016/j.enconman.2007.01.017

KRETSCHMER K., BIASTOCH A., RÜPKE L. and BURWICZ E. (2015): Modeling the fate of methane hydrates under global warming. *Glob. Biogeochem.* 29 (5), 610–625. DOI: 10.1002/2014GB005011

KRISTOFFERSEN Y., HALL J. K. and NILSEN E. H. (2022): Sediment deformation atop the Lomonosov Ridge, central Arctic Ocean: Evidence for gas-charged sediment mobilization? *Mar. Pet. Geol.* 138, 105555. DOI: 10.1016/j.marpetgeo.2022.105555

KROEGER K. F. and FUNNELL R. H. (2012): Warm Eocene climate enhanced petroleum generation from Cretaceous source rocks: A potential climate feedback mechanism? *Geophys. Res. Lett.* 39 (4). DOI: 10.1029/2011GL050345

KROEGER K. F., ONDRAK R., PRIMIO R. di and HORSFIELD B. (2008): A three-dimensional insight into the Mackenzie Basin (Canada): Implications for the thermal history and hydrocarbon generation potential of Tertiary deltaic sequences. *AAPG Bull.* 92 (2), 225–247. DOI: 10.1306/10110707027

KROEGER K. F., PRIMIO R. di and HORSFIELD B. (2009): Hydrocarbon flow modeling in complex structures (Mackenzie Basin, Canada). *AAPG Bull.* 93 (9), 1209–1234. DOI: 10.1306/05220908141

KVENVOLDEN K. A., GINSBURG G. D. and SOLOVIEV V. A. (1993): Worldwide distribution of subaquatic gas hydrates. *Geo-Mar. Lett.* 13 (1), 32–40. DOI: 10.1007/BF01204390

LANE L. S. (2002): Tectonic evolution of the Canadian Beaufort Sea–Mackenzie Delta region: a brief review. *CSEG Recorder* 27 (2), 49–56.

LEI D., FU C., ZHEN Q., WANG Z. and WANG R. (2022a): The lithological characteristics of natural gas hydrates in permafrost on the Qinghai of China. *Sci. Rep.* 12 (1), 13277. DOI: 10.1038/s41598-022-17475-7

LEI L., PARK T., JARVIS K., PAN L., TEPECIK I., ZHAO Y., GE Z., CHOI J.-H., GAI X., GALINDO-TORRES S. A., BOSWELL R., DAI S. and SEOL Y. (2022b): Pore-scale observations of natural hydrate-bearing sediments via pressure core sub-coring and micro-CT scanning. *Sci. Rep.* 12 (1), 3471. DOI: 10.1038/s41598-022-07184-6

LEI L., SEOL Y., CHOI J.-H. and KNEAFSEY T. J. (2019a): Pore habit of methane hydrate and its evolution in sediment matrix – Laboratory visualization with phase-contrast micro-CT. *Mar. Pet. Geol.* 104, 451–467. DOI: 10.1016/j.marpetgeo.2019.04.004

LEI L., SEOL Y. and MYSHAKIN E. M. (2019b): Methane Hydrate Film Thickening in Porous Media. *Geophys. Res. Lett.* 46 (20), 11091–11099. DOI: 10.1029/2019GL084450

LEVELL B., ARGENT J., DORÉ A. G. and FRASER S. (2010): Passive margins: overview. *Geol. Soc. London, Pet. Geol. Conf. Ser.* 7 (1), 823–830. DOI: 10.1144/0070823

LI G., WU D., LI X., ZHANG Y., LV Q. and WANG Y. (2017): Experimental Investigation into the Production Behavior of Methane Hydrate under Methanol Injection in Quartz Sand. *Energy Fuels* 31 (5), 5411–5418. DOI: 10.1021/acs.energyfuels.7b00464

LI Z., SPANGENBERG E., SCHICKS J. M. and KEMPKA T. (2022a): Numerical Simulation of Coastal Sub-Permafrost Gas Hydrate Formation in the Mackenzie Delta, Canadian Arctic. *Energies* 15 (14), 4986. DOI: 10.3390/en15144986

LI Z., SPANGENBERG E., SCHICKS J. M. and KEMPKA T. (2022b): Numerical Simulation of Hydrate Formation in the LArge-Scale Reservoir Simulator (LARS). *Energies* 15 (6), 1974. DOI: 10.3390/en15061974

LIANG Y.-C., POLVANI L. M. and MITEVSKI I. (2022): Arctic amplification, and its seasonal migration, over a wide range of abrupt CO2 forcing. *npj Clim. Atmos. Sci.* 5 (1), 14. DOI: 10.1038/s41612-022-00228-8

LIN B., ZHOU L., LV G. and ZHU A.-X. (2017): 3D geological modelling based on 2D geological map. *Ann. GIS* 23 (2), 117–129. DOI: 10.1080/19475683.2017.1304450

LORENSON T. D., WHITICAR M. J., COLLETT T. S., DALLIMORE S. R. and DOUGHERTY J. A. (2005): Complete gas composition and isotopic geochemistry from the JAPEX/JNOC/GSC et al. Mallik 5L-38 gas hydrate production research well: cuttings, core, gas hydrate, and production testing results. *Scientific Results from the Mallik 2002 Gas Hydrate Production Research Well Program, Mackenzie Delta, Northwest Territories, Canada*. Vol. 585. Geological Survey of Canada, Bulletin 585, 19. DOI: 10.4095/220744

LORENSON T. D., WHITICAR M. J., WASEDA A, DALLIMORE S. R. and COLLETT T. S. (1999): Gas composition and isotopic geochemistry of cuttings, core, and gas hydrate from the JAPEX/JNOC/GSC Mallik 2L-38 gas hydrate research well. *Scientific results from JAPEX/JNOC/GSC Mallik 2L-38 gas hydrate research well, Mackenzie Delta, Northwest Territories, Canada*. Geological Survey of Canada, Bulletin 544, 143–164.

LORENSON T. D., COLLETT T. S. and HUNTER R. B. (2011): Gas geochemistry of the Mount Elbert Gas Hydrate Stratigraphic Test Well, Alaska North Slope: Implications for gas hydrate exploration in the Arctic. *Mar. Pet. Geol.* 28 (2). 343–360. DOI: 10.1016/j.marpetgeo.2010.02.007

LUNARDINI V. J. (1988): *Freezing of soil with an unfrozen water content and variable thermal properties*. Tech. rep. Cold Regions Research, Engineering Laboratory (U.S.); Engineer Research and Development Center (U.S.), 88–2. URL: https://hdl.handle.net/11681/9076.

MACKAY M. E., JARRARD R. D., WESTBROOK G. K. and HYNDMAN R. D. (1994): Origin of bottom-simulating reflectors: Geophysical evidence from the Cascadia accretionary prism. *Geology* 22 (5), 459–462. DOI: 10.1130/0091-7613(1994)022<0459:OOBSRG>2.3.CO;2

MAJOROWICZ J., SAFANDA J. and OSADETZ K. (2012a): Inferred gas hydrate and permafrost stability history models linked to climate change in the Beaufort-Mackenzie Basin, Arctic Canada. *Clim. Past* 8 (2), 667–682. DOI: 10.5194/cp-8-667-2012

MAJOROWICZ J. A., JONES F. W. and JUDGE A. S. (1990): Deep subpermafrost thermal regime in the Mackenzie Delta basin, northern Canada—Analysis from petroleum bottom-hole temperature data. *Geophysics* 55 (3), 362–371. DOI: 10.1190/1.1442844

MAJOROWICZ J., OSADETZ K. and SAFANDA J. (2012b): Gas Hydrate Formation and Dissipation Histories in the Northern Margin of Canada: Beaufort-Mackenzie and the Sverdrup Basins. *J. Geol. Res.* 2012, 1–17. DOI: 10.1155/2012/879393

MAJOROWICZ J., OSADETZ K. and SAFANDA J. (2015): Models of Talik, Permafrost and Gas Hydrate Histories–Beaufort Mackenzie Basin, Canada. *Energies* 8 (7), 6738–6764. DOI: 10.3390/en8076738

MAJOROWICZ J. and SMITH S. (1999): Review of ground temperatures in the Mallik field area: a constraint to the methane hydrate stability. *Scientific results from JAPEX/JNOC/GSC Mallik 2L-38 gas hydrate research well, Mackenzie Delta, Northwest Territories, Canada*. Geological Survey of Canada, Bulletin 544, 45–56.

MAKOGON Y., HOLDITCH S. and MAKOGON T. (2007): Natural gas-hydrates — A potential energy source for the 21st Century. *J. Pet. Sci. Eng.* 56 (1). 14–31. DOI: 10.1016/j.petrol.2005.10.009

MAKOGON Y. F. (1997): *Hydrates of hydrocarbons*. Tulsa, OK, USA: Pennwell Books. URL: https://www.osti.gov/biblio/665385.

MAKOGON Y. F. (2010): Natural gas hydrates – A promising source of energy. *J. Nat. Gas Sci. Eng.* 2 (1), 49–59. DOI: 10.1016/j.jngse.2009.12.004

MALAGAR B. R., LIJITH K. and SINGH D. (2019): Formation dissociation of methane gas hydrates in sediments: A critical review. *J. Nat. Gas Eng.* 65, 168–184. DOI: 10.1016/j.jngse.2019.03.005

MARÍN-MORENO H., GIUSTINIANI M., TINIVELLA U. and PIÑERO E. (2016): The challenges of quantifying the carbon stored in Arctic marine gas hydrate. *Mar. Pet. Geol.* 71, 76–82. DOI: 10.1016/j.marpetgeo.2015.11.014

MASTERSON W. D. and HOLBA A. G. (2021): North Alaska Super Basin: Petroleum systems of the central Alaskan North Slope, United States. *AAPG Bull.* 105 (6), 1233–1291. DOI: 10.1306/01282120057

MATSUMOTO R, TOMARU H, CHEN Y. F., LU H, CLARK I and D (2005): Geochemistry of the interstitial waters of the JAPEX/JNOC/GSC et al. Mallik 5L-38 gas hydrate production research well. *Scientific Results from the Mallik 2002 Gas Hydrate Production Research Well Program, Mackenzie Delta, Northwest Territories, Canada*. Vol. 585. Geological Survey of Canada, Bulletin 585, 14. DOI: 10.4095/220764

MATVEEVA T. V., KAMINSKY V. D., SEMENOVA A. A. and SHCHUR N. A. (2020): Factors affecting the formation and evolution of permafrost and stability zone of gas hydrates: Case study of the laptev sea. *Geosci. (Switz.)* 10 (12), 1–21. DOI: 10.3390/geosciences10120504

MAX M. D. and JOHNSON A. H. (2014): Hydrate petroleum system approach to natural gas hydrate exploration. *Pet. Geosci.* 20 (2), 187–199. DOI: 10.1144/petgeo2012-049

MCNEIL D. H., DIETRICH J. R., ISSLER D. R., GRASBY S. E., DIXON J. and STASIUK L. D. (2011): A New Method for Recognizing Subsurface Hydrocarbon Seepage and Migration Using Altered Foraminifera from a Gas Chimney in the Beaufort-Mackenzie Basin. *Shale Tectonics*. American Association of Petroleum Geologists. DOI: 10.1306/13231315M933425

MEDIOLI B., WILSON N, DALLIMORE S., PARÉ D, BRENNAN-ALPERT P. and ODA H (2005): Sedimentology of the cored interval, JAPEX/JNOC/GSC et al. Mallik 5L-38 gas hydrate production research well. *Scientific Results from the Mallik 2002 Gas Hydrate Production Research Well Program, Mackenzie Delta, Northwest Territories, Canada*. Vol. 585. Geological Survey of Canada, Bulletin 585, 21. DOI: 10.4095/220726

MESTDAGH T., POORT J. and DE BATIST M. (2017): The sensitivity of gas hydrate reservoirs to climate change: Perspectives from a new combined model for permafrost-related and marine settings. *Earth-Sci. Rev.* 169, 104–131. DOI: 10.1016/j.earscirev.2017.04.013

MICHAELIDES E. E. (1981): Thermodynamic properties of geothermal fluids. Vol. 5. Univ. of Delaware, Newark. URL: https://www.osti.gov/biblio/6760030.

MILKOV A. V. (2004): Global estimates of hydrate-bound gas in marine sediments: how much is really out there? *Earth-Sci. Rev.* 66 (3-4), 183–197. DOI: 10.1016/j.earscirev.2003.11.002

MILLER R. D., HUNTER J. A., DOLL W. E., CARR B. J. and COLLETT T. S. (2005): High-resolution seismic imaging of the gas hydrate stability zone at the Mallik L-38 research site. *Scientific Results from the Mallik 2002 Gas Hydrate Production Research Well Program, Mackenzie Delta, Northwest Territories, Canada*. Vol. 585. Geological Survey of Canada, Bulletin 585, 14. DOI: 10.4095/220888

MIN S.-K., ZHANG X., ZWIERS F. W. and AGNEW T. (2008): Human influence on Arctic sea ice detectable from early 1990s onwards. *Geophys. Res. Lett.* 35 (21), L21701. DOI: 10.1029/2008GL035725

MORIDIS G. J., KOWALSKY M. B. and PRUESS K. (2005a): *HydrateResSim users manual: A numerical simulator for modeling the behavior of hydrates in geologic media*. Tech. rep. Berkeley, CA (United States): Lawrence Berkeley National Lab. (LBNL).

MORIDIS G. J. (2014): *User's manual for the hydrate v1.5 option of TOUGH+ v1.5: A code for the simulation of system behavior in hydrate-bearing geologic media*. Tech. rep. Berkeley, CA (United States): Lawrence Berkeley National Lab. (LBNL).

MORIDIS G. J. and COLLETT T. S. (2004): Gas Production from Class 1 Hydrate Accumulations. *Advances in the Study of Gas Hydrates*. Boston, MA: Springer US, 83–97. DOI: 10.1007/0-306-48645-8_6

MORIDIS G. J. and REAGAN M. T. (2011): Estimating the upper limit of gas production from Class 2 hydrate accumulations in the permafrost: 1. Concepts, system description, and the production base case. *J. Pet. Sci. Eng.* 76 (3), 194–204. DOI: 10.1016/j.petrol.2010.11.023

MORIDIS G. (2003): Numerical Studies of Gas Production From Methane Hydrates. *SPE J.* 8 (04), 359–370. DOI: 10.2118/87330-PA

MORIDIS G., COLLETT T., DALLIMORE S., INOUE T. and MROZ T. (2005b): Analysis and interpretation of the thermal test of gas hydrate dissociation in the JAPEX/JNOC/GSC et al. Mallik 5L-38 gas hydrate production research well. *Scientific Results from the Mallik 2002 Gas Hydrate Production Research Well Program, Mackenzie Delta, Northwest Territories, Canada*. Vol. 585. Geological Survey of Canada, Bulletin 585, 21. DOI: 10.4095/221045

MORIDIS G. J., COLLETT T. S., POOLADI-DARVISH M., HANCOCK S., SANTAMARINA C., BOSWELL R., KNEAFSEY T., RUTQVIST J., KOWALSKY M. B., REAGAN M. T., SLOAN E. D., SUM A. K. and KOH C. A. (2011): Challenges, Uncertainties, and Issues Facing Gas Production From Gas-Hydrate Deposits. *SPE Reserv. Evaluation Eng.* 14 (01), 76–112. DOI: 10.2118/131792-PA

MOTTAGHY D. and RATH V. (2006): Latent heat effects in subsurface heat transport modelling and their impact on palaeotemperature reconstructions. *Geophys. J. Int.* 164 (1), 236–245. DOI: 10.1111/j.1365-246X.2005.02843.x

MYHRE G., SAMSET B. H., SCHULZ M., BALKANSKI Y., BAUER S., BERNTSEN T. K., BIAN H., BELLOUIN N., CHIN M., DIEHL T., EASTER R. C., FEICHTER J., GHAN S. J., HAUGLUSTAINE D., IVERSEN T., KINNE S., KIRKEVÅG A., LAMARQUE J.-F., LIN G., LIU X., LUND M. T., LUO G., MA X., NOIJE T. van, PENNER J. E., RASCH P. J., RUIZ A., SELAND Ø., SKEIE R. B., STIER P., TAKEMURA T., TSIGARIDIS K., WANG P., WANG Z., XU L., YU H., YU F., YOON J.-H., ZHANG K., ZHANG H. and ZHOU C. (2013): Radiative forcing of the direct aerosol effect from AeroCom Phase II simulations. *Atmos. Chem. Phys.* 13 (4), 1853–1877. DOI: 10.5194/acp-13-1853-2013

NAGASHIMA A. (1977): Viscosity of water substance—new international formulation and its background. *J. Phys. Chem. Ref. Data* 6 (4), 1133–1166. DOI: 10.1063/1.555562

NITZBON J., WESTERMANN S., LANGER M., MARTIN L. C. P., STRAUSS J., LABOOR S. and BOIKE J. (2020): Fast response of cold ice-rich permafrost in northeast Siberia to a warming climate. *Nat. Commun.* 11 (1), 2201. DOI: 10.1038/s41467-020-15725-8

NITZE I., GROSSE G., JONES B. M., ROMANOVSKY V. E. and BOIKE J. (2018): Remote sensing quantifies widespread abundance of permafrost region disturbances across the Arctic and Subarctic. *Nat. Commun.* 9 (1), 5423. DOI: 10.1038/s41467-018-07663-3

NOLE M., DAIGLE H., COOK A. E., MALINVERNO A. and FLEMINGS P. B. (2018): Burial-driven methane recycling in marine gas hydrate systems. *Earth Planet. Sci. Lett.* 499, 197–204. DOI: 10.1016/j.epsl.2018.07.036

OSADETZ K. G., DIXON J, DIETRICH J. R., SNOWDON L. R., DALLIMORE S. R. and MAJOROWICZ J. A. (2005): A review of Mackenzie Delta-Beaufort Sea petroleum province conventional and non-conventional (gas hydrate) petroleum reserves and undiscovered resources : a contribution to the resource assessment of the proposed Mackenzie Delta-Beaufort Sea marine protected area. DOI: 10.4095/220353

OSADETZ K. G. and CHEN Z. (2010): A re-evaluation of Beaufort Sea-Mackenzie Delta basin gas hydrate resource potential: petroleum system approaches to non-conventional gas resource appraisal and geologically-sourced methane flux. *Bull. Can. Pet. Geol.* 58 (1), 56–71. DOI: 10.2113/gscpgbull.58.1.56

O'SULLIVAN M., BODVARSSON G., PRUESS K and BLAKELEY M. (1985): Fluid and Heat Flow In Gas-Rich Geothermal Reservoirs. *Soc. Pet. Eng. J.* 25 (02), 215–226. DOI: 10.2118/12102-PA

OVERDUIN P. P., DEIMLING T. Schneider von, MIESNER F., GRIGORIEV M. N., RUPPEL C., VASILIEV A., LANTUIT H., JUHLS B. and WESTERMANN S. (2019): Submarine Permafrost Map in the Arctic Modeled Using 1-D Transient Heat Flux (SuPerMAP). *J. Geophys. Res. Oceans* 124 (6), 3490–3507. DOI: 10.1029/2018JC014675

PAN L., LEI L. and SEOL Y. (2021): Pore-scale influence of methane hydrate on permeability of porous media. *J. Nat. Gas Eng.* 87, 103758. DOI: 10.1016/j.jngse.2020.103758

PAN M., ISMAIL N. A., LUZI-HELBING M., KOH C. A. and SCHICKS J. M. (2020): New Insights on a µm-Scale into the Transformation Process of CH4 Hydrates to CO2-Rich Mixed Hydrates. *Energies* 13 (22), 5908. DOI: 10.3390/en13225908

PAN M. and SCHICKS J. M. (2021): Influence of Gas Supply Changes on the Formation Process of Complex Mixed Gas Hydrates. *Molecules* 26 (10), 3039. DOI: 10.3390/molecules26103039

PANG X., JIA C., ZHANG K., LI M., WANG Y., PENG J., LI B. and CHEN J. (2020): The dead line for oil and gas and implication for fossil resource prediction. *Earth Syst. Sci. Data* 12 (1), 577–590. DOI: 10.5194/essd-12-577-2020

PANG X.-Q., JIA C.-Z., CHEN Z.-X., SHI H.-S., CHEN Z.-H., HU T., WANG T., XU Z., LIU X.-H., ZHANG X.-W., WANG E.-Z., WU Z.-Y. and PANG B. (2022): Reduction of global natural gas hydrate (NGH) resource estimation and implications for the NGH development in the South China Sea. *Pet. Sci.* 19 (1), 3–12. DOI: 10.1016/j.petsci.2021.12.006

PANIERI G., BÜNZ S., FORNARI D. J., ESCARTIN J., SEROV P., JANSSON P., TORRES M. E., JOHNSON J. E., HONG W., SAUER S., GARCIA R. and GRACIAS N. (2017): An integrated view of the methane system in the pockmarks at Vestnesa Ridge, 79°N. *Mar. Geol.* 390, 282–300. DOI: 10.1016/j.margeo.2017.06.006

PAULL C., MATSUMOTO R. and WALLACE P. (1996): *Proceedings, initial reports, Ocean Drilling Program, Leg 164, gas hydrate sampling on the Blake Ridge and Carolina Rise*. English. ODP, Texas A and M University, College Station.

PHILLIPS S. L. (1981): *A technical databook for geothermal energy utilization*. Tech. rep. Berkeley, CA (United States): Lawrence Berkeley National Lab. (LBNL). URL: https://escholarship.org/uc/item/5wg167jq.

PRIEGNITZ M., THALER J., SPANGENBERG E., RÜCKER C. and SCHICKS J. M. (2013): A cylindrical electrical resistivity tomography array for three-dimensional monitoring of hydrate formation and dissociation. *Rev. Sci. Instrum.* 84 (10), 104502. DOI: 10.1063/1.4825372

PRIEGNITZ M., THALER J., SPANGENBERG E., SCHICKS J. M., SCHRÖTTER J. and ABENDROTH S. (2015): Characterizing electrical properties and permeability changes of hydrate bearing sediments using ERT data. *Geophys. J. Int.* 202 (3), 1599–1612. DOI: 10.1093/gji/ggv245

PRIEST J. A., REES E. V. L. and CLAYTON C. R. I. (2009): Influence of gas hydrate morphology on the seismic velocities of sands. *J. Geophys. Res. Solid Earth* 114 (B11). DOI: 10.1029/2009JB006284

QIN X.-w., LU J.-a., LU H.-l., QIU H.-j., LIANG J.-q., KANG D.-j., ZHAN L.-s., LU H.-f. and KUANG Z.-g. (2020): Coexistence of natural gas hydrate, free gas and water in the gas hydrate system in the Shenhu Area, South China Sea. *China Geol.* 3 (2), 210–220. DOI: 10.31035/cg2020038

RANTANEN M., KARPECHKO A. Y., LIPPONEN A., NORDLING K., HYVÄRINEN O., RUOSTEENOJA K., VIHMA T. and LAAKSONEN A. (2022): The Arctic has warmed nearly four times faster than the globe since 1979. *Environ. Earth Sci.* 3 (1), 168. DOI: 10.1038/s43247-022-00498-3

RIEDEL M., BELLEFLEUR G., MAIR S., BRENT T. A. and DALLIMORE S. R. (August 2009): Acoustic impedance inversion and seismic reflection continuity analysis for delineating gas hydrate resources near the Mallik research sites, Mackenzie Delta, Northwest Territories, Canada. *Geophysics* 74 (5), B125–B137. DOI: 10.1190/1.3159612

RIPMEESTER J., LU H., MOUDRAKOVSKI I., DUTRISAC R., WILSON L., WRIGHT F. and DALLIMORE S. (2005): Structure and composition of gas hydrate in sediment recovered from the JAPEX/JNOC/GSC et al. Mallik 5L-38 gas hydrate production research well, determined by X-ray diffraction and Raman and solid-state nuclear magnetic resonance spectroscopy. *Scientific Results from the Mallik 2002 Gas Hydrate Production Research Well Program, Mackenzie Delta, Northwest Territories, Canada*. Vol. 585. Geological Survey of Canada, Bulletin 585, 6. DOI: 10.4095/220808

RUPPEL C (2015): Permafrost-Associated Gas Hydrate: Is It Really Approximately 1 % of the Global System? *J. Chem. Eng. Data* 60 (2), 429–436. DOI: 10.1021/je500770m

RUPPEL C. D. and KESSLER J. D. (2017): The interaction of climate change and methane hydrates. *Rev. Geophys.* 55 (1), 126–168. DOI: 10.1002/2016RG000534

SA J.-H., KWAK G.-H., HAN K., AHN D., CHO S. J., LEE J. D. and LEE K.-H. (2016): Inhibition of methane and natural gas hydrate formation by altering the structure of water with amino acids. *Sci. Rep.* 6 (1), 1–9. DOI: 10.1038/srep31582

SAFRONOV A., SHITS E., GRIGOR'EV M. and SEMENOV M. (2010): Formation of gas hydrate deposits in the Siberian Arctic shelf. *Russ. Geol. Geophys.* 51 (1), 83–87. DOI: 10.1016/j.rgg.2009.12.006

SAUL A and WAGNER W. (1989): A Fundamental Equation for Water Covering the Range from the Melting Line to 1273 K at Pressures up to 25 000 MPa. *J. Phys. Chem. Ref. Data* 18 (4), 1537–1564. DOI: 10.1063/1.555836

SAUNOIS M., BOUSQUET P., POULTER B., PEREGON A., CIAIS P., CANADELL J. G., DLUGOKENCKY E. J., ETIOPE G., BASTVIKEN D., HOUWELING S., JANSSENS-MAENHOUT G., TUBIELLO F. N., CASTALDI S., JACKSON R. B., ALEXE M., ARORA V. K., BEERLING D. J., BERGAMASCHI P., BLAKE D. R., BRAILSFORD G., BROVKIN V., BRUHWILER L., CREVOISIER C., CRILL P., COVEY K., CURRY C., FRANKENBERG C., GEDNEY N., HÖGLUND-ISAKSSON L., ISHIZAWA M., ITO A., JOOS F., KIM H.-S., KLEINEN T., KRUMMEL P., LAMARQUE J.-F., LANGENFELDS R., LOCATELLI R., MACHIDA T., MAKSYUTOV S., MCDONALD K. C., MARSHALL J., MELTON J. R., MORINO I., NAIK V., O'DOHERTY S., PARMENTIER F.-J. W., PATRA P. K., PENG C., PENG S., PETERS G. P., PISON I., PRIGENT C., PRINN R., RAMONET M., RILEY W. J., SAITO M., SANTINI M., SCHROEDER R., SIMPSON I. J., SPAHNI R., STEELE P., TAKIZAWA A., THORNTON B. F., TIAN H., TOHJIMA Y., VIOVY N., VOULGARAKIS A., WEELE M. van, WERF G. R. van der, WEISS R., WIEDINMYER C., WILTON D. J., WILTSHIRE A., WORTHY D., WUNCH D., XU X., YOSHIDA Y., ZHANG B., ZHANG Z. and ZHU Q. (2016): The global methane budget 2000–2012. *Earth Syst. Sci. Data* 8 (2), 697–751. DOI: 10.5194/essd-8-697-2016

SCHICKS J. M., STRAUCH B, HEESCHEN K. U., SPANGENBERG E and LUZI-HELBING M. (2018): From Microscale (400 μl) to Macroscale (425 L): Experimental Investigations of the CO 2 /N 2 -CH 4 Exchange in Gas Hydrates Simulating the Iġnik Sikumi Field Trial. *J. Geophys. Res. Solid Earth* 123 (5), 3608–3620. DOI: 10.1029/2017JB015315

SCHICKS J. M., PAN M., GIESE R., POSER M., ISMAIL N. A., LUZI-HELBING M., BLEISTEINER B. and LENZ C. (2020): A new high-pressure cell for systematic in situ investigations of micro-scale processes in gas hydrates using confocal micro-Raman spectroscopy. *Rev. Sci. Instrum.* 91 (11), 115103. DOI: 10.1063/5.0013138

SCHICKS J. M., SPANGENBERG E., GIESE R., LUZI-HELBING M., PRIEGNITZ M. and BEESKOW-STRAUCH B. (2013): A Counter-Current Heat-Exchange Reactor for the Thermal Stimulation of Hydrate-Bearing Sediments. *Energies* 6 (6), 3002–3016. DOI: 10.3390/en6063002

SCHICKS J. M., SPANGENBERG E., GIESE R., STEINHAUER B., KLUMP J. and LUZI M. (2011): New approaches for the production of hydrocarbons from hydrate bearing sediments. *Energies* 4 (1), 151–172. DOI: 10.3390/en4010151

SCHLUMBERGER (2012): Petrel Seismic-to-Evaluation Software, Version 2011.2.7.

SCHUUR E. A., ABBOTT B. W., COMMANE R., ERNAKOVICH J., EUSKIRCHEN E., HUGELIUS G., GROSSE G., JONES M., KOVEN C., LESHYK V., LAWRENCE D., LORANTY M. M., MAURITZ M., OLEFELDT D., NATALI S., RODENHIZER H., SALMON V., SCHÄDEL C., STRAUSS J., TREAT C. and TURETSKY M. (2022): Permafrost and Climate Change: Carbon Cycle Feedbacks From the Warming Arctic. *Annu. Rev. Environ. Resour.* 47 (1), 343–371. DOI: 10.1146/annurev-environ-012220-011847

SELL K., QUINTAL B., KERSTEN M. and SAENGER E. H. (2018): Squirt flow due to interfacial water films in hydrate bearing sediments. *Solid Earth* 9 (3), 699–711. DOI: 10.5194/se-9-699-2018

SELL K., SAENGER E. H., FALENTY A., CHAOUACHI M., HABERTHÜR D., ENZMANN F., KUHS W. F. and KERSTEN M. (2016): On the path to the digital rock physics of gas hydrate-bearing

sediments – processing of in situ synchrotron-tomography data. *Solid Earth* 7 (4), 1243–1258. DOI: 10.5194/se-7-1243-2016

SEROV P., PORTNOV A., MIENERT J., SEMENOV P. and ILATOVSKAYA P. (2015): Methane release from pingo-like features across the South Kara Sea shelf, an area of thawing offshore permafrost. *J. Geophys. Res. Earth Surf.* 120 (8), 1515–1529. DOI: 10.1002/2015JF003467

SHAKHOVA N., SEMILETOV I., LEIFER I., SALYUK A., REKANT P. and KOSMACH D. (2010): Geochemical and geophysical evidence of methane release over the East Siberian Arctic Shelf. *J. Geophys. Res.* 115 (C8), C08007. DOI: 10.1029/2009JC005602

SHAKHOVA N., SEMILETOV I., SERGIENKO V., LOBKOVSKY L., YUSUPOV V., SALYUK A., SALOMATIN A., CHERNYKH D., KOSMACH D., PANTELEEV G., NICOLSKY D., SAMARKIN V., JOYE S., CHARKIN A., DUDAREV O., MELUZOV A. and GUSTAFSSON O. (2015): The East Siberian Arctic Shelf: towards further assessment of permafrost-related methane fluxes and role of sea ice. *Philos. Trans. R. Soc. A* 373 (2052), 20140451. DOI: 10.1098/rsta.2014.0451

SIPPEL J., SCHECK-WENDEROTH M., LEWERENZ B. and KLITZKE P. (2015): Deep vs. shallow controlling factors of the crustal thermal field – insights from 3D modelling of the Beaufort-Mackenzie Basin (Arctic Canada). *Basin Res.* 27 (1), 102–123. DOI: 10.1111/bre.12075

SIPPEL J., SCHECK-WENDEROTH M., LEWERENZ B. and KROEGER K. F. (2013): A crust-scale 3D structural model of the Beaufort-Mackenzie Basin (Arctic Canada). *Tectonophysics* 591. 30–51. DOI: 10.1016/j.tecto.2012.10.030

SLOAN E. D. and KOH C. A. (2007): *Clathrate hydrates of natural gases*. 3rd. Boca Raton, FL, USA: CRC press. DOI: 10.1201/9781420008494

SMITH S. L., O'NEILL H. B., ISAKSEN K., NOETZLI J. and ROMANOVSKY V. E. (2022): The changing thermal state of permafrost. *Nat. Rev. Earth Environ.* 3 (1), 10–23. DOI: 10.1038/s43017-021-00240-1

SMITS K. M., SAKAKI T., LIMSUWAT A. and ILLANGASEKARE T. H. (2010): Thermal conductivity of sands under varying moisture and porosity in drainage–wetting cycles. *Vadose Zone J.* 9 (1), 172–180. DOI: 10.2136/vzj2009.0095

SNOWDON L. R. (1999): Methane and carbon dioxide gas-generation kinetics, JAPEX/JNOC/GSC Mallik 2L-38 gas hydrate research well. *Scientific results from JAPEX/JNOC/GSC Mallik 2L-38 gas hydrate research well, Mackenzie Delta, Northwest Territories, Canada*. Vol. 544. Geological Survey of Canada, Bulletin 544, 125–141. DOI: 10.4095/210772

SPANGENBERG E, KULENKAMPFF J, NAUMANN R and ERZINGER J (2005): Pore space hydrate formation in a glass bead sample from methane dissolved in water. *Geophys. Res. Lett.* 32 (24), L24301. DOI: 10.1029/2005GL024107

SPANGENBERG E. (2001): Modeling of the influence of gas hydrate content on the electrical properties of porous sediments. *J. Geophys. Res. Solid Earth* 106 (B4), 6535–6548. DOI: 10.1029/2000JB900434

SPANGENBERG E., HEESCHEN K. U., GIESE R. and SCHICKS J. M. (2020): "Ester"—A new ring-shear-apparatus for hydrate-bearing sediments. *Rev. Sci. Instrum.* 91 (6), 064503. DOI: 10.1063/1.5138696

SPANGENBERG E., PRIEGNITZ M., HEESCHEN K. and M. SCHICKS J. (2014): Are Laboratory-Formed Hydrate-Bearing Systems Analogous to Those in Nature? *J. Chem. Eng. Data* 60 (2), 258–268. DOI: 10.1021/je5005609

STERN L. A., KIRBY S. H. and DURHAM W. B. (1996): Peculiarities of Methane Clathrate Hydrate Formation and Solid-State Deformation, Including Possible Superheating of Water Ice. *Science* 273 (5283), 1843–1848. DOI: 10.1126/science.273.5283.1843

STOCKER T. F., QIN D., PLATTNER G.-K., ALEXANDER L. V., ALLEN S. K., BINDOFF N. L., BRÉON F.-M., CHURCH J. A., CUBASCH U., EMORI S., FORSTER P., FRIEDLINGSTEIN P., GILLETT N., GREGORY J. M., HARTMANN D. L., JANSEN E., KIRTMAN B., KNUTTI R., KRISHNA KUMAR K., LEMKE P., MAROTZKE J., MASSON-DELMOTTE V., MEEHL G. A., MOKHOV I. I., PIAO S., RAMASWAMY V., RANDALL D., RHEIN M., ROJAS M., SABINE C., SHINDELL D., TALLEY L. D., VAUGHAN D. G. and XIE S.-P. (2013): Technical summary. *Climate Change 2013: The Physical Science Basis. Contribution of Working Group I to the Fifth Assessment Report of the Intergovernmental Panel on Climate Change*. Ed. by T. F. STOCKER, D. QIN, G.-K. PLATTNER, M. TIGNOR, S. K. ALLEN, J. DOSCHUNG, A. NAUELS, Y. XIA, V. BEX and P. M. MIDGLEY. Cambridge, UK: Cambridge University Press, 33–115. DOI: 10.1017/CBO9781107415324.005

STRAUCH B., HEESCHEN K. U., SCHICKS J. M., SPANGENBERG E. and ZIMMER M. (2020): Application of tubular silicone (PDMS) membranes for gas monitoring in CO2–CH4 hydrate exchange experiments. *Mar. Pet. Geol.* 122, 104677. DOI: 10.1016/j.marpetgeo.2020.104677

SU Z., CAO Y., WU N., CHEN D., YANG S. and WANG H. (2012): Numerical investigation on methane hydrate accumulation in Shenhu Area, northern continental slope of South China Sea. *Mar. Pet. Geol.* 38 (1), 158–165. DOI: 10.1016/j.marpetgeo.2012.06.005

SUN L., ZHANG G., WANG X., JIN J., HE M. and ZHU Z. (2021): Numerical modeling of gas hydrate saturation for the Shenhu area, South China Sea. *Mar. Geol. Quat. Geol.* 41 (2), 210–221. DOI: 10.16562/j.cnki.0256-1492.2020050501

TALADAY K., BOSTON B. and MOORE G. (2017): Gas-In-Place Estimate for Potential Gas Hydrate Concentrated Zone in the Kumano Basin, Nankai Trough Forearc, Japan. *Energies* 10 (10), 1552. DOI: 10.3390/en10101552

TAYLOR A. E. and JUDGE A. S. (1976): *Canadian geothermal data collection: northern wells, 1975*. Tech. rep., 142. DOI: 10.4095/8415

TAYLOR A. E., DALLIMORE S. R., HILL P. R., ISSLER D. R., BLASCO S. and WRIGHT F. (2013): Numerical model of the geothermal regime on the Beaufort Shelf, arctic Canada since the Last Interglacial. *J. Geophys. Res. Earth Surf.* 118 (4), 2365–2379. DOI: 10.1002/2013JF002859

TAYLOR A. E., DALLIMORE S. R. and WRIGHT J. F. (2008): Thermal impact of Holocene lakes on a permafrost landscape, Mackenzie Delta, Canada. *Ninth international conference on permafrost*, vol. 2. Fairbanks, AK, USA, 1757–1762.

THORNTON J. M., MARIETHOZ G. and BRUNNER P. (2018): A 3D geological model of a structurally complex Alpine region as a basis for interdisciplinary research. *Sci. Data* 5 (1), 180238. DOI: 10.1038/sdata.2018.238

THOUTAM P., REZAEI GOMARI S., AHMAD F. and ISLAM M. (2019): Comparative analysis of hydrate nucleation for methane and carbon dioxide. *Molecules* 24 (6), 1055. DOI: 10.3390/molecules24061055

TRÉHU A. M., RUPPEL C., HOLLAND M., DICKENS G. R., TORRES M. E., COLLETT T. S., GOLDBERG D., RIEDEL M. and SCHULTHEISS P. (2006): Gas Hydrates in Marine Sediments: Lessons from Scientific Ocean Drilling. *Oceanography* 19 (4), 124–142. DOI: 10.5670/oceanog.2006.11

TUPSAKHARE S. S., FITZGERALD G. C. and CASTALDI M. J. (2016): Thermally Assisted Dissociation of Methane Hydrates and the Impact of CO2 Injection. *Ind. Eng. Chem. Res.* 55 (39), 10465–10476. DOI: 10.1021/acs.iecr.6b02509

UDDIN M, WRIGHT J. F., DALLIMORE S. R. and COOMBE D (2012): Gas hydrate production from the Mallik reservoir: numerical history matching and long-term production forecasting. *Scientific results from the JOGMEC/NRCan/Aurora Mallik 2007-2008 gas hydrate production research well program, Mackenzie Delta, Northwest Territories, Canada*. Vol. 601. Geological Survey of Canada, Bulletin 601, 261–289. DOI: 10.4095/292094

UDDIN M., WRIGHT F., DALLIMORE S. and COOMBE D. (2014): Gas hydrate dissociations in Mallik hydrate bearing zones A, B, and C by depressurization: Effect of salinity and hydration number in hydrate dissociation. *J. Nat. Gas. Sci. Eng.* 21, 40–63. DOI: 10.1016/j.jngse.2014.07.027

VESAKOSKI J.-M., NYLEN T., ARHEIMER B., GUSTAFSSON D., ISBERG K., HOLOPAINEN M., HYYPPA J. and ALHO P. (2017): Arctic Mackenzie Delta channel planform evolution during 1983-2013 utilising Landsat data and hydrological time series. English. *Hydrol. Process.* 31 (22), 3979–3995. DOI: 10.1002/hyp.11315

WAGHORN K. A., VADAKKEPULIYAMBATTA S., PLAZA-FAVEROLA A., JOHNSON J. E., BÜNZ S. and WAAGE M. (2020): Crustal processes sustain Arctic abiotic gas hydrate and fluid flow systems. *Sci. Rep.* 10 (1), 10679. DOI: 10.1038/s41598-020-67426-3

WAGNER W. and PRUSS A. (2002): The IAPWS Formulation 1995 for the Thermodynamic Properties of Ordinary Water Substance for General and Scientific Use. *J. Phys. Chem. Ref. Data* 31 (2), 387–535. DOI: 10.1063/1.1461829

WAITE W. F. and SPANGENBERG E (2013): Gas hydrate formation rates from dissolved-phase methane in porous laboratory specimens. *Geophys. Res. Lett.* 40 (16), 4310–4315. DOI: 10.1002/grl.50809

WAITE W., WINTERS W. and MASON D. (2004): Methane hydrate formation in partially water-saturated Ottawa sand. *Am. Mineral.* 89 (8-9), 1202–1207. DOI: 10.2138/am-2004-8-906

WAITE W., BRATTON P. M. and MASON D. H. (2011): Laboratory formation of non-cementing, methane hydrate-bearing sands. *Proceedings of the 7th International Conference on Gas Hydrates (ICGH 2011)*, Edinburgh, Scotland, United Kingdom, Full–paper.

WAITE W. F., SANTAMARINA J. C., CORTES D. D., DUGAN B., ESPINOZA D. N., GERMAINE J, JANG J, JUNG J. W., KNEAFSEY T. J., SHIN H, SOGA K., WINTERS W. J. and YUN T.-S. (2009): Physical properties of hydrate-bearing sediments. *Rev. Geophys.* 47 (4), RG4003. DOI: 10.1029/2008RG000279

WALLMANN K. and SCHICKS J. M. (2018): Gas Hydrates as an Unconventional Hydrocarbon Resource. *In: Wilkes, H. (eds) Hydrocarbons, Oils and Lipids: Diversity, Origin, Chemistry and Fate. (Handbook of Hydrocarbon and Lipid Microbiology), Springer, Cham.*, 1–17. DOI: 10.1007/978-3-319-54529-5_20-1

WANG J. and LAU H. C. (2020): Thickness of gas hydrate stability zone in permafrost and marine gas hydrate deposits: Analysis and implications. *Fuel* 282, 118784. DOI: 10.1016/j.fuel.2020.118784

WANG P., ZHANG X., ZHU Y., LI B., HUANG X., PANG S., ZHANG S., LU C. and XIAO R. (2014): Effect of permafrost properties on gas hydrate petroleum system in the Qilian Mountains, Qinghai, Northwest China. *Environ. Sci.: Process. Impacts* 16 (12), 2711–2720. DOI: 10.1039/c4em00482e

WASEDA A and UCHIDA T (2005): Organic geochemistry of gas, gas hydrate, and organic matter from the JAPEX/JNOC/GSC et al. Mallik 5L-38 gas hydrate production research well. *Scientific Results from the Mallik 2002 Gas Hydrate Production Research Well Program, Mackenzie Delta, Northwest Territories, Canada*. Vol. 585. Geological Survey of Canada, Bulletin 585, 11. DOI: 10.4095/220756

WEI L., COOK A., DAIGLE H., MALINVERNO A., NOLE M. and YOU K. (2019): Factors Controlling Short-Range Methane Migration of Gas Hydrate Accumulations in Thin Coarse-Grained Layers. *Geochem. Geophys. Geosyst.* 20 (8), 3985–4000. DOI: 10.1029/2019GC008405

WEI L., COOK A. and YOU K. (2022): Methane migration mechanisms for the Green Canyon Block 955 gas hydrate reservoir, northern Gulf of Mexico. *AAPG Bull.* 106 (5), 1005–1023. DOI: 10.1306/06022120134

WEI Z., JINQIANG L., PIBO S., JIANGONG W., ZHIBIN S., LIN L., JIN L. and WEI H. (2018): Migrating pathways of hydrocarbons and their controlling effects associated with high saturation gas hydrate in Shenhu area, northern South China Sea. *Geol. China* 45 (1), 1–14. DOI: 10.12029/gc20180101

WETZEL M., KEMPKA T. and KÜHN M. (2021): Diagenetic Trends of Synthetic Reservoir Sandstone Properties Assessed by Digital Rock Physics. *Minerals* 11 (2), 151. DOI: 10.3390/min11020151

WHITE M., KNEAFSEY T., SEOL Y, WAITE W. F., UCHIDA S, LIN J., MYSHAKIN E., GAI X, GUPTA S., REAGAN M. et al. (2020): An international code comparison study on coupled thermal, hydrologic and geomechanical processes of natural gas hydrate-bearing sediments. *Mar. Pet. Geol.* 120, 104566. DOI: 10.1016/j.marpetgeo.2020.104566

WIERSBERG T, ERZINGER J, ZIMMER M, SCHICKS J and DAHMS E (2005): Real-time gas analysis at the JAPEX/JNOC/GSC et al. Mallik 5L-38 gas hydrate production research well. *Scientific Results from the Mallik 2002 Gas Hydrate Production Research Well Program, Mackenzie Delta, Northwest Territories, Canada*. Vol. 585. Geological Survey of Canada, Bulletin 585, 15. DOI: 10.4095/220743

WINTERS W., WALKER M., HUNTER R., COLLETT T., BOSWELL R., ROSE K., WAITE W., TORRES M., PATIL S. and DANDEKAR A. (2011): Physical properties of sediment from the Mount Elbert Gas Hydrate Stratigraphic Test Well, Alaska North Slope. *Mar. Pet. Geol.* 28 (2). 361–380. DOI: 10.1016/j.marpetgeo.2010.01.008

WINTERS W. J., PECHER I. A., WAITE W. F. and MASON D. H. (2004): Physical properties and rock physics models of sediment containing natural and laboratory-formed methane gas hydrate. *Am. Mineral.* 89 (8-9), 1221–1227. DOI: 10.2138/am-2004-8-909

WOO M.-k. (2012): *Permafrost Hydrology*. Berlin, Heidelberg: Springer. DOI: 10.1007/978-3-642-23462-0

WRIGHT J. F., DALLIMORE S. R., NIXON F. M. and DUCHESNE C (2005): In situ stability of gas hydrate in reservoir sediments of the JAPEX/JNOC/GSC et al. Mallik 5L-38 gas hydrate production research well. *Scientific Results from the Mallik 2002 Gas Hydrate Production Research Well Program, Mackenzie Delta, Northwest Territories, Canada*. Vol. 585. Geological Survey of Canada, Bulletin 585, 11. DOI: 10.4095/220742

WU C.-Y. and HSIEH B.-Z. (2020): Comparisons of different simulated hydrate designs for Class-1 gas hydrate deposits. *J. Nat. Gas. Sci. Eng.* 77, 103225. DOI: 10.1016/j.jngse.2020.103225

WU N. you, LIU C. ling and HAO X. luo (2018): Experimental simulations and methods for natural gas hydrate analysis in China. *China Geology* 1 (1), 61–71. DOI: 10.31035/cg2018008

XIA Y., YANG J., CHEN Y., LU S., WANG M., DENG S., YAO Z. and LU M. (2022): A Review of the Global Polygonal Faults: Are They Playing a Big Role in Fluid Migration? *Front. Earth Sci.* 9. DOI: 10.3389/feart.2021.786915

YAKUSHEV V., SEMENOV A., BOGOYAVLENSKY V., MEDVEDEV V. and BOGOYAVLENSKY I. (2018): Experimental modeling of methane release from intrapermafrost relic gas hydrates when sediment temperature change. *Cold Reg. Sci. Technol.* 149, 46–50. DOI: 10.1016/j.coldregions.2018.02.007

YE J., QIN X., XIE W., LU H., MA B., QIU H., LIANG J., LU J., KUANG Z.-g., LU C., LIANG Q.-y., WEI S.-p., YU Y.-j., LIU C.-s., LI B., SHEN K.-x., SHI H.-x., LU Q.-p., LI J., KOU B.-b., SONG G., LI B.,

ZHANG H.-e., LU H.-f., MA C., DONG Y.-f. and BIAN H. (2020): The second natural gas hydrate production test in the South China Sea. *China Geol.* 3 (2), 197–209. DOI: 10.31035/cg2020043

YIN Z., CHONG Z. R., HOON K. T. and LINGA P. (2019a): Effect of Multi-Stage Cooling on the Kinetic Behavior of Methane Hydrate Formation in Sandy Medium. *Energy Procedia* 158, 5374–5381. DOI: 10.1016/j.egypro.2019.01.627

YIN Z., CHONG Z. R., TAN H. K. and LINGA P. (2016): Review of gas hydrate dissociation kinetic models for energy recovery. *J. Nat. Gas Sci. Eng.* 35, 1362–1387. DOI: 10.1016/j.jngse.2016.04.050

YIN Z., KHURANA M., TAN H. K. and LINGA P. (2018a): A review of gas hydrate growth kinetic models. *Chem. Eng. J.* 342, 9–29. DOI: 10.1016/j.cej.2018.01.120

YIN Z., MORIDIS G., CHONG Z. R. and LINGA P. (2019b): Effectiveness of multi-stage cooling processes in improving the CH4-hydrate saturation uniformity in sandy laboratory samples. *Appl. Energy* 250, 729–747. DOI: 10.1016/j.apenergy.2019.05.077

YIN Z., MORIDIS G., TAN H. K. and LINGA P. (2018b): Numerical analysis of experimental studies of methane hydrate formation in a sandy porous medium. *Appl. Energy* 220, 681–704. DOI: 10.1016/j.apenergy.2018.03.075

YOU K., FLEMINGS P., MALINVERNO A., COLLETT T. and DARNELL K. (2019): Mechanisms of Methane Hydrate Formation in Geological Systems. *Rev. Geophys.* 57 (4), 1146–1196. DOI: 10.1029/2018RG000638

YOU K. and FLEMINGS P. B. (2018): Methane Hydrate Formation in Thick Sandstones by Free Gas Flow. *J. Geophys. Res. Solid Earth* 123 (6), 4582–4600. DOI: 10.1029/2018JB015683

YUN T. S., FRANCISCA F. M., SANTAMARINA J. C. and RUPPEL C. (2005): Compressional and shear wave velocities in uncemented sediment containing gas hydrate. *Geophys. Res. Lett.* 32 (10), L10609. DOI: 10.1029/2005GL022607

ZHANG F.-g., SUN Z.-j., YANG Z.-b. and ZHOU Y.-l. (2019): Geochemical Investigation of Gas Hydrate in the Permafrost Area, China. *Bull. Mineral. Petrol. Geochem.* 38 (6). 1224–1234.

ZHANG L., KUANG Y., ZHANG X., SONG Y., LIU Y. and ZHAO J. (2017a): Analyzing the process of gas production from methane hydrate via nitrogen injection. *Ind. Eng. Chem. Res.* 56 (26), 7585–7592. DOI: 10.1021/acs.iecr.7b01011

ZHANG W., LIANG J., LIANG Q., WEI J., WAN Z., FENG J., HUANG W., ZHAO J., MENG M., DENG W. and CHEN C. (2021): Gas Hydrate Accumulation and Occurrence Associated with Cold Seep Systems in the Northern South China Sea: An Overview. *Geofluids* 2021, 1–24. DOI: 10.1155/2021/5571150

ZHANG W., LIANG J., LU J., WEI J., SU P., FANG Y., GUO Y., YANG S. and ZHANG G. (2017b): Accumulation features and mechanisms of high saturation natural gas hydrate in Shenhu Area, northern South China Sea. *Pet. Explor. Dev.* 44 (5), 708–719. DOI: 10.1016/S1876-3804(17)30082-4

ZHENG R., LI S. and LI X. (2018): Sensitivity analysis of hydrate dissociation front conditioned to depressurization and wellbore heating. *Mar. Pet. Geol.* 91, 631–638. DOI: 10.1016/j.marpetgeo.2018.01.010

ZHU Y.-h., RAO Z. and WU B. (2005): Composition and origin of low-molecular-weight hydrocarbons in the gas-hydrate-bearing sediments from the JAPEX/JNOC/GSC et al. Mallik 5L-38 gas hydrate production research well. *Scientific Results from the Mallik 2002 Gas Hydrate Production Research Well Program, Mackenzie Delta, Northwest Territories, Canada*. Vol. 585. Geological Survey of Canada, Bulletin 585, 9. DOI: 10.4095/220761

ZHU Y., PANG S.-j., XIAO R., ZHANG S. and LU Z. (2021): Natural gas hydrates in the Qinghai-Tibet Plateau: Characteristics, formation, and evolution. *China Geol.* 4 (1), 17–31. DOI: 10.31035/cg2021025

Publications of the author

Li, Z., Chabab E., Spangenberg E., Schicks M. J. and Kempka, T. (2023): Geologic controls on the genesis of the methane hydrate-bearing system in the Beaufort-Mackenzie Delta, Canada. *Frontiers in Earth Science*, 11, 1148765. DOI: 10.3389/feart.2023.1148765

Li, Z., Spangenberg E., Schicks M. J. and Kempka, T. (2022a): Numerical simulation of coastal sub-permafrost gas hydrate formation in the Mackenzie Delta, Canadian Arctic. *Energies*, 15, 14, 4986. DOI: 10.3390/en15144986

Li, Z., Spangenberg E., Schicks M. J. and Kempka, T. (2022b): Numerical simulation of hydrate formation in the LArge-Scale Reservoir Simulator (LARS). *Energies*, 15, 6, 1974. DOI: 10.3390/en15061974

Acknowledgements

The present thesis was financially supported by China Scholarship Council (CSC) and German Research Foundation (DFG).

To start with, I would like to thank my scientific advisors, who made it possible for me to get my dissertation started and completed. First of all, I would like to express my sincere gratitude to Dr. Thomas Kempka, who supervised me during my doctoral study. His efficiency and enthusiasm in scientific research always admired me, and his timely criticism, which I apparently deserved more, educated me. His sense of humour and comprehensive support inspired and guided me through my work. It is my honour to be his student. I am very grateful to my primary supervisor and our section leader, Prof. Michael Kühn, for hosting me in the section of Fluid Systems Modelling, GFZ, as well as in the Institute of Geosciences, University of Potsdam, for organizing weekly section meetings, seasonal events, and annual retreats I took part in, and for our fruitful scientific discussions.

Further, I would like to acknowledge Prof. Judith Schicks and Prof. Ann Cook for agreeing to review this work. Particularly, I thank Prof. Yinxin Zhang, who introduced me to geoscience many years ago and became a good friend. Finally, I reserve my special appreciation to our research partner, Dr. Erik Spangenberg, who actually opened the door for me to enter not only GFZ but also the international academic community through his constant encouragement and for profusely offering his time and expertise. These people are greatly responsible for my growth as a specialist.

I would also like to thank Dr. Elena Chabab and Dr. Peter Berger for proofreading parts of this thesis, as well as Dr. Natalie Nakaten, Dr. Marco De Lucia, Dr. Christopher Otto, Dr. Theresa Hennig, Dr. Maria Wetzel, Dr. Sonja Martens, Evans Manu, Tobias Schnepper, Marie Bonitz, and others, who generously shared their expertise and experience.

I would like to thank my colleagues, who helped to develop and mature our scientific models and papers my co-authors Dr. Elena Chabab, Dr. Erik Spangenberg, Prof. Judith Schicks, and particularly Benjamin Nakaten, who helped me a lot during my utilization of *geomodelator*. I so appreciate our active academic community in Potsdam, and I want to thank all of my friends here for such an enjoyable and exciting time, shared hours of scientific discussions, biking, and hiking. I owe thanks to Jianli Ma for being a special officemate.

Many thanks to Jenny Meistring for her excellent administrative work and her generous, sincere advice for my daily life.

I owe immeasurable gratitude to those whom I left in China, but I have always felt their everlasting support – my parents, grandmother, relatives, friends, and my favorite cities, Quqing, Taiyuan, Harbin, Guangzhou, and Hong Kong. My most enormous acknowledgment goes to my mother, who is always with me and continuously inspires, overcomes, shares, sustains, supports, and loves.

Selbstständigkeitserklärung

Hiermit erkläre ich, Zhen Li, dass ich als Autor der vorliegenden Dissertation mit dem Titel "*Formation of Sub-Permafrost Methane Hydrate Reproduced by Numerical Modeling: Insights from LArge-Scale Reservoir Simulator (LARS) to Mallik Site, Canadian Arctic*", die Arbeit selbstständig und ohne unerlaubte Hilfe angefertigt habe.

Ferner versichere ich, keine anderen als die angegebenen Quellen und Hilfsmittel benutzt zu haben. Alle Ausführungen, die anderen Schriften wörtlich oder inhaltlich entnommenen wurden, sind als solche kenntlich gemacht. Die vorliegende Arbeit wurde in keinem anderen Promotionsverfahren angenommen oder abgelehnt.

_____

Potsdam, 23.06.2023